

Studies on the function of PRG2/PLPPR3 in neuron morphogenesis

Inaugural-Dissertation
to obtain the academic degree
Doctor rerum naturalium (Dr. rer. nat.)

submitted to the Department of Biology, Chemistry, Pharmacy
of Freie Universität Berlin

by

Joachim Fuchs

2021

The work presented in this thesis was conducted from July 2016 to July 2021 under the supervision of Prof. Dr. Britta Johanna Eickholt at the Institute for Molecular Biology and Biochemistry at Charité, Universitätsmedizin, Berlin.

1. Reviewer: Prof. Dr Britta Johanna Eickholt

2. Reviewer: Prof. Dr. Helge Ewers

Date of disputation: 05.01.2022

TABLE OF CONTENTS

Summary	1
Zusammenfassung	2
1 Introduction	3
1.1 Brain function depends on proper development of neuron morphology	4
1.2 Programs of neuron morphogenesis	7
1.3 Orchestrating morphogenesis	12
1.4 PLPPRs are plasticity-related genes with homology to lipid phosphatases	15
1.5 Objectives of this thesis	17
2 Mapping function to PLPPR3 domains	21
2.1 PLPPR3 is a neuron-specific, axon-enriched transmembrane protein	21
2.2 PLPPR3 increases filopodia on N1E-115 cells	25
2.3 Plasma membrane localisation is regulated by conserved domains of PLPPRs	28
2.4 Summary and outlook: Domain mapping provides tools to precisely study PLPPR3	34
3 Generating a <i>Plppr3</i>^{-/-} mouse using CRISPR/Cas9	36
3.1 First exon of <i>Plppr3</i> is a suitable target for preventing <i>Plppr3</i> expression	36
3.2 Excision of exon 1 results in full knockout of <i>Plppr3</i> expression	40
3.3 Summary and outlook: Strategies for creating a conditional PLPPR3 knockout	43
4 PLPPR3 redirects growth to branches	44
4.1 Overall development of neurons is not disturbed in <i>Plppr3</i> ^{-/-}	44
4.2 <i>Plppr3</i> ^{-/-} neurons branch less in vitro	45
4.3 PLPPR3 and the PI3K pathway regulate branching cooperatively	50
4.4 Summary and outlook: Further phenotyping of <i>Plppr3</i> ^{-/-} animals	54

TABLE OF CONTENTS

5	Precursor types predict the stability of neuron branches	56
5.1	Branch stability depends on precursor and neurite type	56
5.2	Removing efficient precursors reduces overall branch stability	59
5.3	Summary and outlook: How could precursors modify branch stability	63
6	Discussion	64
6.1	PLPPR3 and PI3K/PTEN mediated branch formation	64
6.2	Regulating PLPPR3 to regulate efficient branch formation	71
6.3	PLPPR3-induced filopodia branching as an independent morphogenetic rule	73
6.4	Conclusion	75
7	Appendix	76
7.1	Visualising membrane phosphoinositides	77
7.2	Image analysis tools	82
7.3	Fully automated branch classification in developing cultured neurons	86
8	Experimental details	94
9	References	115
	Publications related to this thesis	134
	Statement of authorship	135
	Acknowledgements	136

SUMMARY

Neuron development follows a multifaceted sequence of cell migration, polarisation, neurite elongation, branching, tiling, and pruning. The implementation of this sequence differs between neuronal cell types and even in individual neurons between sub-compartments such as dendrites and axons. Membrane proteins are at a prime position in neurons to couple extrinsic morphogenetic signals with their intrinsic responses to orchestrate this defined morphological progression. The Phospholipid phosphatase-related / Plasticity-related gene (PLPPR/PRG)-family comprises five neuron-enriched and developmentally regulated membrane proteins with functions in cellular morphogenesis. At the start of this project, no publication had characterised the function of PLPPR3/PRG2 during neuron development.

The presented work describes PLPPR3 as an axon-enriched protein localising to the plasma membrane and internal membrane compartments of neurons. Mutagenesis studies in cell lines establish the plasma membrane localisation of PLPPR3 as a regulator of its function to increase filopodia density (Chapter 2). Furthermore, the generation of a *Plppr3*^{-/-} mouse line using CRISPR/Cas9 genome editing techniques (Chapter 3) enabled characterising endogenous phenotypes of PLPPR3 in neurons. In primary neuronal cultures, PLPPR3 was found to specifically control branch formation in a pathway with the phosphatase PTEN, without altering the overall growth capacity of neurons (Chapter 4). Loss of PLPPR3 specifically reduced branches forming from filopodia without affecting the stability of branches. This precise characterisation of PLPPR3 function unravelled the existence of parallel, independent programs for branching morphogenesis that are utilised and implemented differentially in developing axons and dendrites (Chapter 5). Furthermore, this thesis establishes multiple tools to study PLPPR3, the membrane lipid phosphatidylinositol-trisphosphate, and neuron morphogenesis by providing molecular tools, protocols, and semi-automated and automated image analysis pipelines (Appendix Chapter 7) and discusses experiments to test, refine and extend models of PLPPR3 function (Chapter 6).

In summary, this thesis generated and utilised several tools and a *Plppr3*^{-/-} mouse model to characterise PLPPR3 as a specific regulator of neuron branching morphogenesis. This precise characterisation refined and expanded the understanding of axon-specific branching morphogenesis.

ZUSAMMENFASSUNG

Nervenzellen entwickeln ihre komplexe Morphologie durch das Zusammenwirken diverser molekularer Entwicklungs-Programme der Zellkörper-Migration, der Polarisierung und der Morphogenese durch Wachstum, Verzweigung, Stabilisierung und Koordinierung ihrer Neuriten. Dabei unterscheidet sich die exakte Implementierung zwischen Nervenzell-Typen und selbst innerhalb einzelner Zellen zwischen Axonen und Dendriten. Diese unterschiedliche Morphogenese wird dabei speziell durch Membranproteine stark beeinflusst, die durch ihre Präsenz an der Plasmamembran Zell-extrinsische Signale mit den Zell-intrinsischen Morphogeneseprogrammen verbinden und beeinflussen. Die Familie der Phospholipid phosphatase-related / Plasticity-related gene (PLPPR/PRG) Proteine umfasst fünf Nervenzell-spezifische Membranproteine mit Effekten auf die Morphologie von Zellen. Zu Beginn dieses Projektes hatte noch keine Studie die Funktion des Familienmitglieds PLPPR3/PRG2 in Nervenzellen untersucht.

Diese Dissertation beschreibt die Lokalisation von PLPPR3 an der Plasmamembran und in Zell-internen Membranstrukturen von Nervenzellen. Experimente in Zellkultur zeigen eine erhöhte Filopodien-Dichte nach Überexpression von PLPPR3, Mutagenese-Studien deuten eine strikte Kontrolle der Plasmamembran-Lokalisation an (Kapitel 2). Die Generierung einer *Plppr3* Knockout Mauslinie mittels CRISPR/Cas9 Genom-Modifizierung (Kapitel 3) erlaubte eine Charakterisierung der endogenen Funktion von PLPPR3 in Nervenzellen. In Primärzellkultur von Nervenzellen des murinen Hippocampus zeigte sich, dass PLPPR3 im Zusammenspiel mit der Phosphatase PTEN spezifisch die Verzweigung von Nervenzellen kontrolliert, ohne deren Wachstumspotential global zu verändern (Kapitel 4). Dadurch kann PLPPR3 als ein Schalter zwischen Verzweigung und Verlängerung eines Nervenzell-Fortsatzes agieren. Der Verlust von PLPPR3 verursachte reduzierte spezifisch die Anzahl an Verzweigungen, die aus Filopodien entstanden, ohne dabei die Stabilität dieser Verzweigungen zu beeinflussen. Die präzise Charakterisierung dieser Funktion von PLPPR3 deckte auf, dass Verzweigungen von Nervenzell-Fortsätzen durch voneinander unabhängige Entwicklungsprogramme ausgebildet und stabilisiert werden können (Kapitel 5). Diese Programme werden von Axonen und Dendriten in unterschiedlicher Weise eingesetzt. Zusätzlich etabliert diese Arbeit sowohl diverse molekulare Werkzeuge und Visualisierungs-Protokolle zur Analyse von PLPPR3 und dem Membranlipid Phosphatidylinositol-Trisphosphat, als auch automatisierte Quantifizierungssoftware zur Studie der Nervenzellmorphologie (Appendix-Kapitel 7). Abschließend entwickelt und verfeinert die Dissertation mögliche Modelle zur PLPPR3-Funktion und zeigt experimentelle Strategien auf, um diese Modelle besser charakterisieren zu können (Kapitel 6).

Zusammenfassend wurden in dieser Promotionsarbeit diverse Experimental- und Analyse-Strategien und eine *Plppr3*^{-/-} Mauslinie entwickelt und genutzt, um PLPPR3 als einen spezifischen Regulator der Nervenzell-Morphogenese zu etablieren. Diese präzise Charakterisierung des PLPPR3 Phänotyps erlaubte zusätzlich eine Verfeinerung und Erweiterung der Erkenntnisse zur Axon-spezifischen Entwicklung von Verzweigungen.

1 INTRODUCTION

1.1 Brain function depends on proper development of neuron morphology	4
1.1.1 Neurons find their place – migration	5
1.1.2 Specialising input and output regions – polarisation	5
1.2 Programs of neuron morphogenesis	7
1.2.1 Growing the tree – Elongation	7
1.2.2 Covering and reaching multiple areas – Arborisation and branching	8
1.2.3 Limiting growth for specificity – Tiling and pruning	9
1.2.4 Axon morphogenesis requires specific programs	10
1.3 Orchestrating morphogenesis	12
1.3.1 External guidance of growth is modified intrinsically	12
1.3.2 Plasma membrane proteins and lipids relay and modify morphogenetic signals	13
1.4 PLPPRs are plasticity-related genes with homology to lipid phosphatases	15
1.4.1 PLPPRs are neuron-enriched and developmentally regulated	15
1.4.2 PLPPRs are connected to diseases of cellular morphology	15
1.4.3 PLPPRs change excitability, guidance, and morphology of neurons	16
1.5 Objectives of this thesis	17

1.1 BRAIN FUNCTION DEPENDS ON PROPER DEVELOPMENT OF NEURON MORPHOLOGY

Neurons differ from most other cell types by being postmitotic, electrically active and by adopting a highly polarised, characteristic complex morphology. Their concerted action enables autonomous behaviour of animals, allowing them to act, to sense and remember the effects of their actions, and to subsequently plan and execute modified actions.¹

Precise and plastic connectivity is vital in these processes. Psychology and cognitive science study how short- and long-range connections of specialised brain regions give rise to specific behaviours, whereas electrophysiology aims to understand the precise functional connectivity between cell types in specific brain regions and its consequences on signal processing. Networks such as the hippocampal or cortical microcircuits can generate modules capable of information processing operations that are used in parallel or serially to enable a vast range of possible functions.

It is very apparent in the brain that the morphology of neurons shapes this connectivity. Lateral arrangement of cell types with similar morphology allows for establishing specialised input and output regions in cortical layers. The size, density, and shape of dendritic input regions of individual neurons define the size, sensitivity, and specialisation of receptive fields.² Even the exact locations of synaptic contacts on dendrites can profoundly affect the computation in individual cells.³ On top of these preformed configurations, neurons can plastically strengthen or weaken connections to modulate the functional connectivity upon experience.

Interestingly, as artificial neuronal networks⁴ impressively have shown over the last decades, even solely experience-dependent remodelling of random connections can generate specific connectivity patterns and enable powerful computation. However, the brain does not start as a randomly connected network. Brains are remarkably similar between individuals and even between species, thereby conserving advantageous signal processing and behaviour during evolution. Furthermore, recent models envision the brain as capable of producing 'good enough' generalisations most of the time that can be refined in specific situations.¹ Current artificial neuronal networks are only capable of generating context-dependent connections by reducing a (often fully-connected) network. Therefore, to generate robust 'generaliser networks' in the brain, most connections are likely already prevented from forming during development.^{1,5}

Unsurprisingly, development and disease of the central nervous system are tightly coupled. Alterations of the implementation or orchestration of neuron morphogenesis are associated with neurodevelopmental disorders such as autism spectrum disorder, intellectual disabilities, attention deficit hyperactivity disorder, and epilepsy.⁶ Pathological reinitiation of stem cell capacities underlies the formation of tumours in the brain.⁷ However, the restart of developmental programs is also discussed as a treatment strategy after traumatic brain injury.⁸

Therefore, characterising neuron morphogenesis and development provides complementary information to the electrophysiological description of adaptive changes in existent connections and will likely deepen our understanding of cognitive processing and disease.

1.1.1 Neurons find their place – migration

The precise arrangement of neurons and connections follows a sequence of cell division, migration, and polarisation before cell-type-specific morphogenesis and refinement programs establish the network that lets us think and act.

During early embryogenesis, ectodermal structures undergo stereotypic proliferation and folding patterns resulting in the generation of a neural tube. The inside of the tube further matures to the ventricular system of the brain, while symmetric divisions of neuroepithelial precursor cells in the ventricular and subventricular zone enlarge the pool of precursors.⁹ The remarkable speed of adding approximately 3.6 million cells per hour during human brain development partially explains the high energy demand of early developing brains compared to other organs.¹⁰ Starting already during proliferation phases of precursor cells, asymmetrical divisions from these precursors create neurons and macroglia in the central nervous system.⁹

Excitatory cells of the neocortex originate either directly from radial glia cells or from radial-glia-derived neural stem cells.⁹ These newly born neurons migrate along radial glia processes towards the cortical surface. The timepoint of cell birth correlates with the final layer of the neuron.^{9,10} Lower layers form before upper layers in all cortical areas even though the thickness of individual layers differs depending on the brain region (e.g., sensory cortex shows a very prominent layer IV which is less apparent in motor cortex).¹¹ The specific area patterning occurs via signalling gradients and is modulated by differential gene expression and area-specific axonal input from the thalamus.^{11,12}

GABAergic interneurons divide in the ganglionic eminences of basal ganglia precursors and migrate tangentially to their target area and layer and then populate it by radial migration.¹² The medial and caudal regions of the ganglionic eminence create distinct pools of interneurons with some evidence for a temporal code of cell type formation and migration patterns.^{12,13} The timepoints of birth are comparable for GABAergic and glutamatergic neurons. However, GABAergic neuron morphogenesis seems to be affected by circuit features of glutamatergic neurons and therefore occur later.¹⁴

Interestingly, for both excitatory and inhibitory neurons, long-range connecting neurons seem to be born before short-range connecting neurons: GABAergic projection neurons in the striatal globus pallidus form earliest, while more short-range acting cortical GABAergic interneurons develop later.¹² Also lower layer and corticofugal projecting excitatory neurons emerge before intracortical projection neurons.¹⁵ Rather than having to grow extensive lengths, projecting neurons might establish connections as long as distances are still comparably short to then increase their axon length by scaling and stretching mechanisms.¹⁶

1.1.2 Specialising input and output regions – polarisation

After finding the position of their cell body, the neuronal processes develop, specialise, and refine their morphology. Early developing neurons form many short and dynamic protrusions, their neurites. These neurites initially have an equal growth capacity until one of the neurites accelerates growth rapidly and matures into the future output region of the neuron, the axon, in a process termed polarisation. After the axon and its branches elaborated, the remaining neurites mature into the future input

regions, the dendrites. Synaptic contacts ultimately connect axons and dendrites of individual neurons to enable signal transduction. This stereotypic morphogenesis program has been described by Banker et al. in 1988 and divides these processes into five sequential stages.^{17,18}

While localised activity of various factors has been described to trigger polarisation, deletion of many of these factors does not abolish polarisation, and neurons in culture polarise without localised extrinsic signals.^{18,19} Interestingly, intracellularly only few factors are sufficient, necessary, and specifically enriched at the site before axon formation: the signalling related molecules Ras, cyclic adenosine monophosphate (cAMP) and protein kinase A (PKA), phosphatidylinositol-3,4,5-trisphosphate (PIP3) and phosphatidylinositol 3 kinase (PI3K), and phosphorylated liver kinase B1 (LKB1, the mammalian homolog of the Par-complex member Par4).¹⁹ The localised activation or production of these signalling molecules is thought to initially break the symmetry. In absence of extrinsic input, stochastic activity fluctuations of these polarising factors are thought to initially break symmetry.

Mechanistically, polarisation is executed by intrinsic feedback and feedforward activation of polarisation mediating signalling pathways in the future axon, as well as inhibition of these events in other neurites.^{18,19} A powerful local positive feedback loop has been described for PI3K-activity, which directly activates itself through feedback of downstream Rho GTPases,²⁰ and induces autocrine secretion of PI3K-activating neurotrophic factors.²¹ The signalling of PI3K and phosphoinositides will be further discussed in subsequent sections. However, this example illustrates well, how an initially small PI3K-signal can set off a self-amplifying cascade of events capable of majorly reorganising a neurite to become the future axon. Such self-organising processes that are triggered by local signals appear to be common in neuron morphogenesis and will be discussed further in subsequent sections.

To ensure proper polarisation of only one axon, developing neurons also have to prevent this process in the remaining neurites. The exact mechanisms of how an axon signals the polarisation of an axon to other neurites are still under investigation.¹⁹ However, as a consequence of this signal, the other neurites downregulate abundance or activation of the polarising factors discussed above, as exemplified by a local reduction of cAMP levels²² or proteolytic degradation of downstream effectors of the PI3K pathway.²³

How these axon- and neurite-specific signals initiate distinct remodelling mechanisms in the developing axons and neurites is at the core of this thesis and will be discussed in detail in the following section. The close interdependence of morphogenesis and polarisation, however complicates studying both events separately.¹⁸ Furthermore, many of these data have been studied in primary hippocampal and cortical neuron cultures. In vivo, cortical neurons have been described to polarise during migration along radial glia cells where they form a leading process guiding them to the correct layer. This earliest process subsequently matures into the apical dendrite. A second, so called trailing process during this migration is stabilised to form the future axon.¹⁸ Therefore, the previously discussed 'axon-first' model of polarisation might be masked in vivo, or it might not be the only mechanism in which neurons initiate their morphogenesis.¹⁹

1.2 PROGRAMS OF NEURON MORPHOGENESIS

No individual neuron has the exact same morphology as another neuron. Nonetheless, cell types share a general shape as illustrated by cortical pyramidal cells or cerebellar Purkinje cells that have a random branching pattern in their dendritic compartment that nevertheless occupies a stereotypic area.²⁴ It is therefore highly unlikely that the exact positions of branches, let alone synapses are genetically predetermined in a 'genetic blueprint'.²⁴ In contrast, neurons likely rely on a genetically determined set of morphogenetic programs that exploits stochastic modification to ensure robust generation of non-identical but similar morphologies.^{24,25}

On the molecular level, such programs could be conceived as self-organised intrinsic growth programs that are triggered by external inputs and stochastic activity-fluctuations of the triggering pathways. The previous section on polarisation already discussed an example of such a program, and similar higher-level programs are proposed to exist for other steps of neuron morphogenesis.² This section will focus on programs mediating the intrinsic capacity to grow, the optimal coverage of area via branching and tiling, and the subsequent refinement of connections via pruning mechanisms.

While these programs are very powerful in describing specific outcomes of morphogenesis, they nevertheless are likely an incomplete set that includes artificially broad categories. It is unclear whether the molecular implementation of the programs is entirely separable, as many studies do not distinguish effects on specific programs or find effects at multiple levels of morphogenesis. Furthermore, the morphological outcomes of some specified programs such as branching morphogenesis can alternatively emerge from a combination of other morphogenetic programs such as elongation and tiling. Therefore, not every program might be necessary for every cell type, developmental stage, or even compartment of a neuron.

Nevertheless, the spatial and temporal induction of similar programs is capable of reproducing diverse dendritic morphologies in modelling studies.²⁶ Furthermore, the discussed morphogenetic programs could reduce the complexity of a 'blueprint' to generate cell-type- and compartment-specific morphology.²⁴ Lastly, they provide an intuitive framework to more precisely define the function of specific proteins in neuron morphogenesis, as applied in this thesis for PLPPR3.

1.2.1 Growing the tree – Elongation

Growth is at the base of all other morphogenetic programs; it determines the receptivity of neurons at the dendritic level and the number or distance of neurons connected with the axon. Growth is both essential for establishing the initial connections of neurons as well as for scaling the established networks and neuron morphologies with the size of the body.²

Cell growth is mediated by the overall supply of energy and by synthesis, transport, and diffusion of building blocks such as proteins and lipids. Interestingly, the synthesis rate – as visible from the size of neuronal soma – correlates strongly with the length and thickness of neuronal arbours.²⁷ Neuron growth is regulated by major anabolic pathways that also control growth in other cell types.²⁸ The PI3K/AKT/mTOR pathway is a crucial regulator, as illustrated by the increased soma and arbour size of neurons deficient for the inhibitor of the pathway, phosphatase and tensin homolog (PTEN).²⁹

Due to the complexity of their arbours, neurons have a huge membrane-to-cytosol ratio, which creates an extraordinarily high demand for lipid uptake, synthesis, and transport.³⁰ During initial elongation, this membrane is mainly delivered to the growing ends of the axon and dendrites by exocytic events.³¹ The exact location and mechanism for lipid delivery during stretching phases of neurons¹⁶ that already have connected to their target region is still under investigation.³⁰

Synthesis and production surface material can, however, not fully explain the complex morphology of neurons. To structure their surface, neurons require a stable cytoskeleton with microtubules and neurofilaments providing core stability of neurites and actin linking and stabilising more delicate membrane structures such as dendritic spines. Neurites are further stabilised and arranged through neuron-specific tubulin subunits, microtubule-associated proteins, and microtubule-modifying enzymes.^{32,33}

To elongate these stable structures in specific directions, developing dendrites, branches and axons form dynamic growth cones at their tip.³⁴ Growth cones comprise a stereotypical arrangement of F-actin structures consisting of crosslinked lamellipodia and parallel fibered filopodia at their tip. These distal F-actin networks both increase sensitivity to external cues and steer the growth cone.³⁵ At the base of growth cones, a tight F-actin arc presents a border for parallel microtubule bundles to push against. Both dynamic microtubule polymerisation and invasion of microtubules into filopodia are required for elongation of the neurite.^{36,37} While in vitro, elongation clearly depends on adhesion of growth cones to the substrate – by a ‘molecular clutch’ mechanism to pull growth forward³⁸ – the relevance of adhesion for elongation rather than steering in three-dimensional cultures and in vivo is still debated.³⁹

In summary, neuron growth is a global phenomenon dependent on synthesis and supply, while the elongation of neuronal arbours additionally requires local remodelling and global stabilisation of the newly formed cytoskeleton.

1.2.2 Covering and reaching multiple areas – Arborisation and branching

Neurons are, however, not just linear cables with one long dendrite and one long axon twisting and bending to reach their targets. Such as trees, rivers, or even fungi, neurons branch heavily to efficiently cover their preferred input and output regions. At the same time, branching optimally minimises the distance of each point on the arbour to the soma, which facilitates supplying energy and proteins as well as conducting of electrical signals.⁴⁰

In addition to this area filling function, often referred to as terminal branching or arborisation, neurons have to branch interstitially to form specific axon tracts connecting multiple target regions.^{41,42} Migration of excitatory and inhibitory neurons has been described to require branching for sensing and growing towards cues.^{43,44} Thalamic axons pause at the subplate and branch to enter the cortical plate indicating a role in axon guidance.⁴⁵ Even to form eventually unbranched connections, axons often over-shoot into a distant region before entering their specific target by branching and subsequent degeneration of the overextending projection as described for parts of the pyramidal tract⁴⁶ and the retinocollicular projection in the visual system.⁴⁷

Branching can be conceptualised as a localised growth mechanism and therefore shares many mechanisms with growth as described above. It requires localisation of energy supplying mitochondria,^{48,49} as well as local translation of actin isoforms.^{48,50} Lipids and membrane proteins are delivered by local accumulation of endoplasmic reticulum⁵¹ and local exocytosis.^{31,52,53} Even local amplification of signalling by exocytosis of neurotrophins has been described to facilitate branching.⁵⁴

However, similar to elongation, local growth alone does not fully explain how the stable cytoskeleton of a neuron is locally remodelled to form a branch. A natural site for branch induction is the dynamic growth cone; indeed, attraction to multiple guidance cues has been described to cause splitting of the growth cone and subsequent elongation of two branches.^{55,56} Splitting to induce branches is, however, rarely observed⁵⁷ and even the simple bifurcation of dorsal root ganglia axons in the spinal cord seems to be formed by branch induction off the axon shaft rather than splitting.⁵⁸

Overcoming the membrane tension and microtubule stability at a shaft region of axons or dendrites to form a collateral branch begins with a local accumulation and reorganisation of the actin cytoskeleton.^{41,57} Such actin patches⁵⁹ serve as precursors for bundled F-actin filopodia^{60,61} or branched F-Actin lamellipodia.^{62,63} The microtubule cytoskeleton is destabilised by the activity of severing enzymes,^{64,65} to facilitate new polymerisation, transport, and crosslinking of microtubules to the actin-rich branch precursors.^{66–68} Most branches elongate by establishing growth cones at their tips. Finally, the dynamically reorganised microtubule cytoskeleton of the new branch is stabilised by recruiting associated proteins.^{69–71}

In summary, branching shares concepts and mediators with global growth and elongation: it requires induction of anabolic pathways and delivery processes and dynamic cytoskeletal rearrangements, however in a more locally restricted manner. Therefore, several growth mediators present with additional branching phenotypes in global loss of function experiments, and branch-specific functions have been described mainly for regulators of specific steps in the collateral branching program.^{72,73}

1.2.3 Limiting growth for specificity – Tiling and pruning

Interestingly, local induction of growth is not the only program to grow branches: local, contact-mediated inhibition of growth at the elongating process can passively redirect a global supply of growth material to sidewise branches. Such a contact-mediated ‘tiling’ mechanism of avoiding self and others during continuous elongation, furthermore, provides optimal filling of space without overlapping input or output fields of neurons.⁷⁴ It is discussed to underly the formation of layer- and column-specific neuronal arbors.^{2,24,75} Finally, constraining neuron growth to specific areas combined with a variable propensity of sidewise branching, was sufficient to computationally generate dendritic trees of a vast range of different cell types.²⁶

Mechanistically, tiling and self-avoidance require mechanisms for individual neurites to detect whether a contacted neurite is part of the same or of another cell that should be avoided and to subsequently stop elongation. Self-avoidance requires connectivity of cytoplasm and expression of neuron-specific surface markers such as Dscam1 (drosophila) or clustered protocadherins (mouse).^{2,75} The genes of these surface markers contain multiple cassettes of similar but non-identical exons that

are probabilistically spliced to generate cell-specific but inter-cellularly differing codes for each cell. While it has been demonstrated that binding occurs between identical surface markers, how this binding causes homotypic and heterotypic repulsion in specific cases is still debated.²

Already while establishing their morphology, neurons establish and strengthen relevant connections by forming dendritic spines and remodelling them in various synaptic plasticity processes. Even later, superfluous synapses, processes, or even whole cells are removed in a pruning process.⁷⁶ Pruning can initiate either by neuronal activity or remove specific processes in a 'stereotyped' genetically determined program, as already described above in the overshoot-branch-degradation model.⁴⁷

Mechanistically, pruning can depend on stopping predetermined degradative processes by electrical activity of a neuron, as exemplified by the extraordinary number of GABAergic interneurons that die twelve days after their birth if not integrated into functional networks.⁷⁷ Such degradative pruning by fragmentation of specific parts of axons or dendrites shares similarities to Wallerian degradation processes and leaves behind debris to be removed by glial cells.⁷⁶ In a separate mechanism, individual processes can retract by localised proteasome activity or cytoskeletal destabilisation.⁷⁶ Pruning is initiated or prevented by growth signalling, electrical activity, and glial cells, but critically, it is an active, energy-consuming process rather than just passive retraction.

In summary, neurons limit their growth capacity locally and redirect growth to efficiently fill target areas without overlap. They also actively remove connections to refine the morphology of the final network in experience-dependent and genetically predetermined ways.

1.2.4 Axon morphogenesis requires specific programs

Early quantifications of Golgi-stained individual neurons *in vivo* show a dramatically skewed length distribution towards the axon, even though their elongated morphology makes axons especially difficult to study in brain slices.⁷⁸ The overall neurite length of locally projecting GABAergic interneurons is to roughly 90% axon, and the morphology of their axonal arbours can be used to classify them into cell types.⁷⁹ Also the neurites of glutamatergic cells of the cortex comprise 70-90% axon in these data, depending on whether they are local- or long-range projecting. Recent reconstructions of over 1000 individual neurons in mouse cortex using high-resolution imaging and image-classification techniques even show a more dramatic size difference of axons and dendrites.⁸⁰ Neurons are predominantly axon.

Growing such a long axon requires efficient, axon-specific transport and synthesis mechanisms, and an extraordinary stabilisation of the axonal cytoskeleton. Polarisation initiates the reorganisation of the microtubule cytoskeleton towards parallel- and plus end outward-oriented microtubule bundles in the axon.⁸¹ Consequentially, polarisation of microtubules in axons mainly occurs anterogradely,⁸² and microtubule-based axonal transport can be efficiently targeted by plus-end directed kinesin motor proteins.⁸³ Axonal microtubules are preferentially stabilised by post-translational modifications and microtubule-binding proteins and their interaction with the endoplasmic reticulum.^{32,33,84}

Maintaining this enormous length of the axon cannot be achieved only by diffusion or directed transport from the soma but requires supply from external cells and local anabolic activity.⁸⁵ Local production of energy by mitochondria,⁸⁶ local translation,⁸⁷ local lipid synthesis,⁸⁸ and glial support⁸⁹ are critical to elongate and keep the axon alive. As a consequence of the specific need for stabilising axons, the morphogenetic programs shaping axons and dendrites are unlikely to be identical.

While the collateral branch-inducing cytoskeletal program discussed in section 1.2.2 has been mainly studied for axons, it is not clear if its parts are fully axon-specific or if they are modifications of dendrite patterns. Both axons and dendrites branch predominantly collaterally by forming F-actin-rich filopodia and lamellipodia on their shafts that are subsequently stabilised by microtubules.³⁴ However, due to the minimised distance of each point to the origin of material, branching patterns are energetically more favourable compared to elongated structures like the axon. Therefore, undisturbed unidirectional elongation of an axon requires active inhibition of branching and stabilisation of the cytoskeleton.^{58,90} To form branches in such unfavourable conditions, neurons have to destabilise the microtubule cytoskeleton locally by recruiting severing proteins or removing microtubule stabilisers as described in section 1.2.2. Dendrite branches, in comparison, have a lower intrinsic barrier to initiate branches due to their more dynamic microtubule network, which contains more polymerising microtubule ends in various directions,⁸² and their mixed-polarity arrangement, which slows down transport mechanisms and locally enriches material.⁵¹ However, it is not clear, whether these modifications are sufficient to explain all differences of axon and dendrite branching.

A similar question arises for the implementation of terminal arborisation and interstitial branching. While tiling and arborisation could operate independent of precisely localised branch-inducing signals by probabilistic initiation of branches, establishing long-range collateral pathways likely requires more 'deterministic' initiations. Are these mechanisms implemented independently, or does the formation of an axon tract only require a very localised signal to the axon shaft? Is axonal arborisation more closely related to dendritic arborisation than to 'true' interstitial axon shaft branching? How can *in vitro* models of branch morphogenesis distinguish terminal arborisation from genuine interstitial branching? In this respect, it is also interesting to note that due to the technical challenges of analysing individual axons rather than the connections of neuron groups *in vivo*, even the extent to which individual neurons establish such interstitial branches has been unclear until recently.^{80,91}

In summary, axons are by far the largest structure of neurons. Their growth, maintenance, and morphogenesis require modifications of morphogenetic growth programs or even fully axon-specific implementations. However, many studies of neurite morphogenesis focus on axons or dendrites in isolation. By design, they thereby already assume independent programs between the neurite types or complete transferability of findings from one neurite type to the other. Therefore, assessing differential effects of treatments on both neurite types in future studies will likely refine the knowledge about exact differences and commonalities between axon and dendrite morphogenesis.

1.3 ORCHESTRATING MORPHOGENESIS

In addition to their highly polarised axon-dendrite morphology, neurons also differ dramatically in size and shape both between and within cell types. Neurons seem to scale their oscillatory activity, firing rate, and synaptic strengths, their axon diameter, and the length and spread of their connections by orders of magnitude (log-normal) rather than linearly.^{92,93} While these differences in part depend on modified implementations on the molecular level, an additional level of temporal-, cell-type- or even compartment-specific regulation of the discussed programs orchestrates morphogenesis.

1.3.1 External guidance of growth is modified intrinsically

Developing brains express at least 86% of all known protein-coding genes with the largest variability in gene expression and splicing during early development.¹⁰ In transcriptome analyses, the largest concurrent clusters are early-expressed genes that downregulate during maturation, and genes that increase expression in mature neurons.¹⁰ Early-expressing genes are predominantly involved in modifying the execution or initiation of morphogenetic programs to create cell-type-specific and even axon-⁹⁴ or dendrite-specific⁹⁵ expression profiles. Similarly, studies have found cell-type-specific gene expression profiles that also differentially express mediators of the morphogenetic programs.⁹⁶

In addition to temporal and cell-type-specific expression, morphogenetic mediators differentially distribute subcellularly to modify axon- from dendrite-morphogenesis. This is influenced by local translation in the axon,^{50,87} but also differential transport to the axon.⁸³ For the latter, the axon initial segment plays a central role as a gatekeeper of axon identity, by limiting diffusion of cytosolic and membrane proteins and by sorting transport to the axon.⁹⁷ Moreover, post-translational modifications regulate axon enrichment: palmitoylation enriches key growth mediators such as Cdc42, DCC, or Map6 in developing axons.^{98,99}

These intrinsic mechanisms mainly modify the general efficiency and implementation of the morphogenetic programs. In addition, many morphogenetic programs are, as illustrated for polarisation, initiated locally by specific extrinsic cues. This process has been studied best for growth cone guidance, but several critical players also regulate later stages of morphogenesis.

Growth cones utilise the dynamic instability properties of the actin and microtubule cytoskeleton to elongate neurites. Both freezing and strong destabilisation of the cytoskeleton prevent proper elongation.¹⁰⁰ Because this dynamic structure is the primary site for neurite growth, it is also the primary site of regulation to facilitate elongation, turning, or growth cone collapse and repulsion. Actin and microtubule dynamics are regulated by Rho GTPases. The most studied Rho GTPases are the growth-promoting Cdc42, Rac1, and the growth cone collapse-mediating RhoA.^{101,102} Rho GTPases act as molecular switches by hydrolysing guanosine-triphosphate (GTP) to guanosine diphosphate (GDP) to modulate differential regulators of the cytoskeleton depending on their nucleotide status. Their activity is regulated by guanosine exchange factors (GEFs) and GTPase activating proteins (GAPs) that are direct targets of many guidance cues.¹⁰¹

Many guidance cues exist as soluble versions, to provide a general direction via gradients, and membrane attached versions, to provide local, contact-mediated patterning.¹⁰³ The most studied

guidance cues are semaphorins with their plexin and neuropilin receptors, netrins with their DCC- and UNC5-receptors, slit with robo-receptors, and ephrins with Eph receptors.¹⁰⁴ Recently, morphogens such as Shh, Wnt, and BMP, and cell adhesion proteins such as FLRTs were additionally discussed as mediators of growth cone guidance. Even bioactive signalling lipids such as lysophosphatidic acid (LPA) or sphingosine-1-phosphate affect elongation by inducing growth cone collapse via specific G-protein coupled receptors signalling to Rho GTPases.¹⁰⁵

Further layers of complexity – and therefore further options to differentially regulate growth between cells and compartments – are added by crosstalk mechanisms of the various guidance cues. As an illustrative example, FLRT3 has been described to regulate Netrin guidance by interacting with Robo-receptors.¹⁰⁶ Moreover, the extracellular matrix heavily modifies local concentrations of guidance cues and the mechanical stiffness surrounding the growth cone.^{107,108} Even electrical activity of neurons alters growth cone migration by coupling calcium influx from the plasma membrane and local endoplasmic stores to calmodulin-dependent kinases (CaMK) and phosphatases (calcineurin), calcium-sensitive proteases (Calpain), and RhoGTPase activity.¹⁰⁹

Interestingly these same extrinsic cues also regulate other programs of morphogenesis. Repulsion by Semaphorins and Ephrins regulates pruning,⁷⁶ Netrin, Semaphorins, Ephrins, Wnts, and neurotrophins regulate various branching patterns (summarised in Gibson & Ma, 2011).⁵⁸ Downstream Rho GTPases influence growth and branching in a cell type and timepoint-specific manner.¹¹⁰ Electrical activity seems to modulate all programs of development, by speeding up axon growth,¹¹¹ by activity-dependent axon branching,^{112–115} by synaptotrophic growth of dendrites and their spines,¹¹⁶ and by activity-dependent pruning of synapses or spines.^{76,117}

In summary, neurons can modify the molecular components of morphogenetic programs intrinsically. They furthermore spatially and temporally orchestrate the initiation of morphogenetic programs by integrating input from cell-extrinsic cues. The molecular mechanisms of growth cone guidance cues have been studied extensively and several factors also control other parts of neuron morphogenesis.

1.3.2 Plasma membrane proteins and lipids relay and modify morphogenetic signals

Plasma membrane proteins and lipids are at the direct interface to integrate and transfer extrinsic input towards the cell intrinsic growth programs. About 30 percent of all proteins are membrane proteins, many more bind the membrane or membrane proteins transiently.¹¹⁸ The majority of cellular activity, therefore, occurs at membrane compartments, even more so in neurons with their large surface to cytosol ratio.

In this line, the cellular response initiated by morphogenetic cues more often depends on the membrane receptor composition of a cell than the exact cue.¹¹⁹ As an example, Netrin signalling via DCC presents an attractive cue for growth cones, while combined signalling via DCC and Unc5 mediates repulsion.¹²⁰ In this way, broad environmental inputs can be refined to cell-, compartment- and timepoint-specific effects by regulating the membrane abundance of receptors, by trafficking or endocytosis, and proteolytic processing receptors to modulate their activity.¹⁰⁴

Furthermore, several key signalling pathways downstream of morphogenetic signals operate at the plasma membrane. In many cases, activation of membrane-based Ras GTPases downstream of guidance and neurotrophin receptors initiate signalling by phosphatidylinositol-3-kinases (PI3K).¹⁰¹

The PI3K-pathway promiscuously affects cell growth and polarisation, and locally induces cell remodelling.¹²¹ Its negative regulator, phosphatase and tensin homolog on chromosome 10 (PTEN), is a well-described tumour suppressor with disease-related functions in the brain.^{122,123} Activity of the PI3K-pathway causes localised changes in cell morphology,^{124–126} and accumulation of F-actin and formation of protrusions in neurons.^{59,127} Its regulation of microtubule stability,¹²⁸ transport,¹²⁹ and local as well as global translation,^{48,121} are likely involved in its influence on axon elongation, which is most prominently illustrated by the hyper-growth phenotypes induced by neuron-specific loss of PTEN.^{29,130} Even survival and pruning of nerve cells is prevented by PI3K-signalling activity.¹³¹ Being such major orchestrators of morphogenesis, many have described PI3K and PTEN as targets for exerting spatial and temporal control.^{132–141}

To initiate these events, PI3K phosphorylates a membrane lipid – phosphatidylinositol-4,5-bisphosphate (PI(4,5)P₂) – at position 3 of the inositol ring to generate PI(3,4,5)P₃ or PIP₃. PTEN catalyses the reverse reaction from PIP₃ to PI(4,5)P₂. Due to their limited capability for diffusion in only two dimensions, the precise modification of membrane lipids can locally concentrate signals and initiate signal amplifying cascades even with low activity of kinases.¹²¹

The phosphorylation of PI(4,5)P₂ to PIP₃, therefore, is only one – although arguably the most influential – signalling function of phosphoinositide lipids (PIPs). All seven combinations of phosphate residues on the inositol head group of PIPs (three monophosphates (3; 4; 5), three bisphosphates (3,4; 3,5; 4,5) and PIP₃) have exclusive functions, often restricted to different membrane compartments.¹⁴² These functions include the regulation of cytoskeletal dynamics, sorting of organelles, endocytosis, and autophagosomal degradation.^{142,143}

The intracellular effectors of such lipid-signalling-hubs are often cytosolic proteins recruited to the membrane by protein domains capable of distinguishing the phosphate-configuration on the inositol head group of phosphoinositides. As an example, downstream of PI3K-activity, Rho GTPases regulate many cytoskeletal alterations, while the AKT/mTOR side mediates general growth and survival by recruitment to the plasma membrane by direct PIP₃ binding or PIP₃-binding of Rho GEFs.¹²¹

Phosphoinositides, however, also affect and are affected by membrane proteins. Binding of PI(4,5)P₂ has been described to alter the function and localisation of KCNQ, TRP, and Kir channels, potentially as a means to prevent activity in PI(4,5)P₂ sparse internal membrane compartments.^{144–148} On the other hand, proteins clustering PI(4,5)P₂ such as MARCKs or GAP43 are suspected to modify PIP-downstream signalling by enriching local concentrations and shielding of PIPs.^{149,150}

In summary, the signalling orchestrating morphogenesis acts predominantly at the plasma membrane. Membrane proteins and lipids initiate and regulate the downstream morphogenesis but are also targeted by regulatory mechanisms. Especially phosphoinositides and their interactors and regulators emerge as interesting candidates for understanding the orchestration of neuron morphogenesis.

1.4 PLPPRS ARE PLASTICITY-RELATED GENES WITH HOMOLGY TO LIPID PHOSPHATASES

Phospholipid phosphatase-related (PLPPR) proteins comprise a neuron enriched, injury- and disease-related, and developmentally regulated family of membrane proteins and are therefore prime candidates for regulating or participating in specific programs of neuron morphogenesis.

They share homology to phospholipid phosphatases (PLPPs), a family of membrane proteins with six transmembrane spanning domains. PLPPs dephosphorylate bioactive signalling lipids like LPA or S1P to counteract their effects on growth cone guidance (as described in section 1.3.1)¹⁵¹. While the first report on a PLPPR family member suspected similar enzymatic activity for PLPPR4,¹⁵² subsequent studies could not measure any activity against LPA by PLPPR4 or PLPPR1.^{153–155} Although some functions of PLPPRs seem to be linked to LPA-signalling, the exact mechanisms mediating this crosstalk are still actively researched.

1.4.1 PLPPRs are neuron-enriched and developmentally regulated

Expression of *Plppr* genes is highly enriched in neurons,^{156–158} although PLPPR4 has also been observed in smooth muscle cells.¹⁵⁹ PLPPR4 seems enrich in glutamatergic neurons of the hippocampus¹⁶⁰ and of cortical layer IV,¹⁶¹ and its gene is suspected to share regulatory features with *Plppr5* due to their close proximity on the same chromosome.¹⁶² Interestingly, *Plppr* genes seem to express differentially during neuron development of rodents: *Plppr1* expression continuously decreases during development when quantifying whole brain lysates,¹⁶³ *Plppr4* expression seems to peak during adolescence in the hippocampal region,¹⁶⁴ where *Plppr5* seems to peak around birth.¹⁶⁵

The early expressing PLPPR1 and PLPPR5 have been detected in shafts and growth cones of developing neurites.^{163,165} During later stages, PLPPR1 and PLPPR3 localise predominantly to the axonal region,^{163,166,167} although PLPPR1 also has been detected in dendritic spines. PLPPR4 and PLPPR5 seem to enrich predominantly at dendritic processes and even co-localise with postsynaptic densities.^{160,165,168}

This cell-type-specific and developmentally regulated expression and the differential localisation to different compartments of individual neurons suggests that different family members initiate similar functions at different places and times. This could potentially generate a transcriptionally regulated '*Plppr-code*' to modify morphogenesis in a cell-, time- and compartment-specific manner.

1.4.2 PLPPRs are connected to diseases of cellular morphology

Plpprs were first described as genes upregulated in the hippocampus after injury to adjacent cortical areas and therefore initially named plasticity-related genes (PRGs^a).¹⁵² This upregulation has been observed for *Plppr4* transiently in the hippocampus, one to five days after injury,¹⁵² and appeared more

^a This parallel nomenclature has led to an unfortunate situation where PLPPR1 = PRG3, PLPPR2 = PRG4, PLPPR3 = PRG2, PLPPR4 = PRG1, and only PLPPR5 shares the same numbering with its PRG5 name. In this thesis, I will adopt the PLPPR-nomenclature approved by the HUGO gene nomenclature committee to avoid further confusion.

sustained for *Plppr1* in corticospinal motor neurons, four weeks after injuring the pyramidal tract.¹⁶⁹ Other studies reporting an upregulation of *Plppr4* after injury to facial nerve¹⁷⁰ or *Plppr4* and *Plppr1* after developmental^{171,172} or kainite-induced¹⁷³ epileptic seizures, unfortunately, are not conclusive due to their use (or reporting) of noisy methodology without robust statistical tools. Injury related upregulation of *Plppr2*, *Plppr3*, or *Plppr5* expression has not been described yet.

Functional studies have reported improved regrowth of PLPPR1-expressing neurons after injury to the pyramidal tract¹⁶⁹ or the spinal cord,¹⁶⁶ and loss of *Plppr5*-expression seems to correlate with worse outcomes after cerebral palsy in mice.¹⁷⁴ In addition to potential roles in regenerative processes, PLPPR5 also might participate in the pathophysiology of auto-antibody-caused paraneoplastic cerebellar degeneration.¹⁶⁸ *Plppr4*-loss has been shown to cause epileptic activity in neonatal mice by hyperexcitability of cortical and hippocampal regions.^{160,161}

In addition to these functional studies, transcriptomic studies have linked altered expression of *Plppr*-family members to the progression of various cancers: *Plppr1* expression seems to be upregulated in breast cancer,¹⁷⁵ downregulated in glioblastoma,¹⁷⁶ and both up- or downregulated expression seem to correlate with worse outcomes in glioma.¹⁷⁷ *Plppr2* expression seems to be differentially regulated in colorectal,¹⁷⁸ breast,¹⁷⁹ and pancreatic cancer¹⁸⁰ and to be generally linked to tumorigenic transformation.¹⁸¹ Altered expression of *Plppr1*, *Plppr3*, and *Plppr5* was linked to several paediatric cancers,¹⁸² altered expression of *Plppr4* to the formation of metastases of gastric cancers.¹⁸³

1.4.3 PLPPRs change excitability, guidance, and morphology of neurons

Electrophysiological studies of *Plppr4* knockout mice have detected hypo-excitability of sensory cortical neurons two weeks after birth but hyper-excitability three weeks after birth in both sensory cortex¹⁸⁴ and hippocampus,¹⁶⁰ indicating a developmentally regulated role of PLPPR4 in synapse function. Furthermore, PLPPR1 seems to increase axon elongation potentially by counteracting RhoA-mediated growth cone collapse.^{166,169} Interestingly, both effects seem to reverse described LPA mediated functions, indicating some form of LPA-mediated function even though PLPPRs lack evidence for catalytic activity.

Ample evidence points to a role of several PLPPRs in the formation or stabilisation of filopodia. PLPPR1 and PLPPR5 overexpression induces filopodia in multiple cell types, interestingly not via known Rho GTPases.^{155,185,186} PLPPR1, PLPPR4 and PLPPR5 induce these filopodia also when overexpressed in neurons.^{166,185,187} Reduction of PLPPR1 reduces filopodia density in neurons,¹⁶³ and *Plppr4* knockout mice have fewer spines and branches on their dendrites.¹⁸⁷ PLPPR1 expression, furthermore, induced increased branching in neurons.¹⁶⁹ Interestingly, these effects do not seem to depend on LPA-mediated functions at least in the case of PLPPR4.¹⁸⁷

In summary, PLPPRs emerge as a family of developmentally regulated membrane proteins with evidence for recovery-related functions that utilise morphogenetic programs. PLPPRs further seem to affect cellular morphology in developing neurons. These effects involve elongation and guidance of axons, formation of filopodia and branches, and electrophysiologically measurable changes at the synapse.

1.5 OBJECTIVES OF THIS THESIS

The morphogenesis of neurons is regulated by multiple interdependent and co-regulated developmental programs. In axons, morphogenesis faces specific challenges due to their elongated shape and extraordinary length. Whether axon morphogenesis comprises a set of separate growth programs or whether it differs from dendrite growth primarily by specific mediators, is in the focus of numerous studies. In neurons, membrane proteins and lipids are in a key position to mediate and orchestrate these programs and therefore are of increasing interest for understanding neuron morphogenesis. PLPPRs are developmentally regulated, neuron enriched membrane proteins that have been shown to alter morphogenesis. At the start of this project, no study had addressed the specific roles of PLPPR3 in neurons.

Therefore, in an explorative study,¹⁸⁸ I set out to elucidate the function of PLPPR3 in neuron morphogenesis, specifically focusing on roles in regulating membrane lipid composition. To this end, I overexpressed and performed structure-function analyses with PLPPR3 in cell lines and neurons (chapter 2). To study the function of endogenous PLPPR3, I set out to create a conditional knockout mouse of *Plppr3* using the CRISPR/Cas9 technique (chapter 3). Subsequently, I characterised the development and morphogenesis of *Plppr3*^{-/-} neurons in comparison to wild-types. To investigate the cellular mechanisms of PLPPR3 function, I quantified the effects on membrane phosphoinositide composition in neurons involving the growth orchestrating PI3K-pathway (chapter 4). To this end, I optimised visualisation techniques for phosphoinositide membrane lipids, and developed semi-automated analysis techniques to facilitate the quantification of neuronal morphogenesis (chapter 7, appendix). In a final part of this work, I set out to use the *Plppr3*^{-/-} neurons to further characterise the differential regulation of branching morphogenesis in axons and dendrites (chapter 5).

RESULTS

2	Mapping Function to PLPPR3 domains	21
2.1	PLPPR3 is a neuron-specific, axon-enriched transmembrane protein	21
2.1.1	PLPPR3 enriches in axons and internal organelles and plasma membrane protrusions	21
2.2	PLPPR3 increases filopodia on N1E-115 cells	25
2.2.1	Deletion mutants of PLPPR3 alter plasma membrane localisation	26
2.3	Plasma membrane localisation is regulated by conserved domains of PLPPRs	28
2.3.1	Expression level and co-expression alter plasma membrane abundance of PLPPR3	28
2.3.2	Modifications of PLPPR3 in the transmembrane region inform about localisation	29
2.3.3	Catalytic center mutants reduce plasma membrane abundance of PLPPR3	32
2.4	Summary and outlook: Domain mapping provides tools to precisely study PLPPR3	34
3	Generating a <i>Plppr3</i>^{-/-} mouse using CRISPR/Cas9	36
3.1	First exon of <i>Plppr3</i> is a suitable target for preventing PLPPR3 expression	36
3.1.1	PLPPR3 expression is likely regulated by alternative splicing	36
3.1.2	Knockout strategy: insert LoxP sites around first exon using CRISPR-Cas9	38
3.2	excision of exon 1 results in full knockout of <i>Plppr3</i> expression	40
3.2.1	Validation of <i>Plppr3</i> knockout on DNA and protein-level	40
3.2.2	Off-target quality control	40
3.3	Summary and outlook: Strategies for creating a conditional PLPPR3 knockout	43

4	PLPPR3 redirects growth to branches	44
4.1	Overall development of neurons is not disturbed in <i>Plppr3</i> ^{-/-}	44
4.2	<i>Plppr3</i> ^{-/-} neurons branch less in vitro	45
4.2.1	Filopodia numbers are decreased in early polarised <i>Plppr3</i> ^{-/-} neurons	45
4.2.2	Branch density is decreased in fully polarised <i>Plppr3</i> ^{-/-} neurons	46
4.2.3	Cortical Layer II/III <i>Plppr3</i> ^{-/-} neurons have no branching phenotype in vivo	48
4.3	PLPPR3 and the PI3K pathway regulate branching cooperatively	50
4.3.1	No evidence for altered PIP3-levels in <i>Plppr3</i> ^{-/-}	51
4.3.2	Knockdown of PTEN rescues <i>Plppr3</i> ^{-/-} branching deficit in primary neurons	52
4.4	Summary and outlook: further phenotyping of <i>Plppr3</i> ^{-/-} animals	54
5	Precursor types predict the stability of neuron branches	56
5.1	Branch stability depends on precursor and location	56
5.1.1	Branches that initiate from distinct precursor structures differ in lifetime	56
5.1.2	Developing axons stabilise all branches and prefer efficient precursor types	58
5.2	Removing efficient precursors reduces overall branch stability	59
5.2.1	<i>Plppr3</i> ^{-/-} branches have a shorter lifetime	59
5.2.2	<i>Plppr3</i> ^{-/-} reduces branch stability only by removing filopodia	61
5.3	Summary and outlook: How could precursors modify branch stability	63

2 MAPPING FUNCTION TO PLPPR3 DOMAINS

Given the sparsity of information on PLPPR3 in the literature, I set out to describe expression and localisation in both cultured primary neurons and *in vivo*. To gain further insight into the function of PLPPR3 and to locate the domains of PLPPR3 that govern cellular functions, I expressed wild-type and mutant constructs in cultured cells lines.

2.1 PLPPR3 IS A NEURON-SPECIFIC, AXON-ENRICHED TRANSMEMBRANE PROTEIN

The screening of existing protein and mRNA expression datasets^{156–158} suggests PLPPR3 as a neuron-specific protein expressed primarily during development. However, relatively little information on cell-type-specific expression is currently available. With the recent publication of multiple single-cell transcriptomic analyses on mouse brain cells by the Allen Brain institute⁹⁶, such information has become available, at least for adult stages. These studies include two datasets from adult mouse cortex obtained using either SMART- or 10x-RNA-sequencing technology. 10x allows for the screening of many cells. It enriches for mRNA-parts close to the poly-A-tail and therefore is often less sensitive compared to the SMART technology that does not enrich for mRNAs but has a broader coverage and therefore sensitivity (but also a higher chance for false positives).¹⁸⁹ Comparing both datasets using a custom-made R/Shiny-App (<https://github.com/jo-fuchs/Gene-expression-AllenBrainAtlas>) reveals a low to medium expression of *Plppr3* in adult cortical neurons and increased expression in GABAergic interneurons (Figure 1A&D).

Comparing expression levels between ‘neighbourhoods’ – regions with similar gene expression profiles rather than anatomically defined brain regions¹⁹⁰ – reveals caudal ganglionic eminence derived GABAergic cells as the highest *Plppr3*-expressers in adult mice. In comparison, hippocampal and lower-order cortical glutamatergic neurons express less (Figure 1E) or no *Plppr3* (Figure 1B). Sub-categorising these neighbourhoods into clusters of cell types with similar gene expression profiles reveals the highest *Plppr3*-expression in Synuclein-gamma (*Sncg*) positive interneurons (Figure 1C&F). The only paper discussing *Sncg*-interneurons places them as a type of basket cell counter-playing hippocampal Parvalbumin-interneurons in CA1.¹⁹¹ Expression of *Plppr3* seems to be absent in hippocampal dentate gyrus and low in CA1-3 and adjacent regions, while expression in layer II/III seems to be highest across cortical glutamatergic neurons.

2.1.1 PLPPR3 enriches in axons and internal organelles and plasma membrane protrusions

These datasets suggest adult expression of *Plppr3*, primarily in GABAergic cell types. To gain further insight into the developmental expression and localisation of PLPPR3, I obtained coronal sections of embryonic day 17 murine cortex from the Institute of Neuroanatomy (Nikolaus Gräber, laboratory of Prof. Victor Tarabykin) at Charité and immunofluorescently labelled PLPPR3 and the axon marker L1CAM. Interestingly, in these experiments PLPPR3 was found most abundant in L1CAM-positive axonal tracts (Figure 2A&B), which comprise axons of glutamatergic neurons.^{45,192} This localisation matches the localisation of PLPPR3 in embryonic day 16 murine cortex as described by Cheng et al. 2016 (supplementary figure 1)¹⁹³.

Plppr3 expression in two single-cell RNA sequencing datasets from adult mouse cortex

Allen Brain Institute

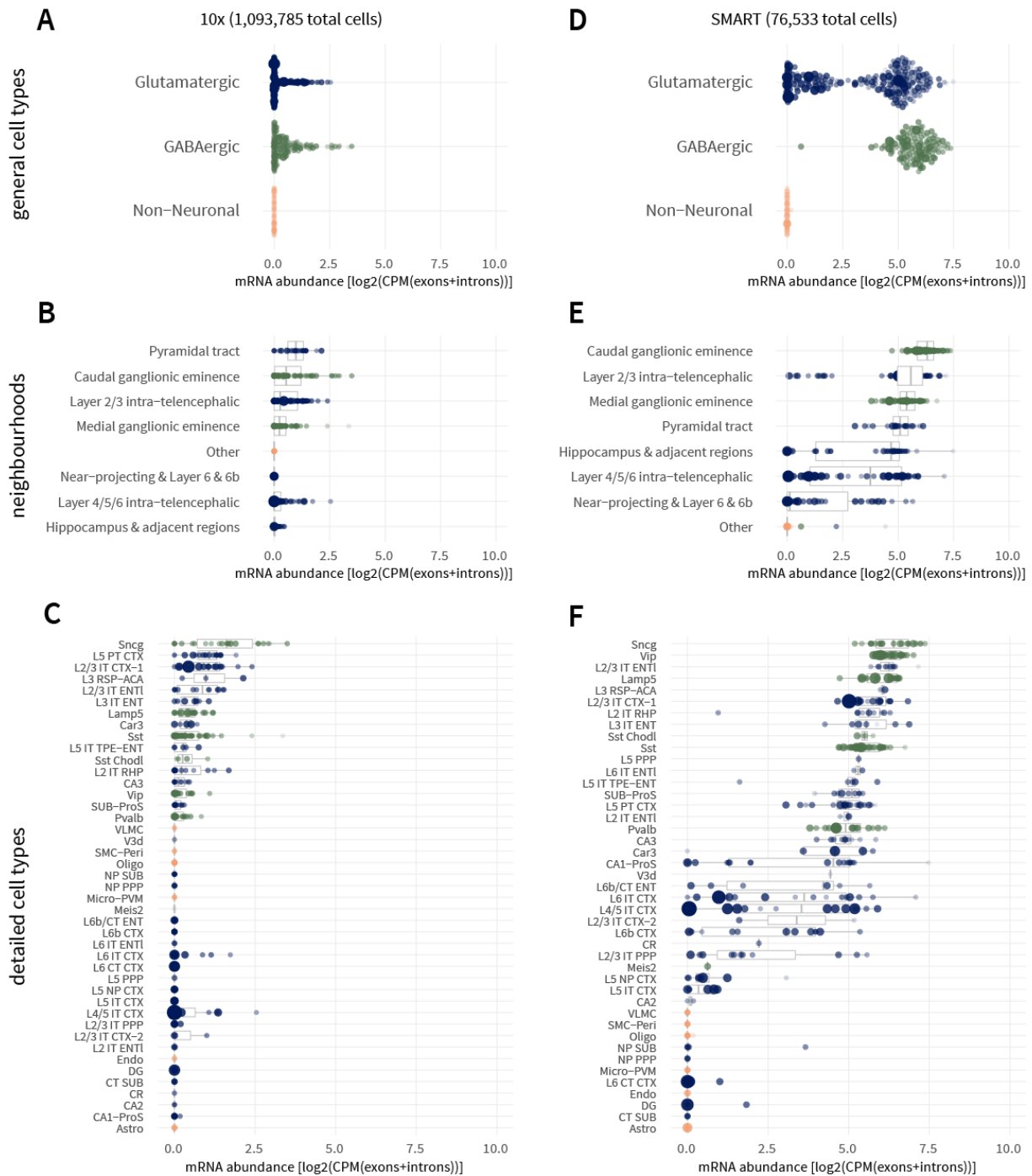
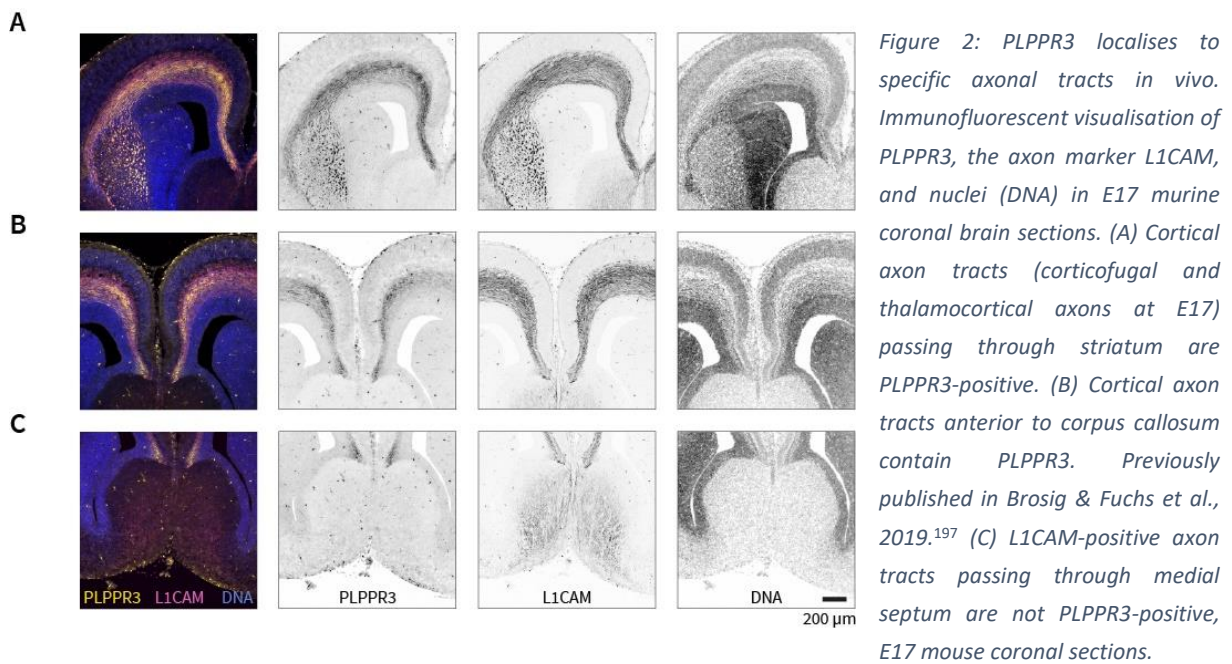


Figure 1: PLPPR3 is a neuron-specific protein and expresses preferentially in GABAergic neurons in adult mice. (A&D) Custom visualisation of two single-cell RNA-sequencing datasets from the Allen Brain Institute¹⁹⁰ reveals mRNA levels of *Plppr3* in individual neuronal cell types (individual dots, size is proportional to number of cells of the respective cell type) and absence of mRNA in non-neuronal brain cells in adult mouse brains. (B&E) Sub-categorisation into ‘neighbourhoods’ indicates highest expression levels in GABAergic interneurons derived from the caudal ganglionic eminence and low expression in hippocampal glutamatergic neurons. (C&F) Further sub-categorisation into ‘cell type clusters’ suggests Synuclein-gamma expressing interneurons as the major *Plppr3*-expressing cell in adulthood. Panels A-C: 10x-dataset, panels D-F: SMART dataset. Data from Allen Brain Institute visualised with a custom R script (<https://github.com/jo-fuchs/Gene-expression-AllenBrainAtlas>).

However, not all L1CAM-positive axonal tracts in embryonic mouse brains seemed to contain PLPPR3. Axon tracts passing through the medial septum appeared PLPPR3-negative (Figure 2C). Axons in the medial septum connect medial septal neurons with the hippocampus and adjacent regions and the hippocampus with olfactory bulb and supramammillary body and have also been described to contain long-range GABAergic projecting axons^{194–196}. These localisation patterns of PLPPR3 at an embryonic timepoint suggest expression and localisation of PLPPR3 predominantly in axons of glutamatergic cells during early development.



To narrow down the exact localisation of PLPPR3 in developing neurons, I fixed and immunolabeled hippocampal neurons after one day in culture (DIV1) to gain insight into localisation in newly developing neurons (stage 1, definition of stages from Polleux & Snider, 2010¹⁸), at DIV3 for predominantly unpolarised neurons (stage 2), at DIV5 for predominantly polarised (stage 3) and at DIV9 for fully polarised neurons (stage 4).

At stage 1, PLPPR3 localised to internal membrane structures and in a subset of neurons also to the plasma membrane (Figure 3A). As perinuclear parts of the membrane structures were also weakly DAPI-positive, the PLPPR3-positive organelle is likely connected to the rough and smooth endoplasmic reticulum. In non-polarised neurons (Figure 3B), PLPPR3 localised equally to internal membranes and growth cones of all neurites, while in polarised cells, the PLPPR3 immunoreactivity was enriched on a newly formed axon and its growth cone membrane (Figure 3C&D). In fully polarised stage 4 neurons, PLPPR3 was highly enriched in axons and the growth cones. Notably, the abundance of PLPPR3 seemed to be highest in concave regions of the growth cone rather than at the most distal protrusions (Figure 3C&D). Focusing on axonal shaft regions at DIV9 revealed a granular pattern of PLPPR3 signal throughout the axon shaft with no apparent enrichment at the plasma membrane (Figure 3E).

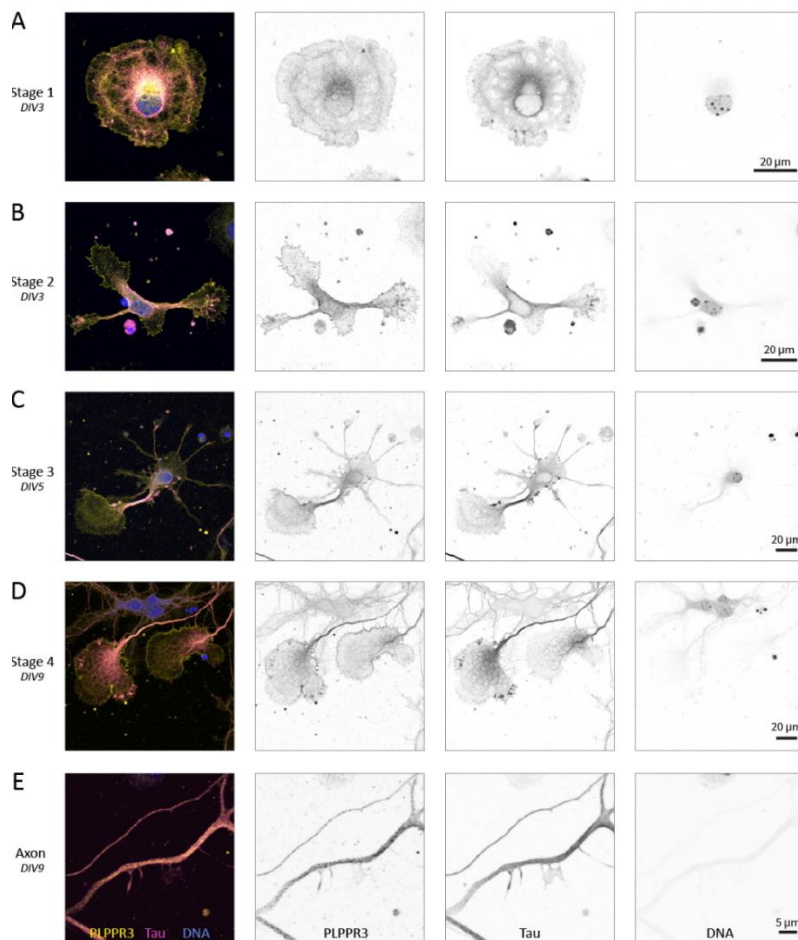
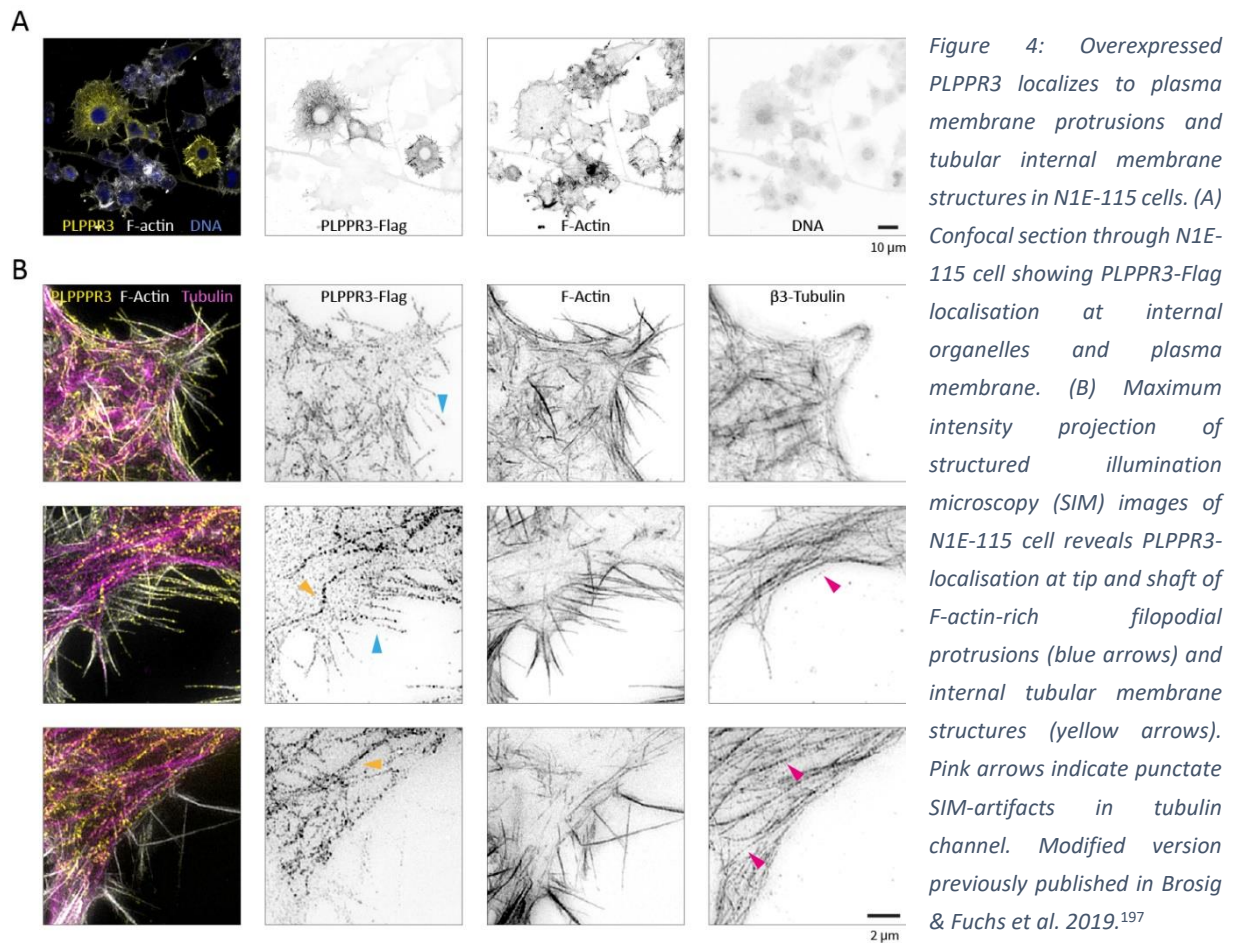


Figure 3: PLPPR3 localises to axonal plasma membrane and internal structures in cultured hippocampal neurons of various ages. (A) Confocal sections of stage 1 hippocampal neurons plated on poly-ornithine reveal PLPPR3 on plasma membrane and in internal membrane compartments (B) PLPPR3 signal in stage 2 neurons equally distributes to all neurites. (C) Abundance of PLPPR3 is highest in axons and growth cones at later developmental timepoints. (D) PLPPR3 signal is strongest in proximal regions of the growth cone. (E) PLPPR3 signal in DIV9 axons is detected as a granular pattern in internal structures and at the membrane. All images represent confocal sections.

To obtain a better signal-to-noise ratio and to avoid unspecific antibody binding, I overexpressed mouse PLPPR3-Flag in cultured N1E-115 neuroblastoma cells. Similar to endogenous PLPPR3 in hippocampal neurons, overexpressed PLPPR3 localised both to internal membrane compartments and the plasma membrane (Figure 4A). Interestingly, PLPPR3 signal at the plasma membrane seemed to enrich in filopodial protrusions. Furthermore, as described for PLPPR-family members,^{155,166,185-187} also PLPPR3-expressing cells appeared to have more filopodia compared to non-expressing cells.

To further resolve PLPPR3-localisation, I collaborated with Dr. Niclas Gimber (AMBIO, Charité) to employ super-resolution structured illumination microscopy (SIM).¹⁹⁸ Overexpressed PLPPR3 appeared in a punctate pattern that localised to the tip and shaft of filopodial protrusions or to tubular internal membrane structures (blue and yellow arrows respectively in Figure 4B). The PLPPR3 signal in filopodial protrusions often reached beyond the F-actin-rich core, as described for other members of the PLPPR-family¹⁸⁶. Furthermore, PLPPR3 did not seem to specifically enrich in protrusions positive for both F-actin and microtubules, suggesting no function in linking the two cytoskeletal structures. The internal tubular signal often located parallel to microtubules (Figure 4B), further strengthening the hypothesis that it may demarcate tubules of the endoplasmic reticulum. The punctate pattern of PLPPR3 in SIM is not entirely conclusive, as similar sized puncta are also found in some of the β 3-Tubulin signal (pink arrow in Figure 4B), and the Wiener-based reconstruction algorithms used in this SIM-experiment have been described to produce artefactual punctate patterns with low-intensity labels.¹⁹⁹⁻²⁰¹



2.2 PLPPR3 INCREASES FILOPODIA ON N1E-115 CELLS

PLPPR3 enriches in protrusions and internal membrane compartments, and family members of PLPPR3 have been described to increase filopodia density in multiple cell types^{155,166,185–187}. However, the precise mechanism and the specific domains of PLPPRs that execute this filopodia-related function have not been conclusively described. All PLPPRs consist of an N-terminal transmembrane domain with six membrane-spanning helices and a cytosolic C-terminal region with varying length. While some studies indicated that the C-terminal region of PLPPRs is critical for filopodia effects,^{165,166} others required the full-length protein rather than only transmembrane or C-terminal regions.^{186,187}

Given that the filopodia-forming capacity of PLPPRs is conserved across the family, the structural regions mediating this function are likely also conserved amongst all family members. Furthermore, there is no evidence that members of the closely related PLPP-family alter filopodia density. Therefore, filopodia-domains are expected to be PLPPR-specific rather than conserved in PLPPs. To narrow down putative filopodia-related domains, I therefore performed sequence alignments of the PLPPR-family using two algorithms with different scoring systems of gaps in the alignments.^{202,203}

PLPPRs share the highest homology in their transmembrane region, making those regions good candidates for mediating the filopodia-related functions (Figure 5). This region, however, also aligns closely to non-filopodia forming PLPPs, so further refinements of transmembrane-alignments (including PLPP-family members) will be shown in subsequent sections.

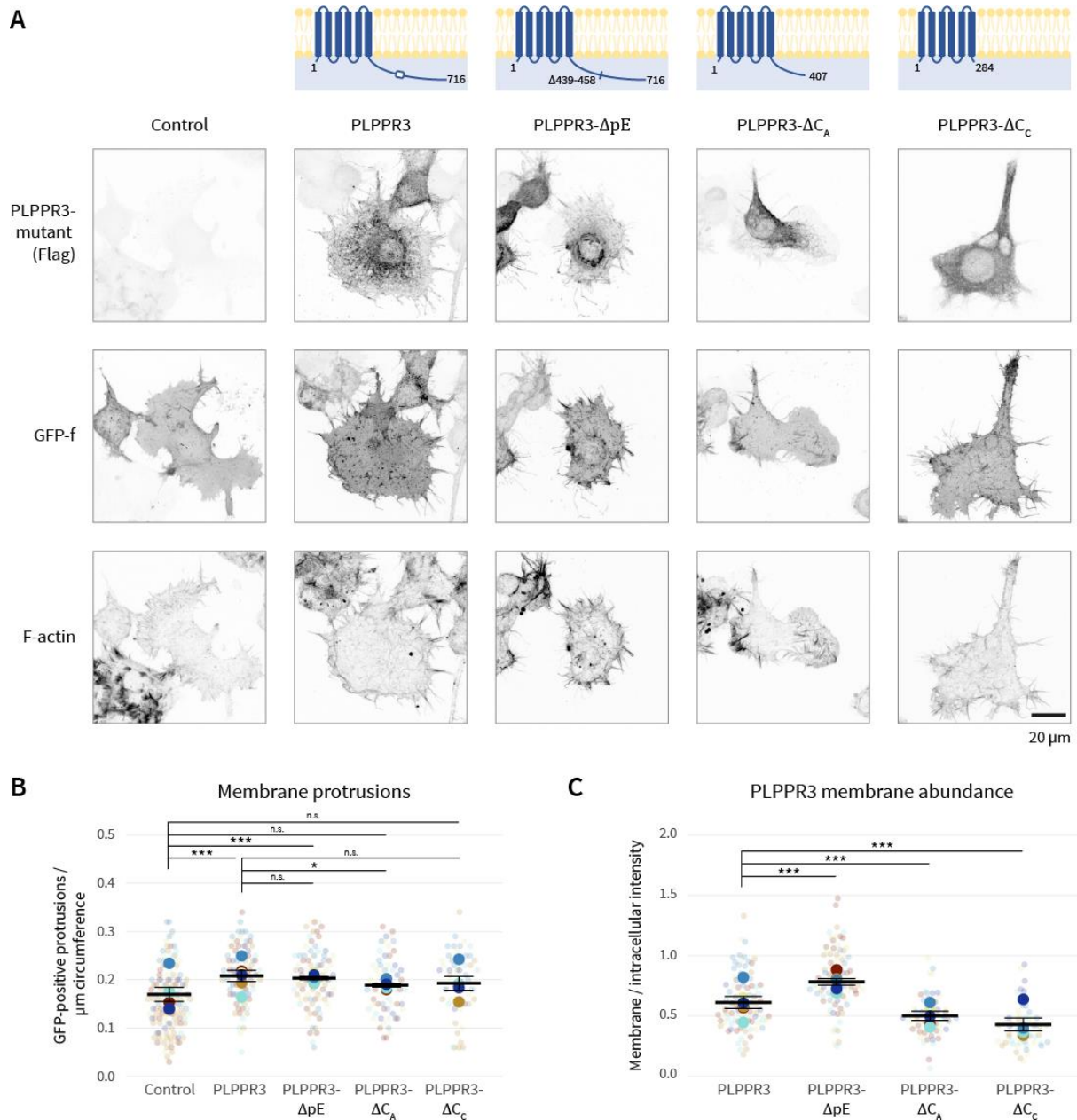


Figure 6: Deletion of C-terminal regions of PLPPR3 alters plasma membrane localisation. (A) Confocal maximum projections of N1E-115 cells expressing a membrane-recruited GFP (GFP-f) and Flag-tagged deletion mutants of PLPPR3 or an empty control plasmid. Note the varying localisation patterns between PLPPR3-constructs from plasma-membrane enriched to internal organelle-enriched. (B) Semi-automated quantification of plasma membrane protrusions per length of cell circumference. Full-length and ΔpE increase protrusion density, phenotypes of C-terminal deletions are unclear. (C) Semi-automated quantification of plasma membrane abundance of PLPPR3-mutants. PLPPR3- ΔpE localises more, C-terminal deletions less to the plasma membrane compared to full-length PLPPR3. Small opaque dots indicate individual cells, large dots indicate means of individual experiments, colour code indicates individual experiments. Effect sizes in Table 5. Error bars represent the SEM between experiments, statistical tests were performed between experiments as described in section 8.12 using mixed effects modelling followed by Holm-corrected post-hoc comparison of individual groups. $n = 6$ experiments (Flag, PLPPR3, ΔpE), $n = 4$ (ΔCA , ΔCC). * $p < 0.05$, ** $p < 0.01$, *** $p < 0.001$

To quantify filopodia forming capacity and membrane localisation, I overexpressed PLPPR3-mutants in N1E-115 cells in combination with a membrane-targeted GFP²⁰⁵ and imaged immunolabelled cells using confocal microscopy. The semi-automated analysis (described in detail in section 7.2.1) included detecting membrane protrusions as intensity maxima outside of the cell and measuring PLPPR3 membrane abundance as the ratio of membrane and intracellular intensity.

Overexpressed PLPPR3 and Δ pE increased protrusion density on N1E-115 cells. The C-terminal deletion mutants require further experiments but tend to induce fewer protrusions compared to wild-type PLPPR3 (Figure 6B, effect sizes in Table 5). However, filopodia-density alterations were difficult to detect in these experiments due to the high baseline density of protrusions in N1E-115 cells. The deletion mutants differed most in their membrane abundance, with the poly-E-box deletion localising more to the plasma membrane and C-terminal deletion mutants localising nearly exclusively to internal membrane structures (Figure 6C, effect sizes in Table 5). Similar phenotypes have been described for PLPPR1 C-terminal deletions¹⁸⁶.

2.3 PLASMA MEMBRANE LOCALISATION IS REGULATED BY CONSERVED DOMAINS OF PLPPRS

The deletion experiments suggest a correlation of filopodia density with PLPPR3 membrane abundance. A minimal level of PLPPR3 at the plasma membrane might be required to mediate the filopodia effects. However, such a correlation complicates the interpretation of experiments testing filopodia density with PLPPR3-mutants altering membrane localisation. To distinguish membrane localisation from filopodia formation defects, I first focused on mechanisms and regions regulating membrane abundance of PLPPR3.

2.3.1 Expression level and co-expression alter plasma membrane abundance of PLPPR3

In the previous experiments, plasma membrane-localised PLPPR3 variants tended to have higher expression levels (data not shown). To further assess the connection of expression strength and membrane localisation, I subcloned wild-type PLPPR3-Flag from the CAG-promoter containing pCAX backbone into the pN1-plasmid that expresses with a slightly weaker CMV-promoter. In subsequent overexpression experiments, this promoter strength also correlated well with plasma membrane abundance of PLPPR3 (Figure 7A).

However, overexpression of C-terminally GFP-tagged PLPPR3 did not localise as efficiently to the plasma membrane as Flag-tagged PLPPR3. Interestingly, co-expression of PLPPR3-Flag with PLPPR3-GFP or any other GFP-tagged PLPPR-family member (Figure 7B) increased membrane localisation of both PLPPR-constructs. Therefore, homo- or heterologous complex formation between PLPPRs might regulate membrane localisation. This link of expression level and membrane localisation for PLPPRs was strengthened in a separate study, where co-expression of PLPPR-family members (with PLPPR1) increased membrane abundance and expression levels of both co-expressed PLPPRs.¹⁸⁶

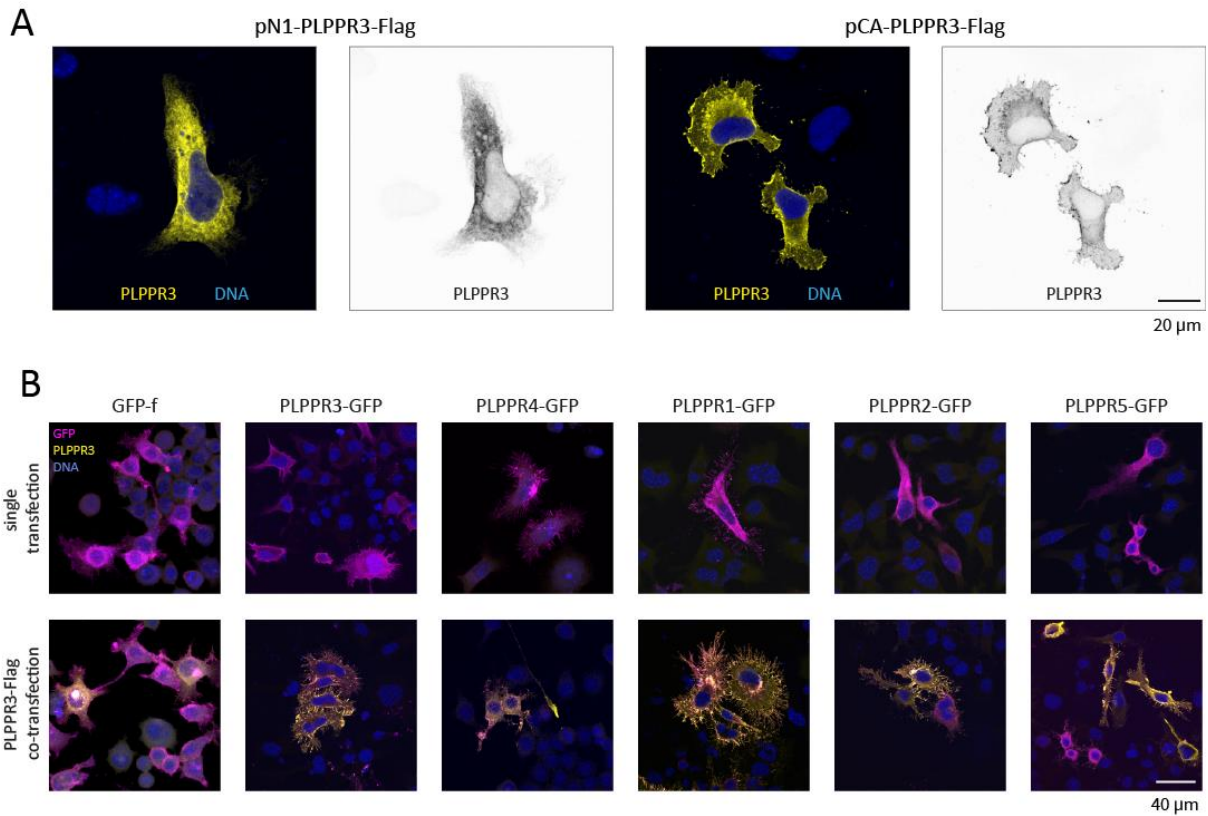


Figure 7: Expression level and co-expression alter localisation of PLPPR3. (A) Expression of PLPPR3-Flag from CMV-promotor (pN1) causes mainly internal localisation, expression from CAG-promotor (pCAX) more plasma membrane abundance. (B) Co-expression of GFP-tagged versions of PLPPR-family members with PLPPR3-Flag increases membrane abundance of both PLPPRs. Both panels show confocal sections of N1E-115 cells overexpressing GFP-tagged PLPPR family members or membrane-targeted GFP (GFP-f) with PLPPR3-Flag. Panel B was previously published in Brosig & Fuchs et al., 2019.¹⁹⁷

2.3.2 Modifications of PLPPR3 in the transmembrane region inform about localisation

Previous experiments in the lab (by Dr. Annika Brosig)²⁰⁶ and studies on PLPPR family members^{155,163,165} have suggested the existence of a modified PLPPR3-version, which shows decreased mobility in SDS-PAGE. This segregation into two pools was reminiscent of the segregation of PLPPR3-variants into pools of internal and plasma membrane compartments. Therefore, with the help of two rotation students, Lars Landgraf (2018-19) and Leandre Ravatt (2021), I assessed the contribution of potential post-translational modifications to the double-band in SDS-PAGE. We furthermore characterised the connection of such potentially modified PLPPR3-species to membrane abundance of PLPPR3.

N-linked glycosylation is among the most discussed modifications in the context of membrane protein trafficking. This glycosylation of asparagine residues occurs co-translationally in the endoplasmic reticulum and is elaborated to glycan trees in the golgi apparatus.²⁰⁷ Glycosylation is required for proper folding of some membrane proteins or acts as a quality control signal for forward trafficking.²⁰⁷ Also some PLPPR proteins^{163,165} and their closely related PLPP-family^{208,209} have been described to depend on glycosylation of an extracellular arginine for plasma membrane localisation. As this arginine is conserved throughout the PLPPR and PLPP family (Figure 8A blue), we created a point-mutant of PLPPR3-N167Q to study the role of this glycosylation event in PLPPR3 membrane abundance.

S-linked palmitoylation of cysteines acts as a regulatable membrane recruitment signal for cytosolic proteins.^{210,211} Membrane proteins can be palmitoylated, even in the middle of their membrane-spanning domains, to alter activity, trafficking to the plasma membrane, or movement to signalling domains.²¹² A prediction of sequence motifs for putative S-palmitoylation sites using the CSS-PALM 2.0 algorithm²¹³ revealed a site in the first transmembrane domain of PLPPR3 (C20) and another site before the third TMD in an intracellular cytosolic loop (C119). These cysteines are conserved throughout the PLPPR-family but absent in the PLPPs (Figure 8A yellow). Given that PLPPR-family-specific motifs likely contain information about PLPPR-specific functions such as filopodia formation, we also designed mutants for both putative palmitoylation sites (C20 and C119) and cloned and tested the PLPPR3-C119A mutant. This work was executed by Leandre Ravatt under my supervision.

Finally, directly adjacent to the third TMD, we found an arginine motif conserved in all PLPPRs that is absent in PLPPs (Figure 8A red). Arginine motifs have been discussed to control trafficking of (clustering) membrane proteins.²¹⁴ Many of these motifs retain proteins in the endoplasmic reticulum and often are binding sites or subject to regulation via phosphorylation (via neutralising the positive charge).^{214,215} Therefore, we neutralised the charge of this PLPPR-specific domain in PLPPR3 by replacing the arginines with glycines to study membrane abundance, filopodia formation, and presence of the double band in Western blots.

Expression of wild-type PLPPR3, the mutant of the putative palmitoylation site C119A and the poly-E-box deletion mutant in N1E-115 cells revealed the double-band in SDS-PAGE experiments visualised via Western blotting (Figure 8B&C). In contrast, the glycosylation-deficient (N167Q) PLPPR3 and the neutralised juxtamembrane region mutant (R>G) showed only the lower band (Figure 8B&C). The ratio of lower to upper band appeared increased in the PLPPR3- Δ pE variant (Figure 8D, effect sizes in Table 5), which presented with higher membrane abundance in section 2.2.1., indicating a correlation of membrane abundance and presence of the double band. Indeed, when visualising the localisation of the other mutants in N1E-115 cells (Figure 8E), the double-band containing versions (wild-type, C119A) partially localised to the plasma membrane, while the single-band versions (N167Q, R>G) localised internally (Figure 8G, effect sizes in Table 5).

These results suggest that glycosylation is required for PLPPR3 presence at the plasma membrane. However, enzymatically removing glycosylations or phosphorylations (by Dr. Annika Brosig and Cristina Kroon, not shown) shifted both bands, rather than specifically targeting only the modified species. Therefore, the exact modification of PLPPR3 resulting in the differential migration on SDS-PAGE is still unclear. However, the reduced membrane localisation of the single-band mutants (N167Q, R>G) suggests that the double is acquired at the plasma membrane.

The internal localisation of the polybasic juxtamembrane mutant was unexpected, as arginine motifs were mainly described to counteract rather than promote plasma membrane recruitment.²¹⁴ However, in particular arginine motifs close to the plasma membrane appear to mediate exit from the endoplasmic reticulum and golgi.²¹⁶ Furthermore, delta opioid receptors require a similar motif to regulate PI3K-dependent trafficking to the plasma membrane.²¹⁷ The positive charge directly adjacent to the plasma membrane and the putative link to PI3K activity suggests binding to negatively charged

Figure 8 (previous page): Presence of a modified PLPPR3 species correlates with plasma membrane abundance. (A) Alignments of putative regulatory motifs in the PLPPR-family compared to related regions in PLPPs. Yellow: predicted palmitoylation sites (CSS-PALM 2.0)²¹³, red: poly-basic juxtamembrane region, blue: conserved N-linked glycosylation. (B&C) Representative Western blots of lysates from N1E-115 expressing mutants of the putative regulatory motifs. C199A: palmitoylation mutant, N167Q: glycosylation mutant, R>G: polybasic mutant. Glycosylation- and R>G-mutant lack the double band. (D) Quantification of upper / lower band intensity. Colour code indicates the person and year of execution, error bars represent SEM. n=4 (mutants tested by Leandre Ravatt) or n=7 (mutants tested additionally by Lars Landgraf). (E) Maximal projections of N1E-115 cells expressing indicated mutants with membrane-targeted GFP (GFP-f). Control: empty plasmid. (F) Quantification of membrane abundance. N167Q and R>G mutants appear less membrane abundant. (G) Quantification of membrane protrusion density. R>G mutant induces fewer filopodia, other mutants are not conclusive. Small opaque dots indicate individual cells, large dots indicate means of individual experiments, colour code indicates individual experiments. Effect sizes in Table 5. Error bars represent the SEM between experiments, n = 6 experiments (ctrl, PLPPR3 & R>G), n = 3 (C119A, N167Q). Statistical test: mixed model between experiments, post-hoc comparisons Holm-corrected. * p < 0.05, ** p < 0.01, *** p < 0.001. (H) Lipid-binding overlay assay (PIP-Strip, Echelon) using purified PLPPR3-Flag-1D4 (provided by Fatih Ipek) shows strong binding to negatively charged lipids in one experiment. (I) PIP-strip with Biotin-labelled peptides spanning polybasic juxtamembrane region indicates charge-dependent binding of this region to negatively charged lipids. Images show an intensity-adjusted average-projection of all replicates. None of the wild-type specific bindings were statistically detectable with n=4 (wild-type) and n=2 (mutant).

To circumvent the need for a complex PLPPR3 purification, I optimised the lipid-binding assay with synthesised, biotin-labelled peptides of the polybasic juxtamembrane region. Although at a much lower signal-to-noise, also the wild-type peptide tends to bind negatively charged lipids (potentially preferring monophosphate phosphoinositides). Replacing the conserved arginines with glycines seems to abolish PIP-binding (Figure 8I). However, the low intensity of binding prevents strong conclusions and makes this experiment a pilot study to test the R>G mutant with purified full-length protein.

Nevertheless, PLPPR3 seems to bind specific membrane lipids, potentially with a region mediating trafficking to the plasma membrane. Detecting different lipid compositions on different organelles could therefore also be an additional regulatory mechanism for PLPPR3 trafficking.

2.3.3 Catalytic center mutants reduce plasma membrane abundance of PLPPR3

Due to the high homology to lipid phosphatases of the PLPP-family, some PLPPR-functions are likely mediated by PLPP-substrates. Indeed, while PLPPR1 and PLPPR4 have been identified to lack hydrolytic activity against lysophosphatidic acid (LPA)^{153–155}, several experiments characterised crosstalk between PLPPRs and LPA-mediated functions^{159–161,218,219}. However, it remains elusive whether these effects are mediated by shared downstream signalling, by direct lipid binding, or by lipid transport mechanisms.

Recently, two structures of a bacterial lipid phosphatase (Phosphatidylglycerophosphatase B, PgpB) have been published.^{220,221} These structures provide insight into the catalytic centre of the homologous PLPPs. PgpB dephosphorylates lipids using a catalytic triad of H163, H207, and D211 (Figure 9A red). All PLPPRs lack histidine 207 in the C3 domain, PLPPR2 and PLPPR5 even lack histidine 163 in the C2 domain. In addition to these catalytic residues, PgpB contains conserved positive charges at positions K97, R104, and R201 to bind the phosphate group of the phospholipid. Two of these phosphate-binding residues are missing in all members of the PLPPR family; PLPPR3 even lacks all of them (Figure 9A blue).

PgpB binds its lipid substrates specifically at its head group using a specific arrangement, the so-called PSGH-loop, in its C2 domain of the catalytic center (for visualisation see Figure 5, Tong et al., 2018).²²¹ The glycine between serine 161 and histidine 163 allows for the entrance of specific lipid head-groups that is blocked by replacement with bulky amino acids. All PLPPRs contain charged bulky amino acids at this position, suggesting a blocked gate before the mutated catalytic centre. Additional to this head group filter, PgpB contains a binding pocket for lipid tails between the second and third transmembrane loops. A small amino acid at position 89 (glycine) has been described as required for distinguishing lipids of different lengths.²²¹ Lysine 93 is mutated to a smaller amino acid in eukaryotic PLPPs and has been described to distinguish lipid species between eukaryotic PLPPs and prokaryotic PgpB.²²¹ Interestingly, compared to other functional domains of PgpB and PLPPs, this potential lipid-binding pocket seems less disturbed in PLPPRs (Figure 9A yellow).

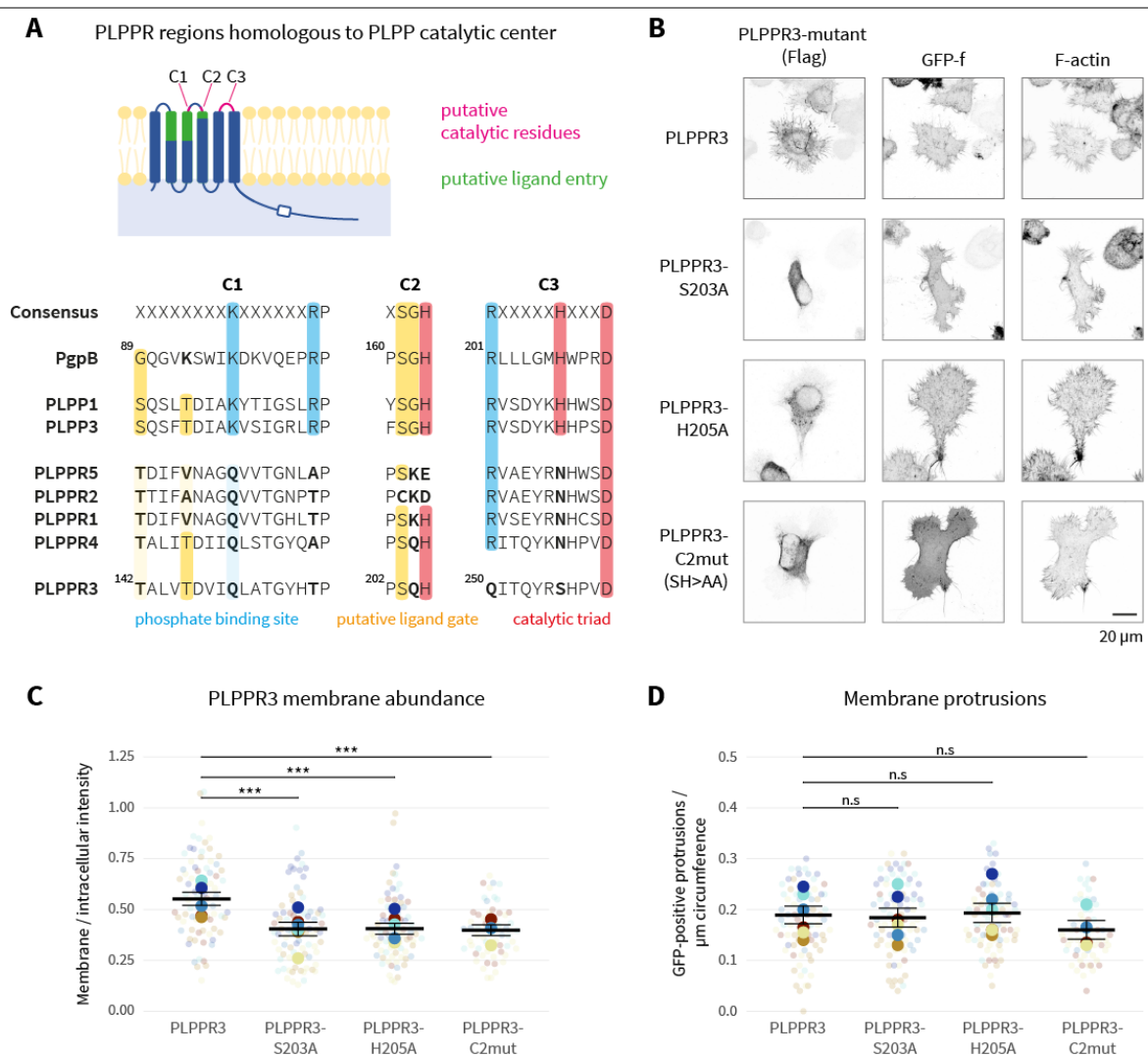


Figure 9: Mutants to the putative catalytic centre of PLPPR3 reduce plasma membrane abundance. (A) Alignments of catalytic domains of *E.coli* PgpB and murine PLPP1, PLPP3 as well as PLPPRs. Colour coded are regions of specific relevance for PgpB and PLPPs. (B) Confocal maximum intensity projections of N1E-115 cells expressing indicated PLPPR3-Flag constructs with membrane-targeted GFP (GFP-f). (C) Quantification of plasma membrane abundance of mutants compared to wild-type PLPPR3. (D) Quantification of protrusion density of mutants. Small opaque dots indicate individual cells, large dots indicate means of individual experiments, colour code indicates individual experiments. Effect sizes in Table 5. Error bars represent the SEM between experiments, $n = 6$ experiments (PLPPR3, S203A, H205A), $n = 4$ (C2mut). Mixed model between experiments, post-hoc comparisons Holm-corrected. *** $p < 0.001$.

Given these mutations of critical catalytic and phospholipid-binding residues in PLPPRs, the lack of hydrolytic activity of PLPPR1 and PLPPR4 is not surprising.^{153–155} As these PLPPRs have the least disturbed catalytic centre of the family, the other PLPPRs are even less likely to be catalytically active against LPA. Nevertheless, mutations of the remaining catalytic histidine in the C2 domain abolish some LPA-mediated functions of PLPPR4¹⁶⁰ and causes PLPPR1-retention to the endoplasmic reticulum.¹⁵⁵ Furthermore, reconstitution of this histidine in PLPPR5 rescues membrane abundance.¹⁶⁵

To test for the role of the C2-domain in PLPPR3, I mutated serine 203 and histidine 205 and measured membrane abundance and filopodia forming capacity in N1E-115 cells (Figure 9B). Interestingly, also these PLPPR3 mutants constrict the protein to internal membrane compartments (Figure 9C, effect sizes in Table 5). Filopodia forming capacity was too variable to allow conclusions (Figure 9D, effect sizes in Table 5). Therefore, even though catalytic activity against lipids is highly unlikely in PLPPRs, their former catalytic centre might mediate plasma membrane localisation. This suggests a potential sensing role of the inactivated lipid-binding region.

2.4 SUMMARY AND OUTLOOK: DOMAIN MAPPING PROVIDES TOOLS TO PRECISELY STUDY PLPPR3 FUNCTION

In summary, these experiments present PLPPR3 as a neuron-specific, axon enriched membrane protein localising to internal and plasma membrane structures. PLPPR3 overexpressing cells contain more filopodia, and membrane abundance of PLPPR3 is tightly regulated by expression levels and by functional domains in its membrane-spanning region. Furthermore, a potentially modified species of PLPPR3 visible in Western blots correlates well with plasma membrane abundance of PLPPR3.

The region mediating the filopodia effects is likely shared across members of the PLPPR-family. My experiments rule out the possibility that the poly-E-box mediates the effects on filopodia density. However, the deletion mutant experiments are not conclusive because filopodia readouts are highly confounded by high baseline filopodia density of N1E-115 cells, altered expression level and, critically, membrane trafficking of mutant versions of PLPPR3. Similar effects have prevented the description of the exact site for PLPPR4¹⁸⁷ and PLPPR1.¹⁸⁶ However, membrane targeting of the C-terminal domain of PLPPR1 seems to effectively increase filopodia density,¹⁶⁶ making regions in the C-terminal domain the best candidate for filopodia functions of PLPPRs.

Furthermore, the high homology of PLPPRs in their transmembrane region with conserved PLPPR-specific mutations, indicates that domains in the membrane region play critical roles to distinguish PLPPR- from PLPP-functions. If the C-terminal regions of PLPPRs indeed harbour filopodia-related domains, the transmembrane regions could localise PLPPRs or activate this function. To test this hypothesis, ideally, one would find a mutant of PLPPR3 that traffics normally but fails to induce filopodia. An interesting candidate mutation could be a mutant of the proline-motif in the C-terminal domain replacing either the negative charges between the prolines, or the prolines directly to alter the secondary structure of the domain. In case such mutants fail to induce the increased filopodia density, they could serve as tools to specifically screen for binding partners that mediate the filopodia effects.

Regarding the regulation of PLPPR3-function, membrane trafficking emerges as a fruitful field of study. The promoter experiments suggest that the expression level drives membrane localisation rather than the reverse. This potentially enables a strategy to de-confound functional studies from localisation phenotypes by adjusting expression levels of the internally localised mutants. The experiments using the mutant of a putative palmitoylation site suggest no role of C119 in plasma membrane localisation. However, the other predicted palmitoylation site C20 and roles of palmitoylation in filopodia formation still pend testing. The glycosylation-deficient mutant N167Q failed to traffic to the plasma membrane. In contrast, the poly-E-box deletion mutant localised more to the plasma membrane. Therefore, these two mutants could serve as tools to differentiate plasma membrane-mediated effects from internal organelle-mediated functions of PLPPR3.

The phosphoinositide binding of PLPPR3, potentially mediated by a polybasic region close to the third transmembrane loop, could be an interesting mechanism to regulate PLPPR3 localisation to the plasma membrane or even to microdomains of the plasma membrane. The trafficking defects of mutants to the catalytic centre further suggest regulation of PLPPR3 function by interaction with bioactive lipids. These studies, however, still lack direct evidence for binding of lipids to PLPPR3 and could be further elucidated by information about the structure of the membrane region of PLPPRs.

In summary, these mutagenesis experiments establish several interesting hypotheses for future experiments and highlight the need for controlling membrane trafficking of PLPPRs to study functional readouts reliably. The analysis tools and the mutants of PLPPR3 generated here can hopefully facilitate such experiments, and the measured effect sizes (Table 5) can inform sample size estimations for subsequent confirmatory experiments.

3 GENERATING A *PLPPR3*^{-/-} MOUSE USING CRISPR/CAS9

The experiments of the previous section have suggested a function of PLPPR3 as a neuron-specific, axon-enriched plasma membrane protein that, following overexpression, increases filopodia density on cells. To study the function of PLPPR3 in a more physiological setting, we decided to generate a knockout mouse for PLPPR3 using the CRISPR/Cas9 technique. This was undertaken in collaboration with Thorsten Trimbuch (Laboratory of Prof. Christian Rosenmund, Viral core facility Charité) and the Transgenic Technology Core Facility (Prof. Geert Michel) of the Centre for Experimental Medicine at Charité (FEM). Results of this section have been partially published in Brosig & Fuchs et al. 2019.¹⁹⁷

The CRISPR/Cas9 (clustered regularly interspaced short palindromic repeat/ CRISPR-associate 9) system uses an RNA-directed nuclease to alter a given genome at precise sites only.^{222,223} Short RNAs guide the nuclease (Cas9) to the genomic target region. Depending on the specific version, Cas9 cleaves both or only one strand of the host-DNA. The resulting DNA-repair mechanisms can be used to introduce frameshift mutations in coding regions (by non-homologous end-joining). Alternatively, by providing an external template for endogenous homology-directed repair mechanisms, they can facilitate the insertion or excision of genomic DNA regions. The induction of these repair mechanisms at specific genomic target regions vastly improves the efficiency of gene editing when compared to conventional gene-editing methods.^{224,225} In this way, CRISPR/Cas9 has tremendously increased the number of genetically modified organisms or cell lines over the last years.

3.1 FIRST EXON OF *PLPPR3* IS A SUITABLE TARGET FOR PREVENTING *PLPPR3* EXPRESSION

We decided to generate a conditional knockout by introducing LoxP sites at the genomic locus of *Plppr3*. To determine a suitable target exon essential for PLPPR3 expression, I inspected the genomic region and transcripts as listed in NCBI and Ensembl databases. Both databases provide evidence for multiple splice variants of PLPPR3 (Figure 10A) that differ in their intracellular C-terminal domain.

3.1.1 PLPPR3 expression is likely regulated by alternative splicing

To study the relevance of these splice variants in developing neurons, I designed primers to amplify the alternative variant containing exons 8 and 9 and purified RNA from developing mouse hippocampus (embryonic day 15). I created complementary DNA using poly-dT-primers to specifically enrich mRNAs and could detect full transcripts containing exons 8 and 9 via PCR (Figure 10B). To study these transcripts in more detail, I subcloned them into pJET plasmids and sequenced multiple clones.

The detected transcripts contained the exact alternative splice event (connecting the middle of exon 7 with exon 8) as listed in the genomic databases (Figure 10C, Var2a). The amino acid surrounding the alternative splicing site in exon 7 codes for G407 before the poly-E-box in the C-terminal domain of PLPPR3, which demarcates the last amino acid of the previously discussed Δ Ca mutant. In addition to the listed splice event, many clones also differed by an alternative acceptor site for exon 8 that introduces a frameshift mutation to remaining exons 8 and 9 (Var2b). This suggests the existence of at least three versions of PLPPR3, differing in the exact ends of their C-terminal region with the Δ Ca mutant (aa 1-407) as the common denominator among all versions.

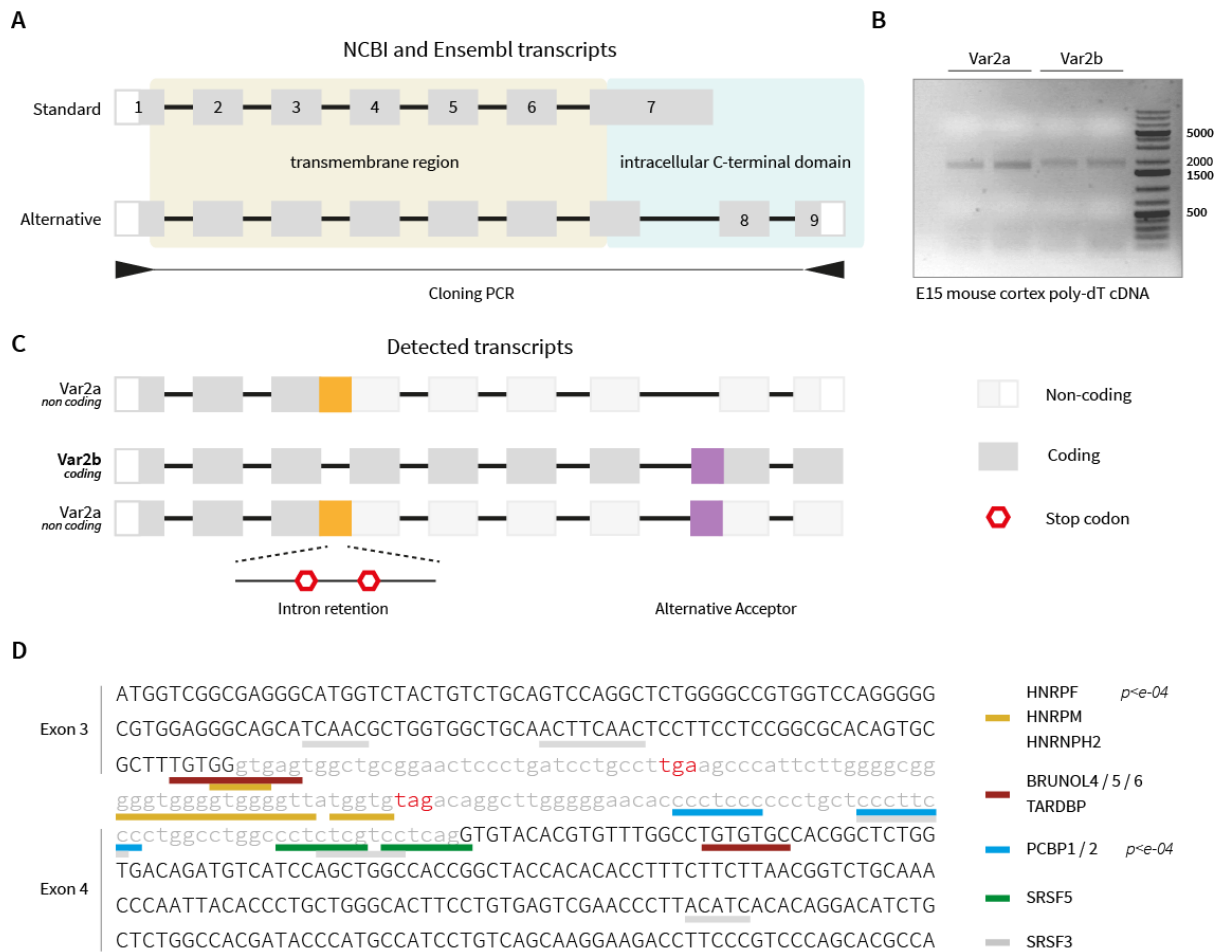


Figure 10: PLPPR3 splice variants differ in C-terminal region and are likely regulated by intron retention. (A) Splicing scheme of conventional (poly-E-box containing) as well as alternative PLPPR3 variants with experimental evidence from transcriptomic and proteomic studies listed in Ensembl and NCBI genome databases. Exons and introns are not drawn at scale to focus on specific alternative splicing events. Arrows indicate primer binding sites for verifying alternative variants in neurons used in panel B. (B) PCR products from cDNA (poly-dT) from RNA of E15 mouse cortex. Two species of the alternative Plppr3 transcript are detectable (Var2a and Var2b). (C) Subcloning and sequencing of Var2a and Var2b transcripts provides evidence for two major alternative splice events: (1) Var2a and Var2b differ in an alternative splice acceptor at exon 8 (purple), which introduces a frameshift of consecutive C-term and therefore three PLPPR3-variants differing in their C-terminal domain. (2) most transcripts contain a retained intron between exons 3 and 4 (orange) that would not introduce a frameshift but harbours two stop codons. (D) Visualisation of binding motifs for RNA-binding proteins in intron 3-4 with similar expression profile and p-values for prediction below 0.001. Intron retention between exons 3 and 4 is therefore likely a mechanism to regulate PLPPR3 levels in presence of high mRNA levels.

Additionally, most alternatively spliced transcripts comprised a short, retained intron between exons 3 and 4 (Figure 10C). Interestingly, this retained intron does not introduce a frameshift in PLPPR3 but does contain two stop codons, thereby likely preventing translation of the alternatively spliced transcripts. All detected Var2a transcripts sequenced so far included the retained intron and are therefore unlikely to exist at the protein level. However, some Var2b transcripts did not contain the retained intron and would therefore be expected to express. This opens interesting questions about the role of the C-terminal domain of PLPPR3, which would be drastically modified in Var2b.

Furthermore, a search for motifs of regulatory RNA-binding proteins performed in collaboration with Dr. Sebastian Rademacher, yielded an exceptionally high density of potential binding motifs in the intron 3-4 region. Figure 10 panel D shows the highest confidence ($p < 0.001$) predictions for RNA-binding proteins that share the neuron-enriched and developmentally regulated expression profile in the Allen Brain RNAseq and Brainspan databases.^{96,226,227} Therefore, the retained intron 3-4 is a likely candidate for regulating PLPPR3 levels (and potentially splice variants) after transcriptional regulation.

3.1.2 Knockout strategy: insert LoxP sites around first exon using CRISPR-Cas9

Inspection of the genomic locus of *Plppr3* (Figure 11A) in Ensembl and NCBI genome browsers shows partial overlap of the *Plppr3* gene with (the splicing regulator) *Ptbp1*, especially in regions around exons 7-9. Any genomic modification of these exons would risk modifying *Ptbp1* expression. The block of exon 2 to exon 6 contains the potentially regulatory intron 3-4 and all introns are shorter than 200 bp, making insertion of any additional sequence potentially harmful. Furthermore, complete excision of the exon 2-6 block would not result in a frameshift mutation, thereby only truncating PLPPR3 protein from its membrane domain instead of yielding a complete lack of expression.

The first exon of *Plppr3* comprises the start of transcription as well as translation for all splice variants. It does not overlap with regulatory features or parts of other genes and is separated from other exons by large introns. Furthermore, exon 1 codes for parts of the first membrane helix. Potential internal start codons in later exons (Figure 11A inset) are predicted to be very unlikely and would generate a protein devoid of the proper transmembrane region of PLPPR3. Should translation nevertheless occur, the generated truncated proteins would be expected to mislocalise or be degraded. We therefore decided to target exon 1 to abolish *Plppr3* expression.

We pursued the strategy to insert LoxP sites (locus of X-overP1) around exon 1 (Figure 11B) to enable using the Cre/LoxP system (causes recombination) for potential cell type or treatment-induced knockouts in addition to full knockout of *Plppr3*.²²⁸ To facilitate the screening for correct genomic modification, we additionally planned to introduce restriction sites for NheI and EcoRI adjacent to the LoxP sites. To facilitate genome editing around exon 1, I designed and tested the efficiency of three CRISPR/Cas9 guide RNAs for each insertion site respectively during my master thesis.²²⁹ The exact binding sites of these guide RNAs were used to design donor templates for homology-directed repair insertion of the genomic modification (LoxP, restriction site).

Following reports of highly efficient (up to 50%) insertion of LoxP sites using short single-stranded oligonucleotides as repair templates,^{224,230} we designed and ordered highly pure long oligonucleotides containing the desired modification and 60 bp homology to either side of the cut point (Figure 11B strategy 1). However, in pilot experiments using these oligonucleotides with our guide RNAs, only about 20% of CRISPR/Cas9 modified blastocysts contained insertions at the target site (not shown). Furthermore, a functional conditional knockout line requires the independent insertion of two LoxP sites on the same chromosome. Therefore, the expected success rate to generate such a floxed allele using this strategy would drop to about 2% (20% site 1 * 20% site 2 * 50% not on the sister chromosome).

We therefore decided to exploit the less efficient strategy of using a plasmid template containing the entire genomic target region (including exon 1 and the LoxP-insertions) with 1 kb homology arms to either side (Figure 11B strategy 2). While the efficiency per insertion in this strategy is usually lower (about 10%)²³¹, a correct insertion would already include both LoxP sites on the same chromosome, thereby increasing the chances for successful genome editing in our case.

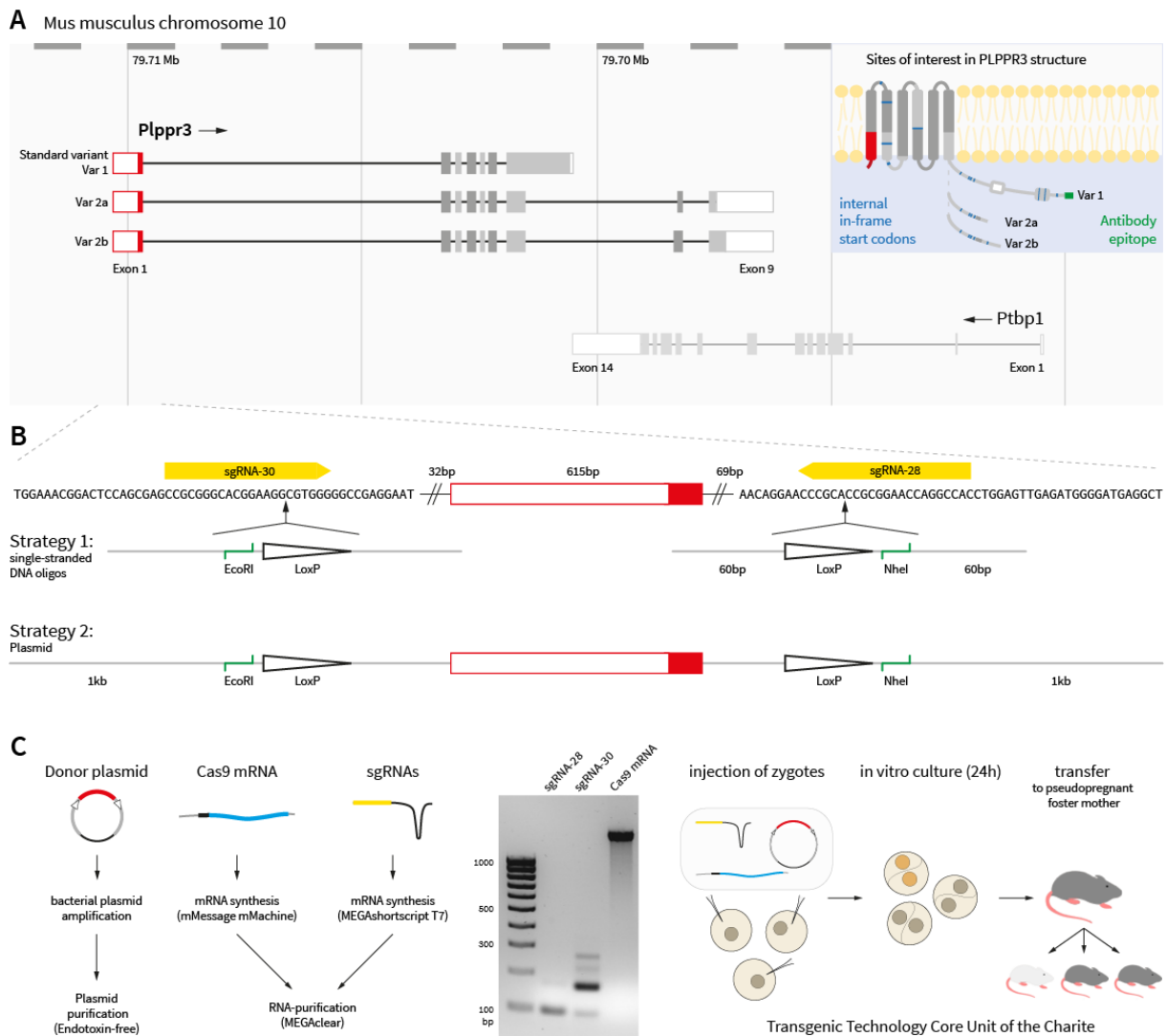


Figure 11: Strategy for generating conditional knockout of murine *Plppr3* using CRISPR/Cas9.

(A) genomic target region on chromosome 10 indicating shared exons between splice variants and overlap with a neighbouring gene (*Ptpb1*) in later exons. Intron and exon sizes at correct scale. Inset indicates position of exons in PLPPR3-protein, splice variants, antibody epitope and potential in-frame start codons that could replace the exon 1 start. (B) exact location of genome editing sites around exon 1 and two strategies followed to induce LoxP insertion via homology-directed repair. (C) Workflow of genome editing: preparation of donor template, Cas9 mRNA and sgRNAs as well as quality control on agarose gels. Injection of zygotes, in vitro culture and fertilisation were performed by Adrian Landsberger and Charlotte Schück at Transgenic Technologies Core Uni (Laboratory of Prof. Geert Michel) of Charité.

Having decided on the tools, I cloned and purified the donor plasmid and amplified and purified Cas9 mRNA as well as guide RNAs (Figure 11C). A mix of 10 ng/ μ l guide RNA, 20 ng/ μ l Cas9 mRNA, and 20 ng/ μ l donor plasmid was injected into pronucleus and cytosol of murine zygotes by Adrian Landsberger and Charlotte Schick at the Transgenic Technology Core unit of Charité. After in vitro culture to the two-cell stage, the remaining zygotes were transferred to pseudo-pregnant foster mice. The offspring of these mice was genotyped according to the strategy described in (Figure 12A).

3.2 EXCISION OF EXON 1 RESULTS IN FULL KNOCKOUT OF *PLPPR3* EXPRESSION

In four rounds, spread over one year, 401 zygotes were injected by two experienced technicians at the Transgenic Technologies Core Unit. Of those, 275 (69%) survived the in vitro culture and were transferred to foster mice. Unfortunately, those gave birth only to 30 mice, none of which showed the desired insertion of LoxP sites at exon 1.

3.2.1 Validation of *Plppr3* knockout on DNA and protein-level

While none of the mice had the desired genetic modification of inserted LoxP sites, in the third injection round, one mouse presented with a large deletion in one genotyping PCR (Figure 12B&C). Further sequencing confirmed the lower band in mouse 7 to lack exon 1 by non-homologous end-joining of the 3' and 5' site.

Crossing this mouse allowed for the analysis of PLPPR3 protein levels in brains of postnatal day 2 (Figure 12D) as well as in cultured neurons (Figure 12E) of all genotypes. Both analyses verified the absence of PLPPR3 protein in homozygous animals lacking exon 1 and demonstrate the lack in expression of truncated PLPPR3 species. Furthermore, it suggests binding of the antibody to a protein of 60kDa (Figure 12D, remaining band in *Plppr3*^{-/-} condition). As the most likely downstream start codons of *Plppr3* would predict sizes of 70 or 35 kDa, this 60 kDa protein is likely recognised unspecifically by the antibody.

This custom-made antibody detects the very last amino acids of the canonical PLPPR3 splice variant. As the splice variants Var2a and Var2b differ in the C-terminal domain and thereby as were the antibody binding site, we cannot exclude residual expression of altered splice variants in the *Plppr3*^{-/-}. However, Var2a and Var2b share most of their sequence (including exon 1 and potential downstream start codons) with the canonical *Plppr3*. Therefore, if the expression of canonical *Plppr3* does not occur, an expression of functional splice variants is also highly unlikely. In summary, these analyses verify absence of canonical PLPPR3 protein in homozygous mice lacking exon 1, yielding a knockout mouse for this *Plppr3* variant.

3.2.2 Off-target quality control

Given its use of DNA damage and repair pathways, CRISPR/Cas9 genome editing has the potential of causing unwanted off-target mutations. While a widely discussed study describing hundreds of such mutations in genomes of CRISPR/Cas9-edited mice has now been retracted due to lack of proper controls,²³² off-target activity of Cas9 nevertheless is of major concern, specifically regarding clinical application in humans.

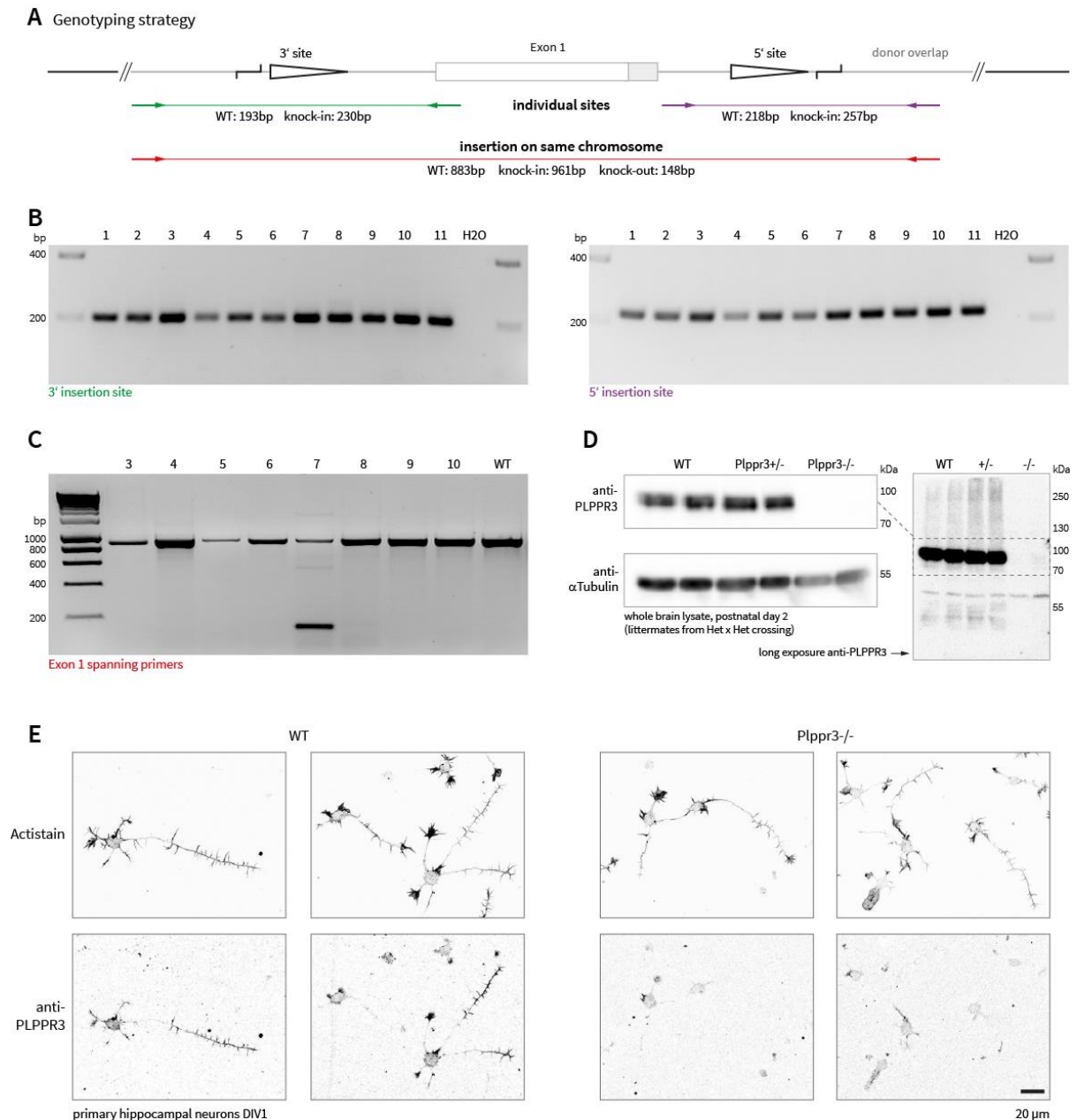


Figure 12: Validation of *Plppr3* knockout at genome and protein level. (A) Genotyping strategy including two PCRs spanning the individual insertion sites as well as a third PCR to verify insertion on the same chromosome. (B) Genotyping PCR of injection round 3 for individual insertion sites. No correct insertion is detectable. (C) Genotyping PCR of same injection round for insertion on same chromosome. Mouse 7 shows a heterozygous large deletion, sequencing confirmed that the end-joining of both target sites excluded exon 1. (D) Western blot of lysates from P2 offspring of mouse 7 shows full lack of PLPPR3 protein expression in homozygous animals lacking exon 1. Note the unspecific binding of the antibody to a protein of 60 kDa (E) Confocal maximum projections show lack of PLPPR3 labelling in DIV 1 hippocampal neurons lacking exon 1 of *Plppr3*.

The frequency of off-target mutations introduced by CRISPR/Cas9 editing has been described to be in the low 0.1%-range and off-targets generally share sequence homology to the guide RNA.²²⁴ Chances for off-target activity decrease further when providing Cas9 transiently via mRNA or protein delivery instead of plasmid expression, as in these experiments.²³³ Nevertheless, during the initial design we screened for guide RNAs with minimal predicted off-targets using tools from Sanger and the Feng Zhang lab.^{234,235}

The target sequence of sgRNA-28 is similar to 55 genomic regions, 9 of which are found in exons. The sequence of sgRNA-30 is found in 38 regions, 8 of which are found in exons. None of the predicted exonic off-targets was found on the same chromosome as *Plppr3* (Figure 13A). Three potential off-targets (with 4 mismatches) were found on chromosome 10 in large intronic regions (*Baz2a*, *Nav3*, *Tmem19*). Off-target frequencies were found to differ based on the location of the mismatches in the guide RNA (proximal or distal to the PAM motif). As most mutations of off-targets cause frameshifts that more severely affect coding regions, we focused a screen for mutations on exonic sites with a high likelihood score (Figure 13A grey background). PCR-amplification and sequencing of these off-target candidate sites showed no modification in the founder mouse of the *Plppr3*^{-/-} line (Figure 13B).

The current gold standard prior to use of CRISPR/Cas9 as a therapeutic additionally uses empirical methods to screen for potential sites (e.g., GUIDE-Seq, CIRCLE-Seq, or whole-exome sequencing).²³⁶ Guide RNAs should be chosen with respect to low off-target frequency as well as potential off-target activity only in genomic regions of lower harm (best intergenic, not exonic, not near tumor suppressors or oncogenes).²³⁶ These considerations, however, generally are of more importance in therapeutic strategies in humans, where usually higher numbers of cells (later developmental timepoints) are treated, and even low-percentage off-target activity could cause harm. For genome editing in mice, relevant (meaning heritable) off-target mutations have to occur in the zygote stage in a short period of time. Furthermore, mutations in non-target chromosomes can be eradicated by backcrossing the gene-edited line to wild-type mice. To secure against potentially undetected off-targets, we backcrossed the *Plppr3*^{-/-} line three times so far, reducing the chance for undetected off-target mutants on other chromosomes by a factor of 8.

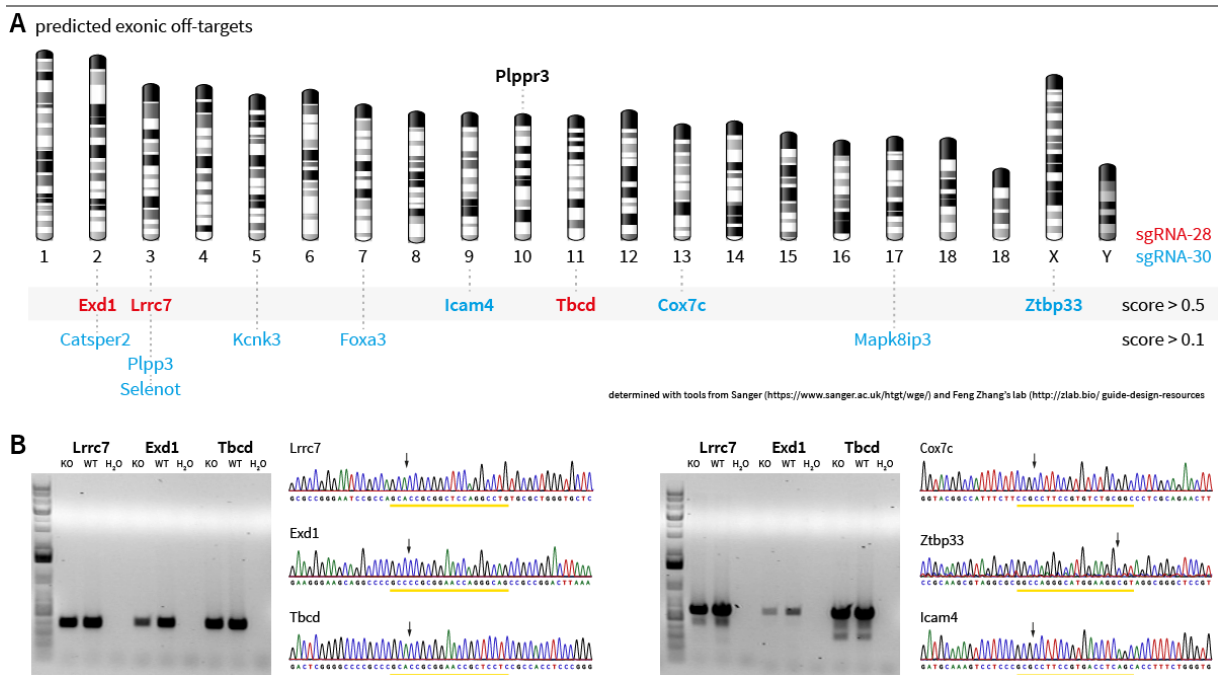


Figure 13: Analysis of potential off-target modifications in *Plppr3*^{-/-} mice. (A) genomic location of predicted off-target sites based on homology to guide RNA sequences. None of the exonic off-targets is found on the same chromosome as *Plppr3*. (B) Sequencing of genomic loci of off-targets with score > 0.5 (Feng Zhang lab tool). No off-target is found to be modified in the founder mouse.

3.3 SUMMARY AND OUTLOOK: STRATEGIES FOR CREATING A CONDITIONAL PLPPR3 KNOCKOUT

In summary, while our initial objective to generate a conditional knockout line for *Plppr3* failed, we successfully established a full *Plppr3* knockout without mutations in the most likely predicted off-target sites. This mouse line was used in the following chapters to characterise endogenous PLPPR3 functions in neurons.

One major obstacle to achieving successful sequence insertion in mice was the low birth rate of only 7% after in vitro fertilisation. At a knock-in efficiency of usually around 10%, the 30 mice were likely just not successfully edited by chance. In pilot experiments, we optimised concentrations of RNAs in the injection solution and improved culture conditions to increase the survival of zygotes in culture, but none of these changes seemed to be linked to the low birth rate of mice. Instead, a major disruption during experimentation might have been caused by changes in personnel and relocation of the facility during the time of experimentation. Therefore, future injection rounds are likely to be more successful even without major optimisations of the protocols.

However, the knock-in efficiency in CRISPR/Cas9 strategies has been drastically optimised over the last years.²³⁷ The largest increases in efficiency were achieved by modifying the knock-in templates: as an example, linearising double-stranded plasmid templates to only contain a fragment with 800 bp homology arms increases efficiency compared to circular plasmids (Tild-CRISPR).²³⁸ Alternatively, the 'Easi-CRISPR' technique uses long, single-stranded DNA fragments as templates achieving astonishing rates of 90-100 % knock-in frequency in mice.^{239,240}

In trial experiments of this Easi-CRISPR technique, we injected such self-made single-stranded DNA to zygotes and, instead of transferring to foster mice, genotyped 32-cell stage blastocysts grown in culture. This small modification of the donor plasmid in our strategy yielded 96% (27/28) of blastocysts with the correct genomic modification and only 36% (10/28) still containing the wild-type genomic locus of *Plppr3*. However, the employed genotyping strategy was susceptible to trace amounts of leftover ssDNA template in the blastocysts with their inherently low amount of DNA at the 32-cell stage. The lack of the wild-type genomic locus in nearly one third of all genotyped blastocysts, nevertheless, suggests successful and even homozygous alteration of a large fraction of injected zygotes. Therefore, long single-stranded DNA templates (as used in the Easi-CRISPR protocol) could be a fruitful strategy to increase knock-in efficiencies also in our experimental setup.

4 PLPPR3 REDIRECTS GROWTH TO BRANCHES

My initial structure-function studies establish PLPPR3 as a neuron-enriched protein capable of inducing membrane protrusions in overexpression studies using N1E-115 cells. Further data by Dr. Annika Brosig²⁰⁶ indicate developmentally regulated expression of *Plppr3* peaking at birth in rat brains and at day-in-vitro 9 (DIV9) in murine primary cortical neuron cultures. Given the role of *Plppr*-family members in neuron growth and morphogenesis, I compared the morphology of *Plppr3*^{-/-} to wild-type neurons. Results of this section have been partially published in Brosig & Fuchs et al. 2019.¹⁹⁷

4.1 OVERALL DEVELOPMENT OF NEURONS IS NOT DISTURBED IN *PLPPR3*^{-/-}

Our animal caretakers did not notice behavioural differences or developmental defects in *Plppr3*^{-/-} mice. Furthermore, breeding heterozygous mice resulted in mendelian distributions of offspring genotypes (Figure 14A), indicating no embryonic lethality due to loss of *Plppr3* expression.

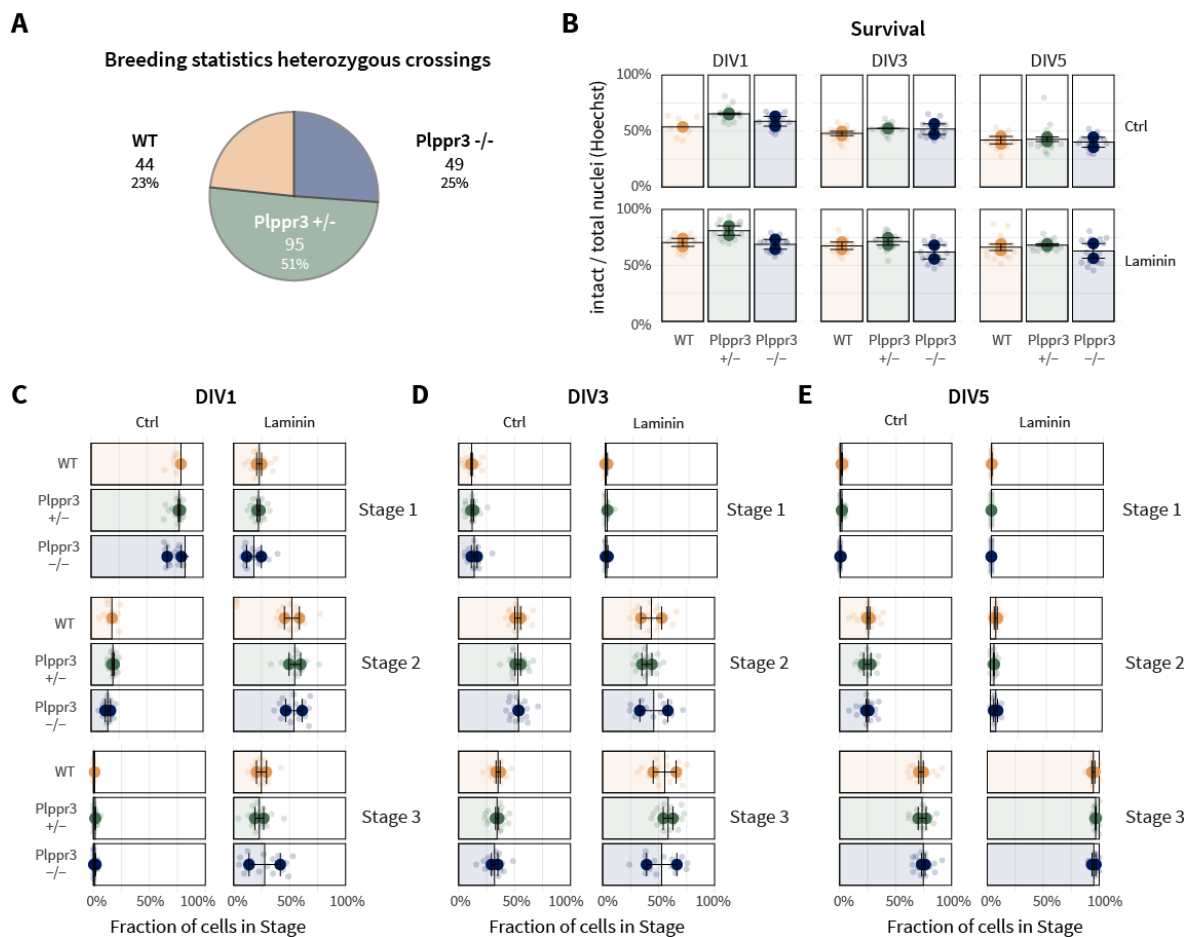


Figure 14: Initial development and survival of neurons are not disturbed by loss of *Plppr3* expression. (A) The breeding statistics of heterozygous parents for neuron cultures show mendelian distribution of offspring. (B) Survival of primary hippocampal neurons is not altered by loss of *Plppr3*. Survival assessed by fraction of non-debris by total DNA-stain positive nuclei in primary hippocampal neurons at various days in vitro (DIV). (C) Distribution of developmental stages (see Dotti, 1988)¹⁷ at DIV1 on poly-ornithine coated (Ctrl) or poly-ornithine + laminin-coated coverslips. (D) Distribution of developmental stages at DIV3 in both growth conditions. (E) Distribution of developmental stages at DIV5 in both growth conditions. Loss of *Plppr3* does not alter distribution of developmental stages. Small opaque dots indicate individual images, large dots indicate means of individual experiments, colour code indicates genotype. Error bars represent the SEM between experiments, $n = 2$ experiments.

To study the effect of PLPPR3 on neuron development, I cultured primary hippocampal neurons of littermate wild-type, heterozygous *Plppr3^{+/-}* and homozygous *Plppr3^{-/-}* mice with two standard protocols using poly-ornithine coated or poly-ornithine and laminin-coated coverslips. In both culture systems, a crude measure of neuron survival (healthy vs. degraded nuclei as stained by DNA dye Hoechst) did not reveal differences between genotypes at three developmental timepoints (DIV1, DIV3, DIV5). In contrast, laminin increased, as expected,²⁴¹ the overall survival of neurons (Figure 14B, control survival at 40-50%, laminin survival at 60-80% depending on genotypes and timepoint).

Analysing the distributions of early developmental stages (Stage 1: lamellipodia- and filopodia-rich soma, Stage 2: developed neurites, Stage 3: polarisation of one neurite as the axon)¹⁷ replicated the published acceleration of neuron development by laminin.²⁴² The stage analysis did, however, not reveal differences between genotypes on DIV1 (Figure 14C), DIV3 (Figure 14D), or DIV5 (Figure 14E). These results indicate no effect of PLPPR3-loss on survival, neurite formation, and polarisation of hippocampal neurons.

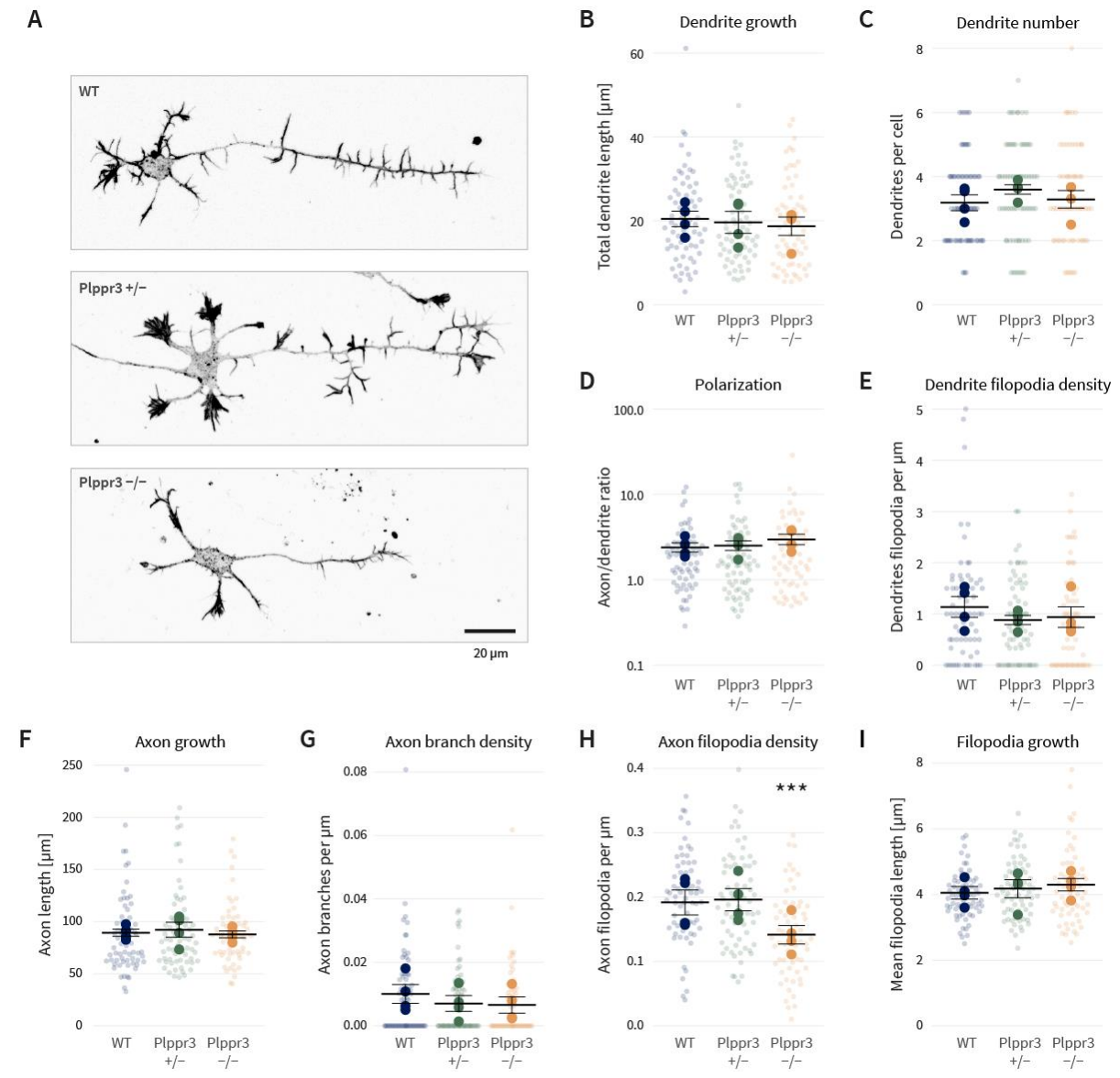
4.2 *PLPPR3^{-/-}* NEURONS BRANCH LESS IN VITRO

We previously identified that PLPPR3 localised to axons (as described in 2.1) and that its expression peaked during timepoints of axon elaboration (Dr. Annika Brosig).²⁰⁶ Therefore, I focused my further analyses on the morphology of early polarised (DIV1) neurons, late stage 3 neurons (DIV5), and a well-studied in vivo model for axon morphology.⁴⁹ All following experiments were performed on primary neurons cultured with laminin, as it accelerated polarisation, increased survival rates, and neuron health in the previous experiment (section 4.1).

4.2.1 Filopodia density is decreased in early polarised *Plppr3^{-/-}* neurons

At DIV1, approximately 25% of neurons cultured on poly-ornithine + laminin already contained a distinct axon (Figure 14C). Interestingly, axons of DIV1 wild-type neurons were densely decorated with filopodia, while *Plppr3^{-/-}* axons only presented with sparse filopodia (Figure 15A). When analysing individual lengths of axons, neurites and filopodia manually, *Plppr3^{-/-}* neurons showed a slight decrease in axon filopodia density (Figure 15H, effect size Hedge's g : $g_{Exp} = -1.3$, Table 6) but not in mean filopodia length (Figure 15I, $g_{Exp} = 0.6$, Table 6). Also the density of filopodia on dendrite precursors (Figure 15E, $g_{Exp} = -0.4$, Table 6) trended towards a decrease (statistically not detectable at four analysed cultures). As supported by the stage analysis (Figure 14C-E), also general polarisation of *Plppr3^{-/-}* neurons seemed to be unaltered (Figure 15D). Interestingly, the heterozygous neurons did not show intermediate phenotypes but rather followed either wild-type or *Plppr3^{-/-}* phenotypes, depending on the readout. These results suggest that PLPPR3 controls the incidence but not the elongation of filopodia on early developing neurons.

*Figure 15 (next page): Early polarised *Plppr3^{-/-}* neurons contain fewer filopodia on axons. (A) Maximum intensity projections of F-actin stained cultured hippocampal neurons of wild-type, *Plppr3^{+/-}* and *Plppr3^{-/-}* genotype at DIV1. (B-I) various morphology parameters between genotypes. *Plppr3^{-/-}* neurons have decreased density of axon filopodia without altered filopodia lengths. Small opaque dots indicate individual images, large dots indicate means of individual experiments, colour code indicates genotype. Error bars represent the SEM between experiments, $n = 4$ experiments. Mixed model between experiments, post-hoc comparisons Holm-corrected. *** $p < 0.001$. Figure previously published in Brosig & Fuchs et al., 2019.¹⁹⁷*



4.2.2 Branch density is decreased in fully polarised *Plppr3*^{-/-} neurons

The increased length of neurites and the resulting overlap of neurons hinders directly assessing the morphology of neurons at later developmental stages. To circumvent this problem, I sparsely labelled individual neurons by transfecting all genotypes at DIV2 with a plasmid encoding Synapsin-promoter-driven GFP. To analyse morphology, cells were fixed and immunolabelled at DIV5 (Figure 16A).

Overall growth of *Plppr3*^{-/-} neurons was similar to wild-type both in dendritic and axonal compartments (Figure 16B&F). *Plppr3*^{-/-} neurons seemed to develop normal numbers of dendrites (Figure 16C), and the density of branches on dendrites was slightly decreased (Figure 16E, $g_{Exp} = 1.2$, Table 7). Given that many developing dendrites did not contain any branches and remained short at DIV5, these differences should be taken with caution and verified at later developmental timepoints more suited for studying dendrite morphology.

In line with the decreased filopodia density at early developmental timepoints, *Plppr3*^{-/-} neurons at DIV5 also exhibited a decreased axon branch density (Figure 16I, $g_{Exp} = 2.1$, Table 7). The unaltered total axon length appears to cause a redistribution of growth to the primary axon (Figure 16G,

$g_{Exp} = 0.5$, Table 7) and the remaining branches (Figure 16H, $g_{Exp} = 1.4$, Table 7). These results imply that PLPPR3 specifically controls branching morphogenesis without affecting overall growth of neurons. These effects were most pronounced in axons, where PLPPR3 localises abundantly, but also detectable in early developing dendrites.

A

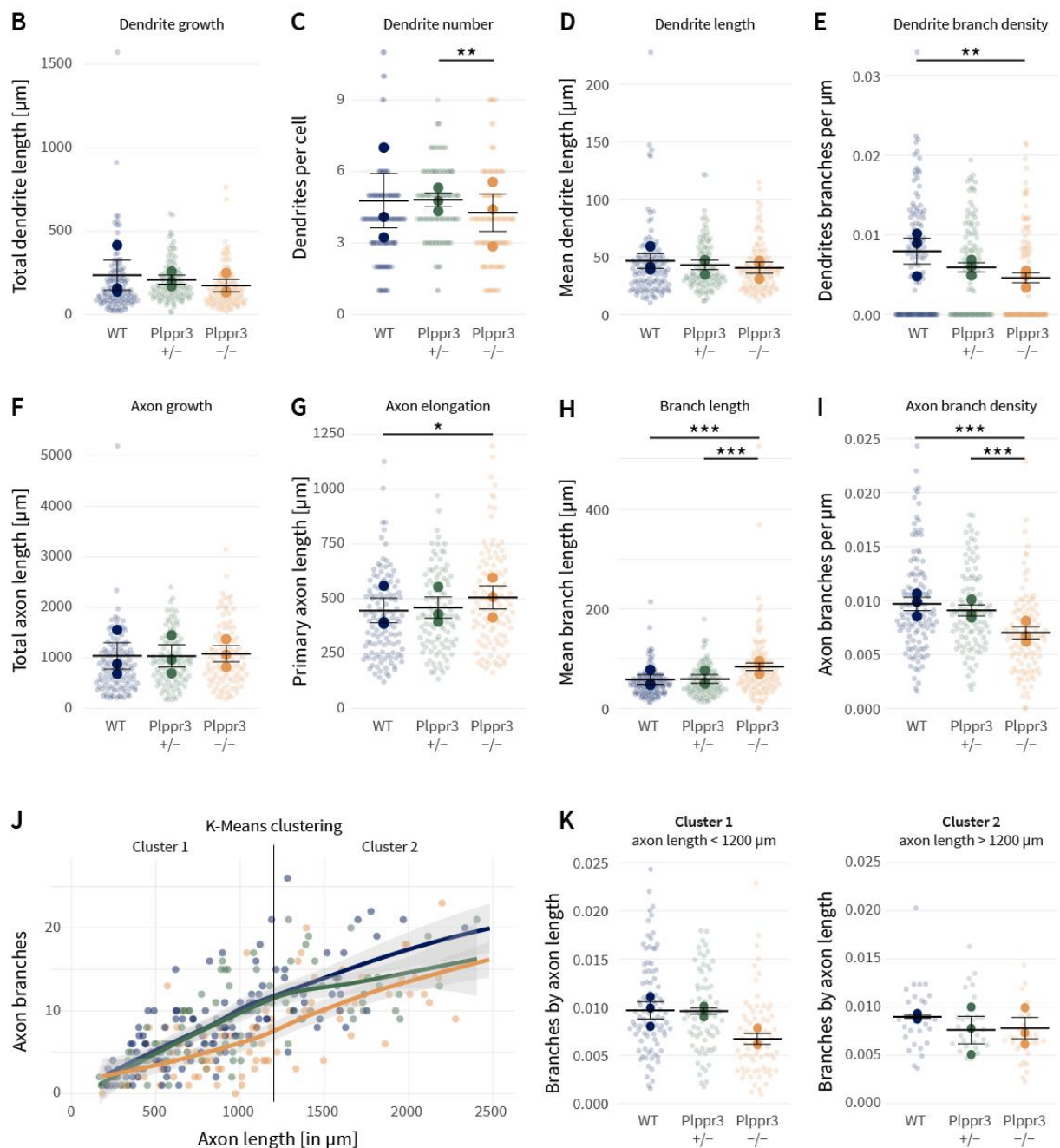
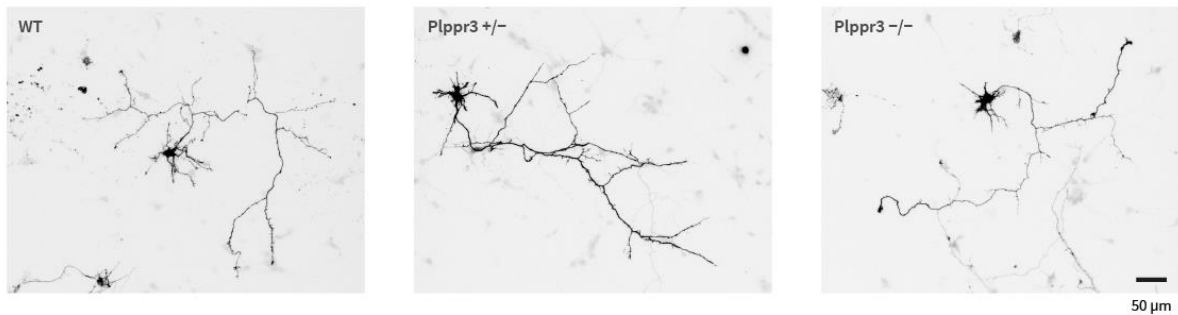


Figure 16: (previous page) Fully polarised *Plppr3*^{-/-} neurons branch less. (A) Epifluorescent images of sparsely GFP-transfected cultured hippocampal neurons of indicated genotypes fixed at DIV5 (B-E) Morphology parameters of developing dendrites. Dendrite length appears unaltered while *Plppr3*^{-/-} contain less branches (F-I) Morphology parameters of axons. *Plppr3*^{-/-} contain less branches and redirect their unaltered total growth to the remaining processes. Small opaque dots indicate individual images, large dots indicate means of individual experiments, colour code indicates genotype. Error bars represent the SEM between experiments, n = 3 experiments. Mixed model between experiments, post-hoc comparisons Holm-corrected. * p < 0.05, ** p < 0.01, *** p < 0.001. (J) Scatter plot of branch number versus total axon length of individual neurons including local averages (loess) and border defined by K-means clustering. (K) Axon branch density of clusters as determined in (J). Short *Plppr3*^{+/-} neurons show a similar branch density to wild-type neurons, long *Plppr3*^{+/-} neurons seem to be more alike to *Plppr3*^{-/-} neurons. Parts of the figure previously published in Brosig & Fuchs et al., 2019.¹⁹⁷

Interestingly, the heterozygous neurons showed similar growth behaviour to wild-type neurons in every analysed parameter except for the branch density of developing dendrites (Figure 16E). However, specifically the morphology of large *Plppr3*^{+/-} neurons appeared more similar to *Plppr3*^{-/-} neurons. Indeed, K-means clustering of axon branch numbers versus total axon length detected two clusters of cells distinguished by a total axon length of 1200 μm (Figure 16J). Comparing the axon branch density of *Plppr3*^{+/-} neurons between these two clusters revealed similarity to wild-type neurons when they are small, but similarity to *Plppr3*^{-/-} neurons when they are large (Figure 16J&K).

Although levels of PLPPR3 in heterozygous brains did not seem to differ from wildtypes (Figure 12D), this indicates some form of density requirement of PLPPR3 function at DIV5 – with enough PLPPR3 in smaller heterozygous neurons to compensate for the reduction in expression but too little expression in large neurons. However, given the sharp boundary of branch density at 1200 μm total axon length rather than a gradual decrease (Figure 16J), it could also be conceivable that the two clusters represent different cell types in our hippocampal cultures with distinct dependency on PLPPR3 for their morphogenesis.

4.2.3 Cortical Layer II/III *Plppr3*^{-/-} neurons have no branching phenotype in vivo

The most prominent effects of PLPPR3 loss on neuron morphology presented in the axon, where PLPPR3 enriched most. To assess the in vivo relevance of this evidence from primary cultured neurons, I collaborated with Dr. Julia Ledderose to sparsely label layer II/III pyramidal neurons of the sensory cortex. For this, she in-utero electroporated the GFP plasmid used for quantifying neuron morphology in E14 mouse embryos of heterozygous *Plppr3*^{+/-} crosses. After fixation, sectioning, and labelling for GFP and DNA, she imaged the ipsilateral cortical region using an SP8 confocal microscope at a magnification of either 10x or 20x. I subsequently quantified the branch density of these pyramidal neurons in layer V by measuring the intensity in the respective layer and normalising it to the number of GFP-expressing cell bodies in layer II/III (Figure 17A&D).

These labelled layer II/III pyramidal neurons did not reveal evidence for decreased branch density at the layer V either at postnatal day 7 (Figure 17C, $g_{P7} = -0.03$,) or day 15 (Figure 17F, $g_{P15} = 0.7$, Table 8). As we had previous evidence for morphological differences using a simultaneous knockdown of *Plppr3* and *Plppr4* in cultured primary neurons (Dr. Annika Brosig),²⁰⁶ we also characterised the effect of this knockdown in wild-type animals. While the double-knockdown consistently presented with a smaller number of electroporated cells compared to control animals (Figure 17G&H, $g_{\text{LayerV}} = 3.4$, $g_{\text{Cells}} = 2.4$),

also this reduction of both PLPPR3 and PLPPR4 levels did not decrease branch density of layer II/III neurons at layer V in vivo (Figure 17I, $g_{\text{shRNA}} = -0.4$, Table 8). Interestingly, cultured neurons transfected with this shRNA consistently showed less labelled cells,²⁰⁶ indicating a survival defect by the loss of these PLPPRs. A similar phenotype was described for knockdown of *Plppr4* in rat primary neurons.²⁴³

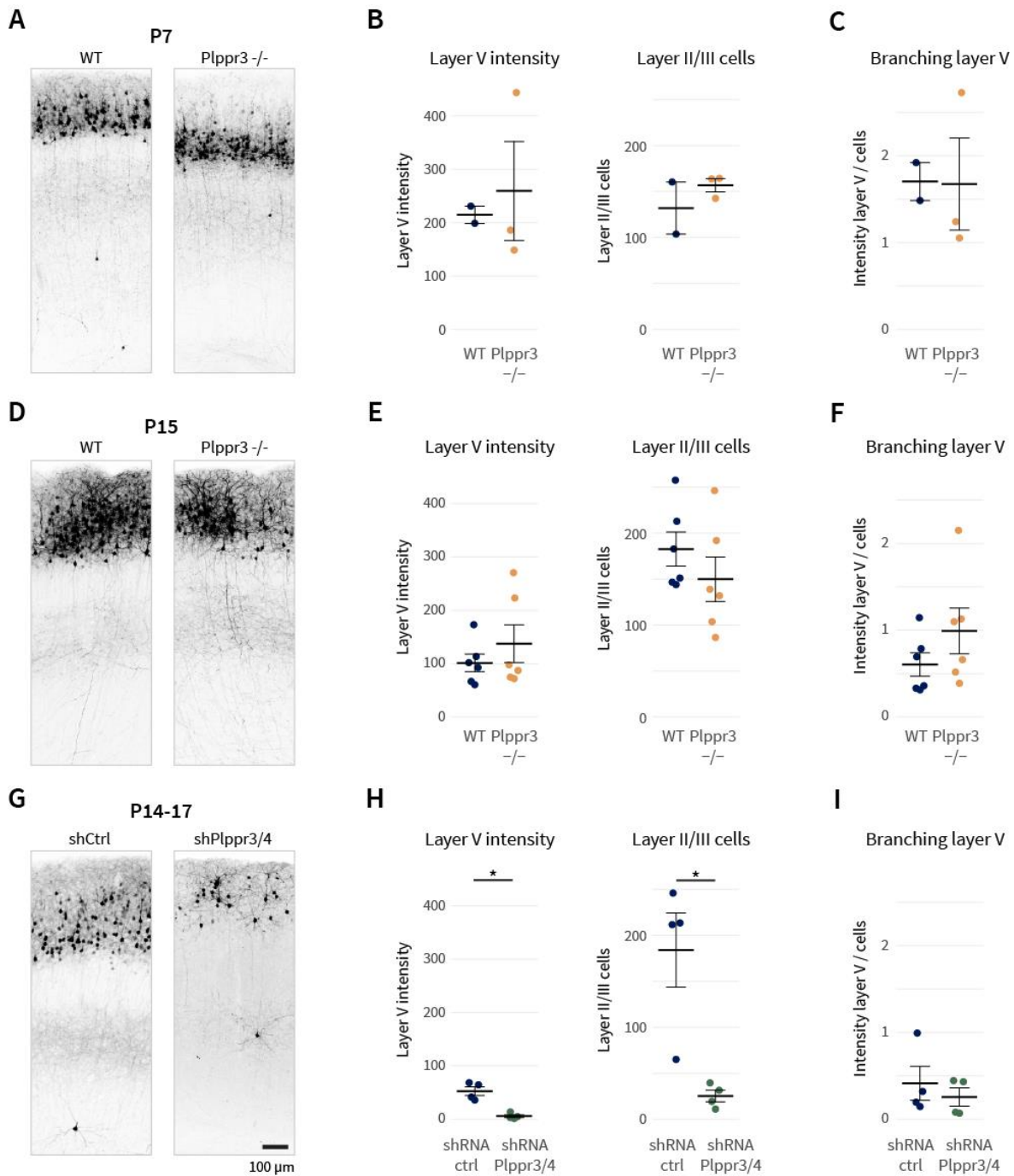


Figure 17: Branching of layer II/III cortical neurons to layer V seems to be unaffected by loss of *Plppr3* expression. (A) Summed intensity projections of GFP-expressing layer II/III neurons at postnatal day 7 (P7) in wild-type versus *Plppr3*^{-/-}. (B) GFP intensity in layer V and number of GFP-positive cell bodies in layer II/III are similar between wild-type and *Plppr3*^{-/-}. (C) Branch density at layer V is not affected by loss of PLPPR3. $n(\text{wild-type}) = 2$ animals, $n(\text{Plppr3}^{-/-}) = 3$ animals. (D-F) respective graphs for animals analysed at postnatal day 15. $n = 6$ animals per genotype. (G-I) respective graphs for wild-type animals electroporated with shRNA against *Plppr3* and *Plppr4* or control respectively. Double knockdown of *Plppr3* and *Plppr4* does not decrease branch density (I) but the number of GFP-positive cells. $n = 4$ animals for both conditions. Error bars indicate SEM between animals, statistical analysis by *t*-test * $p < 0.05$.

4.3 PLPPR3 AND THE PI3K PATHWAY REGULATE BRANCHING COOPERATIVELY

Numerous studies have established the PI3K pathway and PTEN as master regulators of neuron growth and morphogenesis (summarised in section 1.3.2). Interestingly, previous work in our lab by Dr. Michiel van Diepen, Dr. Annika Brosig, Dr. George Leondaritis, Dr. Sandra Schrötter, and Fatih Ipek identified a tight cooperation of PLPPR3 and PTEN. PLPPR3 was found as a brain-specific interactor of PTEN,²⁴⁴ which could be verified endogenously in E18 rat brain lysates and DIV9 cortical neurons.²⁰⁶ The interaction is direct, as verified using microscale thermophoresis with purified PTEN and PLPPR3, and does not seem to require the distal C-terminus, as also the PLPPR3-ΔCa variant was found to interact.²⁰⁶ Furthermore, overexpressed PLPPR3 appeared to enrich endogenous PTEN at the plasma membrane of N1E-115 cells.

This interaction does seem to affect PTEN rather than PLPPR3. Pilot experiments implied that PLPPR3 expression downregulates PTEN levels in N1E-115 cells (Dr. Annika Brosig). PTEN immunoprecipitated after co-expression with PLPPR3 was found to dephosphorylate less PIP3 in a cell-free phosphatase activity assay.¹⁹⁷ Moreover, in several cell line experiments, co-expression of PLPPR3 counteracted known PTEN functions: phosphorylation of AKT at serine 473 was found to be independent of PTEN activity when co-expressed with PLPPR3 (n=5 blots);¹⁹⁷ phosphoinositide accumulations at the plasma membrane (monitored by GFP-AKT1 translocation) were independent of PTEN activity in cells co-expressing PLPPR3 (n=2 experiments, 50 cells);¹⁹⁷ finally, co-expression of PTEN and PLPPR3-Flag decreased the PTEN effect on F-actin accumulations (n=3 exp, 60 cells).¹⁹⁷

Furthermore, in embryonic stem cell-derived motoneurons, PLPPR3-Flag overexpression increased filopodia and branch density, perfectly reversing the *Plppr3*^{-/-} phenotypes described above. These increases were prevented by pharmacological inhibition of PI3K, further strengthening the link between PI3K-activity and PLPPR3 function.¹⁹⁷ However, PLPPR3 overexpression did not appear alter the levels of phosphorylated AKT (a typical downstream marker of PI3K activity) in these motoneurons.¹⁹⁷ Additionally, pilot experiments in developing primary *Plppr3*^{-/-} cortical neurons did not indicate altered AKT phosphorylation (not shown). Finally, PTEN knockout was not able to rescue the growth defects of shRNA-mediated double-knockdown of *Plppr3* and *Plppr4* (n=3 cultures, 197 cells).²⁰⁶ These data argued that PLPPR3 is clearly capable of counteracting PTEN function to facilitate PIP3 signalling in cell lines. They furthermore showed responsiveness of PLPPR3 functions to PI3K-inhibition in neuron-like cells but mixed phenotypes of PLPPR3 on PI3K-pathway activity in primary neurons.

Therefore, to directly characterise the relation of PLPPR3 and PTEN in regulating the morphogenesis of primary hippocampal neurons, I quantified the effects of PTEN knockdown in wild-type and *Plppr3*^{-/-} neurons. Moreover, I measured the levels of PIP3 in wild-type and *Plppr3*^{-/-} neurons in a localised manner using orthogonal tools.

4.3.1 No evidence for altered PIP3-levels in *Plppr3*^{-/-}

To substantiate the evidence from cell culture, that PLPPR3 inhibits PTEN, I compared levels of PIP3, the phosphoinositide produced by PI3K and mainly degraded by PTEN, in wild-type versus *Plppr3*^{-/-} neurons. We hypothesised that, if PLPPR3 inhibits PTEN in neurons, PIP3 levels would drop upon loss of PLPPR3. As my morphological analyses of *Plppr3*^{-/-} neurons implied no overall growth defects but an axon localised redirection of growth, I focused the PIP3 quantification to the axon shaft, where we expected the strongest effects.

To this end, I established and tested several PIP3 visualisation protocols for specificity and sensitivity (see Appendix, section 7.1). The protocols employed overexpression and translocation assays of tagged PH-domains and labelling using specific lipid-preserving protocols. The PIP3 labelling protocol exhibited a higher sensitivity than PH-domain overexpression and was able to detect changes in PIP3 in GABAergic neurons upon BDNF stimulation (section 7.1.3). Furthermore, it has contributed to a collaborative study with James Fawcett and Richard Eva (Cambridge University) verifying the reduction of endogenous PI3K activity during development in CNS neurons and understanding the mechanisms of specific PI3K isoforms in promoting regrowth of injured CNS neurons.²⁴⁵

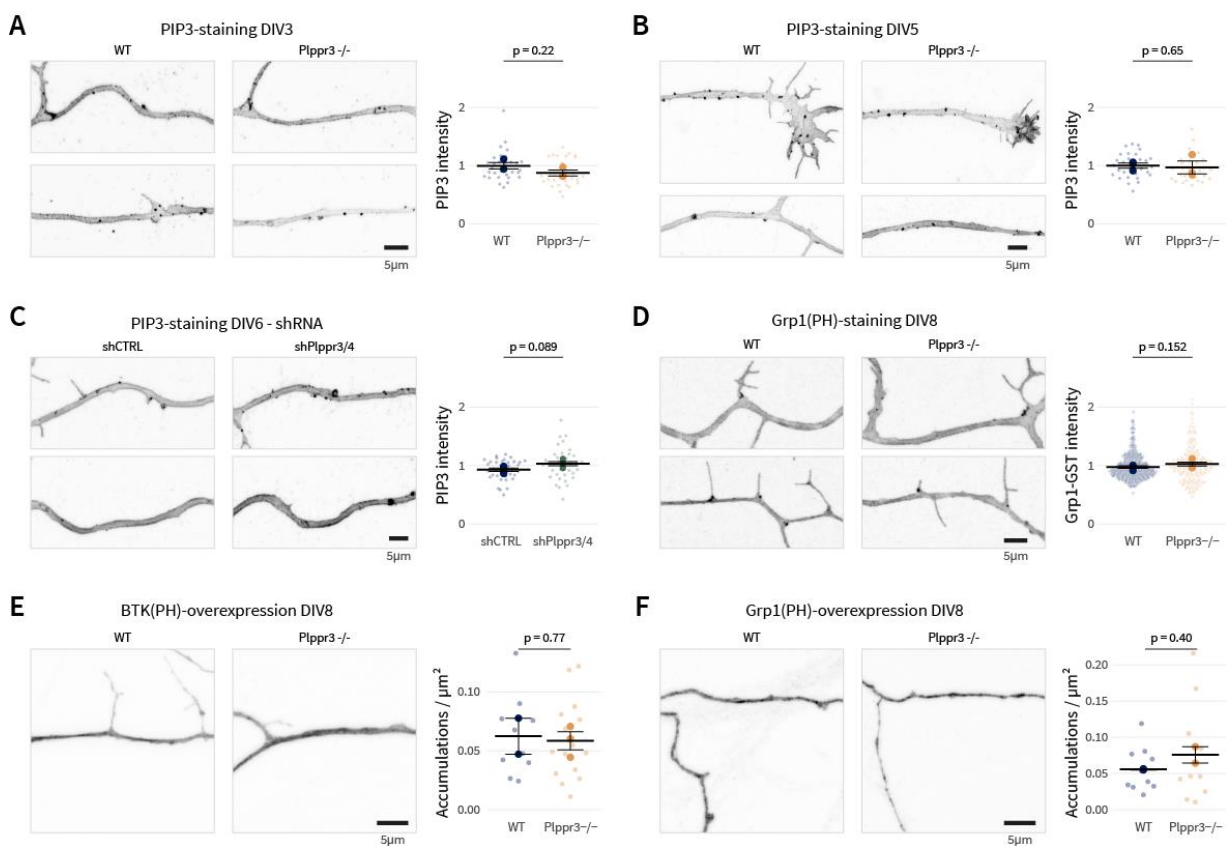


Figure 18: No evidence for altered PIP3 levels in *Plppr3*^{-/-} axons. (A) PIP3-antibody labelling in DIV3 wild-type vs. *Plppr3*^{-/-} axons. n=3 experiments. (B) PIP3-antibody labelling in DIV5 wild-type vs. *Plppr3*^{-/-} axons. n=3 experiments. (C) PIP3-antibody labelling in DIV6 wild-type vs. *shPlppr3/4* treated axons. n=4 experiments. (D) GST-Grp1(PH) labelling in DIV8 wild-type vs. *Plppr3*^{-/-} axons. n=3 experiments. (E) BTK(PH)-GFP overexpression in DIV8 wild-type vs. *Plppr3*^{-/-} axons. n=3 experiments. (F) Grp1(PH)-mCitrine overexpression in DIV8 wild-type vs. *Plppr3*^{-/-} axons. n=3 experiments. Small opaque dots indicate individual images, large dots indicate means of individual experiments, colour code indicates genotype. Error bars represent the SEM between experiments. Values of A-D are normalised within experiments to the mean of the wildtype condition to aid visualisation. Mixed models were calculated between experiments using raw intensity values.

Quantifying PIP3 intensity in axons using this immunolabelling protocol revealed no differences of wild-type and *Plppr3*^{-/-} at DIV3 (Figure 18A, $g_{Exp} = -0.1$, Table 10) or DIV5 (Figure 18B, $g_{Exp} = -0.1$, Table 10). The accumulations of PIP3 signal visible in these micrographs likely represent a methodological artifact due to residual movement of unfixed lipids (discussed in 7.1), and a quantification of number or size of these puncta did not reveal differences between wild-type and *Plppr3*^{-/-} axons (not shown). Measuring PIP3 levels in the axons of DIV6 neurons after double-knockdown of *Plppr3* and *Plppr4* showed a trend towards increased PIP3-levels (Figure 18C, $p=0.089$, $g_{Exp} = 0.3$, Table 10). A different probe for detecting PIP3 (purified GST-tagged PH-domain of Grp1) in DIV8 cultures suggested unaltered or slightly increased PIP3 levels in *Plppr3*^{-/-} (Figure 18D, $g_{Exp} = 0.3$, Table 10).

Interestingly, quantifying PIP3 by overexpressing fluorescently tagged Grp1-PH domain in cultures from these same preparations replicated the trend towards increased PIP3, when measuring the number of PH-domain accumulations per axon area (Figure 18F, $g_{Exp} = 1.0$, Table 10). In connection with the experiments in section 7.1, this corroborates a congruence of both staining and overexpression visualisations of PIP3 in neurons. Finally, also using a different PH-domain (BTK-PH) for measuring PIP3 using the overexpression strategy revealed no difference in PIP3 between wild-type and *Plppr3*^{-/-} neurons (Figure 18E, $g_{Exp} = -0.2$, Table 10). In summary, these PIP3-studies provided no evidence for decreased PIP3-levels in axons of *Plppr3*^{-/-}.

4.3.2 Knockdown of PTEN rescues *Plppr3*^{-/-} branching deficit in primary hippocampal neurons

In a separate experiment more directly assessing the hypothesised connection of PTEN and PLPPR3 in regulating branching morphogenesis, I tested whether losing PTEN rescued for the loss of PLPPR3. To this end, I infected littermate wild-type and *Plppr3*^{-/-} primary hippocampal neurons with viruses encoding for shRNA against PTEN (or scrambled control, previously described in Shi et al. 2014)²⁴⁶ two hours after plating. I then analysed morphology as described above, by sparsely transfecting cells GFP at DIV2 and fixing and immunolabelling at DIV5 (Figure 19A). As the experiment included two independent treatments (*Plppr3*-Genotype and PTEN-reduction), I analysed these data with a two-way ANOVA to check for independence or an interaction of both effects (results in Table 9). In case of interactions, I subsequently performed one-way ANOVA comparing all experimental groups followed by Holm-corrected post-hoc analysis.

In this experiment, PTEN knockdown slightly increased overall dendrite and axon growth (Figure 19B&F) as previously described.^{128,133} Interestingly, for axon branch density (Figure 19I), the two-way ANOVA detected a statistical interaction of PTEN- and PLPPR3-loss indicating a cooperation of both proteins for this phenotype. Specifically, axon branch density decreased in *Plppr3*^{-/-} (shCTRL Wt vs. *Plppr3*^{-/-}, $g_{Exp} = -1.5$) and did not with additional knockdown of PTEN (shPTEN Wt vs. *Plppr3*^{-/-}, $g_{Exp} = -0.3$). Similarly, the increased primary axon length of *Plppr3*^{-/-} neurons (Figure 19G, shCTRL Wt vs. *Plppr3*^{-/-}, $g_{Exp} = 1.2$) disappeared with concurrent PTEN-reduction (shPTEN Wt vs. *Plppr3*^{-/-}, $g_{Exp} = 0.2$). Moreover, the increased mean axon branch length of *Plppr3*^{-/-} neurons reduced to wildtype levels by additional loss of PTEN (Figure 19H, shCTRL Wt vs. *Plppr3*^{-/-}, $g_{Exp} = 0.5$; shPTEN Wt vs. *Plppr3*^{-/-}, $g_{Exp} = 0.1$). This rescue of PLPPR3-loss by additional PTEN knockdown indicates that PTEN and PLPPR3 indeed operate in one pathway and that PLPPR3-effects on axon branching depend on PTEN inhibition.

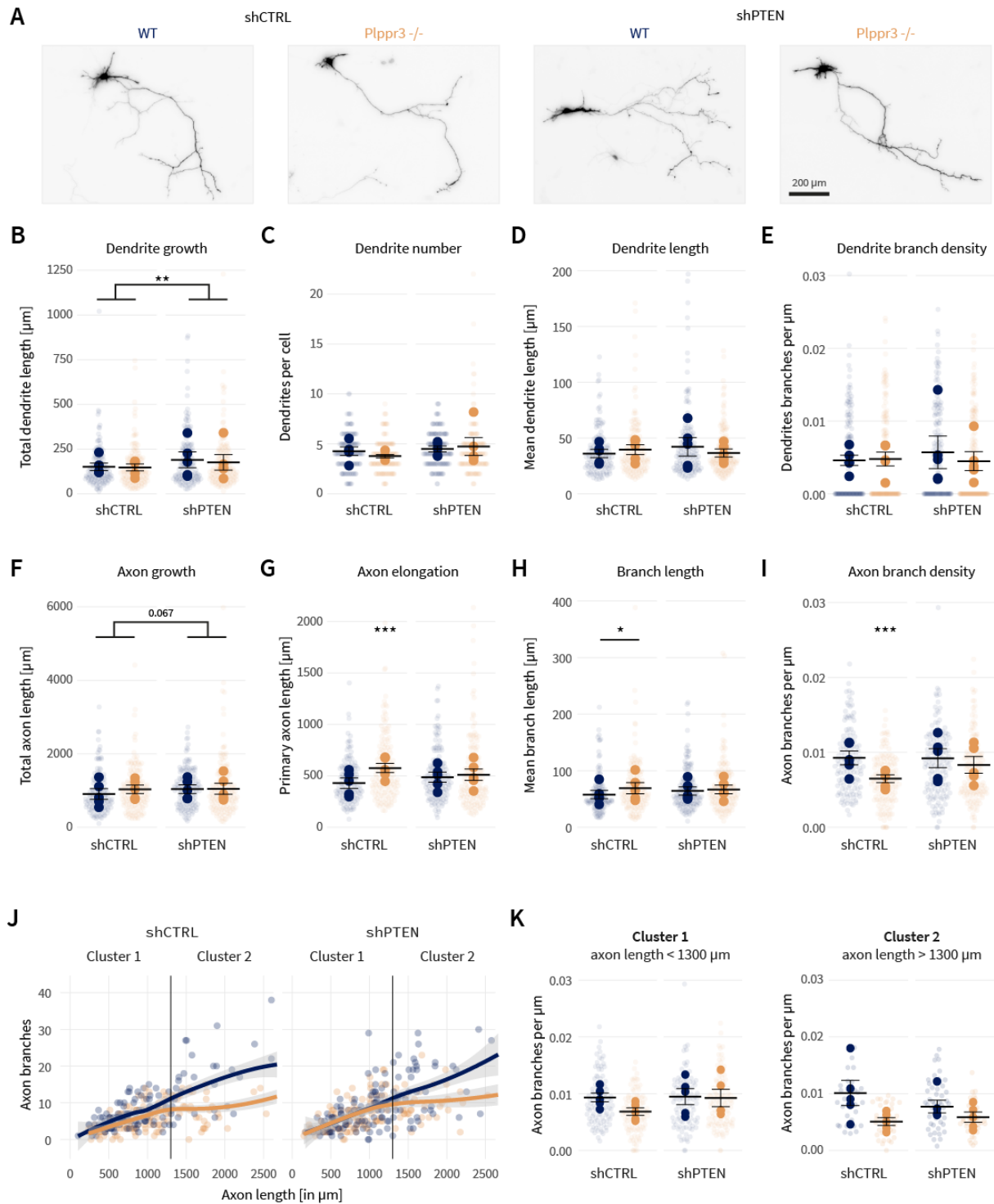


Figure 19: Reduction of PTEN levels increases branching in *Plppr3*^{-/-} neurons. (A) Epifluorescent images of GFP-filled cultured hippocampal neurons of indicated genotypes and treatments. (B-E) Morphology parameters of developing dendrites. (F-I) Morphology parameters of axons. Small opaque dots indicate individual images, large dots indicate means of individual experiments, colour code indicates genotype. Error bars represent the SEM between experiments, $n = 3$ experiments. Two-way ANOVA mixed model between experiments, in case of interaction one-way mixed model, post-hoc comparisons Holm-corrected. * $p < 0.05$, ** $p < 0.01$, *** $p < 0.001$. (J) Scatter plot of branch number versus total axon length of individual neurons including local averages (loess) and border defined by K-means clustering. (K) Axon branch density of clusters as determined in (I). Short (cluster 1) *Plppr3*^{-/-} neurons with PTEN knockdown show a similar branch density to wild-type neurons, long (cluster 2) *Plppr3*^{-/-} neurons with PTEN knockdown seem to be more alike to *Plppr3*^{-/-} without PTEN reduction. Figure previously published in Brosig & Fuchs et al., 2019.¹⁹⁷

Interestingly, similar to heterozygous *Plppr3^{+/-}* neurons, large cells seemed to respond differently to PTEN loss than short cells (Figure 19J&K). Also in this experiment, K-means clustering detected a specific axon length that distinguishes the branching behaviours at DIV5. With 1300 μm this length threshold was very similar to the 1200 μm distinguishing long and short heterozygote *Plppr3^{+/-}* neurons as described in Figure 16J. In short neurons (Cluster 1, Figure 19K), PTEN-reduction in *Plppr3^{-/-}* perfectly rescued branch density to wild-type levels, while the same treatment in long neurons (Cluster 2, Figure 19K) seemed to have no effect. Whether this is a result of dose-dependent effects of PTEN on PLPPR3 or whether it depends on different neuron types in the culture system, could be an interesting route for future experiments.

4.4 SUMMARY AND OUTLOOK: FURTHER PHENOTYPING OF *PLPPR3^{-/-}* ANIMALS

In summary, the experiments described in this chapter establish PLPPR3 as an axon enriched protein increasing the density of filopodia and branches on growing hippocampal neurons without altering overall growth or elongation. PLPPR3 thereby effectively redirects growth to branches and could act as a switch from elongation to branching behaviour in developing axons. The branching patterns of *Plppr3^{-/-}* cortical layer II/III neurons to layer V appeared unaffected in vivo. Directly visualising PIP3 in axons provided no evidence for decreased PI3K signalling in *Plppr3^{-/-}*. However, the PTEN knockdown experiment corroborated the clear link between PIP3-levels and PLPPR3 function.

In conjunction with the experiments by my colleagues, the results of this chapter have established PLPPR3 as a novel regulator of branching morphogenesis in a pathway with PTEN (published in Brosig & Fuchs et al., 2019).¹⁹⁷ Furthermore, the presented model of localised PTEN inhibition to facilitate PIP3 microdomain formation along the axon shaft has implications for the molecular mechanisms of both neuron development and regeneration of adult injured neurons (discussed in Fuchs, Eickholt & Leondaritis, 2020).²⁴⁷ The precise implementation of PLPPR3 function appears multifaceted and will be discussed in section 6.1.

Interestingly, the quantification of branch density in *Plppr3^{-/-}* cortex did not suggest a conservation of this branch-inducing function of PLPPR3 in vivo. Critically, however, this experiment only tested a specific interstitial branch formation event of a specific cortical cell type. In this respect, it would be informative to characterise terminal branching of these layer II/III neurons, which has been shown to be regulated by different mechanisms as the studied interstitial branching at layer V.⁴⁹ Furthermore, the morphogenesis of other cell types might depend more on PLPPR3 in vivo. Especially GABAergic interneurons could be more affected by PLPPR3 loss, as they appear to express *Plppr3* at the highest levels during adulthood (Figure 1). Via affecting GABAergic interneurons specifically, PLPPR3 could putatively regulate excitation-inhibition balance that has been discussed to underly multiple psychiatric disorders.²⁴⁸ To this end, behavioural analyses of anxiety, social or reward behaviours might provide further insight into PLPPR3 function in vivo.

Furthermore, in parallel to this thesis, the laboratory of Prof. Johannes Vogt (University Medicine Mainz) characterised in vivo phenotypes of an independently generated *Plppr3*-knockout line.¹⁹³ They describe defective thalamocortical projection development that depends on LPA-mediated axon guidance. The behavioural assessment of this *Plppr3*^{-/-} line revealed neither differences in motor or memory performance (as measured in Morris water maze), nor differences in motor strength of fore- and hindlimbs. However, these *Plppr3*^{-/-} animals lacked the higher-order cognitive ability to discriminate texture coarseness of surfaces. In rodents, this skill has been described to depend on thalamocortical-projections to the cortical layers IV and I of the sensory barrel cortex²⁴⁹ and the higher-order processing by layer II/III cortical neurons.²⁵⁰

Remarkably, thalamocortical axons require both LPA-mediated stopping at the cortical plate as well as subsequent branching to enter the correct target region.⁴⁵ Therefore, determining whether the behavioural defects of this *Plppr3*^{-/-} line are influenced by an altered branching capacity of thalamocortical or cortical neurons in addition to the described LPA-mediated growth cone guidance, could be a fruitful research question.

These precisely defined functions in neuron morphogenesis, place PLPPR3 as a fine tuner of neuron development with narrow outcomes on cognitive processing. In isolation, these effects may seem minimal. However, viewed from a different angle such narrow effects can enable a much tighter control of experimental parameters compared to targeting broad (and therefore unspecific) mediators of neuron development. In this way, the precise modification of neuron development (e.g., by targeting fine tuners such as PLPPR3) could provide a valuable tool to refine the understanding of the multifaceted and interdependent regulation of cognitive processing and disease.

5 PRECURSOR TYPES PREDICT THE STABILITY OF NEURON BRANCHES

Neuron branch density depends on both the formation and the stabilisation of branches. While branch initiation has been attributed mainly to F-actin reconfiguration, branch stability seems to be primarily controlled by microtubule stability.⁴¹ To this end, direct pharmacological manipulation of microtubule stability increases the length of axons and their branches,²⁵¹ and manipulation of GSK3-activity modifies branching versus growth phenotypes via the regulation of microtubule stability.^{18,252} The microtubule associated protein Map6 stabilises microtubules and axon growth in general,⁹⁹ Map7 specifically stabilises microtubules in branches.^{70,71} The Sip1 effector Ninein controls axon outgrowth and branching in vivo by regulating microtubule stability.²⁵³ Interestingly, also the de-stabilisation of microtubules is required for the formation of branches, suggesting mechanisms of crosstalk and spatiotemporal control at various stages of branching morphogenesis.⁴¹ To further elucidate this regulation of branch maintenance, I quantified the stability of branches in our primary hippocampal culture system using long-term live-cell imaging. Data from this section are currently under revision and have been published on BioRxiv (<https://doi.org/10.1101/2021.04.23.441127>).

5.1 BRANCH STABILITY DEPENDS ON PRECURSOR AND NEURITE TYPE

The experimental setup comprised wild-type versus littermate *Plppr3*^{-/-} hippocampal cultures plated on laminin and poly-Ornithine, as in the experiments of the previous section. These cultures were imaged at DIV3 using phase-contrast microscopy with a 10min interval for 24h under 5% CO₂ at 37°C. I manually scored timepoints of initiation and (if applicable) full retraction of all branches forming in the field of view (for a detailed description of the methodology, see Figure 34). Before analysing the effects of *Plppr3*-loss, I quantified the impact of other influences on the lifetime of branches.

5.1.1 Branches that initiate from distinct precursor structures differ in lifetime

Branches have been described to initiate from multiple, morphologically distinct F-actin-rich precursor structures: thin filopodia, wider lamellipodia, or splitting of the growth cone.^{41,254} All precursor types gave rise to branches on both axons and developing dendrites and could be distinguished by morphology in my live-cell imaging (Figure 20A). As I noticed numerous branches originating from filopodia that were invaded by lamellipodia before branch elongation (as also reported by Flynn et al. 2009 and Withers & Wallace 2020),^{62,63} I distinguished these precursors from the other three canonical precursors as a 'mixed' class.

Interestingly, branches originating from the different precursor structures appeared to differ in lifetime. Most branches originating from lamellipodia or splitting events collapsed soon after formation (visible as a diagonal 3-4h "thick" diagonal band in Figure 20B). A considerable number of branches originating from filopodia or mixed events, however, did not collapse during the observed time window of 24 hours (Figure 20B, vertical band at 24h timepoint). This strong right-censoring of the lifetime quantification would strongly bias any comparison of raw measured lifetimes. Especially the lifetime of filopodia and mixed branches would be drastically underestimated both by assuming a collapse at timepoint 24 h or by only measuring branches that have collapsed.

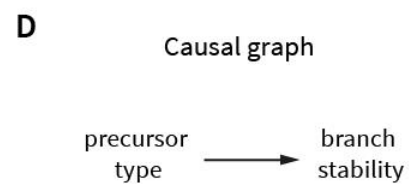
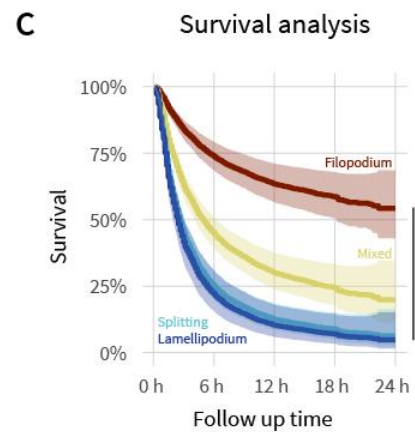
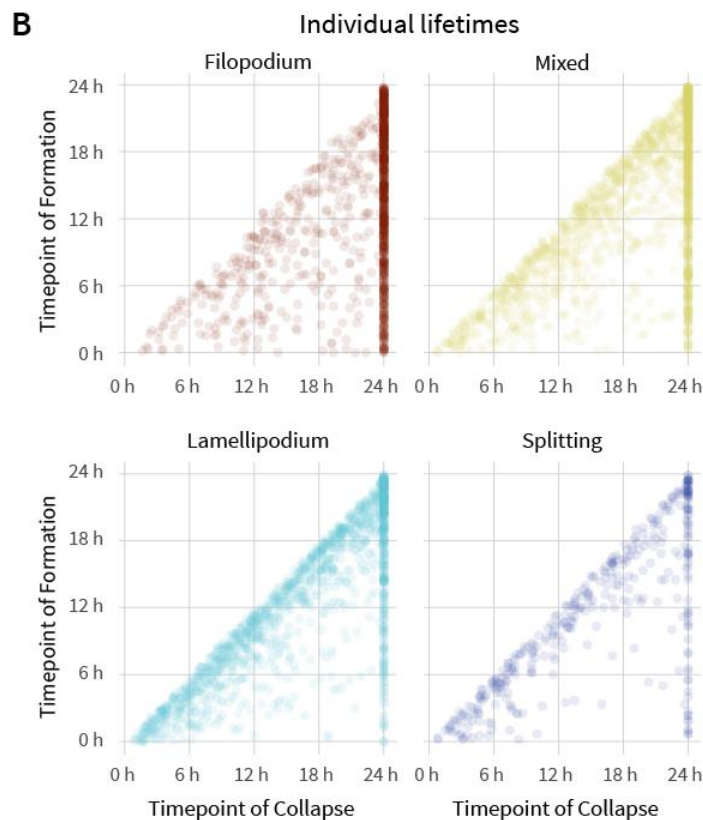
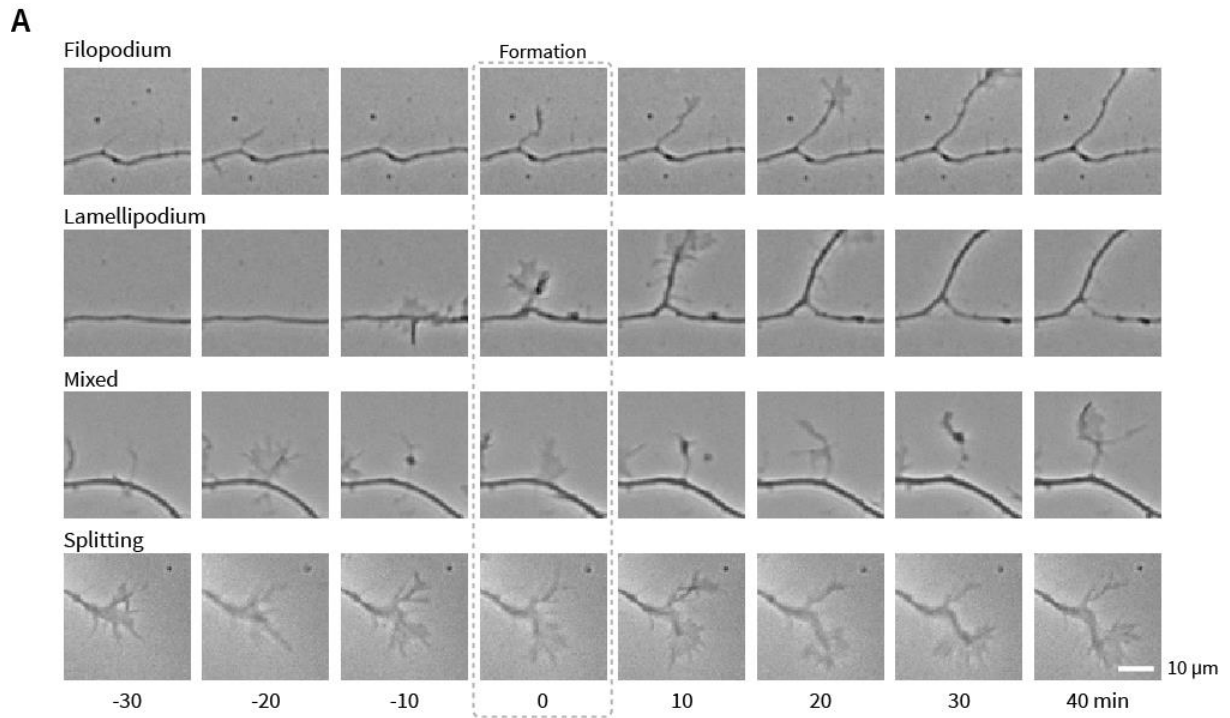


Figure 20: Precursor type predicts the stability of developing neuronal branches. (A) Morphologically distinct precursor types giving rise to a branch at timepoint 0. In addition to filopodia, lamellipodia, and splitting, also mixed precursors were observed. (B) Timepoint of formation versus timepoint of collapse for all individual branches separated by precursor type. Note the strong right-censoring (non-collapsing branches as a vertical line at the end of the 24h window of observation). (C) Survival analysis reveals a high risk for collapse for lamellipodia- and splitting-originating branches compared to filopodia originating branches. *** $p < 0.001$. (D) Causal diagram describing the link of precursor type and branch stability. $n_{\text{Ind}}=2317$ (WT) & 2165 ($Plpp3^{-/-}$), $n_{\text{Exp}}=6$ (six independent cultures), transparent ribbons show 95% confidence intervals in survival curves. Figure submitted as part of a manuscript at BioRxiv (<https://doi.org/10.1101/2021.04.23.441127>) and currently under revision.

I therefore analysed these data with a method commonly used in clinical trials to handle such censored datasets: survival analysis. Survival analysis has been developed to allow for characterising lifesaving or -extending treatments without having to observe the full lifespan of all study participants. The rationale is, that even incomplete observations (i.e., lack of knowledge of the exact lifetime) can carry information when compared to shorter (but defined) observations of a separate (placebo) treatment.²⁵⁵ Instead of estimating the exact lifetime of all study participants, a risk score (the hazard ratio) is calculated for each treatment compared to control. Hazard ratios above 1 indicate greater risk (meaning shorter lifetimes), hazard ratios below 1 indicate a decreased risk.

Applied to this scenario, even non-collapsed branches during the 24-hour time window of the experiment carry information when compared to shorter-lived branches with a fully measured lifetime. Splitting the dataset artificially into 'fully measured' and 'non-collapsed' branches, would inevitably report lifetimes that depend on the length of the time window. Survival analysis, instead, estimates a risk for collapsing for all groups that controls for the observational window. As a formation of any branch close to the end of the observational time window has a higher chance for censoring, I normalised for the timepoint of formation and employed a Cox proportional hazard model.²⁵⁶

Such a survival analysis revealed a high risk of collapsing for branches originating from lamellipodia or splitting events when compared to filopodia-originating branches (hazard ratio (HR): $HR_{Spl}=5.0$ (3.8-6.6), $HR_{Lam}=4.6$ (3.6-5.7), both $p<0.001$). Branches from mixed precursors were at an intermediate risk of collapse ($HR_{Mix}=2.6$ (2.1-3.3), $p<0.001$). Therefore, even though the actin-based branch precursors are long replaced by microtubules before branch lifetime is maintained hours later, the type of precursor seems to predict the stability of the branch (Figure 20D).

5.1.2 Developing axons stabilise all branches and prefer efficient precursor types

Axons have been described to elongate and accumulate branches before dendrites.¹⁷ Also in our culture system, axons accumulated branches while dendrites remained mostly unbranched during the observation (Figure 21B). This accumulation of branches could, however, not be explained by an increased formation of branches on the developing axon, as developing dendrites initiated similar numbers of branches (Figure 21A). Interestingly however, the composition of precursor types differed between axons and dendrites. Axons initiated most branches from filopodia or mixed precursors, while dendrites relied predominantly on lamellipodial or splitting precursors.

The comparison of individual branch lifetimes indicated that a large proportion of dendrite branches collapsed soon after formation (visible as a strong diagonal band in the right panel of Figure 21C). In contrast, nearly 50% of axonal branches persisted beyond the end of the imaging sessions (vertical band at 24 hours, left panel in Figure 21C). A survival analysis confirmed this higher risk of collapse on developing dendrites ($HR=5.2$ (4.6-5.9), $p<0.001$).

The effect of precursor types on branch stability (Figure 20) and the shifted composition towards efficient precursors on the axon suggest that branch stability on the axon is heavily influenced by the choice of efficient precursors. Interestingly however, in addition to this altered precursor composition, all branches persisted longer on axons, irrespective of the precursor type (quantified in Figure 23B).

Therefore, axons appear to stabilise branches in two distinct ways: by preferentially initiating branches from efficient precursors (i.e., filopodia), and by stabilising branches in general (Figure 21D).

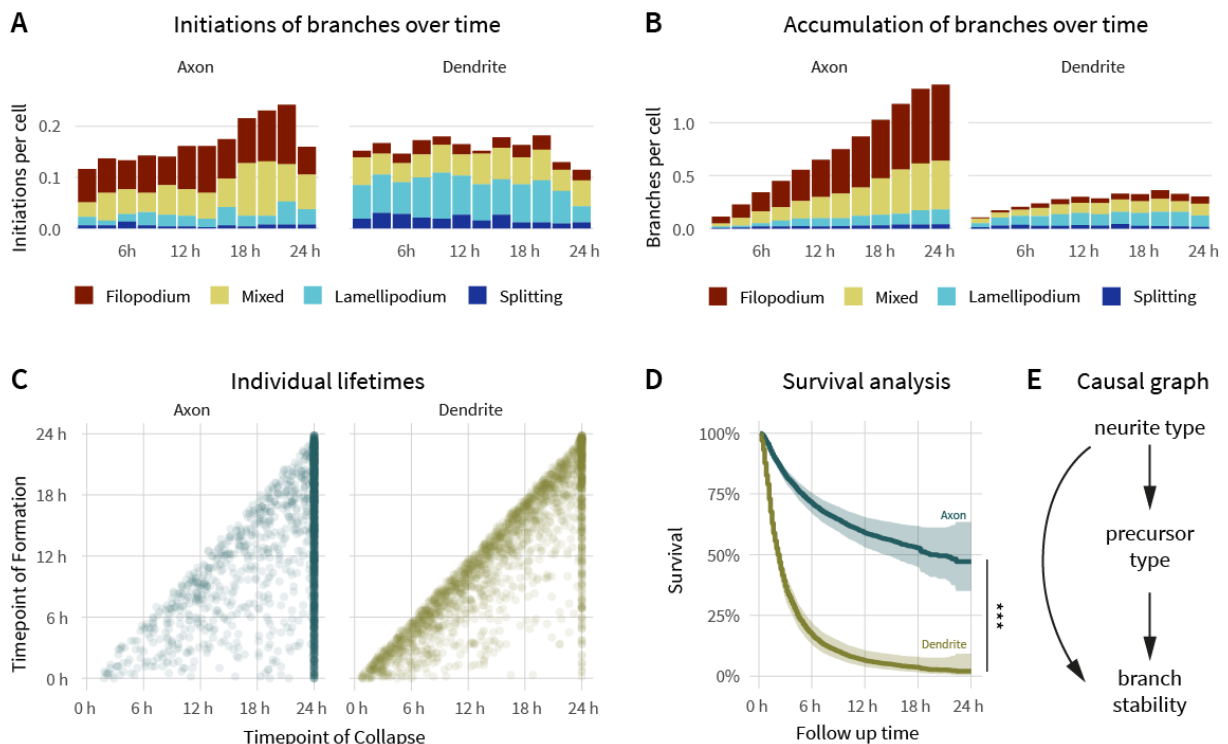


Figure 21: Axons stabilise branches and initiate from efficient precursors. (A) Initiation of branches per cell over time, split by axonal or neuritic location and colour-coded by precursor type. Developing dendrites initiate similar numbers of branches from different precursors when compared to axons. (B) Accumulation of branches over time, split by axonal or neuritic location and colour-coded by precursor type. Branches on axons accumulate, specifically those from filopodial and mixed origin. (C) Timepoint of formation versus timepoint of collapse for all individual branches separated by location of origin. (D) Survival analysis reveals a high risk for collapse for neurite-originating branches compared to axon originating branches. *** $p < 0.001$. (E) Causal diagram describing the links of location and precursor type on branch stability. $n_{ind} = 2317$ (WT) & 2165 (*Plppr3*^{-/-}), $n_{Exp} = 6$ (six independent cultures), transparent ribbons show 95% confidence intervals in survival curves. Parts of the figure submitted in the manuscript at *BioRxiv* (<https://doi.org/10.1101/2021.04.23.441127>) and currently under revision.

5.2 REMOVING EFFICIENT PRECURSORS REDUCES OVERALL BRANCH STABILITY

In the previous chapter, PLPPR3 has been characterised to control filopodia and branching morphogenesis predominantly on developing axons in a pathway with PTEN and PI3K. Furthermore, the PI3K pathway alters multiple stages of branching morphogenesis (introduced in section 1.3.2). I therefore assessed, whether in this setting, with axons and filopodia influencing branch stability, also loss of PLPPR3 altered the stability of branches.

5.2.1 *Plppr3*^{-/-} branches have a shorter lifetime

To compare the lifetime of wild-type and *Plppr3*^{-/-} branches, the above cultures were quantified blind to genotypes and in a randomised order during the manual classification of branch formation and collapse and only unblinded when calculating the effect of PLPPR3. The distribution of individual lifetimes of branches from *Plppr3*^{-/-} neurons appeared similar to wild types, with a slight reduction in

censored datapoints (Figure 22A). Indeed, a survival analysis indicated a slightly shorter lifetime of *Plppr3*^{-/-} branches (Figure 22B, HR: 1.2 (95% CI: 1.1-1.3), p=0.006).

In these cultured wild-type neurons, collateral branches (originating from filopodia, lamellipodia, and mixed precursors) forming on the shaft of all neurites make up the majority of branches compared to growth cone splitting (Figure 22C). Similar findings have been reported *in vivo*.²⁵⁷ In *Plppr3*^{-/-}, however, initiations specifically from filopodia precursors are less common (Figure 22C, $g_{\text{Filopodia}} = 1.7$, p=0.046). In summary, PLPPR3 appears to both alter precursor type distribution and branch stability (Figure 22D), as conceivable by a modulation of PI3K signalling.

However, the effects of PLPPR3 loss appear to intensify very little during the maturation stages of a branch. The effect size of reduced filopodia density on early polarising axons in of *Plppr3*^{-/-} (Figure 15H, $g_{\text{Exp}} = -1.3$), this effect size of fewer initiations of branches from filopodia (Figure 22C, $g_{\text{Exp}} = -1.7$), and

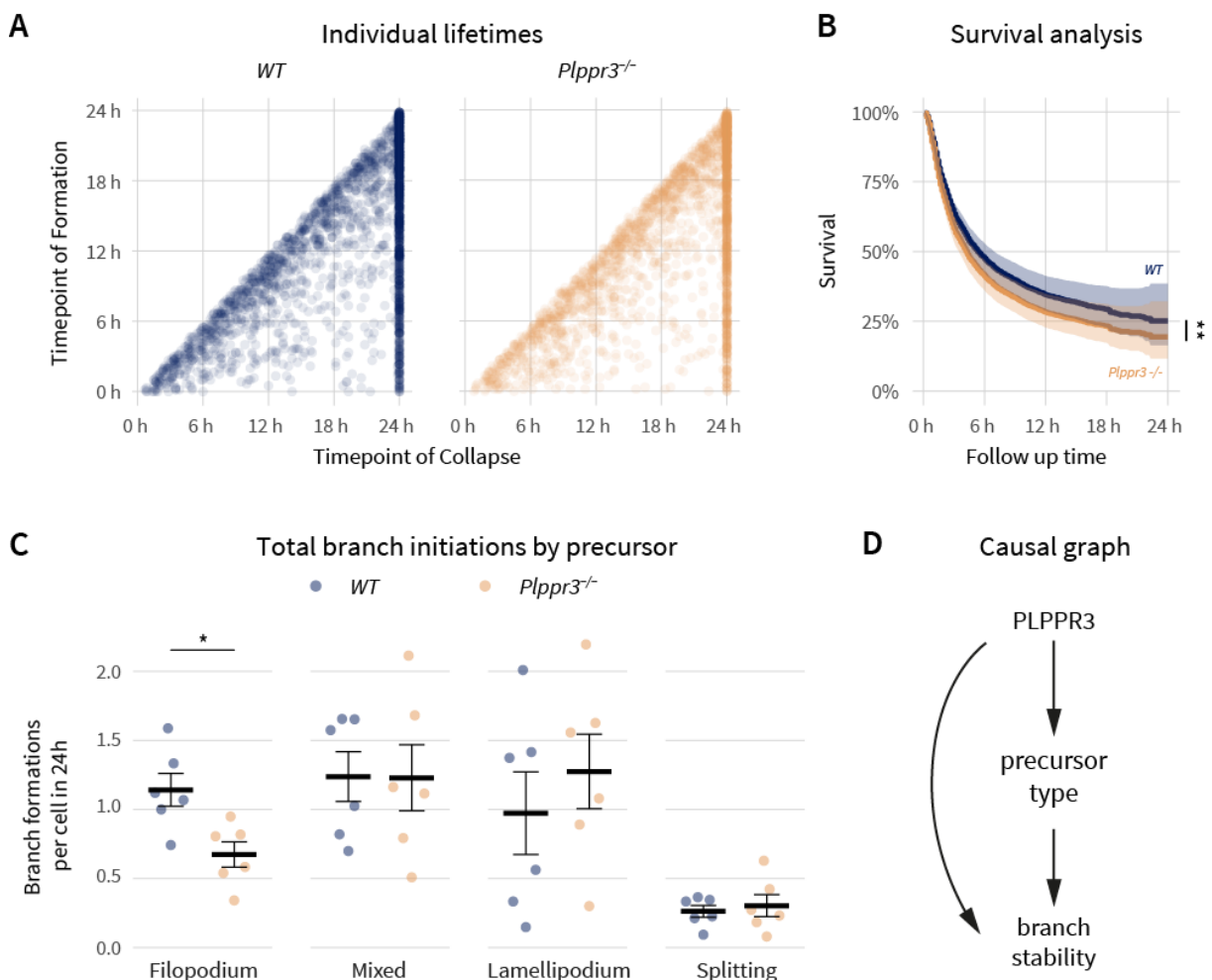


Figure 22: Loss of PLPPR3 decreases stability of branches and the number of branches initiating from filopodia precursors. (A) Timepoint of formation versus timepoint of collapse for all individual branches separated by genotype. (B) Survival analysis reveals a small but detectable risk for collapse in *Plppr3*^{-/-} neurons. *** $p < 0.001$. $n_{\text{ind}} = 2317$ (WT) & 2165 (*Plppr3*^{-/-}), $n_{\text{Exp}} = 6$ (six independent cultures), transparent ribbons show 95% confidence intervals. (C) Comparison of branch initiations per cell during the analysis period shows a loss of filopodia originating branches in *Plppr3*^{-/-} neurons. * $p < 0.05$, $n_{\text{Exp}} = 6$. (D) Causal diagram describing the links of location and precursor type on branch stability. Parts of the figure submitted in the manuscript at BioRxiv (<https://doi.org/10.1101/2021.04.23.441127>) and currently under revision.

the effect size of decreased branch density at DIV5 (Figure 16I, $g_{Exp} = -2.1$, Figure 19I, $g_{Exp} = -1.5$) are very similar. Therefore, an effect of PLPPR3 at multiple levels of the branching programs is unlikely. This suggests that the increased filopodia density through PLPPR3 could be the main determinant of branch abundance at later stages rather than an additional effect on branch stability.

5.2.2 *Plppr3*^{-/-} reduces branch stability only by removing filopodia

The previous discussion highlights that it is difficult to attribute the contribution of all effects on branch stability when only executing individual analyses. In such scenarios, related fields such as ecology^{258,259} or epidemiology²⁶⁰ use multifactorial statistical models to facilitate the interpretation of complex data by quantifying the individual contributions of each effect. Specifying a multifactorial model, however, requires choosing which factors are essential and which are unlikely to matter. Leaving an important confounder unaccounted, misleads the interpretation. However, including a so-called collider into the analysis introduces selection bias.²⁶¹

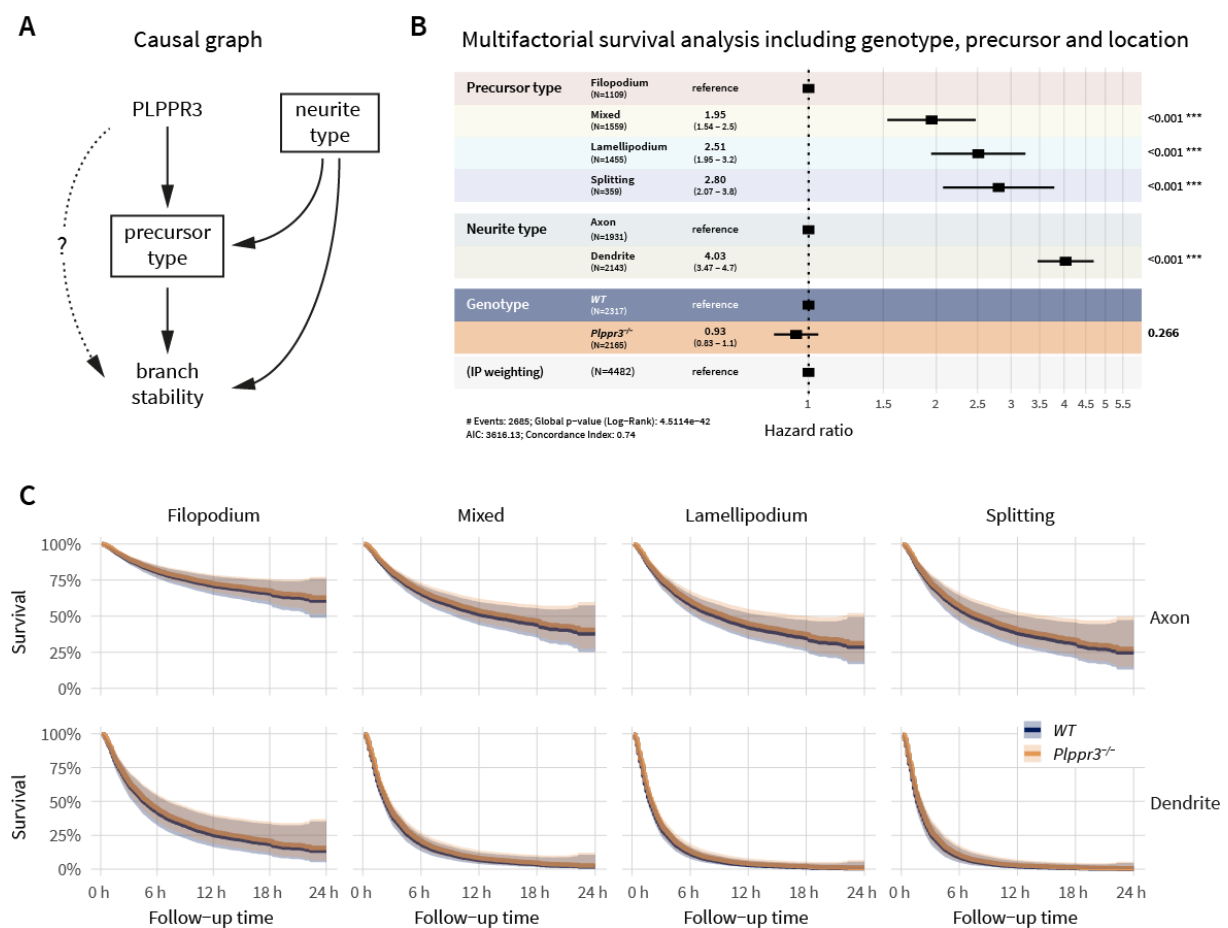


Figure 23: PLPPR3 alters branch stability only by altering precursor type distribution. (A) Causal diagram aggregating the information from previous experiments. To estimate a direct contribution of PLPPR3 on branch stability, a multifactorial analysis has to account for the effects of both location and precursor type. (B) Forest plot of survival analysis including genotype, precursor type, and location. Genotype of *Plppr3*^{-/-} does not confer an additional risk for collapsing after accounting for the other factors. (C) Survival curves for precursor type – location connections show identical lifetimes for *Plppr3*^{-/-} branches. $n_{Ind}=2317$ (WT) & 2165 (*Plppr3*^{-/-}), $n_{Exp}=6$ (six independent cultures), transparent ribbons show 95% confidence intervals. Parts of the figure submitted in the manuscript at *BioRxiv* (<https://doi.org/10.1101/2021.04.23.441127>) and currently under revision.

Causal diagrams, also referred to as directed acyclic graphs,^{260,262} have been put forward as a tool of causal inference to visualise and subsequently test the causal connections between multiple factors in the same system.^{261,263,264} Such causal graphs are usually built from previous knowledge and therefore represent a hypothesis. In cases where experimental interventions would be unethical or not possible (as exemplified for the link of smoking and lung cancer), these and related tools of causal inference can be used to recover causal structures from purely observational data.^{265,266}

Using these tools, I aggregated the evidence accumulated above into a causal diagram (Figure 23A) and used it to specify a multifactorial survival analysis to understand the direct contribution of PLPPR3 on branch stability. The model estimated the direct effect of PLPPR3 on branch stability by accounting for the effects of precursor and neurite type. In such a multifactorial Cox proportional-hazards model, both the precursor types as well as the neurite type strongly affect branch lifetime independently of each other (Figure 23B). However, the loss of PLPPR3 did not alter branch stability beyond its effects on precursor type distribution (Figure 23B, HR_{Plppr3} : 0.93 (0.83-1.1), $p = 0.27$).

In other words, the remaining filopodia branches on *Plppr3*^{-/-} axons do not seem to differ in stability from wild-type branches (Figure 23C, top left panel), nor does any other branch precursor-neurite type combination (Figure 23C). *Plppr3* does not contribute to branch stability directly but facilitates an inherently branch-stabilising filopodia program especially on axons.

5.3 SUMMARY AND OUTLOOK: HOW COULD PRECURSORS MODIFY BRANCH STABILITY

In summary, this chapter establishes a role of morphologically distinct branch precursors in affecting downstream branch maintenance. All precursors are found on both axons and dendrites, but axons seem to preferentially utilise the most efficient ones. In addition, axons appear to stabilise all branches irrespective of precursor type. These findings explain the reduced branch stability observed in hippocampal neurons cultured from *Plppr3*^{-/-} mice and place PLPPR3 as part of a program to induce efficient branch formation on developing axons. The lack of effects of PLPPR3 loss on branches from other precursors indicates that the precursors initiate mechanistically independent 'branching programs'.

These results raise the question of how F-actin precursors could modify branch stability that is predominantly under the control of microtubules. Filopodia and lamellipodia branches could differ in their reliance on adhesion or in the way they provide microtubules to start growing. Specifically lamellipodia-enriched actin waves are in a position to mechanically de-bundle microtubules and pull them into newly forming protrusions.²⁶⁷ Alternatively, the precursor types could recruit alternative microtubule-severing enzymes to locally destabilise the neuronal cytoskeleton. Interestingly, the microtubule-severing enzymes Spastin and Katanin appear to induce branches in distinct ways.⁶⁴ Filopodia and lamellipodia could also capture and crosslink microtubules differentially either by differing mechanical properties^{268,269} or by recruiting different actin-microtubule crosslinkers.²⁷⁰ Here Drebrin predominantly found newly forming filopodia branches emerges as an interesting candidate.⁶⁷

The distinct stability of branches induced from filopodia and lamellipodia is, however, most likely controlled by distinct microtubule stability in later stages of branching morphogenesis. Therefore the precursors could recruit different post-translationally modifying enzymes of microtubules³³ or different microtubule-stabilising proteins.^{32,271} Also membrane organelles have been described to alter microtubule stability to control neuron morphogenesis.^{84,272} Interestingly, the regulation could also act reversely, from microtubules to the actin cytoskeleton: some microtubule-binding proteins stabilise actin to regulate neuron morphogenesis,^{73,100,273,274} and lamellipodia on axons seem to require dynamic microtubules.²⁷⁵

Future studies could therefore directly measure microtubule stability in branches from distinct precursors using non-stabilising live-cell probes.²⁷⁶ Furthermore, such studies could focus on microtubule-binding proteins enriching specifically in filopodia- or lamellipodia-initiated branches. Interesting candidates could be verified by loss-of-function studies using the described live-cell strategy. In general, the analyses from these chapter show, that defining the precise role of a branch stabilising protein appears to require measuring the stabilities of branches by accounting for the different precursor types.

6 DISCUSSION

The results from Chapter 2 present PLPPR3 as a neuron-specific, axon-enriched protein localising to the plasma membrane and tubular internal membrane compartments. Plasma membrane localisation of PLPPR3 appears to depend on both C-terminal and transmembrane regions, and PLPPR3 overexpression increases filopodia density in N1E-115 cells. Generating a knockout mouse line for *Plppr3* using the CRISPR/Cas9 technique (Chapter 3) allowed for the analysis of the endogenous role of PLPPR3 in neurons. Cultured hippocampal *Plppr3*^{-/-} neurons seem to survive and polarise normally but show less filopodia and branching during early axon development (Chapter 4). This specific decrease of filopodia-induced branches without altering those originating from other precursors suggests the existence of separate branching programs differing in their maintenance (Chapter 5). Mechanistically, PTEN-inhibition was able to counteract the loss of PLPPR3, but optimised visualisation techniques (Appendix 7.1) could not detect altered levels of the PTEN-substrate PIP3 in *Plppr3*^{-/-} axons.

6.1 PLPPR3 AND PI3K/PTEN MEDIATED BRANCH FORMATION

PI3K-signalling has a central role in neuron survival and development (section 1.3.2). Recent evidence (using the optimised PIP3-detection protocol) suggests that downregulating PI3K activity participates in the loss of regenerative capacity of adult central nervous system neurons.²⁴⁵ Differential regulation of PIP3-levels in excitatory versus inhibitory neurons (7.1.3) might contribute to PI3K/PTEN dependent forms of neurodevelopmental disorders.¹²³ Moreover, regulating the activity or localisation of PTEN, the main suppressor of the PI3K pathway, has essential roles for neuron development and regeneration.^{123,138,247,277,278}

Interestingly, PLPPR3 interacts with PTEN and counteracts PTEN function in cell lines, as measured by phospho-AKT levels and membrane accumulations of AKT1-GFP and F-actin. Furthermore, PTEN purified from PLPPR3 expressing cells was less active in hydrolysing PIP3 in a cell-free assay (Dr. Annika Brosig and Dr. George Leondaritis).²⁰⁶ In embryonic stem cell-derived motoneurons, PI3K-activity was required for PLPPR3-induced filopodia and branching (Dr. Sandra Schrötter & Dr. George Leondaritis), and the knockdown of PTEN in this thesis was able to mimic PLPPR3 function in primary hippocampal neurons. These experiments establish a clear link of PI3K-signalling and PLPPR3 function and suggest that PLPPR3 inhibits PTEN to accumulate PIP3 for induction of filopodia (Figure 24A).

However, localised production of PIP3 on axons has been shown to induce the formation of both filopodia⁵⁹ and lamellipodia.¹²⁷ As loss of *Plppr3* only affects filopodia-induced branching, the inhibition of PTEN alone does not suffice to explain the specific branching phenotypes of PLPPR3. Furthermore, an inhibition of PTEN by PLPPR3 would suggest that PIP3 levels decreased in axon shafts of *Plppr3*^{-/-}. However, distinct strategies of PIP3-quantification (PH-domain overexpression or immunolabelling) that are specific in neurons (section 7.1) and sensitive enough to detect developmental downregulation of PI3K-activity in neurons²⁴⁵ or local accumulations of PIP3 preceding branch formation in dorsal root ganglia axons,⁵⁹ did not provide evidence for lower baseline PIP3 levels or fewer accumulations in axons of *Plppr3*^{-/-}. Furthermore, a downstream marker of PI3K-activity,

phosphorylation of AKT at S473, neither implied differences of PI3K-signaling strength in cortical neurons lacking PLPPR3 (not included) nor in ES-cell derived PLPPR3-expressing motoneurons (Figure 5A, Brosig & Fuchs et al. 2019). It is possible, that these readouts lacked the required sensitivity or local resolution to detect the changes induced by PLPPR3. However, also extensions or refinements of the model connecting PLPPR3 and PTEN could explain the observed phenotypes.

Models connecting PLPPR3 and PI3K signalling for filopodia formation

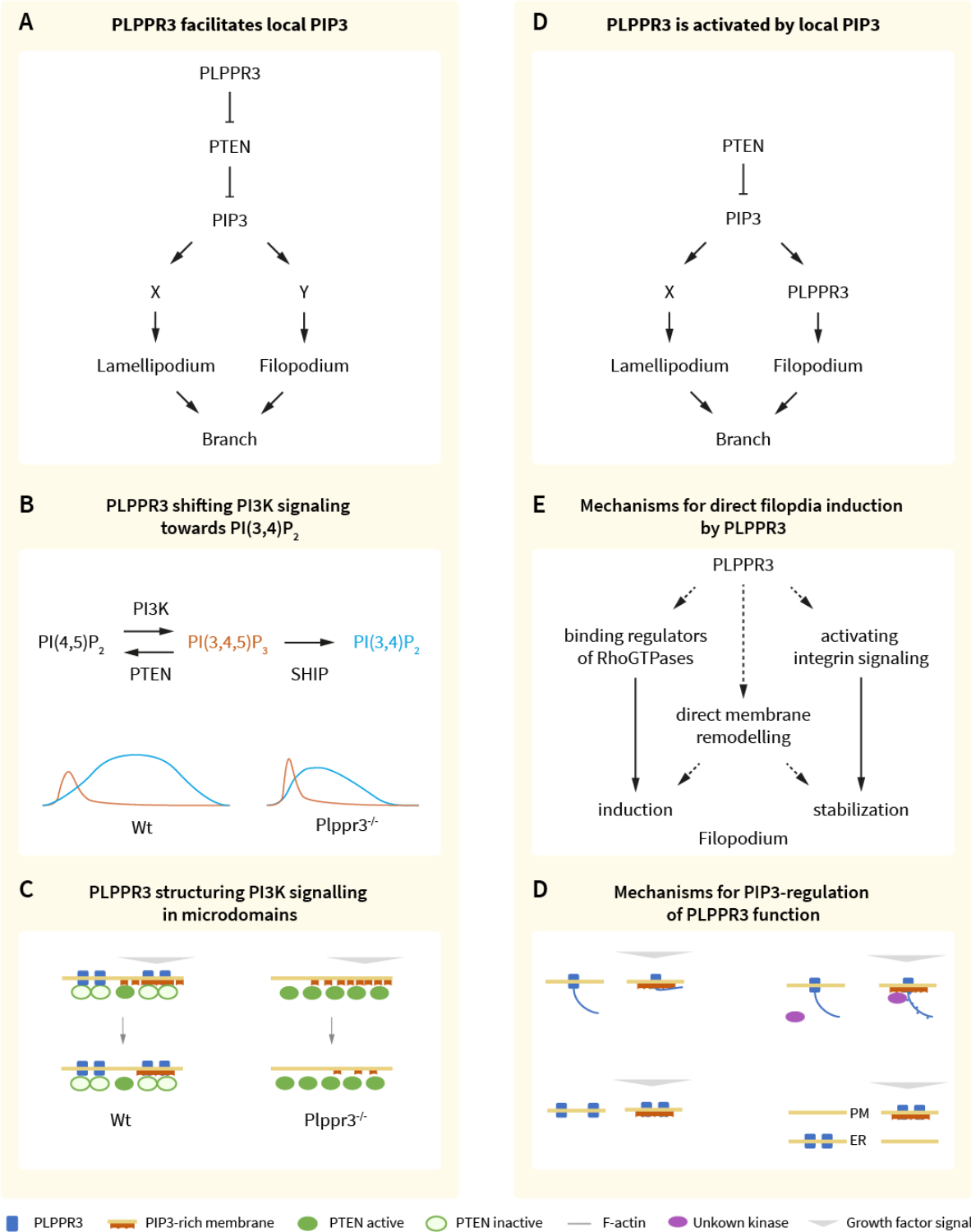


Figure 24: Models connecting PLPPR3 and PI3K signalling for filopodia formation.

The following sections will discuss how PLPPR3 could provide additional structure to PI3K-signalling by shifting PI3K signalling towards the production of PI(3,4)P₂ (Figure 24B, section 6.1.1), or by clustering PIP3 and inhibiting PTEN only in membrane microdomains (Figure 24C, section 6.1.2). Alternatively, a model placing PLPPR3 downstream of PIP3 to specifically induce filopodia (Figure 24D) could distinguish PIP3-effects specifically on filopodia and does not require PIP3- or pAKT levels to change by loss of PLPPR3. In such a model, PI3K-activity would be required to activate PLPPR3 function in ES-cell-derived motoneurons, and PTEN would counteract PIP3-mediated PLPPR3 functions in hippocampal neurons. Loss of PTEN could rescue the loss of PLPPR3 via PIP3-dependent but PLPPR3-independent branching mechanisms – such as lamellipodia. However, such a model would require both – yet unknown – mechanisms for PI3K signalling to activate PLPPR3 (Figure 24F), and – yet unknown – mechanisms for direct effects on filopodia by PLPPR3 (Figure 24E) and will be discussed in section 6.1.3.

6.1.1 PLPPR3 shifting PI3K signalling to PI(3,4)P₂

PI3K initiates signalling by phosphorylating the most abundant plasma membrane phosphoinositide PI(4,5)P₂ to generate PI(3,4,5)P₃ (Figure 24B). The primary mechanism to remove the generated PIP3 is by PTEN mediated dephosphorylation back to PI(4,5)P₂. Other phosphatases (e.g., SHIP1 and SHIP2) can dephosphorylate PIP3 at the 5' position, generating PI(3,4)P₂. This alternative dephosphorylation of PIP3 has been described to be the main source for plasma membrane localised PI(3,4)P₂, making PI(3,4)P₂ equally susceptible to pharmacological inhibition of PI3K.^{279,280} Furthermore, PIP3 signals seem to be rather short events that are followed by longer increases of PI(3,4)P₂.²⁸¹ Recent evidence even suggests PTEN mediated dephosphorylation of PI(3,4)P₂ to PI(4)P.^{282,283} Inhibiting PTEN activity by PLPPR3 could therefore strongly shift PI3K-signalling towards PI(3,4)P₂ mediated functions.

Only few studies have addressed the differences of PI3K-induced effects mediated by PI(3,4)P₂ rather than PIP3. Many effector proteins (e.g., AKT1) can bind both phosphoinositide species with similar affinity,²⁸⁴ although other AKT isoforms seem to differ in their PI(3,4)P₂ / PIP3 targeting.²⁸⁵ Interestingly, PI(3,4)P₂ rather than PIP3 appears to induce F-actin reorganisation downstream of PI3K activity in neurons.²⁸⁶ Therefore, it could be PI(3,4)P₂ rather than PIP3 that is mediating PLPPR3 effects downstream of PTEN.

Indeed, some PI3K-dependent effects on axon branching⁵⁹ as well as the readouts for PLPPR3-PTEN mediated PI3K-activity in cell lines have been analysed using AKT1-probes that also detect PI(3,4)P₂. Therefore, pinpointing a role for the specific phosphoinositide in axon branching has not yet been fully achieved. Furthermore, when assuming fast conversion of PIP3 to PI(3,4)P₂ and PI(3,4)P₂-mediated PLPPR3 functions, the levels of PIP3 would not necessarily have to differ in *Plppr3*^{-/-}. Even though pilot immunolabeling experiments did not suggest strong differences in intensity or distribution of PI(3,4)P₂ in *Plppr3*^{-/-} (not shown), this seems like an interesting route to follow – especially because the probe used for these pilot experiments has not yet been validated for sensitivity and specificity in neurons.

In summary, accumulating PI(3,4)P₂ rather than PIP3 downstream of PLPPR3 activity could explain the observed similarity of PIP3 in wild-type and *Plppr3*^{-/-} neurons. However, as lamellipodia were described to require PI(3,4)P₂ for their formation as well as maturation,^{287,288} preferential accumulation PI(3,4)P₂ is unlikely to be the sole mechanism of PLPPR3 to induce filopodia but not lamellipodia.

As PIP3 signals have been observed to be very transient while PI(3,4)P₂ followed and persisted for longer,²⁸¹ PLPPR3-mediated PTEN inhibition could additionally alter the time course of a PI(3,4)P₂ signal. It would be interesting to study whether a distinct temporal pattern or a distinct ratio of PIP3 to PI(3,4)P₂ is able to distinguish the generation of filopodia from lamellipodia. Such experiments would be conceivable in cell lines using photoactivatable phosphoinositides²⁸⁹ (PIP3 and/or PI(3,4)P₂) with different durations of stimulation, but likely require extensive optimisation procedures.

6.1.2 PLPPR3 creating signalling microdomains

In a separate layer of regulation, spatially restricted induction of PIP3/PI(3,4)P₂ could contribute to differential F-actin reorganisation to form wide lamellipodia or thin filopodia protrusions. PLPPRs are capable of forming homomeric and heteromeric complexes with other PLPPR proteins,¹⁸⁶ and PLPPR1,^{163,186} PLPPR4,¹⁶⁰ and PLPPR5^{165,186} endogenously localise to microscopically distinct puncta. Also PLPPR3 was found to form complexes and appears in a punctate pattern along the axon shaft when visualised in confocal or structured illumination microscopy (Dr. Annika Brosig).²⁰⁶ It is therefore conceivable, that these localised PLPPR3 puncta create membrane microdomains to structure PI3K-signalling spatially (Figure 24C).

Membrane microdomains have been described to participate in multiple signalling pathways by providing means to locally increase concentration without having to globally upregulate production of signalling mediators.²⁹⁰ Especially low affinity interactions or enzymatic reactions that require high concentrations could be stabilised very locally in such microdomains.²⁹⁰ Local synthesis or local disinhibition of global degradation are mechanisms extensively described for compartmentalised PI3K-signalling.^{132–140} In this respect, PLPPR3-mediated inhibition of PTEN restricted to clusters could create such PIP3/PI(3,4)P₂ microdomains along the axon and enable a coincidence detection mechanism of activating PI3K and, at the same time, inhibiting PTEN. The putative PIP-interaction of PLPPR3, as well as of PLPPR5 could further facilitate clustering of PIP3/PI(3,4)P₂ as described for the microdomain generation by clustering of phosphoinositides through multivalent PIP-interacting proteins.^{149,150}

These mechanisms would imply a modification of the plasma membrane composition by proteins. However, lipids also tend to self-organise into clusters differing in their mobility via liquid-liquid phase separation of lipid species differing in saturation or length.²⁹¹ This process is facilitated by cholesterol and sphingomyelin and readily observable in artificial as well as cell membrane derived vesicles.²⁹¹ In living cells, phase separated lipid domains – even more so than protein-induced cytosolic phases²⁹² – still evade direct observation, suggesting mechanisms to actively suppress lipid de-mixing or structuring of lipids into sub-microscopic domains.²⁹³

Nonetheless, some studies indicate functional importance for lipid-order microdomains especially for receptor tyrosine kinase mediated signalling.²⁹⁰ B-cell receptor clustering has been shown to activate downstream signalling by de-mixing membrane-bound kinases and phosphatases to distinct microdomains in a process that is partially controlled by distinct lipid phases.²⁹⁴ Interestingly, even artificial clustering of the lipid phase was sufficient to induce downstream signalling, thereby establishing a link of lipids controlling plasma membrane protein localisation and signalling.

Also phosphoinositides show some tendency of de-mixing into distinct domains: PIP3 has been described to reside in nanodomains distinct to those enriched in PI(4,5)P₂.²⁹⁵ While the localisation of PI(4,5)P₂ is not necessarily restricted to ordered lipid domains, some cytoskeletal or axon enriched proteins are assumed to specifically enrich it there.^{296,297} Similarly, PIP3 does not show a specific tendency to reside in ordered or disordered lipid domains but it appears to be selectively produced in ordered domains²⁹⁸ and hydrolysed (through PTEN) in disordered lipid domains.²⁹⁹ This potentially enriches PI3K signalling in less mobile membrane domains. These findings suggest an influence of lipid microdomains on the PI3K pathway and could contribute to the recently described effects of membrane microdomains in neuron development and regeneration.^{300,301}

Interestingly, PLPPR4¹⁸⁷ and the closely homologous PLPP1 and PLPP3^{302,303} have been detected in detergent resistant membranes, indicating a localisation of PLPPRs to specific lipid microdomains. Furthermore, the size of PLPPR3 clusters detected by structured illumination microscopy (ca. 200 nm, Dr. Annika Brosig)²⁰⁶ is in the range of lipid domains as described in the literature.^{290,304} Moreover, similar to other plasma membrane proteins that reside in lipid microdomains,³⁰⁵ treatment with actin depolymerising Latrunculin A increased the distance of PLPPR3 clusters (Dr. Annika Brosig).²⁰⁶ These experiments suggest that PLPPR3 clustering might be facilitated by association with such lipid domains. However, the stable interaction in lipid-free co-immunoprecipitation experiments suggests that PLPPR3 clusters form before the lipid phases. As a consequence, the PLPPR3-clusters could even instruct the formation of membrane microdomains, as described for specific F-actin arrangements.³⁰⁶

In summary, PLPPR3 could constrict PIP3/PI(3,4)P₂ to membrane microdomains via multiple potential mechanisms. Experiments to support a role for membrane microdomains in PLPPR3 function could aim on assessing co-localisation measures of PLPPR3 and PIP3 or PI(3,4)P₂. They furthermore could compare lipid microdomain organisation in relation to PLPPR3-loss or overexpression. In this respect, immunolabelling PLPPR3 and PIP3 or overexpressing PIP3-specific PH-domains did not indicate specific co-localisation or reorganisation of PIP3 in neurons. However, higher spatial resolution or improved signal-to-noise ratios by more evolved PIP3-sensors (discussed in 7.1), or specific PI3K-stimulation paradigms such as optical uncaging²⁸⁹ or focusing on PI(3,4)P₂ could be required to uncover such phenotypes. Furthermore, the localisation of PLPPR3 or PIP3 to domains of different membrane order could provide insight into the exact contribution of lipid microdomains to PLPPR3 effects. To this end, lipid-order sensitive or -specific probes (eg. Laurdan or FRET-sensors), or single molecule tracking could be employed to either study PLPPR3 or PIP3/PI(3,4)P₂ localisation and mobility.²⁹¹

To determine whether confining PI3K signalling to microdomains is sufficient to explain filopodia-specific PLPPR3 effects, future studies could aim at manipulating the microdomain distribution of PLPPR3 either by mutagenesis or pharmacological strategies. Such treatments could be screened for by assessing their effect on PLPPR3-complex formation in co-immunoprecipitation experiments. In case further structure-function experiments verify the C-terminal region of PLPPR3 as the main contributor to filopodia formation, fusion of this domain to a single-pass transmembrane domain could allow for manipulating clustering from the extracellular side using multivalent antibodies or beads. Such experiments could be followed up with interactomics to detect microdomain-specific interactors.

In case manipulating PLPPR3 clustering remains evasive, targeting PTEN clustering directly might be an alternative strategy to test the contribution of PI3K signalling microdomains to PLPPR3 effects. Fusing chemical or optical dimerising modules (such as Cry2/CIBN or FKBP/FRB or SNAP)³⁰⁷ to PTEN and artificial membrane-domain enriched probes or probes that can easily be clustered by extracellular application of antibodies could mimic PLPPR3 function in cell lines or even *Plppr3*^{-/-} neurons. Such a system would, however, not directly mirror PLPPR3-mediated PTEN inhibition inside of PIP3 clusters but rather would create PTEN-depleted microdomains between the clusters. An ideal chemical tool to study the effect of PIP-microdomain clustering could combine a double-membrane spanning hydrophobic lipid with a non-hydrolysable PIP3 or PI(3,4)P₂ on the internal leaflet and a corresponding 'clustering-anchor' on the outer leaflet side. Synthesising such a construct and testing whether it would even be possible to insert it to plasma-membranes would require extensive optimisations and collaboration with experts in organic chemistry.

6.1.3 PLPPR3 mediating branch formation downstream of PI3K/PTEN signalling

Microdomain localisation or creation does, however, mainly explain PLPPR3 action before and during the timepoint of formation of an actin patch or a subsequent filopodium. The presence of PLPPR3 along the axon shaft and on all parts of filopodia (without inducing a function), suggests additional mechanisms to activate or inhibit PLPPR3 function. This could occur either by a coincidence mechanism requiring both PI3K-signalling as well as PLPPR3-mediated inhibition of PTEN as discussed above, or by PIP3/PI(3,4)P₂ directly altering PLPPR3 function (Figure 24F).

If PLPPR3-mediated effects on filopodia would not require altering PTEN activity, how else could it affect filopodia density on cells? The shared filopodia phenotypes across the PLPPR-family suggest shared downstream mechanisms (Figure 24E). Due to their well described role in neuron morphogenesis,¹⁰¹ Rho-and Ras-GTPases were a target of several studies addressing PLPPR1 and PLPPR5 functions. PLPPR1 does not seem to require Cdc42, nor other known actin-remodelling proteins such as Vasp or Arp2/3 for its filopodia phenotypes.¹⁵⁵ Similarly, PLPPR5 increases filopodia independently of Cdc42 activity.¹⁸⁵ Interestingly, both PLPPR1 and PLPPR5 seem to counteract RhoA-activity,^{185,218} although it is not clear, whether these effects are acting in a linear pathway or whether they converge on a shared downstream mediator of RhoA-functions. PLPPR1 furthermore seems to counteract Rac1 activity,³⁰⁸ and interact with the Ras guanosine exchange factor 1 (RasGRF1, Cdc25).¹⁷⁷

It is conceivable that PLPPRs regulate Rho- or Ras-GTPase activity to induce filopodia, although the most described filopodia-inducing candidate genes Cdc42 and Rac1 do not seem to mediate the effects. Rather, modulating RhoA effects seems to emerge as a target pathway. A recent large-scale siRNA screen on the effects of 219 Rho-GTPase associated proteins on neuron morphogenesis described multiple proteins with similar loss of function phenotypes as PLPPR3.³⁰⁹ In addition to Cdc42 and RhoA, also Tsg101, Pard3, Gna13, Hip1, Igf1R and multiple additional proteins emerge as branch-specific regulators. Interestingly, also the actin-microtubule crosslinker Gas2L1 shows very similar neuron morphogenesis phenotypes to PLPPR3 in loss of function.⁷³ It could be fruitful to study, whether these candidates act in the same or in parallel pathways to PLPPR3 for inducing branches.

A second line of evidence suggests PLPPR-effects in adhesion. Cultured PLPPR1- and PLPPR4-expressing cells adhere stronger to cover slips and their migration seems to leave behind trailing fibers that resemble filopodia.^{183,308} Also PLPPR5 seems to prevent LPA or Nogo-induced cell rounding.¹⁸⁵ Mechanistically, PLPPR1 seems to stabilise focal adhesions by slowing down their disassembly,³⁰⁸ and PLPPR4 seems to alter surface abundance of active Integrin β 1.¹⁸⁷ This activation of Integrins does not involve direct interaction but binding of the Integrin deactivating phosphatase PP2A and can explain the increased dendritic filopodia density of PLPPR4-expressing cells.¹⁸⁷ PLPPRs therefore might not induce the formation of filopodia but rather stabilise them against retraction. Interestingly, both PLPPRs and Integrins seem to be found in ordered lipid domains, and integrin signalling seems to even require such membrane microdomains.^{187,290,310} Studying the adhesive properties in *Plppr3*^{-/-} neurons could provide further insight whether this mechanism contributes to PLPPR3 function.

Furthermore, PLPPR3 and PLPPR4 also seem to participate in neuron morphogenesis programs controlled by the ubiquitin ligases TRIM9 and TRIM67. Both TRIM-proteins have been found to interact with PLPPR3 and PLPPR4.^{311,312} Functional studies have established TRIM9 and TRIM67 as regulators of neurite formation and axon branching with mechanisms involving Netrin signalling and Vasp activity to alter exocytosis, filopodia dynamics and branching.^{52,53,313–315} Although PLPPR3 did not seem to interact with the Netrin receptor DCC in pilot co-immunoprecipitation and co-localisation analyses in overexpression settings (not shown), other mediators of TRIM9 or TRIM67 controlled branching might cooperate with PLPPR3 to form branches.

A last, and very unconventional hypothesis would assume direct actin-nucleating or membrane deforming events by PLPPRs. It is based on the observation that PLPPR3 (Figure 4) and PLPPR1 (ref³⁰⁸) are often found on membrane protrusions containing little F-actin, or tubular rather than flat portions of internal membrane compartments. PLPPRs could have a curvature sensing or even inducing function similar to reticulons that control the tubular structure of certain pools of the endoplasmic reticulum.³¹⁶ Transmembrane proteins have been described to alter curvature of membranes without need for cytoskeletal support,^{317,318} and also cytosolic membrane deforming proteins of the I-BAR family were described to deform the membrane before F-actin invasion.^{319,320} Interestingly, the effect of the I-BAR protein IRSp54 is suspected to depend on association with phosphoinositides and curved membranes to subsequently cluster Vasp for filopodia elongation.^{319,321}

Binding of phosphoinositides by PLPPR3 could serve as a similar coincidence detection mechanism to induce filopodia formation in response to PI3K activity. Alternatively, phosphoinositide binding could alter the localisation of PLPPR3 as described for Syntaxins. Syntaxin 1A clusters upon PI(4,5)P₂ or PIP₃ binding using a highly similar region to the PLPPR-family conserved polybasic juxtamembrane domain described in section 2.3.^{322,323} Phosphoinositide binding is furthermore hypothesised to open binding pockets for regulating NMDA- and EGF-receptor signalling in a competition with calcium/calmodulin.¹⁵⁰ Similarly, binding of PIP₃ could alter the conformation of PLPPR3. Lastly, PI3K activity could alter the phosphorylation status of PLPPRs by downstream kinases with PTEN acting as a protein phosphatase to counteract such PI3K-induced PLPPR-mediated effects. Interestingly, PTEN and mTOR have been found to also interact with PLPPR1.¹⁸⁶

As most of the mechanisms how PIP3 could activate PLPPR3 require direct binding of the two, future studies could focus on verifying the interaction and localising the exact PIP-binding site in PLPPR3. Such knowledge could allow for specific mutagenesis of the PIP-binding site to study its effects on PTEN-inhibition and filopodia density. This would allow for a more precise description of the nature of the PI3K/PTEN and PLPPR3 connection. In addition, interactomic studies of PLPPR3 or shared interactomes of PLPPR family members could provide further insight into the filopodia forming pathways. In this respect, screening for PLPPR3 mutants that express and localise normally but fail to introduce filopodia could allow for refined experiments to distinguish filopodia-related from other interaction partners.

In conclusion, several models could explain the effects of PLPPR3 and PTEN on branching morphogenesis. Even though these discussed models of the PLPPR3 and PTEN connection differ in whether PLPPR3 influences or is influenced by PI3K-activity, the true nature of the interaction could include multiple mechanisms. Combining PTEN-inhibition with PIP-binding and microdomain localisation or with structural changes in PLPPR3 could present with emergent properties that might not be fully replicated by only the individual functions. Effects on downstream pathways such as modulation of Rho-GTPases or adhesion could contribute to induction of PIP3 microdomains through feedback mechanisms.²⁰ While PI3K-activity and PLPPR3 therefore very likely cooperate during filopodia formation, the exact nature of their connection could be multifaceted and opens the door for exciting new directions.

6.2 REGULATING PLPPR3 TO REGULATE EFFICIENT BRANCH FORMATION

While the exact molecular mechanisms of PLPPR3 function await further clarification, this thesis established a physiological role in branch formation. Therefore, regulating PLPPR3 could be used by neurons to regulate their branched morphology. No matter whether it requires separate coincident or activating signals to initiate branches (as discussed in the previous sections), PLPPR3 is likely additionally controlled spatially or temporally by transcriptional and trafficking mechanisms.

The expression patterns of *Plppr3* in adult cortical mouse neurons indicate a potential cell type specific control. *Plppr3* expression appears highest in adult GABAergic neurons, specifically of caudal ganglionic eminence derived Sncg and VIP neurons. Such interneurons mostly exert short-range effects with a largely local but highly branched axon.^{12,78} Furthermore, expression seems to be lowest in long-range projecting, and therefore less branched, excitatory neurons of the pyramidal tract or lower cortical layers. Interestingly, PTEN presents with an opposite expression gradient, with lower expression in GABAergic and highest expression in long-range projecting glutamatergic neurons, again strengthening the idea that PLPPR3 and PTEN antagonise each other.

GABAergic interneurons have been described to migrate to their target region before adopting their final morphology.¹² It could, therefore, alternatively be possible that the enrichment of *Plppr3* mRNA in GABAergic cells just is a consequence of their delayed morphogenesis. *Plppr3* was found highly expressed during early development (as quantified by Dr. Annika Brosig)²⁰⁶ in largely glutamatergic neuron cultures. This suggests different expression time-courses of *Plppr3* for different cell types depending on the timepoint they establish their morphology. Supporting this hypothesis, the expression level of *Plppr3* in the adult datasets seems to inversely correlate with the time of birth of

glutamatergic neuron types – with earlier-born, lower layer neurons expressing less *Plppr3* at P55 than later-born, upper layer cortical neurons (Figure 1C&F). It would be very interesting to compare these results to a similar dataset of embryonic mouse cortex to further elucidate the temporal and cell type specificity of *Plppr3* expression. Furthermore, given their ability to form heteromeric complexes and the described effects on neuron morphology, it would be interesting to screen for co-expression of various PLPPRs in different cell types or at different developmental timepoints that could create a ‘PLPPR-code’ for morphogenesis.

In addition to potential cell-type-specific effects, PLPPR3 highly enriches in axons of neurons. This axonal localisation could potentially be controlled by transport of mRNA and local translation in the axon. In such a setting, the retained intron 3-4 with its two stop codons might act as ‘transport-lock’ to only allow for translation at the desired destination. While spliceosomes so far only have been described in the nucleus, extranuclear splicing has been reported in dendrites.^{324,325} Functional roles of the intron 3-4 retention event could be assessed by designing probes against the intron to localise transcripts, and by shRNA-targeting this intron and analysing PLPPR3 localisation.

PLPPR3 axon localisation is, moreover, likely controlled at the protein level. Here the axon initial segment likely participates in sorting of PLPPR3-containing vesicles and limiting diffusion of membrane localised PLPPR3 out of the axon.^{97,326} Therefore, especially plasma membrane localisation of PLPPR3 emerges as a potential axon-enrichment mechanism. Furthermore, it is likely that neurons use PLPPR3’s membrane localisation ‘sensitivity’ (most PLPPR3 mutants seemed to alter the membrane localisation in my overexpression experiments) to regulate PLPPR3 function. The expression dependency of plasma membrane localisation could, as an example, contribute to the selective loss of PLPPR3 function in long heterozygous *Plppr3*^{+/-} neurons.

Membrane localisation of PLPPR3 could also be regulated by PI3K- or phosphoinositide-mediated effects. The conserved polybasic juxtamembrane region in PLPPRs seems to be required for plasma membrane localisation of PLPPR3. A similar region in Syntaxin 1A has been described to mediate PI(4,5)P₂ and PIP3 binding and subsequent clustering of Syntaxin 1A.^{322,323} Phosphoinositide binding is also required for plasma membrane localisation of various ion channels.¹⁴⁸ Interestingly, the distance of PLPPR3 clusters seems to slightly increase by PI3K-inhibition (Dr. Annika Brosig),²⁰⁶ indicating lower plasma membrane abundance of PLPPR3. Further studies could focus on PI3K-inhibiting or activating treatments in PLPPR3 expressing cell lines with a focus on plasma membrane abundance of PLPPR3.

Furthermore, also lipid-order defined microdomains could regulate PLPPR3 membrane localisation. Lipid order differs drastically between organelles. The plasma membrane presents with highest order and endomembranes with more mobile lipids.^{327,328} Furthermore, association with ordered lipid domains has been described to control plasma membrane localisation of several proteins.^{329,330} The association of proteins, also of membrane proteins, with such ordered lipid domains has been described to depend on palmitoylation.^{212,331,332} Palmitoylation, in addition, has been described to control axonal enrichment of proteins.^{98,99} Even though the putative palmitoylation site C199 of PLPPR3 does not seem to contribute to membrane localisation, other predicted residues such as C20, might still be interesting candidates to regulate PLPPR3 localisation.

Finally, also the region homologous to the catalytic centre of PLPPs appears to regulate PLPPR3 membrane localisation. This indicates regulatory functions exerted by the lipid substrates of PLPPs (such as LPA) on PLPPR3. The effect of PLPPRs to LPA has mainly been described to counteract LPA-induced functions, be it migration, neurite collapse, hyperexcitability or NT3 secretion.^{159,160,218,219} Mechanistically, these effects are suspected to be mediated by an 'interaction' of LPA with PLPPRs, that has been inferred by altered uptake of phosphatidic acid of LPA in a PLPPR4-dependent manner but not been measured directly.^{160,161} Such an interaction could either decrease LPA-activity on LPA-receptors as suggested above, or alter LPAR-signalling by locally enriching or segregating LPA through binding – as has been described for BDNF with a truncated TrkB-receptor variant in the mammary gland.³³³ However the observed altered membrane localisation of PLPPR1¹⁵⁵ and PLPPR3 (section 2.3.3) after mutation of the 'catalytic centre' suggest a more direct action of LPA on PLPPR-localisation or function. Future experiments could verify the direct interaction despite the drastic mutations (discussed in section 2.3.3) of the putative binding site in the former 'catalytic centre'. They furthermore could assess membrane localisation of PLPPR in response to LPA-treatments.

In summary, the transmembrane region of PLPPR3 emerges as a potential target for regulating PLPPR3 function. However, the exact link of membrane localisation and filopodia inducing function has not yet been sufficiently characterised (as discussed in section 2.4). The high sensitivity of PLPPR3 membrane localisation furthermore complicates the unbiased quantification of PLPPR3 function. Less plasma membrane localised PLPPR3 mutants (such as the C-terminal deletion mutants) might not rescue branching just because of their specific localisation rather than their lacking binding domains for downstream interactors. Therefore, precise mapping of the domains on PLPPR3 that control localisation versus filopodia forming functions will be required to facilitate our understanding of PLPPR3 function. The characterised glycosylation-deficient mutant (N167Q) could serve as a tool to study non-membrane localised PLPPR3, while the delta-poly-E-box mutant could provide insight on predominantly membrane localised functions or interactors. In conclusion, studying PLPPR3-function precisely seems to require to first understand and control its regulation.

6.3 PLPPR3-INDUCED FILOPODIA BRANCHING AS AN INDEPENDENT MORPHOGENETIC RULE

As highlighted in Chapter 5, studying PLPPR3 functions on branching can also inform on the interplay of morphogenetic programs in developing neurons. Neurons likely control morphogenesis in a cell type or even compartment-specific manner by selectively initiating distinct strategies or by modifying the morphogenetic programs themselves (as introduced in section 1.2 and 1.3).

Interestingly, the *Plppr3*^{-/-} phenotypes discussed in Chapter 5 suggest that even the narrow branching morphogenesis program seems to be executed by multiple subprograms: lamellipodia-induced branches appear to collapse quite fast, while filopodia-induced branches persist longer. Changing only filopodia number, by loss of *Plppr3*, does not change the stability of branches from other origins. However, loss of the long-lived filopodia branches indirectly decreases the observed stability of the remaining branches. Similarly, reducing only lamellipodia branch initiations appears to equip the neurons indirectly with more stable branches.³³⁴ This lack of crosstalk between stabilising mechanisms indicates that separate downstream mediators control branch maintenance between the different

precursor types. Interestingly, neurons seem to utilise these distinct programs on distinct compartments. This results in a high turnover of lamellipodia-induced branches in neurites and an accumulation of filopodia-induced branches in axons.

These results raise the question, whether both branch types are relevant *in vivo*, or whether this distinction may only be an artifact of cell culture. Most reviews describe filopodia as the relevant branch precursor *in vivo*.⁵⁷ However, in three-dimensional cultures that more closely mimic the microenvironment of developing neurons *in vivo*, lamellipodia exhibit a cone-like shape that is morphologically much closer to 2D-culture filopodia than lamellipodia.³⁹ In a pilot reanalysis of branch lifetime in this dataset, that was kindly provided by Barbara Schaffran from the laboratory of Prof. Frank Bradke (DZNE, Bonn), overall branch lifetime closely matched the lamellipodia-lifetimes measured in my cultures (not shown). This suggests a relevant role for lamellipodia-induced branching in 3D. Furthermore, *in vivo* live-cell imaging of retinal ganglion cells revealed very short-lived branches of similar lifetime to the lamellipodial branches observed here.³³⁵

Interestingly, lamellipodia were also described to induce branching on dendritic leading processes of migrating neurons *in vivo*.³³⁶ The branching events are described to improve sensing of guidance cues,³³⁷ and the selective stabilisation of branches was indicated for steering the migration.⁴⁴ It is conceivable, that the dendritic lamellipodia-induced branching observed in my experiments is controlled by similar mechanisms as this ‘migratory branching’. In that case, the filopodia branch mechanisms could have evolved as a separate layer for more specific branch formation during later morphogenesis.

This raises the question, whether dendrite branching in general depends more on lamellipodial precursors or whether the observed predominantly lamellipodial branching is just a consequence of the early developmental stage of the analysed neurons. Similarly to axon branches, dendrite branches are considered to emerge from filopodia,³³⁸ although dendritic filopodia seem to contain a more lamellipodia-like Arp2/3-crosslinked cytoskeleton compared to axonal filopodia.³³⁹ On the other hand, the dendrites of interneuronal granule cells in the olfactory bulb seem to depend on GABA-induced lamellipodia as branch precursors.³⁴⁰ It is therefore conceivable that lamellipodia-induced branching still contributes to mature dendrite morphogenesis. Studying dendrites at later developmental timepoints using the strategy described here is, however, complicated by the need for very sparse culturing to study cell-cell adhesion independent branching.

Further insight could, however come from the regulation of branching patterns between axons and dendrites. Stochasticity has large implications for biological phenotypes by generating inter-cellular variability while preserving robust phenotypes.^{25,341} Interestingly, the exact locations of branches on both axons and dendrites are not deterministically defined.^{26,342} Stochastic formation combined with tiling and retraction mechanisms are sufficient to model layer and column specificity of dendritic and axonal arborisation.²⁴ Even experimentally, recent studies have established both stochastic as well as more deterministic parts of dendrite branch morphogenesis.^{343,344} Interestingly, the fast extension and short lifetime of lamellipodial branches appears like a stochastic ‘trial-and-error’ branching mechanism compared to the more ‘determined’ filopodial branches that have a slower turnover. Therefore,

regulation of these branching programs could be an intriguing mechanism to explain stochastic versus deterministic branching.

The distinct branching modes could even differentially affect terminal arborisation and interstitial branching. Interstitial branches likely require more deterministic solutions to trigger only one branch to innervate a distant brain region. Arborisation in contrast does not necessarily require specific branch initiation modes but could emerge from a high likelihood of stochastic splitting or collateral branch formation combined with contact-mediated stopping of growth.³⁴¹ While the filopodia-branching induced by PLPPR3 appears to be well suited to control interstitial branching, it could be nevertheless fruitful to analyse PLPPR3's effects on terminal arborisation. Specifically, the presented high abundance of PLPPR3 in distal regions of the axon, the lack of an effect on interstitial branch formation in layer II/III cells in vivo, and the described functions of PLPPR-family members in dendrite morphogenesis^{163,165,187} that depends more on arborisation, argues for functions of PLPPR3 in arborisation than interstitial branching.

The phenotypes of specific mediators of morphogenesis, such as PLPPR3, are often mild and easily compensated by parallel branch programs when compared to general mediators, such as tubulin, actin, or PTEN. However, they can enable experimental paradigms to unravel the exact coordination of branching programs during neuron morphogenesis as illustrated in chapter 5. Studies on narrow mediators of morphogenesis could, therefore, contribute to answering whether terminal axon branching is closer related to dendritic branching or axon interstitial branching or whether arborisation and interstitial branching are indeed regulated independently. And they could subsequently be targets to precisely study multifaceted phenomena such as cognitive processing or neurological disease.

6.4 CONCLUSION

In this thesis, I established PLPPR3 as a membrane-protein controlling axon-enriched filopodia and branch formation during neuron development. Mechanistically, PLPPR3 increases filopodia and branch abundance but not branch stability in a pathway with PI3K and PTEN. PLPPR3 function is likely regulated via its plasma membrane abundance, microdomain generation or localisation, and cell type or even axon-specific expression. Elucidating this narrow function of PLPPR3 suggested the existence of separately regulated branch morphogenesis programs that differ in their downstream maintenance.

In addition, I developed and optimised multiple experimental paradigms and semi-automated analysis strategies to study plasma membrane phosphoinositides and PLPPR3-function in cell lines and primary neuron cultures and generated a *Plppr3*^{-/-} mouse line using CRISPR/Cas9. In conclusion, my findings open multiple new directions and provide valuable tools to study the molecular control of neuron morphogenesis.

7 APPENDIX

7.1 Visualising membrane phosphoinositides	77
7.1.1 Benchmarking the sensitivity of PH-domain overexpression	77
7.1.2 Optimising sensitive and specific immunolabelling for membrane lipids	78
7.1.3 PIP3 accumulates differently in GABAergic and glutamatergic neurons	80
7.2 Image analysis tools	82
7.2.1 Filopodia and membrane localisation analysis cultured cells	82
7.2.2 Membrane recruitment of PH-domains	84
7.3 Fully automated branch classification in developing cultured neurons	86
7.3.1 Segmentation of neuronal processes and soma reconstruction	86
7.3.2 Classification of axon, dendrites, and branches	88
7.3.3 Comparison of segmentation and classification strategies	90
7.3.4 Evaluation of sensitivity to detect biological phenotypes	92

7.1 VISUALISING MEMBRANE PHOSPHOINOSITIDES

Phosphoinositide membrane lipids (PIPs) serve diverse signalling functions in cellular compartments.^{142,143} They differ by amount and location of phosphates on their inositol head group, creating seven distinct phosphoinositide species: three monophosphates (PI(3)P, PI(4)P, PI(5)P), two bisphosphates (PI(3,4)P₂, PI(3,5)P₂, PI(4,5)P₂) and one trisphosphate PI(3,4,5)P₃ (commonly abbreviated with PIP₃).

Distinguishing the configuration of individual phosphate groups on a sugar head group of a membrane lipid requires highly specific detection methods³⁴⁵. Thin-layer chromatography in combination with radiolabelling has been used for quantifying phosphoinositide species by the number but not the positions of phosphate groups on inositol rings. Recent developments of lipid mass spectrometry³⁴⁶ allow for the sensitive quantification of all subspecies simultaneously. However, localising the various PIPs in cells by these strategies requires robust purification of subcellular compartments and precludes studying microdomain localisation of PIPs. In this section I compare two microscopy-based methods of quantifying localised PIP abundance with respect to specificity, sensitivity, and applicability to cells with complex morphologies: cultured primary neurons.

7.1.1 Benchmarking the sensitivity of PH-domain overexpression

Cells initiate downstream signalling of distinct phosphoinositides by recruitment and local enrichment of effector proteins such as, in the case of PIP₃, AKT and PDK.^{142,143} These effectors contain specialised domains capable of distinguishing the head group configuration of different PIPs. The most characterised domains in this respect are FYVE- (Fab 1, YOTB, Vac 1, and EEA1) and PH- (Pleckstrin homology) domains. Membrane recruitment of GFP-tagged PH-domains, in the case of PIP₃ the PH-domains of AKT1, BTK and GRP1 (Figure 25A), is a widely used tool to characterise PIP₃ in cells.³⁴⁵

I expressed AKT1-GFP, PH(BTK)-GFP and PH(GRP1)-mCitrine (data not shown but it mirrors PH(BTK)-GFP) in N1E-115 cells and stimulated or inhibited PI3K activity for 2 minutes before fixing using Insulin or the GDC-0941 respectively (Figure 25). Even though membrane recruitment often enriches local density of PH-domain containing proteins, the intensity of none of the tested PH-sensors responded to treatments of PI3K-activity (Figure 25B). However, in these same cells it was possible to measure the successful manipulation of PI3K-activity via the phosphorylation status of AKT using a staining with AKT-pS473-antibody (Figure 25C). Overexpressing AKT, further increased the sensitivity for measuring PI3K-activity at the level of AKT-phosphorylation (AKT-GFP in Figure 25C).

Interestingly, the pAKT-activation was more pronounced in GFP-expressing control cells when compared to PH-domain overexpressing cells (BTK vs. GFP in Figure 25C), suggesting partial interference of downstream signalling when visualising PIP₃ using the PH-domain overexpression strategy. Overexpression of PH-domains has been described to stabilise PIP₃ in cells³⁴⁷, as well as interfere with downstream signalling by preventing binding of endogenous effectors.³⁴⁸ Interpretation of PIP₃-signalling measured by this strategy therefore requires careful selection of controls.

Membrane recruitment of PH(Grp1) and PH(BTK) – as measured by a newly developed semi-automated strategy further described in 0 – served as a reliable and sensitive readout of PI3K activity

in cultured cells (Figure 25D, $g_{\text{DMSO:Ins}} = 1.3$). The quantification of membrane recruitment in neurons is complicated additionally by the thin tubular shape of processes where membrane versus cytosolic localisation is more difficult to detect. While accumulation or clustering of PH domains along the length of an axon have been used to infer the localisation of PIP3 microdomains,⁵⁹ such accumulations could also come about by PIP3-independent accumulation of cytosolic material due to transport or degradation mechanisms. More sensitive quantification of PIP3 in neurons via the PH-domain overexpression method might be achieved by co-expression of a cytosolic marker or a PIP3-binding deficient PH-domain mutant and quantifying the ratio of PH-domain to cytosolic marker.³⁴⁸

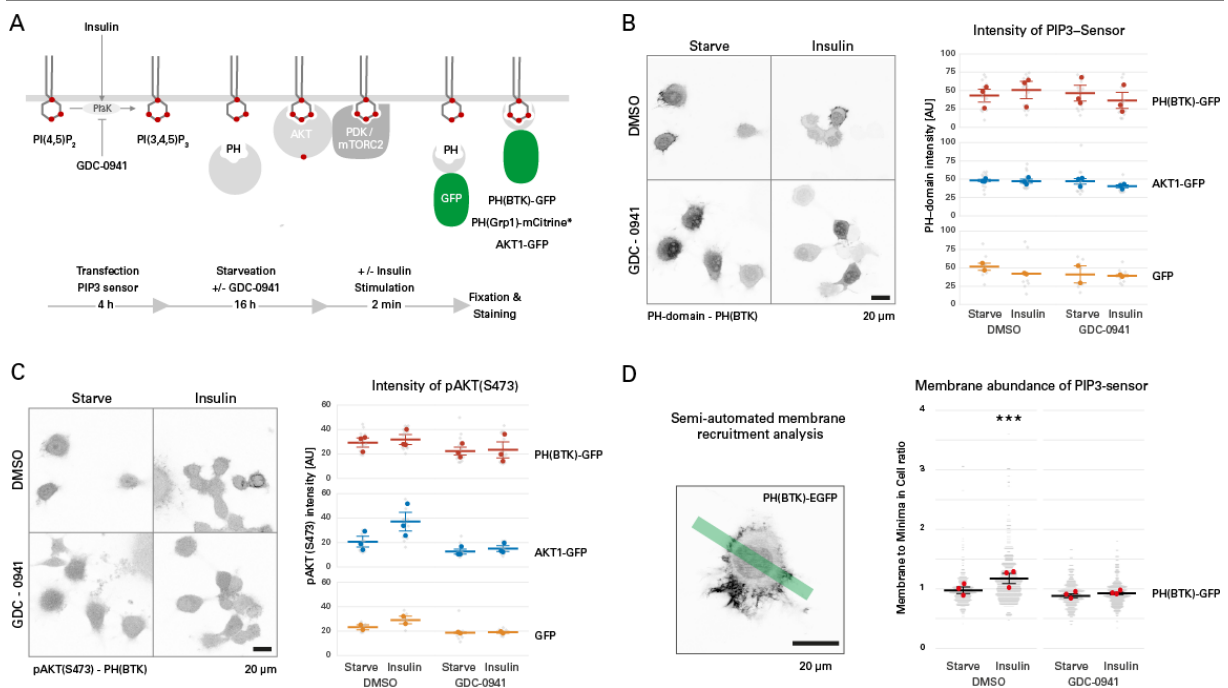


Figure 25: Membrane recruitment but not intensity of fluorophore-tagged PH-domains reports on PIP3 levels in cells. (A) Downstream signalling of PIP3 is mediated by recruiting PIP3-binding PH-domain containing proteins to the plasma membrane (AKT, PDK, mTORC2). Membrane recruitment of such PH-domains can serve as a readout for PIP3 abundance in cells. (B) Fluorescence intensity of GFP-tagged BTK-PH-domain or AKT1-GFP does not change upon stimulation or inhibition of PI3K-activity. (C) Stimulation and inhibition increase and decrease phosphorylation of AKT (S473) respectively. The pAKT increase is higher in GFP-transfected than in PH-domain expressing cells indicating interference of the PH-domain with downstream signaling. pAKT is detected more sensitively when overexpressing full-length AKT1-GFP. (D) Semi-automated analysis of membrane recruitment of PH(BTK)-GFP reliably reports on PI3K activity. Small grey dots indicate individual cells, colored dots indicate means per experiment. Error bars indicate standard errors of the mean between experiments. $n = 3$ experiments. Mixed model between experiments, post-hoc comparisons Holm-corrected, *** $p < 0.001$

7.1.2 Optimising sensitive and specific immunolabelling for membrane lipids

These challenges of visualising PIPs with the overexpression method, raise the question of why not immunolabelling them like commonly performed for assessing the phosphorylation status of proteins. While there are commercially available antibodies capable of distinguishing these minimal epitopes of just one phosphate on a sugar head group of lipids, standard fixation and labelling protocols do not preserve the localisation and abundance of lipids (Figure 26A). I therefore optimised a protocol developed for visualising PI(4,5)P₂ by Hammond et al, 2009³⁴⁹ to preserve PIP3 during immunolabelling (Figure 26B). Briefly, the optimised protocol uses a cytoskeletal stabilising buffer (PHEM-buffer) and fixes the cells using paraformaldehyde and glutaraldehyde to stabilise cortical actin and therefore

membrane composition. It furthermore permeabilises the cells using saponin to retain PIPs in the membrane. To prevent diffusion of lipids, all steps after fixation, including PIP3-detection, are performed on ice before fixing the PIP3-probe (a protein) and performing a standard immunodetection of the probe. I used either a specific monoclonal antibody (Echelon) or a GST-tagged purified PH-Grp1 domain subsequently visualised using anti-GST-labelling as a PIP3 probe.

The localisation of PIP3 using this protocol was specific to plasma membrane compartments (Figure 26C, lower panel), while standard immunolabelling techniques using the same PIP3-probes produced an artefactual punctate pattern at and below the plasma membrane. Performing the same specificity test as for PH-domain overexpression in the previous experiment, PIP3-staining specifically and sensitively detected PI3K activation and inhibition (Figure 26D, $g_{\text{DMSO:Ins}} = 3.2$). The sensitivity (effect size 3.2) was considerably higher than using membrane recruitment of overexpressed PH-BTK-GFP (effect size 1.3) to quantify PIP3 abundance. Furthermore, PIP3-labelling can be quantified with an easier readout of only intensity rather than membrane translocation.

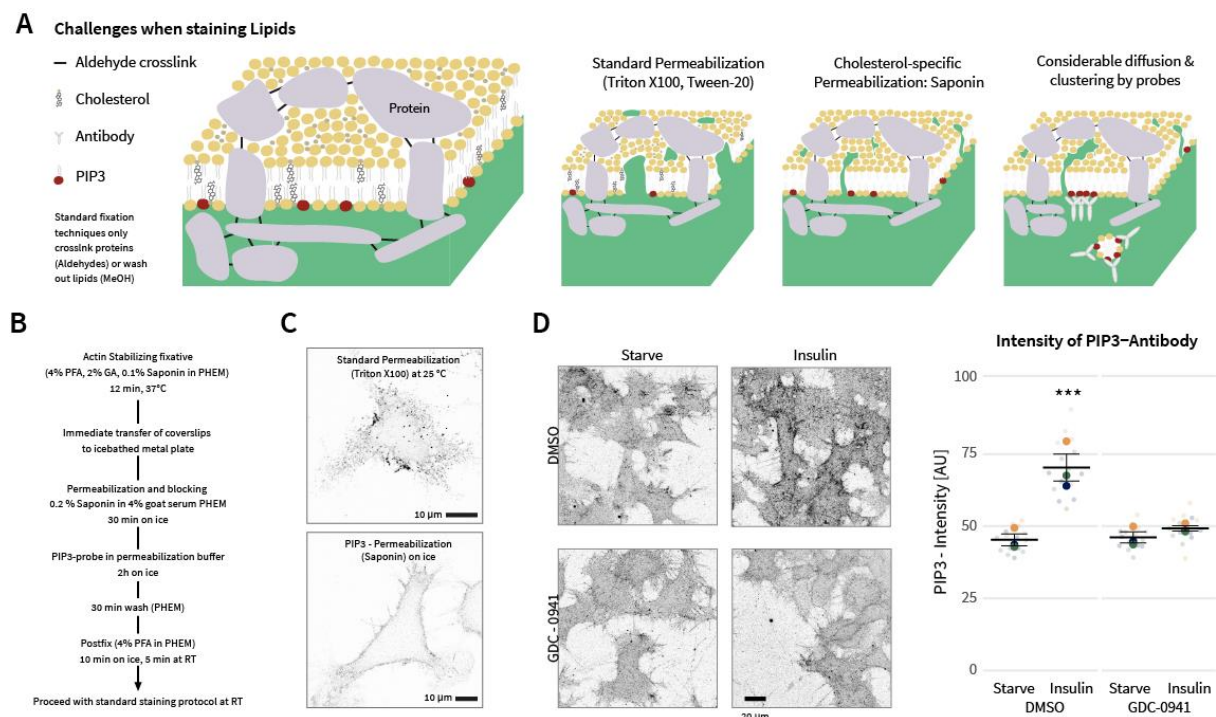


Figure 26: Optimised staining protocol specifically and sensitively detects PIP3. (A) Challenges when staining lipids: Commonly used aldehyde fixation crosslinks amino groups (mostly proteins indicated in grey), while lipids still stay diffusible. Commonly used permeabilisation techniques (to get probes inside of the cell to label proteins and inner-leaflet lipids) like Triton X100 or Methanol unspecifically wash out lipids and therefore alter the lipid composition. Saponin specifically removes cholesterol from membranes. Finally, antibodies tend to cluster and relocalise unfixed antigens, precluding an exact localisation of PIPs. (B) Optimised fixation and labelling protocol based on Hammond et al., 2009 adapted to PIP3.³⁴⁹ (C) Comparison of standard labelling techniques and the optimised protocol in confocal planes of N1E-115 cells. Note the artefactual clustering of PIP3-signal using standard techniques. (D) Sensitivity and specificity of PIP3-staining on PI3K stimulated or inhibited N1E-115 cells. Small dots indicate fields of view, large dots and color indicate experiments, error bars indicate standard error of the mean. $n = 3$ experiments. Mixed model between experiments, post-hoc comparisons Holm-corrected, *** $p < 0.001$. Panel D was published as part of Nieuwenhuis et al, 2020, *Embo Mol Med*.²⁴⁵

7.1.3 PIP3 accumulates differently in GABAergic and glutamatergic neurons

Due to the easier quantification and interpretability, and the higher sensitivity when compared to the overexpression protocols, I applied the immunolabelling protocol to label PIP3 in primary hippocampal and cortical neurons. The protocol sensitively and specifically labelled PIP3 also in PTEN-deficient neurons stimulated with PI3K-activating growth factor BDNF and failed to do so where neurons were pretreated over night with the PI3K-inhibitor GDC-0941 (Figure 27A&B). Interestingly, baseline levels for PIP3 appeared low in PTEN-deficient neurons as untreated conditions hardly showed more PIP3-labelling when compared to PI3K-inhibited neurons. Corroborating this minimal change in PIP3 levels in neurons upon PI3K-inhibition, also stimulation of wild-type neurons with BDNF hardly increased PIP3 levels, while PTEN-deficient neurons showed a time-dependent increase in PIP3 (Figure 27C&D). Whether PIP3 is transiently elevated in wild-type neurons only very early (2 min timepoint) after BDNF-stimulation, requires more repetitions. But these data suggest that the labelling protocol works in neurons and that PIP3 levels are more tightly controlled in neurons when compared to cell lines.

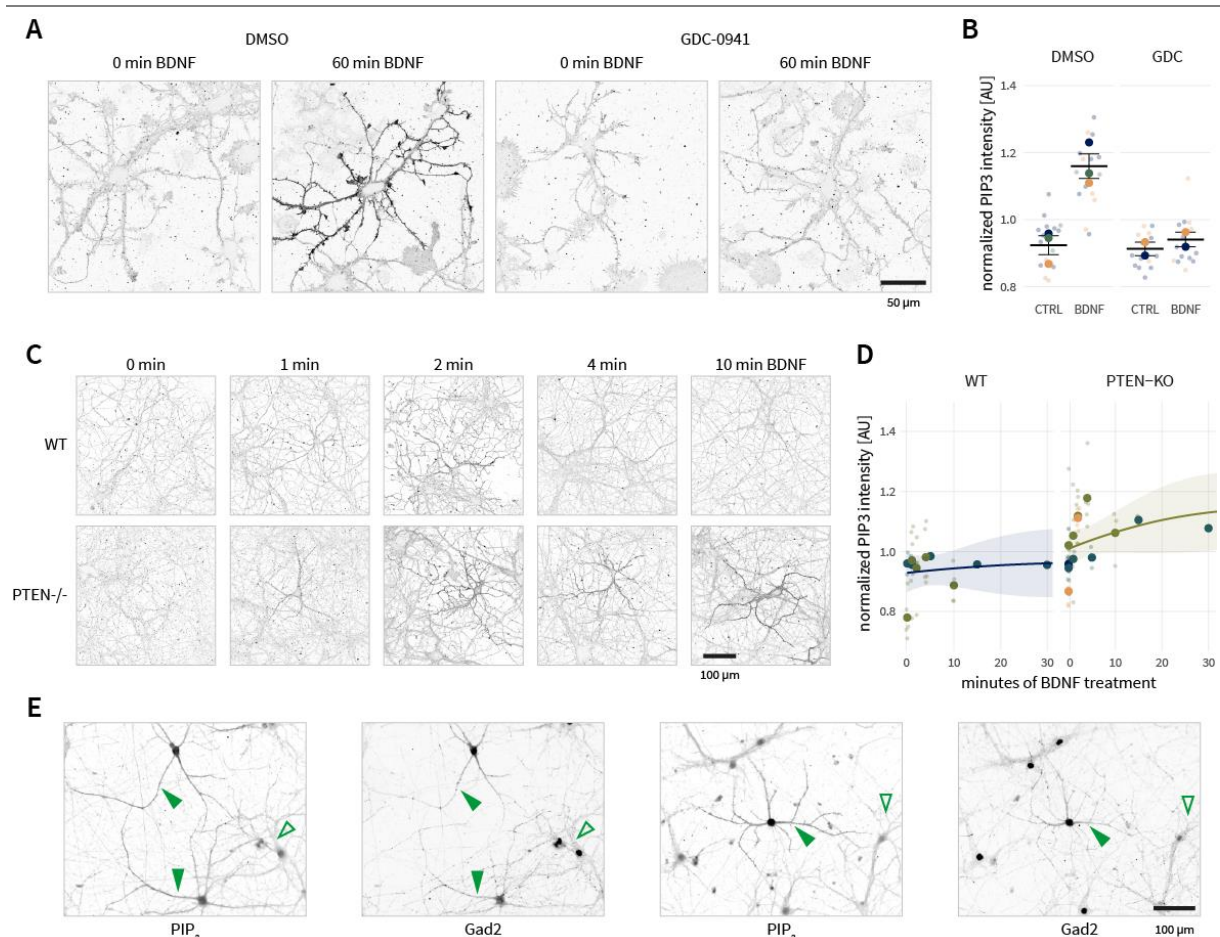


Figure 27: Immunolabelling reliably visualises PIP3 in neurons. (A) Specificity test for PIP3-labelling in PTEN-deficient (DIV6) neurons treated with BDNF, the PI3K-inhibitor GDC-0941 or the combination. (B) Quantification of PIP3 response to these interventions. $n=3$ experiments. (C) Comparison of BDNF-mediated PIP3 increase over time in wild-type versus PTEN deficient neurons. Note the enrichment of PIP3 signal only in individual cells in PTEN^{-/-}. (D) Quantification of the PIP3 intensity shows general trend for increased PIP3 levels over time (with large variability) only in PTEN deficient neurons. (E) High-intensity PIP3 staining after BDNF-stimulation is found in Gad2-enriched cells (closed arrows), non-Gad2 positive cells are low in PIP3 (open arrows). Note: due to bleedthrough, the Gad2-channel also includes signal for nuclear localised RFP (the probe reporting infection of CRE for PTEN-deletion). Dots and colour indicate individual experiments, error bars represent SEM, gray ribbon in D represents the 95% confidence interval.

Interestingly, even in PTEN-deficient neurons, PIP3 seemed to accumulate after BDNF-stimulation only in a subset of cells. Co-labelling cells for PIP3 and the GABA-synthesising Glutamate decarboxylase 2 (Gad2), as well as the comparably low percentage of PIP3-accumulating cells in cortical and hippocampal cultures suggests that these cells are GABAergic interneurons (Figure 27E).

This raises interesting questions about the regulation of PI3K-signaling in glutamatergic compared to GABAergic cells. Does BDNF only increase PIP3 in GABAergic cells? The expression of the BDNF-receptor TrkB in adult cortical neurons is higher in GABAergic cells, and especially hippocampal glutamatergic neurons seem to express low levels of TrkB.⁹⁶ Nevertheless, BDNF has been shown to affect glutamatergic neurons,³⁵⁰ suggesting a differential downstream signaling of PIP3-dominated effects in GABAergic and non-PIP3-dominated signals in glutamatergic neurons. In this respect it is also interesting to note, that the expression of Akt1, a major downstream effector of the PIP3-side of TrkB correlates well with the expression of TrkB in GABAergic cells, while not so well in glutamatergic cells (data again from adult single-cell transcriptomic study as discussed above and in Figure 1).⁹⁶ Alternatively, PTEN-deficiency could target GABAergic cells differently to glutamatergic cells. In this respect it is interesting to note that PTEN expression appears higher in adult glutamatergic neurons compared to GABAergic.⁹⁶

Future experiments using different PI3K-stimuli (as an example, Fgf-receptor 1 expresses strongly in glutamatergic compared to GABAergic neurons) could test whether this PIP3-increase is BDNF-specific or whether PI3K-signaling in general is regulated differently in glutamatergic neurons. In any case, this differential PIP3-accumulation in glutamatergic vs. GABAergic neurons opens interesting questions regarding the PI3K/PTEN contribution to neurodevelopmental diseases with hypothesised imbalance of excitatory and inhibitory signalling such as autism spectrum disorder.¹²³

Regarding the sensitivity of PIP3-probes in cells, several groups have proposed modifications of the overexpression strategy. These improvements mainly facilitate the sensitive quantification of membrane versus cytosol recruitment by either employing FRET,³⁴⁸ or microinjecting PH-domains tagged with solvatochromic fluorophores that report membrane recruitment by a wavelength shift.²⁸⁵ While all the PH-membrane recruitment techniques allow for live-monitoring of PIP3-dynamics, they have been shown to interfere more with endogenous PIP3-signaling than immunolabelling strategies on fixed cells.³⁴⁷ Adaptations of the immunolabelling strategy have focused on immobilising membrane lipids while still retaining the possibility to label the internal leaflet of the plasma membrane or increasing signal intensity. Strategies include freeze-fracture electron microscopy,³⁵¹ quantum-dot labelled PH-domains²⁸¹ or feeding cells with chemically modified fixable lipids.³⁵²

7.2 IMAGE ANALYSIS TOOLS

To facilitate high throughput screening of PLPPR3-mutants, I developed semi-automated image analysis strategies using a combination of ImageJ macros followed by data analysis in R. This section will describe the general idea and usage and discuss advantages and caveats of two elaborated analysis pipelines. All macros and scripts are publicly accessible under <https://github.com/jo-fuchs>.

7.2.1 Filopodia and membrane localisation analysis cultured cells

All filopodia density and membrane abundance measurements of *Plppr3* effects in cultured cells in Chapter 2 were performed with the ImageJ macro described below (https://github.com/jo-fuchs/Filopodia_Membrane_recruitment). It requires confocal images of a cell labelled for the protein of interest and an independent membrane marker, and optionally can include information from a nuclear staining.

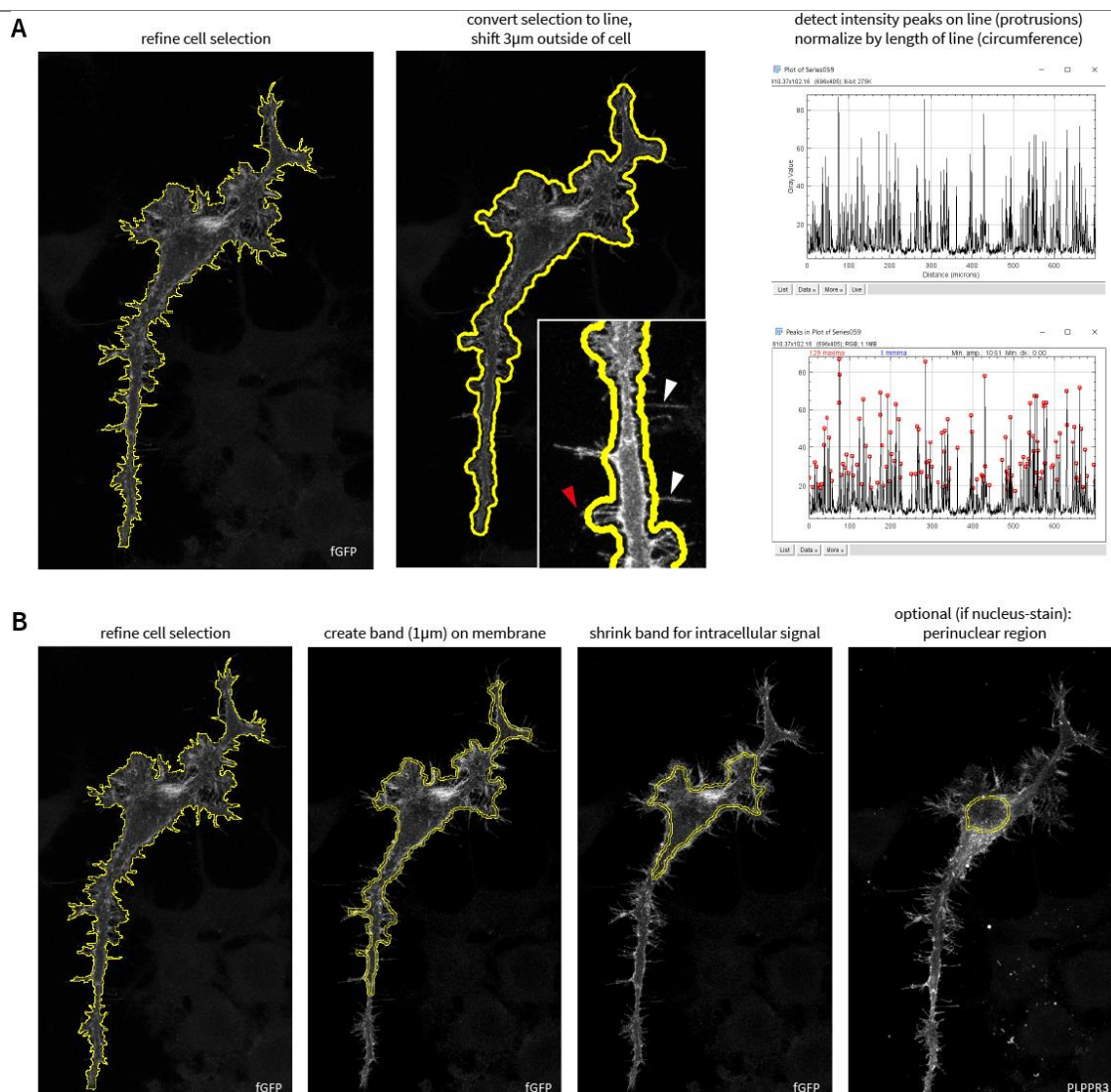


Figure 28: Filopodia and membrane recruitment analysis: (A) Filopodia detection begins by refinement of a cell area selection. This area is converted to a 1 μ m thick line and shifted outside of the cell to then detect peaks of the resulting intensity profile as protrusions. Dense protrusive areas are sometimes detected as bulges of the cell surface (red arrow, circumference overestimated) but protrusions are nevertheless registered (white arrows). (B) Membrane abundance is quantified by creating selection band around the membrane and shrinking the selection 3 μ m inside for intracellular signal. If nuclei are visualised, the macro optionally finds and measures the perinuclear area by shifting a selection band outside of the nuclear selection.

The macro sequentially quantifies filopodia density of cells and membrane abundance of a protein of interest in a semiautomated technique that only requires selection of the cell of interest. For quantification of filopodia density (Figure 28A), the cell selection is refined using the cell membrane channel by median filtering followed by a Huang threshold (on a duplicate of image) and removing small particles by particle analysis. To reduce details introduced by small protrusions and noise for a less overestimated quantification of cell circumference, this selection will be opened (shrinking with consecutive dilation of selection) and subsequently converted to a line. To detect membrane protrusions, intensity peaks are detected on an intensity profile of this line using the detect peaks function of the BAR plugin³⁵³ of ImageJ with an adaptive threshold (median intensity on line) and a minimal peak distance of 1.5 μm . The filopodia density is calculated as the number of peaks divided by cell circumference as measured by the length of this line. Comparison with manually measured filopodia density shows generally similar trends but a tendency for more filopodia detections, slightly overestimated circumferences and slightly more variability than manual measurements (not shown). Filopodia densities measured by this macro should only be interpreted after semiautomatically measuring many individual cells (> 15-20 per condition). Furthermore, the macro is more sensitive to compare biological treatments within an experiment than for detecting absolute density of filopodia.

To quantify membrane abundance of a target protein (Figure 28B), the refined selection from above is compressed by 1 μm and converted to a selection band of 1 μm thickness to match the plasma membrane signal. For highest sensitivity of membrane intensity to internal membrane ratio, the intracellular signal is measured close to the plasma membrane (internal membrane signals tend to be lowest in peripheral cell areas, as visible in the right panel of Figure 28B). To this end, the membrane selection is compressed by 3 μm . To secure against fragmentation of the internal selection following shrinking, only large enough areas are kept. In case of elongated narrow cells this is sometimes not possible, as these elongate thin areas often fragment to many small areas after shrinking. The intensities of membrane and intracellular band are subsequently measured in the channel of the protein of interest as specified by the user.

For many ER-based proteins, the signal intensity is strongest around the nucleus (perinuclear). In case the comparison of membrane intensity to perinuclear area is more interesting for a biological question, a nuclear stain can be used to find a selection for the perinuclear area in this macro: the nucleus is detected by median-filtering and Moments-threshold (on a duplicate of the nucleus channel of the image) and removing small particles by particle analysis. Subsequently, a selection band around the nucleus is created and used to measure the intensity of the protein of interest in its channel. In case of multinucleated cells, a convex hull around all nuclei in the cell selection is treated as the 'relevant nucleus' for perinuclear band generation.

All membrane abundance quantifications in Chapter 2 were based on the membrane to internal membrane intensity ratio. The reliability of the measurements has been validated by manually scoring the plasma membrane abundance of the PLPPR3 catalytic-centre mutants (section 2.3.3, Figure 9) giving same trends for the quantified mutants when comparing this ratio with the fraction of membrane-recruited cells / total cells.

7.2.2 Membrane recruitment of PH-domains

For more localised accumulations, the total plasma membrane vs. cytosol ratio as provided above would not be a sensitive or meaningful readout. Therefore, for PH-domain accumulations used to report plasma membrane PIP3 (Section 7.1.1), membrane recruitment was determined using a line profile across responding parts in a cell followed by an analysis pipeline including ImageJ and R (https://github.com/jo-fuchs/PH_domain_membrane_recruitment).

The manual part of this analysis comprises drawing lines across all cells on a confocal stack in the z-plane that best describes the membrane recruitment of a protein of interest (PH-domain) and storing them in the ImageJ ROI manager. The recommended thickness of this line is above 10 px to reduce the influence of noise on subsequent measurements. A macro then exports the intensity profiles of the line stored in ROI-manager as individual txt-files.

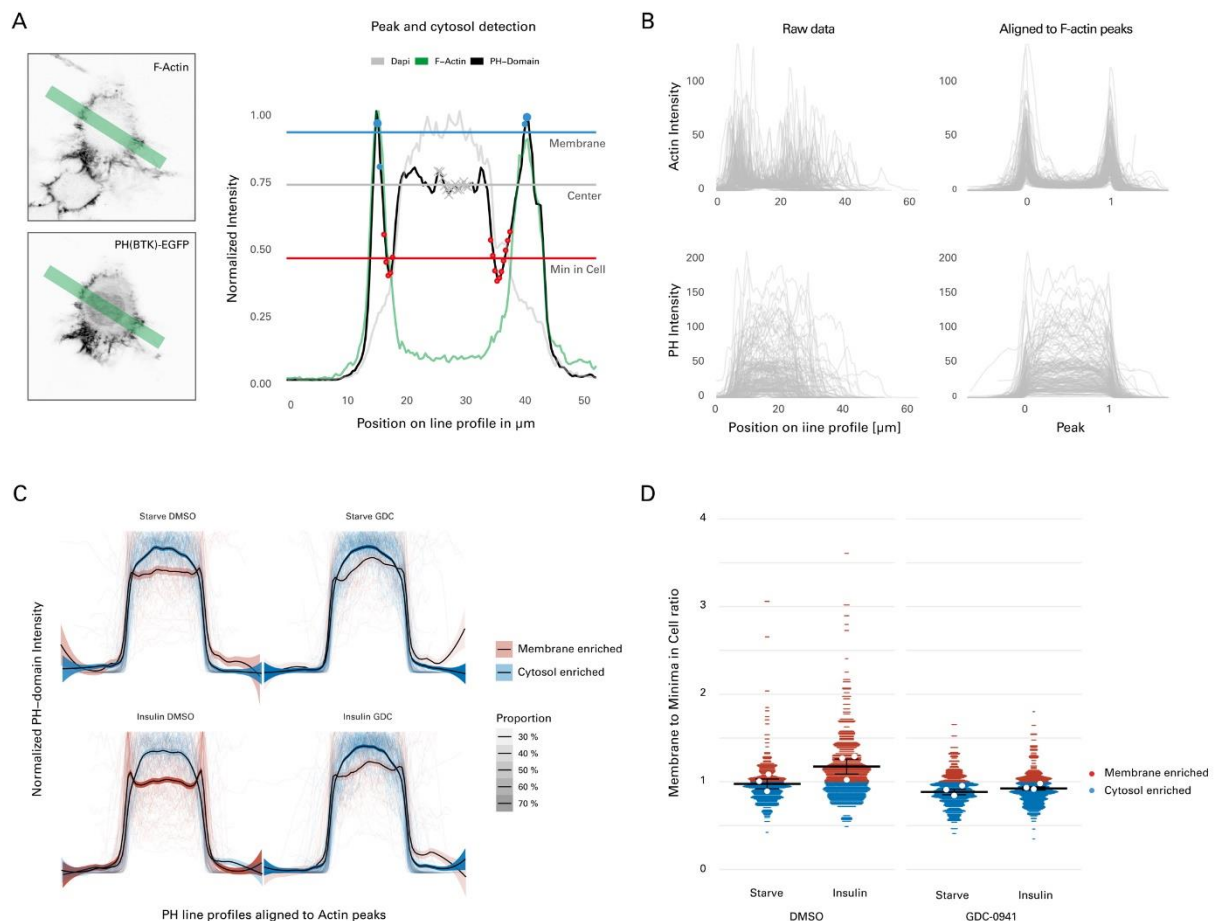


Figure 29: PH-domain membrane recruitment analysis. (A) Line profiles reliably report for membrane recruitment of PH-domains. Cell surface visualised by F-actin, cell nuclei by Dapi. Line profile comparison shows overlap of F-actin and PH-membrane peaks, and localisation of PH-domain to nucleus. The analysis allows for automated quantification of membrane to cytosol ratio by the cytosol defined as the center area between the actin peaks or as the minimal region of PH-domain signal in the cell to avoid confounding by nuclear localisation of probes. (B) Aligning individual line profiles (grey lines) by position of the two largest F-actin or membrane marker peaks allows for more precise estimation of membrane recruitment variability between cells. (C) Visualising trend lines for membrane enriched (red) versus cytosol enriched (blue) cells captures phenotypes of pharmacological treatments and also variability between cells (further described in section 7.1). (D) Ratio of PH-BTK membrane intensity and minimal intensity in cytosol reliably and sensitively reports on PIP3 levels.

Further processing uses R for quantifying the membrane abundance compared to the cytosolic signal defined as centre area between the cell membrane peaks – as defined by either a membrane marker or cell cortex enriched F-actin. As some PH-probes (e.g., BTK(PH)-GFP) enrich also in the nucleus, cytosolic signal is better captured as the ‘minimal signal’ in cells. (Figure 29A).

For a better visualisation of cell to cell variability, this R-script also allows to overlay line profiles by aligning the PH-domain signal to the two largest F-actin peaks (Figure 29B), and normalising to the maximal intensity of the PH-domain probe (Figure 29C). Classification of these individual traces by their membrane to cytosol ratio (Figure 29D) and plotting the local average (loess) with 95% confidence intervals allows for a more realistic visualisation of the variability between cells in various biological treatments when compared to traces of individual cells. Indeed, the membrane enrichment of PH-domains was not dramatic, when comparing multiple cells rather than only the highest responders. Nevertheless, it sensitively and specifically reported pharmacological manipulations of PI3K activity (Figure 29D, experiment described in Figure 25, section 7.1.1).

7.3 FULLY AUTOMATED BRANCH CLASSIFICATION IN DEVELOPING CULTURED NEURONS

Quantification of the morphology of cultured neurons as performed in Chapter 4 is a powerful tool to refine the exact structure of neuron development and their contributing proteins. Unfortunately, specifically axon morphology is mainly quantified manually in the field (using tools like NeuronJ³⁵⁴ as for the experiments presented in Chapter 4) due to the lack of accurate and time-saving automated solutions. To facilitate screening of PLPP3-mutants and pharmacological treatments in cultured neurons, I collaborated with Dr. Amin Zehtabian from the laboratory of Prof. Helge Ewers (Biochemistry, Freie Universität Berlin) to develop a fully automated analysis tool capable of providing the desired readouts. The strategy was developed in close collaboration and the initial implementation of the software in MATLAB was executed by Dr. Amin Zehtabian. I subsequently refined and recoded the classification and parts of the segmentation step as well as validated the software on manually analysed neurons from section 4.2.2 and 4.3.2 of this thesis. Results and figures from this section are currently being prepared for submission.

The developed tool first detects neuronal processes and the soma of individual neurons on epifluorescence images or intensity-projections of confocal images (in steps referred to as 'segmentation' and 'soma reconstruction'). Subsequently, the exact borders of the soma are detected, and processes are classified as axon or dendrite with their respective branches. The final step measures individual lengths of each classified process as well as summary statistics per neuron.

7.3.1 Segmentation of neuronal processes and soma reconstruction

Neuronal processes are tubular structures of similar diameter. MATLAB's `fibermetric` function that uses Hessian-based multiscale filtering to detect vessel-like structures on images,³⁵⁵ also enhances neuronal processes well on our images (Figure 30A&B) if provided with a reliable estimate of neurite diameter. Default thickness is set to 1 μm but can be specified by users according to the exact neuron type in question. The tubule-enhanced image is subsequently binarised by thresholding.

As edges introduced by stitching of images are also often mis-detected as neurites, an artifact-removal step deletes all perfectly horizontal or vertical stretches of the image that exceed 300 pixel in length. An optional gap-bridging step can be used to repair incomplete segmentations due to low signal to noise or varying thickness of processes. It connects the closest endpoints of separate objects on an image that are below a maximal allowed gap size by extending an algorithm described in the MATLAB-user forum (https://de.mathworks.com/matlabcentral/answers/219818-binary-image-edge-linking#comment_289138). Gap bridging can successfully reconnect low-intensity protrusions but also sometimes creates artifacts as visualised in the small insets in Figure 30B. Therefore, the gap size should be chosen carefully and optimised to the specific images.

This enhancement of tubular structures detects neurite morphology well but fails to find the exact extent of the cell body. The soma is subsequently reconstructed either by filling enclosed structures in the detected neurite skeleton or, if unsuccessful, by subsequent intensity thresholding of the raw image (Figure 30C). The filling strategy begins with finding soma candidate regions where filled regions in the skeleton overlap most with an intensity thresholded image. The two largest candidate regions

are dilated and used to select the subregion of the skeleton most likely to contain the soma. If filling in only this region increases the size of the largest object on the image by over 1%, it is accepted as the soma. Otherwise, the soma is found by a thresholding strategy that first finds candidate regions based on overlap of intensity threshold and skeleton. The largest candidate region is used to select the soma by intensity thresholding.

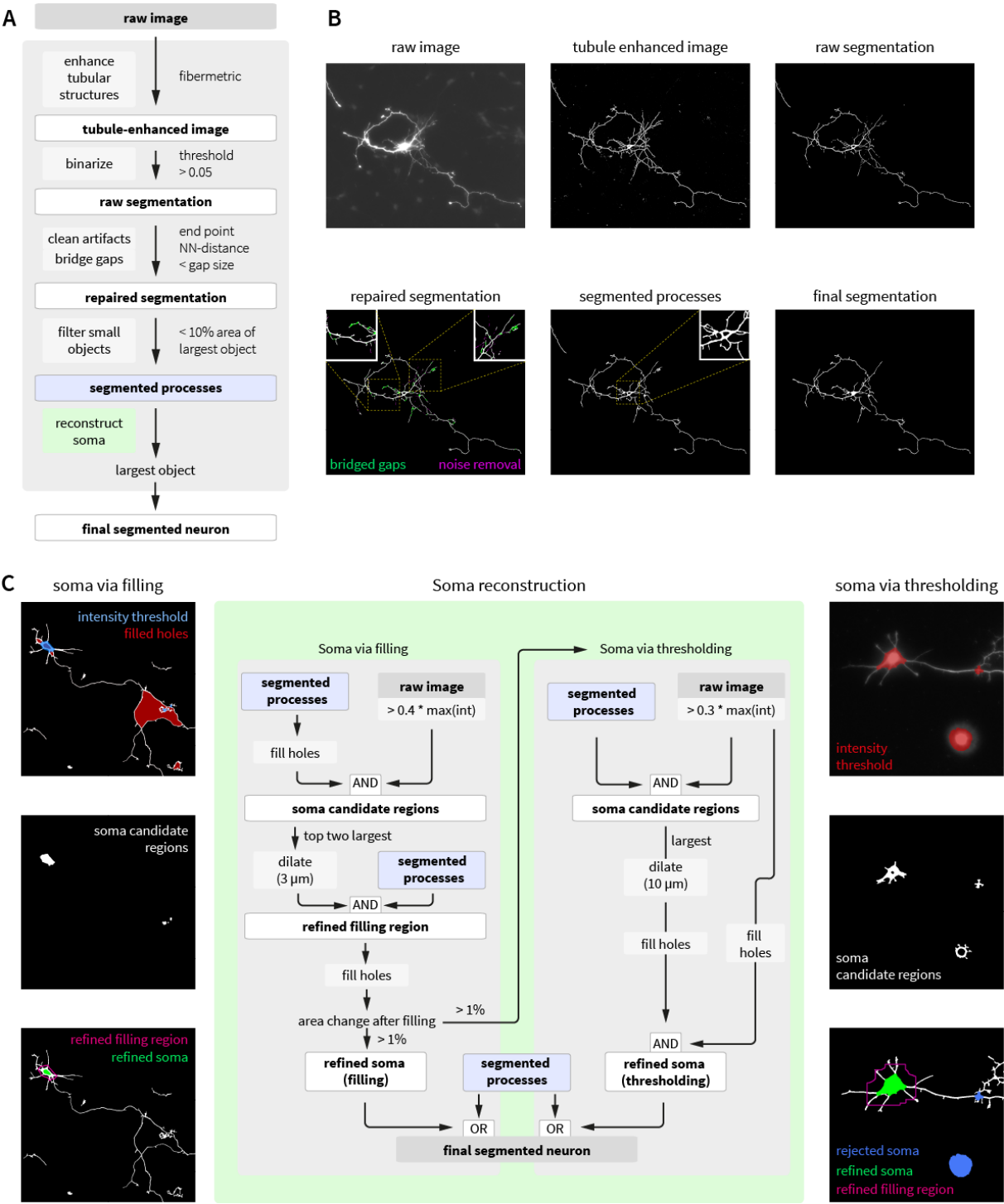


Figure 30: Segmentation strategy for epifluorescence images of GFP-transfected cultured neurons. (A) Workflow of segmentation algorithm with example images for each step in (B). (C) Soma reconstruction via filling of candidate regions defined by intensity thresholding or by intensity thresholding of raw image. Figure in preparation to submission.

7.3.2 Classification of axon, dendrites, and branches

The classification step (Figure 31A) begins with a detection of the exact outlines and area of the soma using a threshold of area to bounding box. Subsequently, the segmented image is transformed to a skeleton of 1px-thick paths and paths coinciding with the soma are removed. On this image, processes originating from the soma are detected and classified as axon (the longest path) and dendrites (remaining paths). Branches are detected iteratively starting with primary branches of the axon, followed by as many higher-order branches as are detected before proceeding with the same sequence for dendrite branches. The iterative branch detection has a hard cap of maximal 10 orders of branches, however most neurons do not exceed 4 orders of branches.

At the core of this neuron-classifier is a multifunctional ‘find paths’ algorithm (Figure 31B). From any given start point (selection discussed below) it will find the longest connected path based on the geodesic distance transform from the start point. The geodesic distance transform pixelwise counts the distance of any point on a connected path to its origin.³⁵⁶ Unconnected parts of the skeleton are labelled as infinitely distant. If the maximal distance from a start point is reached at an endpoint of the analysed skeleton, it is subtracted from the geodesic distance transform from that endpoint. The minimum of the difference of both transforms gives the direct connection (Figure 31C).

If the skeleton contains circular structures, the maximal geodesic distance is often not found on an endpoint. In such cases, circular structures are removed by back-tracing from the maximally distant point to the branching point that gives rise to the circular structure. Subsequently the connecting pixel of one of the two branches is deleted and the path detection for the given start point is restarted. If the length of this path surpasses a minimal length threshold, it is stored as a preliminary classified path, otherwise both start- and endpoints are deleted, and the detected path is removed from the currently analysed skeleton. This ensures following refining steps are repeated only on relevant parts of the skeleton. Often, the classified paths in preliminary set overlap with each other. Therefore, in case overlap is detected, the longest path is transferred to the classification result and removed from the skeleton to avoid detection when reclassifying the other paths. All remaining start points are iteratively reclassified until no further overlap is detected.

Start points on the soma are defined as morphological endpoints of the soma that overlap with the refined skeleton lacking the soma parts (Figure 31D). Start points on any given process or set of processes for subsequent branch detection are found as the difference of end- and branchpoints before and after removing the given process from the skeleton (Figure 31E).

The general strategy of this classifier is to iteratively remove classified parts from the skeleton. This avoids overlap between classified paths and speeds up classification with every iteration. The minimal length threshold allows for a detection of branches independently of branch precursor structures. Furthermore, in contrast to morphological branch-point detection, the length thresholding is less susceptible to noise and tortuous paths of the skeleton that often give rise to minor processes of only few pixels in size. In case branch precursor structures are of interest, the minimal length threshold can be adjusted and potentially combined with a filter for maximal protrusion length to distinguish branches later.

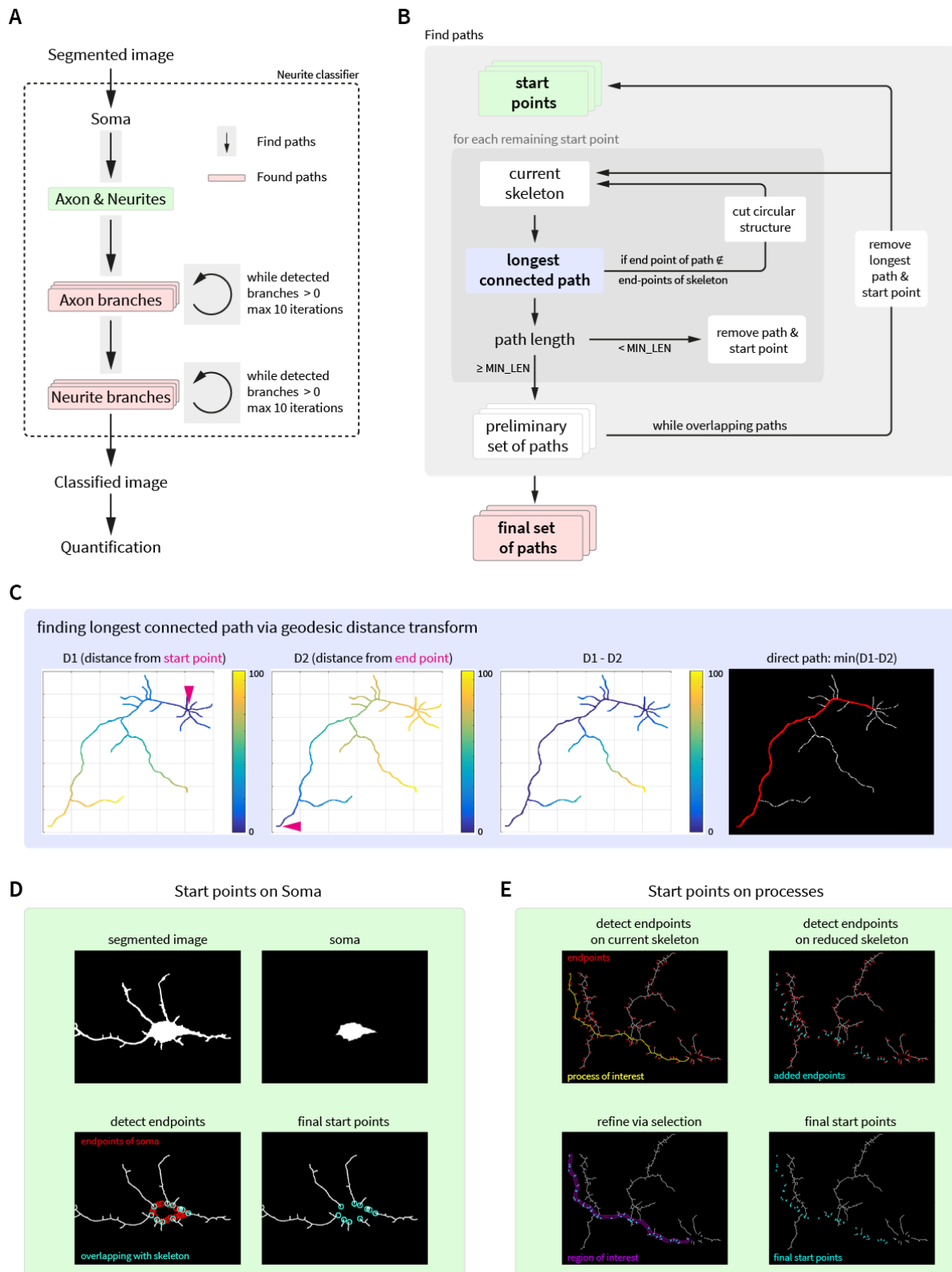


Figure 31: Classification strategy of segmented images. (A) General classification workflow. After classification of the soma region, one function ("find paths") iteratively proceeds to detect axon and dendrites, their primary and subsequently higher-order branches. (B) Architecture of find paths algorithm. Each start point (as found in D & E), uses the geodesic distance transform to find the longest connected path. For robust and accurate detection, circular structures are fixed and overlaps are resolved during the classification. (C) The minimum of the difference of geodesic distance transforms finds the direct connection between two points. (D) Detection of start points for path detection on soma. (E) Detection of start points on processes. Figure in preparation to submission.

7.3.3 Comparison of segmentation and classification strategies

To evaluate, the tool was tested on the manually analysed neurons described in sections 4.2.2 and 4.3.2. I compared the reliability, accuracy, and speed of different versions during development: v02 refers to the original segmentation algorithm by Dr. Amin Zehtabian; v03 refined the soma-reconstruction and noise removal of stitching artifacts, v05 introduced additional gap-bridging. The original classifier was only tested with v02 of the segmentation algorithm on a random subset of the data due to the long processing duration discussed below.

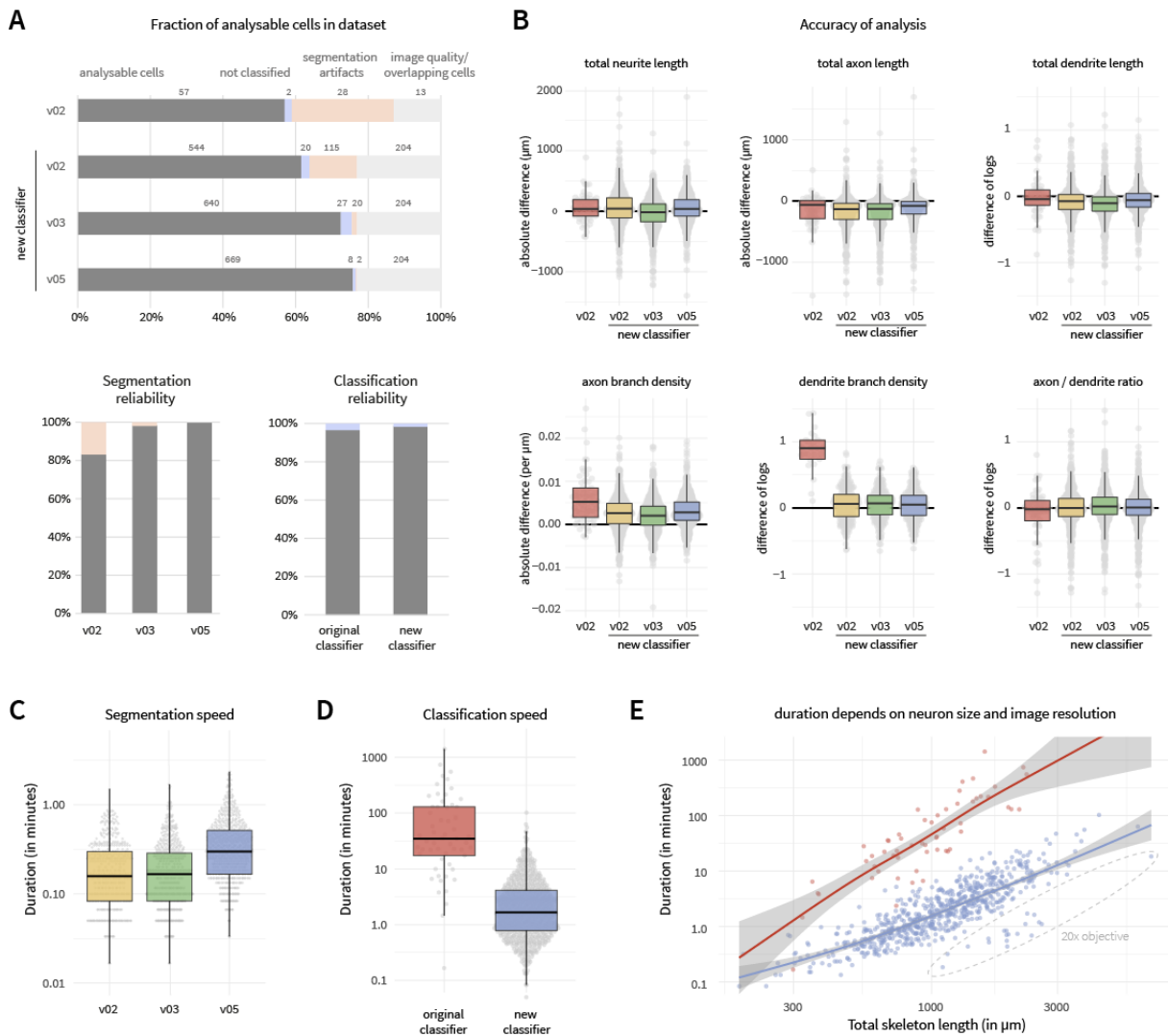


Figure 32: Comparison of segmentation and classification strategies on a manually analysed dataset of neurons (section 4.2.2 and 4.3.2). (A) Fraction of analysable cells, segmentation and classification reliability using different strategies. (B) Comparison of quantitative readouts generated from segmentation and classification algorithms to manual quantification. (C) Duration of segmentation algorithms. Bridging gaps by connecting endpoints (v05) adds approximately 8 sec per neuron. (D) Duration of classification algorithms. New classification strategy is an order of magnitude faster (median original: 35 min, median new: 1:40 min). (E) Duration of classification versus total length of neurons. Analysis time scales exponentially with neuron size. Measurements in C-E are on logarithmic scales, individual dots indicate individual neurons. Compared strategies: v02 = original segmentation algorithm developed by Dr. Amin Zehtabian; v03 = modified artifact removal and soma reconstruction described above; v05 = v03 with added gap bridging. Original classifier as developed by Dr. Amin Zehtabian, new classifier uses a completely refined classification algorithm as described above.

The analysed dataset comprised 883 epifluorescence images of cultured DIV5 hippocampal neurons transfected with GFP. As the automated analysis strategy is only length- and connectivity-based, the tool is unable to distinguish overlapping cells or staining artifacts connected to the neuron of interest. Therefore 204 images were removed (due to low signal-to-noise ratio or due to multiple overlapping cells) prior to submitting them to the batch analysis (Figure 32A). Users of the tool are therefore advised to adjust labelling and imaging settings accordingly to produce a high ratio of sparsely labelled healthy cells that do not overlap.

Of the remaining 679 neurons, all were segmented and analysed with the new classifier. For the original classifier, only a set of 100 neurons was random sampled due to the long duration of the classification (Figure 32A top). The original segmentation (v02) reconstructed approximately 80% of neurons without obvious artifacts such as missing somata or large stitching artifacts (Figure 32A bottom left). The refined segmentation without (v03) or with gap bridging (v05) captured most neurons without large defects (98-99%). Classification was scored unsuccessful only if individual processes were not classified at all. Both classifiers presented with a very high reliability to produce results (Figure 32A bottom right). The refined versions of the segmentation algorithms allowed for the automated analysis of more images than the original segmentation.

The accuracy of segmentation and classification was determined by comparing quantitative measurements of the automated and manual datasets between individual neurons (Figure 32B). All segmentation and classification versions very closely matched total lengths of the complete skeleton, of the axons and the dendrites. Dendrite branch density of original classifier was overestimated due to a lacking check for a minimal length for dendrites. Axon branch density very closely matched manually measured densities, although all versions slightly overestimate. Gap-bridging (v05) slightly reduced the absolute deviation to the manual quantification as visible by a reduced variability in Figure 32B.

All analyses were performed on a laptop (Intel(R) Core(TM) i7-8565U CPU @ 1.80GHz, 1.99 GHz, 16 GB RAM, Windows 10 64bit system) and are therefore likely faster on more powerful desktop workstations. Nevertheless, the median time per segmentation was in the range of few seconds per image: v02: 9 sec; v03: 10 sec; additional gap-bridging (v05): 18 sec per image (Figure 32C). The original classifier, however, took 35 min per neuron (median) with individual neurons classifying for 16 hours. The recoded classifier took 1:40 min per neuron (median). For this reason, only a sample of 100 neurons was analysed with the original classifier and the reliability and accuracy estimates for the original classifier in Figure 32A&B are only partially comparable to the results on the full dataset with the new classifier.

The durations of both segmentation and classification scale exponentially with the length of the neuron and size of the image (Figure 32E). Therefore, lower resolution images (labelled 20x objective instead of the original 40x objective images in Figure 32E) are classified orders of magnitudes faster while large images or neurons can easily take over an hour even for the new classifier. The tool is mainly suited for early developmental stages when neurons are still small.

7.3.4 Evaluation of sensitivity to detect biological phenotypes

The final evaluation of accuracy and sensitivity of the tool was performed using version 5 of segmentation in combination with the new classifier on the neurons manually analysed for sections 4.2.2 (DIV5 Wt versus *Plppr3*^{+/-} and *Plppr3*^{-/-}) and 4.3.2 (DIV5 Wt, *Plppr3*^{-/-} with or without shPTEN).

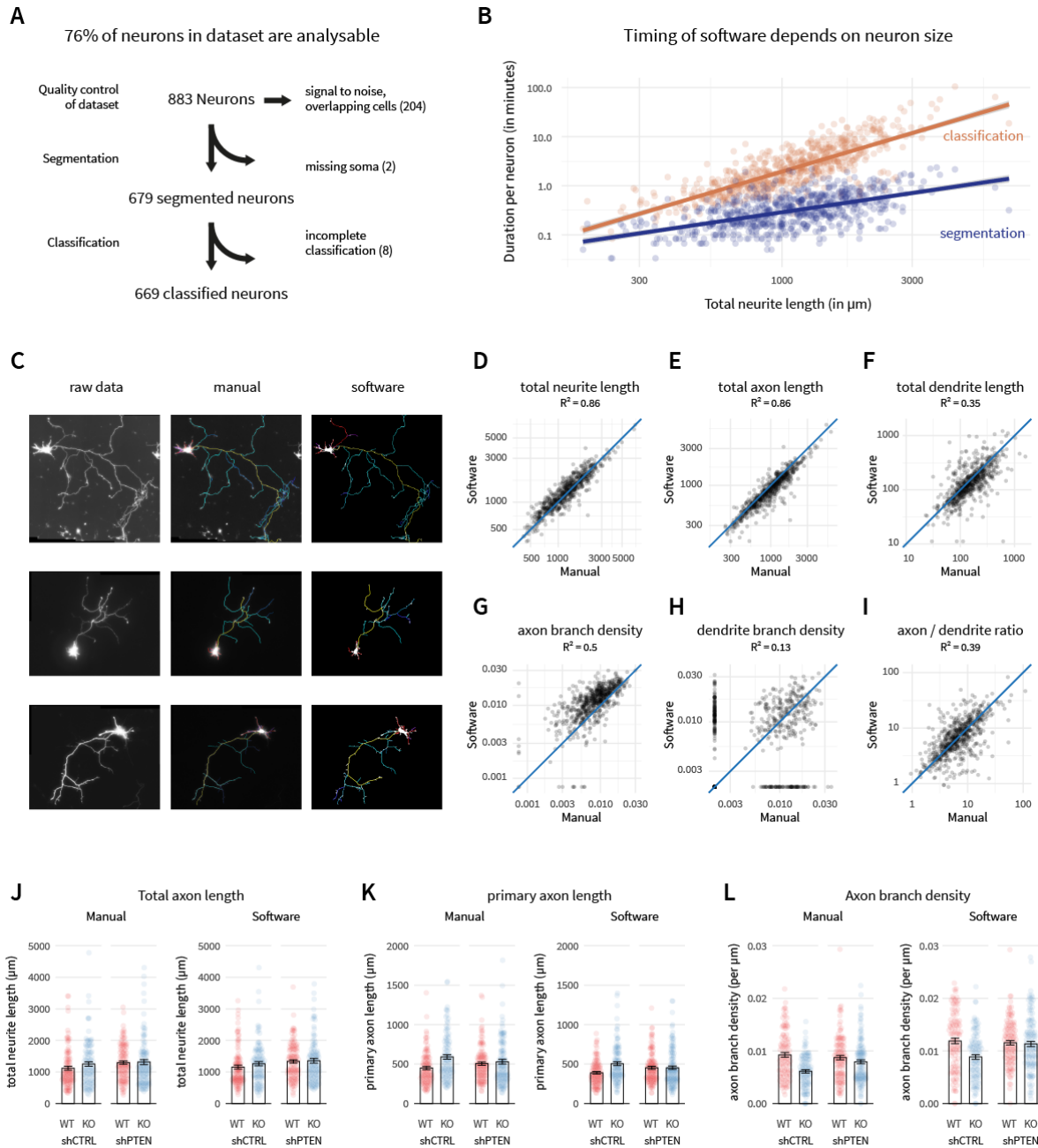


Figure 33: Testing automated classification accuracy on a manually analysed dataset of neurons (section 4.2.2 and 4.3.2). (A) Description of the dataset. 204 neurons were excluded prior to analysis due to noise or overlapping neurons. (B) Duration of the classification and segmentation steps of the software compared to neuron size. Plot shows logarithmically scaled axes. (C) Example classification results comparing manual and automated analysis. (D-I) Comparison of manual and automated quantifications of most relevant morphometric parameters for individual neurons. Total lengths of neurons (D), axons (E) or dendrites (F) and their ratio (I) very closely match manual quantifications. Automatic quantification of axon branch density (G) correlates well but slightly overestimates, dendrite branch density (H) is less accurate but largely susceptible to the small dendrite size in the dataset. (J-L) Comparison of manually and automated quantification of experimental groups from section 4.3.2. The correlation of automated to manual quantification is high enough to detect biological differences between treatments. Figure in preparation to submission.

As described in the previous section, 24% of images were excluded prior analysis due to signal-to-noise and overlap of multiple cells (Figure 33A). Of the remaining cells, only 10 were not fully classified. Classification is the time-consuming step in the analysis and scales exponentially with neuron size (Figure 33B). Even though the new classifier iterates through several images per hour, individual neurons can therefore take exceptionally long. Users are advised to start the classification on a batch of neurons overnight rather than proceeding image by image.

Automated classification results closely match manual classification, even though some paths are classified differently due to the inability of the software to distinguish crossing from branching (middle and bottom panel of Figure 33C). Nevertheless, the measured lengths of all processes, of the axon, the dendrites (Figure 33D-F), and the ratio of axon to dendrite length (Figure 33I) correlate quite well with manual quantifications. The accuracy of dendrite branch density (Figure 33H) is difficult to interpret, due to the developmental stage of the neurons analysed here which is characterised by short dendrites but more elaborated axons. Furthermore, the order of classification with axons before dendrites biases the software towards accurately detecting developing axons.

Furthermore, the tool has not been validated on later developmental timepoints when dendrites are more mature. Likely, this automated analysis will provide less accurate descriptions of axons and dendrites in such cases as the morphological complexity of neurons increases with development and especially more mature dendrites tend to overlap with each other and with the axon in neuron cultures. As later developmental timepoints are mainly analysed to study dendrite morphology, existing tools implementing dendrite-specific Sholl analysis might be better suited.³⁵⁷

Although absolute values of branch density might be not identical between software and manual, they still show a correlation. Axon branches are slightly over-detected (Figure 33G), mainly because the current version of the software cannot distinguish crossing processes from branches. Subsequent modifications could use information of the individual neurite intensities or their propagation vectors to distinguish crossing from branching for more accurate classifications. However, the quantification still accurately represents the morphological complexity of neurons and allows for the detection of biological phenotypes as apparent when reanalysing the shPTEN wild-type versus *Plpp3*^{-/-} experiment described in section 4.3.2 (Figure 33J-L).

In summary, this tool allows for the fully automated quantification of neuron morphology of large datasets of 2D-cultured neurons and can facilitate screening of effects of treatments on neuron morphogenesis. Its architecture biases the results to accurate quantification of early developing axons, as analysing larger neurons will take exponentially longer and likely produce less accurate results due to more crossing of neurites.

8 EXPERIMENTAL DETAILS

8.1 Key resources	95
8.2 Cloning	97
8.3 CRISPR/Cas9	101
8.4 Genotyping of <i>Plpp3</i>^{-/-} and putative off-targets	101
8.5 Animal procedures	102
8.6 Primary neuron culture	103
8.7 Cell line culture	104
8.8 Protein biochemistry	104
8.9 Immunofluorescent labelling	105
8.10 Microscopy	107
8.11 Image analysis	108
8.12 Data analysis, statistics and visualisation	110
8.13 Effect sizes of key experiments	111

8.1 KEY RESOURCES

Table 1: Key resources

REAGENT or RESOURCE	SOURCE	IDENTIFIER
Antibodies (<i>species</i>)		
AKT (<i>rabbit</i>)	Cell Signalling	9272
phospho-S473 AKT (<i>rabbit</i>)	Cell Signalling	4060
Biotin (<i>rabbit</i>)	Cell Signalling	5597
Flag M2 (<i>mouse</i>)	Sigma	F1804
GFP (<i>chicken</i>)	Abcam	Ab13970
GAD2 (<i>guinea pig</i>)	Synaptic systems	198104
GST (<i>rabbit</i>)	Abcam	ab9085
PI(3,4,5)P ₃ (<i>mouse</i>)	Echelon Biosciences	Z-P345b
PLPPR3 (<i>rabbit</i>), CAESYRRMQARRYQD	custom-made (Eurogentec)	N/A
Tau1 (<i>mouse</i>)	Millipore	MAB3420
α-Tubulin (<i>mouse</i>)	Sigma	T6199
β3-Tubulin (<i>rabbit</i>)	Biozol	802001
Actistain 488	Cytoskeleton	PHDG1
Phalloidin 647	Life Technologies	A22287
Hoechst	Sigma	14530
Dapi		
Anti-mouse IgG – HRP	Vector Labs	PI-2000
Anti-rabbit IgG – HRP	Vector Labs	PI-1000
Chemicals, Peptides, and Recombinant Proteins		
B27	Life Technologies	17504044
BDNF	R&D systems	248-BD
ECL Western Blotting Substrate	Promega	W100A
Amersham ECL Prime	GE healthcare	28980926
GDC-0941	Selleckchem	S1065
GoTaq G2 DNA polymerase	Promega	M7841
GST-PH(Grp1)	Echelon	G-3901
Insulin	Sigma	I9278
KOD Hot Start DNA polymerase	Merck Millipore	71086
Laminin (1-2 mg/ml)	Sigma	L2020
Lipofectamine 2000	Thermo Scientific	11668030
Neurobasal-A medium	Life Technologies	21103-049
Poly-DL-ornithine-hydrobromide	Sigma	P8638
Protease inhibitor cocktail III	Calbiochem	539134
Saponin Quillaja sp.	Sigma	S4521
T4 DNA ligase	NEB	M0202

REAGENT or RESOURCE	SOURCE	IDENTIFIER
Critical Commercial Assays		
MEGAscript T7-Kit	Life technologies	AM1354
mMessage mMachine Kit	Life technologies	AM1344
MEGAclear Kit	Life technologies	AM1908
PIP-Strip	Echelon	P-6001
Experimental Models: Cell Lines		
N1E-115	ATCC	CRL-2263
Experimental Models: Organisms/Strains		
Mouse: <i>Plppr3</i> ^{-/-} : C57 Bl/6NCrl <i>Plppr3</i> ^{-/-}	N/A	N/A
Mouse: wild-type: C57 Bl/6NCrl	FEM	N/A
Mouse: <i>Pten</i> ^{fl/fl} : C57 Bl/6NCrl <i>Pten</i> ^{fl/fl}	Trotman et al., 2003 (ref ³⁵⁸)	N/A
Software and Algorithms		
Fiji (ImageJ 1.51n-1.53c)	Schindelin et al., 2012 (ref ³⁵⁹)	https://imagej.net/Fiji
NeuronJ (version 1.4.3)	Meijering et al., 2004 (ref ³⁵⁴)	https://imagescience.org/meijering/software/neuronj/manual/
RStudio (version 1.4.1106)	RStudio	https://www.rstudio.com/
R (version 4.0.4)	R Core Team, 2021 (ref ³⁶⁰)	https://www.R-project.org/
MATLAB (2021a)	Mathworks	https://mathworks.com/
Custom analysis algorithms	This thesis	https://github.com/jo-fuchs
Other		
High-precision #1.5 coverslips	Carl Roth	LH24.1

Table 2: Solutions

SOLUTION	INGREDIENTS
Mowiol	Mowiol 4-88 (10 g), PBS (40 mL), Glycerol (Molecular Biology grade, 20 mL), DABCO (2 g)
PBS	PBS Tablets pH 7.4 (for 500 mL, Applichem, A9191)
PHEM	60 mM PIPES, 25 mM HEPES, 10 mM EGTA, 20 mM MgSO ₄ , pH 7.4
Phosphatase inhibitor cocktail	1 mM Na ₂ MO ₄ , 1 mM NaF, 20 mM β-glycerophosphate, 1 mM Na ₃ VO ₄ , 500 nM cantharidin
RIPA	50 mM Tris-HCl, pH 7.4, 150 mM NaCl, 0.5% sodium deoxycholate, 1% NP40, 0.1% sodium dodecyl sulphate
TAE	TAE buffer, 10x (AppliChem, A4227)

8.2 CLONING

Sections 2 and 3 of this thesis involved the generation of multiple plasmids. The general backbone of expression plasmids is pCAX (ampicillin-resistant, CAG promoter), GFP and mRuby2 plasmids are in pN1 backbone (kanamycin-resistant, CMV promoter), shRNAs in a lentiviral modified FUGW backbone (U6 promoter shRNA, synapsin promoter GFP or NLS-RFP). *Plppr3* sequences correspond to the mouse Ensembl sequence ENSMUST00000167250.8 (*Plppr3*-207) and were obtained from obtained from ABgene Surrey, UK; clone ID 6808849, GenBank: BC066006. To facilitate exchanging tags or plasmid backbones, all *Plppr3*-plasmids have shared restriction sites for insertion (N-terminal NheI, C-terminal NotI, between *Plppr3* and tag BamHI). All cloned *Plppr3*-mutants exist as C-terminally 3xFlag tagged versions, additional tags for full-length *Plppr3* include eGFP, mRuby2, AU1 and HA. All tags are separated from *Plppr3* by a flexible GSGGG-linker.

Mutagenesis and subcloning were performed using standard PCR (for truncation mutants and tags) or splice-overhang-extension PCR (for point mutations or internal deletions) followed by digest with the corresponding restriction enzymes, gel purification, ligation and transformation into competent *E. coli* (NEB- β , XL-10gold or DH5 α).

Standard PCR protocols used KOD Hot Start DNA polymerase (Merck Millipore) according to manufacturer's protocol for reagents. Template DNA was used at concentrations of 10-90 ng/ μ l. Temperature cycling was adjusted to 3 minutes of 95°C prior cycling, and 3 minutes of 70°C after cycles. Cycles (30-35) comprised of 30 seconds of 95°C, 20 seconds of decreasing annealing temperatures from 65-55 °C (10 cycles 65, 10 x 60, 10 x 55), and 30 – 90 seconds extension time depending on the length of the PCR product. Decreasing annealing temperatures helps with amplifying very specific targets (at high annealing temperature) while amplifying to a higher yield (at low annealing temperature) once the specific product dominates in the reaction.

Point mutations or internal deletions were introduced using overlapping primers in a twostep PCR first producing fragments from either end of *Plppr3* to the mutation and the second PCR merging the two fragments to a full product including the mutation. The first PCRs were performed with the protocol described above; the second PCR used similar amounts of reagents with gel-purified template PCR-products from the previous PCR diluted 1 in 10. In contrast to standard PCRs, the first 10 cycles (30 sec 95°C, 45 sec 56°C, 90 sec 70°C) of this splice-overhang extension PCR are performed without any primers in the reaction to facilitate self-annealing and therefore amplification of merged PCR products. After this first step, the non-mutagenesis primers (those binding to the ends of the desired full PCR product) are added to the same reaction and the merged PCR product is amplified for 30-35 cycles (30 sec 95°C, 20 sec 63°C, 30-90 sec 70°C).

PCR-products and plasmid backbones were digested using restriction enzymes of the FastDigest system (Thermo Scientific). All reactions were performed for one hour at 37°C in 50 μ l total volume (filled up with ddH₂O) with 1-2 μ g of vector or the full purified product from PCRs described above, including 5 μ l FastDigest buffer and 1 μ l of each respective enzyme. Initial PCR products and digested plasmids or digested PCR-products were separated by size electrophoretically on 1-2% agarose gels in

TAE-buffer. Correctly sized products were then excised from the gel and purified into 20 μ l using the NucleoSpin Gel and PCR Clean-up kit (Macherey-Nagel) according to the manufacturer's protocol.

7 μ l of digested plasmid and 9 μ l insert was ligated for 4-5 hours at room temperature using 2 μ l T4 ligase, 2 μ l T4 ligase buffer (both NEB) and subsequently transformed into chemically competent bacteria. Transformation was performed by incubating the ligation mix in 100 μ l bacteria thawed on ice for 10-15 minutes and a 40 second heat-shock at 42°C. After 2 additional minutes on ice and addition of 500 μ l SOC medium (NEB) without antibiotics, bacteria were shaken at 900 RPM for 30-45 minutes before plating them on precast agar including the corresponding selection antibiotic and growing overnight at 37°C. Individual colonies were picked and amplified in LB-medium including antibiotic and plasmid DNA was purified using the NucleoSpin Plasmid Mini kit (Macherey-Nagel) according to the manufacturer's protocol.

Control digests were performed (if possible) with enzymes harbouring one restriction site in the insert and one outside rather than with the cloning enzymes to avoid screening for unintended inserts of similar size and orientation. Correctly digested plasmids were sent for sequencing with Eurofins (start of thesis) or LGC (second half). Correctly sequenced plasmids were further amplified by transformation into chemically competent bacteria as described above. In contrast to plating on agar, the transformation mixes were, however, directly added to 300 ml LB with respective antibiotic and rotated at 180 RPM overnight at 37°C. High yields of plasmid DNA were purified using the NucleoBond Xtra Maxi Plus kit (Macherey-Nagel) according to the manufacturer's protocol. Concentration and purity were determined using a ND-1000 Spectrophotometer (Thermo Fisher Scientific).

Cloning of shRNAs or short tags was performed via oligonucleotide annealing. For shPTEN and the corresponding scrambled control, the vector backbone was digested with AgeI and PaeI and gel purified as described above. 16 μ l of linearised purified plasmid was dephosphorylated using 2 μ l thermosensitive antarctic phosphatase (Promega) and 2 μ l of corresponding buffer for 30 min at 37°C. The enzyme was inactivated at 75°C for 15 min and the dephosphorylated plasmid entered ligation without further purification. Partially overlapping oligonucleotides spanning the full shRNA-insert and creating matching AgeI and PaeI sticky-ends were annealed by heating to 95°C for 5 minutes and stepwise decreasing temperature to room temperature in a course of 40 minutes. Annealed oligonucleotides were subsequently phosphorylated using T4 PNK and corresponding buffers. The final ligation (4-5 hours at room temperature) includes 1 μ l of dephosphorylated vector, 2 μ l of phosphorylated oligonucleotides, and 1 μ l of T4 ligase and buffer respectively.

Table 3: Generated and used plasmids

PLASMID	MUTATION	CLONING PRIMERS	DESCRIPTION
pCAX (A)	N/A	N/A	Empty plasmid, CAG promoter (
pCAX-PLPPR3-Flag (A)	N/A	PLPPR3-fw (used also for all mutants): GCTAGCgtcaccATGCTTGCTATG, PLPPR3-rev (used also for all point mutants): accagaaccaccaccgatccGTCCTGGTACCTC	Full-length mouse PLPPR3
pCAX-PLPPR3- Δ Cc-Flag (A)	Δ 284-716	PLPPR3-fw + PLPPR3- Δ Cc-rev: ccaccgatccCTGGAAGTTGCC	Deletion of intracellular C-terminal region
pCAX-PLPPR3- Δ Ca-Flag (A)	Δ 408-716	PLPPR3-fw + PLPPR3- Δ Ca-rev: ccaccgatccACCGATAAGCTGCCTGG	Deletion of all parts not shared between splice-variants
pCAX-PLPPR3- Δ pE-Flag (A)	Δ 439-458	PLPPR3-fw, PLPPR3-rev + dpE-fw: GAGCAGGTAGCAGGGCCTGTCCACCCTCACTC dpE-rev: TGGAACAGGCCCTGCTACCTGCTCTGCTGGGG	Deletion of poly-E-box
pCAX-PLPPR3-C119A-Flag (A)	C119A	PLPPR3-fw, PLPPR3-rev + C119A-fw: CAACGCTGGTGGCgCAACTCAACTCC C119A-rev: GGAGTTGAAGTTGgGCCACCAGCGTTG	Putatively palmitoylation-deficient at C199
pCAX-PLPPR3-N167Q-Flag (A)	N167Q	PLPPR3-fw, PLPPR3-rev + N167Q-fw: GGTCTGCAAACCCcAgTACACCCTGCTGG N167Q-rev: CCAGCAGGGTGTAcTgGGGTTTGCAGACC	Putatively glycosylation-deficient at N167
pCAX-PLPPR3-R>G-Flag (A)	R126G + R127G + R130G	PLPPR3-fw, PLPPR3-rev + R>G-fw: CAACTCCTTCTCTcGgGGGCACAGTgGCTTTGTGGGTG R>G-rev: CACCCACAAAGCcCACTGTGCcCCcGAGGAAGGAGTTG	Polybasic juxtamembrane region
pCAX-PLPPR3-S203A-Flag (A)	S203A	PLPPR3-fw, PLPPR3-rev + S203A-fw: GACCTTCCCGgCCCAGCACGCCAC S203A-rev: GTGGCGTGCTGGGcCGGGAAGGTC	Mutant of former catalytic C2 domain
pCAX-PLPPR3-H205A-Flag (A)	H205A	PLPPR3-fw, PLPPR3-rev + H205A-fw: CTTCCCGTCCCAGgcCGCCACTCTGTC H205A-rev: GACAGAGTGGCGgcCTGGGACGGGAAG	Mutant of former catalytic C2 domain
pCAX-PLPPR3-C2mut-Flag (A)	S203A and H205A	PLPPR3-fw, PLPPR3-rev + C2mut-fw: GACCTTCCCGgCCCAGgcCGCCACTCTGTC C2mut-rev: GACAGAGTGGCGgcCTGGGcCGGGAAGGTC	Mutant of former catalytic C2 domain
pN1-GFP-F (K)	Farnesylation signal from K-RAS (ref ²⁰⁵)	N/A	Membrane localised GFP

A: Ampicillin-resistant, K: Kanamycin-resistant, table continued on next page

PLASMID	MUTATION	CLONING PRIMERS	DESCRIPTION
pX330_sgRNA-28 (A)	N/A	Targeting sequence: GTGGCCTGGTTCCGCGGTGC	Cas9-Flag and guide RNA-coding plasmid (gRNA 28)
pX330_sgRNA-30 (A)	N/A	Targeting sequence: GCCGCGGGCACGGAAGGCGT	Cas9-Flag and guide RNA-coding plasmid (gRNA 30)
f(syn)-NLS-RFP_U6(shPTEN) (A)	N/A	Targeting sequence: CGACTTAGACTTGACCTATAT	shRNA against PTEN (sequence from ref ²⁴⁶)
f(syn)-NLS-RFP_U6(shCTRL) (A)	N/A	Targeting sequence: CAACAAGATGAAGAGCACCAA	Scrambled version of shRNA against mouse PTEN
f(syn)-GFP (A)	N/A	N/A	GFP under Synapsin-promoter
f(syn)-GFP-U6(shPLPPR3/4) (A)	N/A	Targeting sequence: GCTGCAACTTCAACTCCTTC	shRNA against mouse PLPPR3 and PLPPR4
f(syn)iCreRFP-P2A-MSCW (BL-150)	N/A	N/A	NLS-RFP-coupled CRE recombinase (Viral core facility Charité)
f(syn)-NLS.RFP-P2A-MSCW (BL-181)	N/A	N/A	Same plasmid encoding NLS-RFP (Viral core facility Charité)
pN1-PH(BTK)-EGFP (K)	N/A	N/A	PH-domain of BTK, kind gift from Oliver Rocks (MDC & Charité Berlin)
pN1-PH(Grp1)-mCitrine (K)	N/A	N/A	PH-domain of Grp1, kind gift from Oliver Rocks
pN1-PLPPR3-Flag (K)	N/A	N/A	Full-length PLPPR3 under CMV-promoter
pN1-PLPPR1-GFP (K)	N/A	N/A	Mouse PLPPR1-GFP kind gift from Antje Bräuer (University Oldenburg)
pN1-PLPPR2-GFP (K)	N/A	N/A	Mouse PLPPR2-GFP kind gift from Antje Bräuer
pCAX-PLPPR3-GFP (K)	N/A	GFP-fw: AAGGATggatccggtggtggttctgtATGGT GagcAAGGG GFP-rev: cgaggcggccgctTACTTGTACAGC	GFP subcloned to pCAX-PLPPR3 backbone
pCAX-PLPPR4-GFP (A)	N/A	PLPPR4-fw: gagCTAGCgtcaccATGCAGCGCGCTGG PLPPR4-rev: caccggtatccATCCTTATAAGCCC	mouse PLPPR4-GFP kind gift from Antje Bräuer, cloned into pCAX
pN1-PLPPR5-GFP (K)	N/A	N/A	Mouse PLPPR5-GFP kind gift from Antje Bräuer

A: Ampicillin-resistant, K: Kanamycin-resistant

8.3 CRISPR/CAS9

Selection and generation of guide RNAs is described in detail in my master thesis.²²⁹ Briefly, 3 guide RNAs were chosen for both desired LoxP-insertion sites by their predicted efficiency and low off-target activity (using tools by Sanger <http://www.sanger.ac.uk/htgt/wge/> and Feng Zhang <http://crispr.mit.edu/>). Guide RNAs were cloned by oligo-annealing, the plasmid donor template by Gibson assembly of PCR-amplified regions between both LoxP-sites and the homology arms from either LoxP 1kb outwards (as exemplified in Figure 11B, strategy 2). The assembled modified genomic region was inserted into a pDTA backbone. The efficiency of the individual guide RNAs for inducing homology-directed repair was further tested in a cell culture model as described in Mashiko 2013.³⁶¹ The most efficient guide RNAs with least predicted off-target effects were chosen for genome editing (sgRNA28: GTGGCCTGGTCCGCGGTGC and sgRNA30: GCCGCGGGCACGGAAGGCGT in Figure 11).

To generate guide RNAs and mRNA for Cas9 for zygote injection, I used in vitro transcription and purification kits according to the manufacturer's protocols. Guide RNAs were generated by PCR-amplification to add a T7 promoter and subsequent in vitro transcription using the MEGAscript KIT (Life technologies). Cas9 mRNA was transcribed from pT7-Cas9 (Origene) using the mMessage mMachine Ultra Kit (Life technologies). Remaining DNA was degraded by TURBO DNase (Thermo Fisher) treatment for 15 min at 37°C before purifying RNAs using the MEGAClear Kit (Life technologies). The donor template was purified using the NucleoBond Xtra Midi Plus EF (Macherey-Nagel) for endotoxin-free plasmids. Injection solutions contained indicated amounts of guide RNAs, Cas9 mRNA and donor plasmid as measured by Nanodrop. A centrifugation step (14000 RPM, 4°C, 15 min) and transfer of only the top 80% of the supernatant has proven necessary to reduce the viscosity to levels required for injections into the pronucleus of zygotes.

Injection of zygotes and in vitro fertilisation was performed by members of the Transgenic Core facility (Laboratory of Prof. Geert Michel) at FEM Charité. Briefly, zygotes were prepared from superovulated (PMSG and HCG injection) C57 BL6/NCrl mice by hyaluronidase dissociation of the oviducts. Zygotes were injected in KSOM medium at 37°C, 5% CO₂ until microinjection to their pronucleus. Healthy zygotes were further cultured in SHTF medium enriched with the non-homologous end-joining inhibitor SCR7 (50 µM) to facilitate integration of LoxP-sites. Two-cell zygotes were then transferred to pseudopregnant foster mothers and their offspring was genotyped to check for modification of the *Pppr3* locus and putative off-targets.

8.4 GENOTYPING OF *PLPPR3*^{-/-} AND PUTATIVE OFF-TARGETS

Genomic DNA for genotyping from ear biopsies of mice was isolated using the NucleoSpin Tissue kit (Macherey Nagel) according to the manufacturer's protocol. Genomic DNA from blastocysts for efficiency tests in the CRISPR/Cas9 experiments was prepared using the HotSHOT preparation protocol.³⁶² Briefly, blastocysts were obtained in 1-2 µl culture medium, diluted with 10 µl alkaline lysis reagent (25 mM NaOH, 0.2mM EDTA, pH 12) and heated to 95°C for 30 minutes to disrupt cell and nuclear membranes. After cooling to room temperature, the solution is neutralised with 10 µl 40 mM Tris-HCl, pH 5. This unpurified cell lysate is directly used in the individual genotyping PCRs described in section 3.2 with the protocol described below.

All genotyping PCRs used GoTaq DNA polymerase (Promega). Reagents were diluted in 25 µl total volume with 5 µl GoTaq Green buffer, 1 µl of each primer (10 µM), 1 µl DMSO, 2µl purified genomic DNA, 0.25 µl GoTaq and 14.75 µl ddH₂O. The temperature cycling starts with 3 minutes 95°C before cycles and ends with 5 minutes 72°C and a storing step at 8°C. The 35 Cycles include 30 seconds of 95°C, 30 seconds of 65-55 °C (10 cycles 65°C, 10 cycles 60°C, 15 cycles 55°C) and 70 seconds of 72 °C. Sizes of PCR products are compared on a 1% agarose gel (TAE-buffer) as illustrated in Figure 12. Off-targets were analysed using the same PCR-protocol with primers spanning the predicted off-target region. All genotyping primers are listed below.

Table 4: Genotyping primers

Primer	Sequence
Plppr3 genotyping fw	CAGGGACCTCACCATGGAAACG
Plppr3 genotyping rev	TTGCAACTCCTACTCGACCTG
Plppr3 individual 3' fw	ACGCCGAAGGACAGCATGCACTC
Plppr3 individual 3' rev	= Plppr3 genotyping rev
Plppr3 individual 5' fw	= Plppr3 genotyping fw
Plppr3 individual 5' rev	GTGCCTTCTGTGCGCCTTG
Lrrc7 fw	TACCACCCGCAGCTTTTAGA
Lrrc7 rev	AAGCAGACCTTTTCCTTGGG
Exd1 fw	CTCGTTTCGTGGGTTTGTT
Exd1 rev	GGAGAGAAACAAGGGGTGGA
Tbcd fw	TGCTGGCAGGATGGTACT
Tbcd rev	TCGTAGGAGGCAGGTTTCATC
Cox7c fw	CTCCCACCGAACCTTCCAG
Cox7c rev	ACAGCTCAGGTCCCATTGAA
Zbtb33 fw	CTTCGCAGTCACGAAAGAG
Zbtb33 rev	CAAAGCGGACGAATGGAGAG
Icam4 fw	GGTCCAGAACTGTGCAATGG
Icam4 rev	CCGGTCTCCCTCACTGTAAG

8.5 ANIMAL PROCEDURES

All animals were housed and handled under the local ethical guidelines and animal handling protocols in the facilities of the Charité Center for Experimental Medicine (FEM) under standard conditions in a 12 hours light-dark-cycle with unrestricted access to water and food. Experiments were registered and performed under the licenses T0347/11 (primary neuron cultures, tissue harvesting for expression and localisation analyses) and G0261/12 (in utero electroporation) of the Landesamt für Gesundheit und Soziales Berlin (LaGeSo). *Plppr3*^{-/-} mice were bred in a B16/NCrI background, control animals in neuron culture experiments were wild-type littermates from heterozygous breeding. No experiments were performed stratified by animal sexes.

In-utero electroporations were performed by Dr. Julia Ledderose. Briefly, mice were injected intraperitoneally with 5 mg/kg of the analgetic Caprofen prior and three days after operation. For in utero-electroporations, pregnant mice were anesthetised with Isoflurane on embryonic day 14.5 of pregnancy and operated to access their uterus. Individual embryos were injected with a plasmid containing either GFP under synapsin promoter or additional shRNA against *Plppr3* and *Plppr4* into one cortical ventricle and electroporated to specifically target neuronal precursor cells that are close to the ventricle at this developmental stage. At embryonic day 14 to 15, precursor cells migrate to cortical layers II/III, allowing for a specific analysis of branching in a layer-specific manner. After electroporation, the abdomen of mice was stitched and the mouse was treated with Metamizole through the drinking water until three days prior to delivery. The offspring was sacrificed at postnatal day 7 or 14-16 as indicated in Figure 17. In vivo branching experiments comparing *Plppr3*^{-/-} and wild types were performed with homozygous breedings of *Plppr3*^{-/-} and matched ages of wild-type BL6/NCrl. *shPlppr3/4* were compared to shControl both in littermate wild type BL6/NCrl and separate age-matched BL6/NCrl. No experiments were performed stratified by animal sexes.

8.6 PRIMARY NEURON CULTURE

Primary hippocampal and cortical neurons were prepared by Kristin Lehmann, Kristin Schlawe or me from E16.5 embryos of BL6/NCrl wild-type mice or breedings of heterozygous *Plppr3*^{+/-} parents. Briefly, mothers were sacrificed and their uteri including the embryos were stored on ice in HBSS (Life Technologies) before isolating hippocampal and cortical region of individual embryos. For *Plppr3*-cultures, individual hippocampi and cortices were stored separately until genotyping from tail tips of the embryos allowed for pooling of the genotypes. After pooling, extracellular matrix of hippocampi or cortices was degraded with 10% Trypsin (Life Technologies) in HBSS for 15 min at 37°C before washing with HBSS and inactivating remaining Trypsin with 10% horse serum in HBSS. Brain regions were triturated to single cells in Neurobasal A medium containing 2% B27 (Life Technologies), 1 % penicillin/streptomycin (Life Technologies), 1% GlutaMax (Life Technologies) and 100 µM β-mercaptoethanol (Applichem) as well as 0.1 % DNase using a glass-pipet. After a final wash with the Neurobasal medium containing the same supplements without DNase, neurons were directly plated (without storing on ice) at a density of 15,000 cells/cm² for imaging experiments on laminin (20µg/ml)- and poly-D-ornithine (15 µg/ml) coated glass cover slips and cultured at 37°C, 5% CO₂.

For sparse labelling of neurons for morphometric studies or PIP3-quantification using PH-domain overexpression, I transfected 4 µg of the respective plasmid DNA per well (12-well plate) using a calcium-phosphate transfection protocol. For this, plasmid DNA was diluted in 250 mM CaCl₂ and slowly mixed with an equal volume of 2xBBS buffer (50 mM BES, 280 mM NaCl, 1.5 mM Na₂HPO₄, pH 7.3). After addition of supplemented neurobasal medium without Pen/Strep this mixture was incubated for 30 minutes at 37°C before it replaced the culture medium of growing neurons for 45-60 minutes at 37°C. After this incubation, neurons were washed 3-5 times with prewarmed washing buffer (135 mM NaCl, 4 mM KCl, 1 mM Na₂HPO₄, 2 mM CaCl₂, 1 mM MgCl₂, 20 mM HEPES, 20 mM d-Glucose, pH 7.3) before applying a mixture of 50% fresh supplemented neurobasal medium and 50% original medium of the cells and growing the neurons for 2-3 more days depending on the

experimental question. For the shRNA or CRE treatments of *Plppr3*^{-/-} or *Pten*^{fl/fl} cultures, 25 µl of viral particles obtained from the viral core facility of Charité (<https://vcf.charite.de/en/>) was applied per well (12-well plate) two hours after plating (DIV0). Details to plasmids and viruses are described in Table 3. Pharmacological manipulation of PI3K-activity was performed by addition of 500 nM GDC-0941 (Selleckchem) or 10 ng/ml BDNF (R&D systems) for the indicated times prior to fixation.

8.7 CELL LINE CULTURE

N1E-115 cells (male murine neuroblastoma, ATCC) were cultured at 37°C, 5% CO₂ in DMEM high-glucose with GlutaMax (Life technologies) with supplemented 10% fetal bovine serum and 1% penicillin/streptomycin. For PLPPR3-localisation and protrusion density experiments (section 2.2 and 2.3), cells were plated at a density of 4,500 cell/cm², for analysis of PLPPR3 modifications by protein biochemistry (section 2.3.2), cells were plated at a density of 130,000 cells/cm².

Transfection of plasmid DNA was performed using Lipofectamine 2000 (Life technologies). Briefly, DNA and Lipofectamine were mixed at a ratio of 2 volumes per microgram DNA in 50 µl Optimem (Life technologies) with 1µg of total DNA per well (24-well), 2µg per well (12-well), or 4 µg per well (6-well plate). The transfection mix was incubated for 30 minutes at 37°C before adding it to the growth medium of the cells. After 4-6 hours, the medium was completely exchanged with fresh prewarmed DMEM with supplements as described above. For studies measuring PI3K-activity (section 0), medium was exchanged to serum-free DMEM including 500 nM GDC-0941 in the PI3K-inhibition conditions. To stimulate PI3K-activity, 20µg/ml Insulin (Sigma) was added for the indicated times before fixation.

8.8 PROTEIN BIOCHEMISTRY

Lysis of N1E-115 cells or whole mouse brains was performed in RIPA buffer (50 mM Tris-HCl, pH 8.0, 150 mM sodium chloride, 1.0% NP-40, 0.5% sodium deoxycholate and 0.1% sodium dodecyl sulfate), with protease inhibitor cocktail III (Calbiochem), lab-made phosphatase inhibitor cocktail (see Table 2) by scraping cells or mechanical disruption of tissue and rotating for 20 min at 4°C. Cell debris was removed by centrifuging 15min at 4°C and 14000 RPM. 5µl of supernatant was used to determine protein concentration against a standard curve of bovine serum albumin in the lysis buffer using the Pierce® BCA Protein Assay kit. The supernatant was denatured with addition of one in three 4x RotiLoad I (Roth) and boiling at 95°C for 2 minutes before storage at -20°C until further use.

For separation of proteins by size, 4µg of protein per condition was loaded onto SDS-PAGE gels (4% stacking gel, 8% resolving gel) alongside 5µl of size marker PageRuler™ Plus Prestained Protein Ladder, 10 to 250 kDa (Thermo fisher), separating at 80V for the stacking gel and 120V for the resolving gel. Subsequently proteins were blotted onto nitrocellulose membranes (pore size 0.2 µm, Roth) using the WET/Tank Blotting System (BioRad) for 2.5 hours at 400 mA or overnight at 20V in transfer buffer (Table 2). The quality of blotting was controlled with Ponceau red stain (AppliChem). Washing steps were performed with Tris-buffered saline with Tween20 (TBS-T, 5mM Tris-HCl, 15mM NaCl, 0.005% Tween20, ph 7.4). Unspecific binding sites were blocked with 5% skim milk (Roth T145.3 Blotting grade) in TBS-T for 1 hour at room temperature, primary antibodies (anti-PLPPR3: 1:1000, anti-Flag: 1:1000 or anti-αTubulin 1:3000) were incubated overnight in fresh 5% milk in TBS-T, rolling in 50ml falcon at

4°C. After washing for 30 min at room temperature, rolling in TBS-T (3-4 replacements of solution), secondary HRP-coupled antibodies were added at 1:3000 dilution in 5% milk in TBS-T for 2-3h rolling at room temperature. The last wash lasted 30-60 min with multiple changes of TBS-T rolling at room temperature. Visualisation of HRP was performed using ECL Western Blotting Substrate (Promega) or Amersham ECL Prime (GE healthcare) under a Vilber Lourmat Fusion SL 4 system using FusionCapt software version 16.05. Quantification of band intensities was performed using ImageJ's gel analysis tool by measuring the integrated intensity of each band of interest.

To study phosphoinositide interaction, either purified full-length 1D4-tagged PLPPR3 (Fatih Ipek, Fos-Choline 14 solubilised, 2016), or biotin-labelled peptides synthesised by the in-house peptide-synthesis facility was tested with PIP-Strips (Echelon). PIP-strips were initially blocked in 3% BSA (Roth) in TBS-T for 1.5 hours at room temperature before incubating 0.5 µg/ml purified PLPPR3 protein (1D4 and flag tagged, purified by Fatih Ipek) in blocking solution for 1 hour at room temperature. After washing three times in 5 minutes with TBS-T, PLPPR3 was labelled using anti-Flag M2 (Sigma) at 1:1000 for 1h in blocking solution. Subsequent washing steps were kept at maximal 15 minutes to retain PLPPR3-binding to PIPs as much as possible, also the secondary antibody (anti-mouse HRP 1:3000 in blocking solution) was incubated only for 1 hour at room temperature. Signals were visualised using the super-sensitive ECL.

For peptide overlay experiments in Figure 8, peptides (0.5 mg) were solved in 40% PBS, 60% DMF with the wild-type peptide mostly dissolving and the G-mutated with precipitating in part. Nanodrop-determination of concentration indicated halved concentration in G-mutant peptide, which was verified using concentration curves on dot-blot using anti-biotin labelling. Therefore, the wild-type peptide was further diluted with 40%PBS, 60% DMF until dot-blot indicated equal amounts of solved peptide to the mutant. As this adjustment of concentration is close but not perfect, future studies should focus on more accurately determining peptide concentration in solution to reliably compare PIP-binding affinities between these peptides. Ideally, however, the PIP-strips would be performed not with peptides but with purified full-length protein with or without point mutations.

PIP-strips with peptides were blocked identically (1.5h, 3% BSA in TBS-T, room temperature), followed by an incubation of 0.4 µg/ml wild-type or mutant peptide in blocking solution for 1h at room temperature. Subsequent detection of peptide was identical as described before by using rabbit anti-Biotin (1:1000) and anti-rabbit HRP (1:3000) with Promega ECL. Due to low signal to noise, for illustrative purposes the signal of all measured PIP-strips (4x wild-type, 2x mutant) was equalised and averaged in ImageJ. For quantifications, the mean intensity values in each PIP-dot were measured in ImageJ on the raw images and normalised in each PIP-strip to the signal of the "blank"-dot.

8.9 IMMUNOFLUORESCENT LABELLING

All cultured cells were fixed at room temperature using aldehyde solutions in the cytoskeleton-stabilising PHEM buffer (Table 2) followed by three directly consecutive washing steps in PHEM. For labelling endogenous PLPPR3 and morphometric analyses, neurons were fixed with prewarmed 4% paraformaldehyde, 4% sucrose in PHEM-buffer for 12 minutes. PLPPR3-overexpressing N1E-115 cells

were fixed with prewarmed 4% paraformaldehyde, 0.2% glutaraldehyde, 4% sucrose in PHEM-buffer for 12 minutes.

Immunolabelling for both neurons and overexpressing N1E-115 cells started by blocking and permeabilisation for 30 minutes in 4% goat serum in PHEM + 0.2% TritonX100. Antibodies were incubated in 4% goat serum in PHEM, with all primary antibodies overnight at 4°C and all fluorophore-coupled secondary antibodies (or F-actin- and DNA-dyes) for 2-3 hours at room temperature unless stated otherwise. Washing steps were performed with PHEM buffer 4 times in 30 min total time. Coverslips were finally mounted in Mowiol after rinsing in ddH₂O. *Plppr3*-constructs for section 2 were stained with mouse anti-Flag-M2 (1:1000), fGFP signal was amplified with chicken anti-GFP (1:1000) and respective secondary fluorophore-coupled antibodies from Dianova and Jackson research (1:500). F-actin was visualised with Phalloidin-647 (1:250), nuclei with Dapi (1:1000). Endogenous PLPPR3 in neurons was visualised using rabbit anti-PLPPR3 (1:500, custom-made²⁰⁶), co-staining included mouse anti-Tau1 (1:1000) as an axon marker and Hoechst 33342 (1:10000, Thermo fisher, 20 mM) as a DNA marker. Morphometric analyses of *Plppr3*^{-/-} at DIV1 was labelled using Actistain-488 (1:250), mouse anti- α Tubulin (1:1000), rabbit anti-PLPPR3 (1:500) and Hoechst (1:10000). Morphometric analyses of *Plppr3*^{-/-} at DIV5, GFP-signal was amplified by chicken anti-GFP (1:1000), mouse anti-Tau1 (1:1000), rabbit anti-PLPPR3 (1:500) and Hoechst (1:10000).

For structured illumination microscopy, cells were plated on acid-washed, poly-ornithine/laminin-coated high-precision #1.5 coverslips (Carl Roth LH24.1). Immunolabelling was performed as described above except for mounting in ProLong Gold antifade reagent (Invitrogen). Cytoskeleton and over-expressed PLPPR3 were visualised using Actistain-488 (1:250), mouse anti-Flag M2 (1:1000, detected by anti-mouse Cy3) and rabbit anti- β 3-Tubulin (1:1000, detected by anti-mouse 647).

The procedure and rationale for the PIP3 staining is illustrated in Figure 26. Fixation was performed with prewarmed 4% paraformaldehyde, 0.2% glutaraldehyde, 4% sucrose in PHEM-buffer for 10min at room temperature. Subsequently fixative was removed by washing three times with ice-cold PHEM and directly transferring the coverslips to a metal plate emerged in an ice box (made hydrophobic with tesa-strips on its surface). Permeabilisation and blocking was performed on this ice-cold metal plate with 4% goat serum in PHEM including 0.2% Saponin for 30 min. anti-PIP3 (1:150) or GST-PH(Grp1) (1:250) was incubated in 4% goat serum, 0.2% Saponin in PHEM on ice for 2h followed by washing 3-4 times in 30 min with PHEM. The PIP3-probe was fixed with precooled 4% paraformaldehyde in PHEM for 10 min on ice, followed by 5 min at room temperature, fixative was removed with three PHEM washes. To sensitively visualise the PIP3-probe, cells were permeabilised again using 4% goat serum in PHEM with 0.2% TritonX100 for 30 min at room temperature. Subsequent staining for the PIP3-probe was performed as described above with either rabbit anti-GST (1:2000, for PH(Grp1)) followed by anti-Rabbit 488 (1:500) or only anti-mouse 488 (1:500, for anti-PIP3) overnight at 4°C and mounting in Mowiol. Neurons were co-labelled with guinea pig anti-Tau (1:1000, Synaptic systems) and Phalloidin-647 (1:250) or anti-GAD2 (1:500). N1E-115 cells were co-labelled with anti-pS473-AKT (1:500), phalloidin 647 (1:250) and Dapi (1:1000).

For visualising endogenous PLPPR3 in brain slices, embryonic mouse brains (E16.5) were fixed in 4% paraformaldehyde in PBS over night at 4°C, subsequently incubated in 15% sucrose in PBS for 8 hours at 4°C before transferring it to 30% sucrose over night at 4°C. Before slicing (20µm from cryostat), brains were embedded in OCT slices 20µm. All antibody incubation and blocking steps were performed in PBS with 1% BSA, 2% goat serum and 0.2% TritonX100, washes were performed with PBS. Blocking and permeabilising lasted for 1 hour, changing blocking solution every 15 minutes. Anti-PLPPR3 antibody (1:200) and anti-L1 (1:500) were incubated over night at 4°C, secondary antibodies (1:200, rabbit-488, rat-633) and Hoechst (1:10000) were incubated for 2 hours at room temperature. Washing steps lasted 1 hour with exchanging PBS 4 times. After the last wash, slices were washed two times in ddH₂O and air dried in the dark for 30min before embedding in glycerol.

8.10 MICROSCOPY

Phase contrast live cell imaging (for branching dynamics in section 5) was performed on an inverted Nikon Ti with a small stagetop incubator and a full incubator enclosure at 37°C and 5% CO₂ and humidity using a 20x air objective with phase contrast (Ph2). Illumination was adjusted for optimal signal to noise before every experiment via the Köhler procedure. Cells were plated in 4-well glass-bottom chamber slides (µ-Slide, Ibidi). For comparable movies between groups, I searched for areas of similar densities between wells and programmatically imaged 3 fields of view per condition every 10 min for 24-72 hours. The resulting images are in 12-bit format saved as .nd2 files. Prior to analysis movies were converted to .tif and cropped to matching developmental timepoint windows of 24 hours.

Epifluorescence of GFP-filled neurons for morphology at DIV5 was imaged on the same inverted Nikon Ti with 20x or 40x air objectives without adjusting atmosphere. All microscopy slides were re-labelled by an independent person before imaging to avoid bias during imaging. Signals of Tau (Cy3) and GFP (488) were sequentially acquired. Images of large neurons were automatically stitched using Nikon's large-image scan functionality. Resulting images included two channels at 12-bit.

PLPPR3-overexpression experiments and PIP3-intensity in N1E-115 cells, in vivo localisation of PLPPR3, DIV1 morphology neurons and PIP3-intensity on axons were all acquired using a Leica SP5 confocal microscope. N1E-155 cells and neuronal DIV1 morphology were imaged using a 63x objective with sequential acquisition of wavelengths (long wavelengths before short) and adjusted filters to minimise crosstalk of fluorophores. The Z-distance was kept constant at 0.6 µm while imaging the full extent of cells, resulting in stacks of different height depending on size of cells. For PIP-signal on axons, I used an additional optical zoom of 3x. For experiments with intensity readouts I kept the gain constant between images and imaging sessions (PIP3-analyses, PLPPR3-intensity on developmental timepoints), for experiments of morphology (N1E-115 PLPPR3 overexpression or DIV1 filopodia), gain was adjusted to optimise signal to noise ratio. In vivo PLPPR3 signal was imaged at 20x magnification sequentially without adjusting signal intensities between images (z-step: 2µm). Structured illumination microscopy on PLPPR3-overexpressing N1E-115 cells was performed by Niklas Gimber on OMX V4 Blaze system (GE Healthcare). Images were acquired as 512 x 512 pixel fields of view with a spacing of 125 nm in Z. Reconstruction of SIM images was performed using default protocols of the OMX-software including

background-reduction, Wiener-filtering and channel-specific k0-angles. Reconstructed stacks were subsequently max-projected and intensity-thresholded to remove low-intensity SIM artifacts.

8.11 IMAGE ANALYSIS

All image analysis has been performed in FIJI/ImageJ³⁵⁹ using built in functions or custom macros followed by data analysis in R/Rstudio³⁶⁰. The quantification of membrane abundance and filopodia density in N1E-115 cells (as performed for section 2) is described in detail in Appendix section 7.2 and accessible at https://github.com/jo-fuchs/Filopodia_Membrane_recruitment.

Morphometric analyses of chapter 4 were performed manually before unblinding images. For the analysis of developmental stages, on randomly selected fields of view I scored Tau and F-actin-stained neurons as stage 1 (round cell filo/lamellipodia rich), stage 2 (presence of neurites) or stage 3 (presence of one tau-enriched process). Survival was assessed by DNA-stain and quantified as the fraction of healthy nuclei by total DNA-stained nuclei.

For the filopodia analysis of DIV1 neurons, confocal stacks were maximum-projected and the F-actin channel was used to trace individual cells using the ImageJ plugin NeuronJ.³⁵⁴ Individual processes were classified as axon (Tau-positive originating from soma, and longest process), developing dendrite (other neurites originating from soma), branch (tubulin-signal in process) or filopodium (only actin signal). Summary statistics per neuron were generated using a custom-made R-script (<https://github.com/jo-fuchs/Filopodia-fixed>).

For the analysis of neuron morphology at DIV5 (wild-type versus *Pippr3*-genotypes and shPTEN-experiment), GFP-channel of epifluorescence images was converted to 8-bit before analysing with NeuronJ. Axons were classified as tau-positive but mainly as longest processes from soma, dendrites as other processes, branches as protrusions longer than 10 μm . Also here, summary statistics per neuron were generated using a custom-made R-script (https://github.com/jo-fuchs/Branching_fixed).

Collateral branching of layer II/III cortical neurons in vivo was analysed on sum-intensity projections of similar-sized substacks (representing the consecutive 20 slices with brightest signal of the stack). Layer V intensity was measured using a manual rectangular selection excluding migrating cells in the layer. Cell number in layer II/III was counted manually in the region directly vertical to the intensity selection to estimate only the relevant number of cells. Branch density was then approximated as layer V intensity divided by number of cells in layer II/III.

PIP3-immunolabelling intensity was detected by measuring mean intensity of a maximum projection in axons, as defined by a mask generated in the Tau channel (DIV3, DIV5, DIV8) or in the GFP-channel (to measure only shRNA-transfected cells). PIP3 intensity in N1E-115 cells or PTEN^{-/-} neurons was measured as the mean intensity of the brightest parts of the image (https://github.com/jo-fuchs/Microscopy_analysis_snippets/blob/master/ImageJ/Intensity_measurements.ijm). PH-domain-accumulation in axons was measured by detecting local maxima based on the expression level (measured as mean intensity) in transfected axons (https://github.com/jo-fuchs/Microscopy_analysis_snippets/blob/master/ImageJ/Local_accumulations_per_area.ijm), and subsequently normalised to axon area.

The analysis of live-cell phase contrast imaging for chapter 5 is outlined in Figure 34. After acquisition, movies were randomised and blinded using a custom-made R-script (https://github.com/jo-fuchs/Microscopy_analysis_snippets/blob/master/R/Randomize_folder.R). Subsequently, I manually classified branch-forming events by precursor type according to their morphology (as filopodia, lamellipodia, splitting or mixed). I furthermore recorded the timepoint of formation (starting to elongate) and collapse of a branch (completely retracting or retraction of the ‘mother branch’). To normalise for uneven cell densities between groups, I also counted the number of cells on each field of view. Further processing steps to unblind, calculate lifetime and accumulation of branches, to calculate Cox proportional hazards models and statistical tests, and for generating figures are all described in <https://github.com/jo-fuchs/Branch-Lifetime-PRG2>.

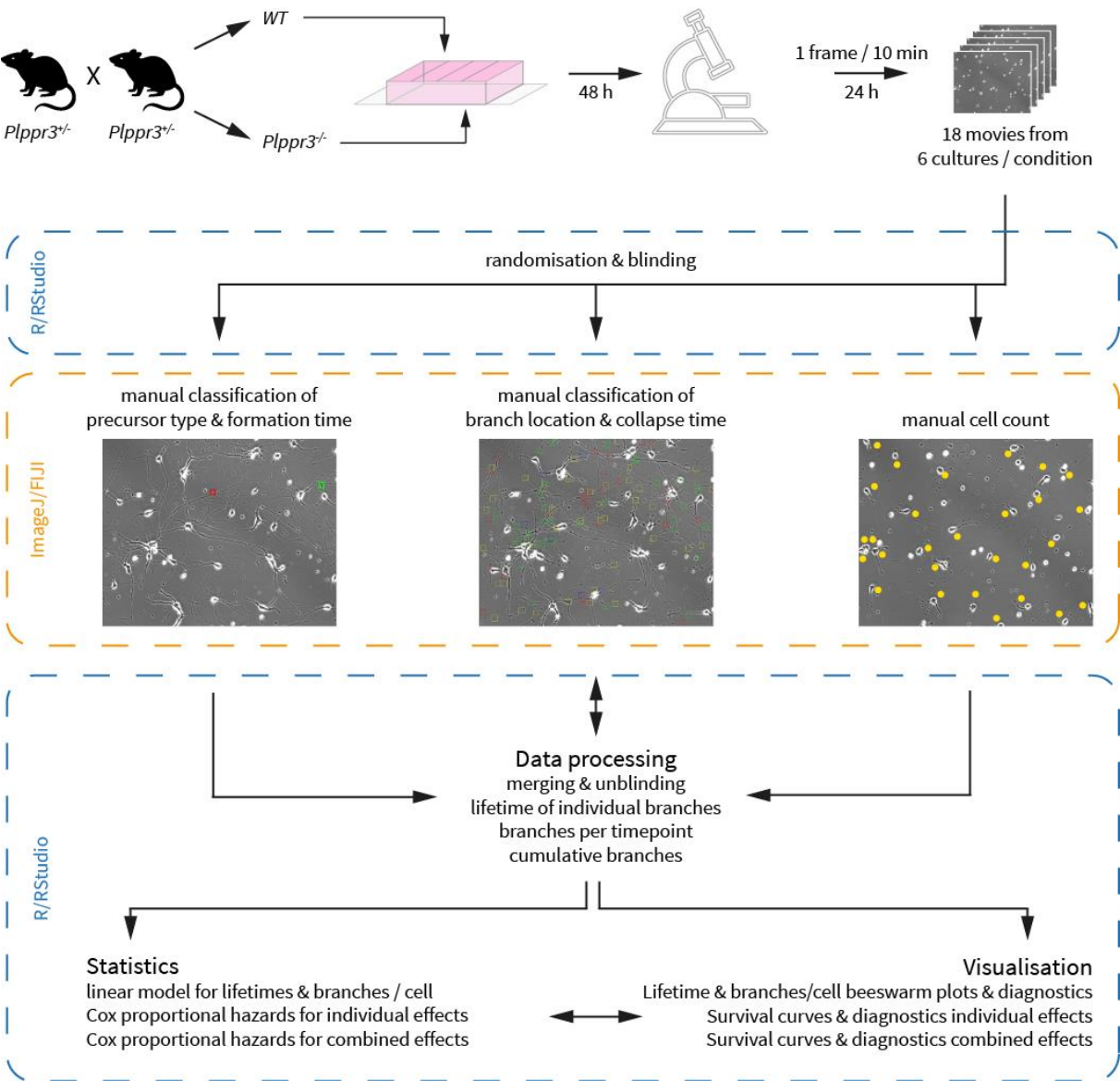


Figure 34: Scheme for branching dynamics experiment in chapter 5. Figure part of a manuscript submitted to *BioRxiv* (<https://www.biorxiv.org/content/10.1101/2021.04.23.441127v1>) and currently under revision

8.12 DATA ANALYSIS, STATISTICS AND VISUALISATION

All data processing steps, calculation of per-cell and subsequent per experiment averages, visualisation of variables and model assumptions as well as statistics have been performed in R/RStudio, heavily using tidyverse packages.³⁶³ All scripts used to generate plots and statistical tests in this thesis are stored next to the original data files.

Visualisation of the single-cell RNA-seq data of the Allen Institute⁹⁶ in Figure 1 was performed using a custom-made R-script and shiny tool. The raw data (csv files of 'Gene Expression by Cluster, trimmed means' and 'Table of cell metadata') was downloaded from <https://portal.brain-map.org/atlas-and-data/rnaseq/mouse-whole-cortex-and-hippocampus-smart-seq> (SMART) and <https://portal.brain-map.org/atlas-and-data/rnaseq/mouse-whole-cortex-and-hippocampus-10x> (10x-dataset). Filtering for individual genes or gene families, merging metadata and expression data, and visualisation of gene expressions in cell types, neighbourhoods or individual cell clusters was performed as described in <https://github.com/jo-fuchs/Gene-expression-AllenBrainAtlas>.

Statistical comparisons were performed using mixed effect models (of the nlme package) with treatment conditions as fixed factors and experiments as the random factor to test for between experiment variability while still accounting for between-cell variability. For all experiments except the shPTEN experiment, there was only one fixed factor to compare. For shPTEN-treatment in addition to the *Plppr3*^{-/-} genotype, I used a two-factor mixed effects model (*Plppr3*-Genotype and shPTEN-treatment as fixed factors) followed by a model with one fixed effect (Genotype by shTreatment interaction) after detecting significant interactions. Between group comparisons were calculated by Tukey's post hoc comparison with Holm-correction. *Plppr3*-mutant expressions were compared only to wild-type PLPPR3 and control-transfected rather than between all groups. Model assumptions were tested graphically using qq-plots (normality), residual plots (homogeneity of variance) and Cook's distance (influential individual datapoints).

Survival analysis was performed as Cox proportional hazards model (using the survminer package) including either singular fixed effects (genotype, precursor type or neurite type) or, in the final test (Figure 23), a combination of all three. An interaction of any of the effects did not increase the model fit as tested using a log-likelihood test and was therefore not included. Assumptions of the Cox proportional hazard model were tested via a Schoenfeld test (to test proportional hazards) and graphically by plotting deviance residuals (to detect effects of influential datapoints).

Due to the explorative nature of these experiments and the lack of information on effect sizes, sample sizes were not chosen by a priori power analysis but to exceed typical sample sizes of the field, where possible. Due to the exploratory nature of this thesis, however, it would be critical to test key experiments in independent confirmatory experiments. To facilitate this, I calculated both between experiment and between cells effect sizes as Hedges g to correct for differences in group sizes, using the R-package effsize.

All plots were created with in R (R version 4.0.4)/RStudio (Version 1.4.1106) using ggplot, cowplot, glue, scico & ggbeeswarm packages. Final styling of figures was performed in Adobe Illustrator.

8.13 EFFECT SIZES OF KEY EXPERIMENTS

The following tables summarise the effect sizes of key experiments as Hodge's g to facilitate the estimation of sample sizes for confirmatory experiments. The tables also include the effect sizes between individual cells to allow for an estimation of the required number of cells per repetition.

Table 5: Effect sizes of PLPPR3 overexpression experiments in N1E-115 cells (Chapter 2)

Readout	Reference group	Treatment group	Effect size (cells)	Effect size (experiments)
Figure 6B (protrusions deletion)	Empty ctrl	PLPPR3	0.84	1.11
	Empty ctrl	PLPPR3- Δ pE	0.67	1.21
	Empty ctrl	PLPPR3- Δ Ca	0.41	0.64
	Empty ctrl	PLPPR3- Δ Cc	0.47	0.62
	PLPPR3	PLPPR3- Δ pE	-0.16	-0.20
	PLPPR3	PLPPR3- Δ Ca	-0.45	-0.81
	PLPPR3	PLPPR3- Δ Cc	-0.35	-0.47
Figure 6C (Membrane abundance deletion)	PLPPR3	PLPPR3- Δ pE	0.75	1.61
	PLPPR3	PLPPR3- Δ Ca	-0.61	-0.95
	PLPPR3	PLPPR3- Δ Cc	-0.98	-1.38
Figure 8C (Double-band)	PLPPR3	PLPPR3-R>G	-	-1.37
	PLPPR3	PLPPR3-C119A	-	-0.38
	PLPPR3	PLPPR3-N167Q	-	-1.17
	PLPPR3	PLPPR3- Δ pE	-	0.86
Figure 8F (Membrane abundance PTM)	PLPPR3	PLPPR3-R>G	-0.58	-1.59
	PLPPR3	PLPPR3-C119A	0.18	-0.02
	PLPPR3	PLPPR3-N167Q	-0.34	-1.02
Figure 8G (protrusions PTM)	Empty ctrl	PLPPR3	0.80	1.16
	Empty ctrl	PLPPR3-R>G	0.30	0.48
	Empty ctrl	PLPPR3-C119A	0.33	0.23
	Empty ctrl	PLPPR3-N167Q	0.53	0.61
	PLPPR3	PLPPR3-R>G	-0.48	-0.54
	PLPPR3	PLPPR3-C119A	-0.46	-0.80
	PLPPR3	PLPPR3-N167Q	-0.21	-0.20
Figure 9B (Membrane abundance Catalytic)	PLPPR3	PLPPR3-S203A	-0.86	-1.69
	PLPPR3	PLPPR3-H205A	-0.87	-1.86
	PLPPR3	PLPPR3-C2mut	-1.03	-1.97
Figure 9C (protrusions Catalytic)	PLPPR3	PLPPR3-S203A	0.16	-0.1
	PLPPR3	PLPPR3-H205A	0.15	0.09
	PLPPR3	PLPPR3-C2mut	-0.33	-0.65

Table 6: Effect sizes of DIV1 neuron morphology in *Plppr3*^{-/-} primary hippocampal neurons (corresponding to Figure 15)

Readout	Reference group	Treatment group	Effect size g (cells)	Effect size g (experiments)
B) dendrite length	Wt	<i>Plppr3</i> ^{-/-}	-0.12	-0.37
	Wt	<i>Plppr3</i> ^{+/-}	-0.05	-0.16
	<i>Plppr3</i> ^{+/-}	<i>Plppr3</i> ^{-/-}	-0.08	-0.16
C) dendrite number	Wt	<i>Plppr3</i> ^{-/-}	0.08	0.17
	Wt	<i>Plppr3</i> ^{+/-}	0.26	0.88
	<i>Plppr3</i> ^{+/-}	<i>Plppr3</i> ^{-/-}	-0.16	-0.61
D) Axon-dendrite ratio	Wt	<i>Plppr3</i> ^{-/-}	0.21	0.73
	Wt	<i>Plppr3</i> ^{+/-}	0.06	0.19
	<i>Plppr3</i> ^{+/-}	<i>Plppr3</i> ^{-/-}	0.15	0.59
E) dendrite filopodia density	Wt	<i>Plppr3</i> ^{-/-}	-0.23	-0.43
	Wt	<i>Plppr3</i> ^{+/-}	-0.27	-0.72
	<i>Plppr3</i> ^{+/-}	<i>Plppr3</i> ^{-/-}	0.03	0.16
F) axon length	Wt	<i>Plppr3</i> ^{-/-}	0.00	-0.22
	Wt	<i>Plppr3</i> ^{+/-}	0.10	0.22
	<i>Plppr3</i> ^{+/-}	<i>Plppr3</i> ^{-/-}	-0.10	-0.35
G) axon branch density	Wt	<i>Plppr3</i> ^{-/-}	-0.21	-0.55
	Wt	<i>Plppr3</i> ^{+/-}	-0.21	-0.48
	<i>Plppr3</i> ^{+/-}	<i>Plppr3</i> ^{-/-}	-0.01	-0.08
H) axon filopodia density	WT	<i>Plppr3</i> ^{-/-}	-0.84	-1.28
	WT	<i>Plppr3</i> ^{+/-}	-0.04	0.10
	<i>Plppr3</i> ^{+/-}	<i>Plppr3</i> ^{-/-}	-0.78	-1.49
I) axon filopodia length	WT	<i>Plppr3</i> ^{-/-}	0.29	0.56
	WT	<i>Plppr3</i> ^{+/-}	0.23	0.23
	<i>Plppr3</i> ^{+/-}	<i>Plppr3</i> ^{-/-}	0.09	0.22

Table 7: Effect sizes of DIV5 neuron morphology in *Plppr3*^{-/-} primary hippocampal neurons (corresponding to Figure 16)

Readout	Reference group	Treatment group	Effect size (cells)	Effect size (experiments)
B) total dendrite length	Wt	<i>Plppr3</i> ^{-/-}	-0.20	-0.42
	Wt	<i>Plppr3</i> ^{+/-}	0.01	-0.19
	<i>Plppr3</i> ^{+/-}	<i>Plppr3</i> ^{-/-}	-0.29	-0.50
C) dendrite number	Wt	<i>Plppr3</i> ^{-/-}	-0.10	-0.24
	Wt	<i>Plppr3</i> ^{+/-}	0.28	0.02
	<i>Plppr3</i> ^{+/-}	<i>Plppr3</i> ^{-/-}	-0.40	-0.42
D) mean dendrite length	Wt	<i>Plppr3</i> ^{-/-}	-0.48	-0.11
	Wt	<i>Plppr3</i> ^{+/-}	-0.31	-0.08
	<i>Plppr3</i> ^{+/-}	<i>Plppr3</i> ^{-/-}	-0.24	-0.03
E) dendrite branch density	Wt	<i>Plppr3</i> ^{-/-}	-0.41	-1.26
	Wt	<i>Plppr3</i> ^{+/-}	-0.16	-0.77
	<i>Plppr3</i> ^{+/-}	<i>Plppr3</i> ^{-/-}	-0.28	-1.03
F) total axon length	Wt	<i>Plppr3</i> ^{-/-}	0.26	0.09
	Wt	<i>Plppr3</i> ^{+/-}	0.09	0.00
	<i>Plppr3</i> ^{+/-}	<i>Plppr3</i> ^{-/-}	0.19	0.11
G) primary axon length	Wt	<i>Plppr3</i> ^{-/-}	0.38	0.51
	Wt	<i>Plppr3</i> ^{+/-}	0.11	0.12
	<i>Plppr3</i> ^{+/-}	<i>Plppr3</i> ^{-/-}	0.29	0.42
H) mean axon branch length	Wt	<i>Plppr3</i> ^{-/-}	1.36	0.53
	Wt	<i>Plppr3</i> ^{+/-}	0.05	0.08
	<i>Plppr3</i> ^{+/-}	<i>Plppr3</i> ^{-/-}	1.41	0.47
I) axon branch density	Wt	<i>Plppr3</i> ^{-/-}	-0.69	-2.09
	Wt	<i>Plppr3</i> ^{+/-}	-0.16	-0.49
	<i>Plppr3</i> ^{+/-}	<i>Plppr3</i> ^{-/-}	-0.59	-1.76

Table 8: Effect sizes of in vivo branching of *Plppr3*^{-/-} layer II/III neurons in layer V (corresponding to Figure 17Figure 15)

Timepoint	Reference group	Treatment group	Effect size (animals)
P7	Wt	<i>Plppr3</i> ^{-/-}	-0.03
P15	Wt	<i>Plppr3</i> ^{-/-}	0.70
P14-17	shCTRL	sh <i>Plppr3/4</i>	-0.43

Table 9: Results of mixed two-way ANOVA (shPTEN, *Plppr3*^{-/-}) with random factor experiment (corresponding to Figure 19), n(Obs)=562, n(exp)=5

Readout	Fixed effect	Estimated difference [unit of measurement]	t-value	p-value
B) total dendrite length [μm]	Wt vs. <i>Plppr3</i> ^{-/-}	2.11	0.13	0.89
	shCTRL vs. shPTEN	49.19	3.20	0.001
	Interaction	-24.54	-1.14	0.25
C) dendrite number [#]	Wt vs. <i>Plppr3</i> ^{-/-}	-0.38	-1.68	0.09
	shCTRL vs. shPTEN	0.35	1.51	0.13
	Interaction	0.58	1.81	0.07
D) mean dendrite length [μm]	Wt vs. <i>Plppr3</i> ^{-/-}	3.87	1.32	0.18
	shCTRL vs. shPTEN	7.17	2.45	0.01
	Interaction	-10.72	-2.62	0.009
E) dendrite branch density [#/ μm]	Wt vs. <i>Plppr3</i> ^{-/-}	0.0000	0.08	0.93
	shCTRL vs. shPTEN	0.0014	1.91	0.06
	Interaction	-0.0015	-1.50	0.13
F) total axon length [μm]	Wt vs. <i>Plppr3</i> ^{-/-}	126.00	1.77	0.08
	shCTRL vs. shPTEN	130.08	1.83	0.07
	Interaction	-119.41	-1.20	0.23
G) primary axon length [μm]	Wt vs. <i>Plppr3</i> ^{-/-}	140.44	4.23	0.000
	shCTRL vs. shPTEN	59.18	1.78	0.07
	Interaction	-120.66	-2.61	0.009
H) mean axon branch length [μm]	Wt vs. <i>Plppr3</i> ^{-/-}	12.49	2.68	0.008
	shCTRL vs. shPTEN	6.40	1.38	0.16
	Interaction	-9.55	-1.47	0.14
I) axon branch density [#/ μm]	Wt vs. <i>Plppr3</i> ^{-/-}	-0.0027	-6.10	0.000
	shCTRL vs. shPTEN	-0.0002	-0.57	0.57
	Interaction	0.0020	3.23	0.001

Table 10: Effect sizes of PIP3 quantifications in *Plppr3*^{-/-} primary hippocampal neurons (corresponding to Figure 18)

Readout	Reference group	Treatment group	Effect size g (images/axons)	Effect size (experiments)
A) PIP3 DIV3	Wt	<i>Plppr3</i> ^{-/-}	-0.15	-0.11
B) PIP3 DIV5	Wt	<i>Plppr3</i> ^{-/-}	-0.08	-0.07
C) PIP3 DIV6 sh	shCTRL	sh <i>Plppr3/4</i>	0.28	0.25
D) Grp1 DIV8	Wt	<i>Plppr3</i> ^{-/-}	0.16	0.29
E) BTK(PH) OE DIV8	Wt	<i>Plppr3</i> ^{-/-}	-0.11	-0.17
F) Grp1(PH) OE DIV8	Wt	<i>Plppr3</i> ^{-/-}	0.36	1.00

9 REFERENCES

1. Buzsáki, G. *The Brain from Inside Out*. (Oxford University Press, 2019). doi:10.1093/oso/9780190905385.001.0001.
2. Lefebvre, J. L., Sanes, J. R. & Kay, J. N. Development of Dendritic Form and Function. *Annu. Rev. Cell Dev. Biol.* **31**, 741–77 (2015).
3. London, M. & Häusser, M. Dendritic computation. *Annu. Rev. Neurosci.* **28**, 503–532 (2005).
4. LeCun, Y., Bengio, Y. & Hinton, G. Deep learning. *Nature* **521**, 436–444 (2015).
5. Zador, A. M. A critique of pure learning and what artificial neural networks can learn from animal brains. *Nat. Commun.* **10**, (2019).
6. Parenti, I., Rabaneda, L. G., Schoen, H. & Novarino, G. Neurodevelopmental Disorders: From Genetics to Functional Pathways. *Trends Neurosci.* **43**, 608–621 (2020).
7. Azzarelli, R., Simons, B. D. & Philpott, A. The developmental origin of brain tumours: A cellular and molecular framework. *Dev.* **145**, (2018).
8. Griffin, J. M. & Bradke, F. Therapeutic repair for spinal cord injury: combinatory approaches to address a multifaceted problem. *EMBO Mol. Med.* **12**, 1–29 (2020).
9. Bystron, I., Blakemore, C. & Rakic, P. Development of the human cerebral cortex: Boulder Committee revisited. *Nat. Rev. Neurosci.* **9**, 110–122 (2008).
10. Silbereis, J. C., Pochareddy, S., Zhu, Y., Li, M. & Sestan, N. The Cellular and Molecular Landscapes of the Developing Human Central Nervous System. *Neuron* **89**, 248 (2016).
11. Cadwell, C. R., Bhaduri, A., Mostajo-Radji, M. A., Keefe, M. G. & Nowakowski, T. J. Development and Arealization of the Cerebral Cortex. *Neuron* **103**, 980–1004 (2019).
12. Lim, L., Mi, D., Llorca, A. & Marín, O. Development and Functional Diversification of Cortical Interneurons. *Neuron* **100**, 294–313 (2018).
13. Miyoshi, G. *et al.* Genetic fate mapping reveals that the caudal ganglionic eminence produces a large and diverse population of superficial cortical interneurons. *J. Neurosci.* **30**, 1582–1594 (2010).
14. Lodato, S. & Arlotta, P. Generating Neuronal Diversity in the Mammalian Cerebral Cortex. *Annu. Rev. Cell Dev. Biol.* **31**, 699–720 (2015).
15. Sur, M. & Leamey, C. A. Development and plasticity of cortical areas and networks. *Nat. Rev. Neurosci.* **2**, 251–262 (2001).
16. Pfister, B. J., Iwata, A., Meaney, D. F. & Smith, D. H. Extreme stretch growth of integrated axons. *J. Neurosci.* **24**, 7978–83 (2004).
17. Dotti, C. G., Sullivan, C. A. & Banker, G. A. The establishment of polarity by hippocampal neurons in culture. *J Neurosci* **8**, 1454–1468 (1988).
18. Polleux, F. & Snider, W. Initiating and growing an axon. *Cold Spring Harb. Perspect. Biol.* **2**, a001925 (2010).
19. Cheng, P. L. & Poo, M. M. Early events in axon/dendrite polarization. *Annu. Rev. Neurosci.* **35**, 181–201 (2012).
20. Wang, F. *et al.* Lipid products of PI(3)Ks maintain persistent cell polarity and directed motility in neutrophils. *Nat. Cell Biol.* **4**, 513–518 (2002).

21. Cheng, P.-L. *et al.* Self-amplifying autocrine actions of BDNF in axon development. *Proc. Natl. Acad. Sci. U. S. A.* **108**, 18430–5 (2011).
22. Shelly, M. *et al.* Local and Long-Range Reciprocal Regulation of cAMP and cGMP in Axon/Dendrite Formation. *Science (80-.)*. **327**, 547–552 (2010).
23. Yan, D., Guo, L. & Wang, Y. Requirement of dendritic Akt degradation by the ubiquitin–proteasome system for neuronal polarity. *J. Cell Biol.* **174**, 415–424 (2006).
24. Hassan, B. A. & Hiesinger, P. R. Beyond Molecular Codes: Simple Rules to Wire Complex Brains. *Cell* **163**, 285–291 (2015).
25. Harton, M. D. & Batchelor, E. Determining the Limitations and Benefits of Noise in Gene Regulation and Signal Transduction through Single Cell, Microscopy-Based Analysis. *J. Mol. Biol.* **429**, 1143–1154 (2017).
26. Cuntz, H., Forstner, F., Borst, A. & Häusser, M. One rule to grow them all: A general theory of neuronal branching and its practical application. *PLoS Comput. Biol.* **6**, (2010).
27. Fitzgibbon, T., Funke, K. & Eysel, U. T. Anatomical correlations between soma size, axon diameter, and intraretinal length for the alpha ganglion cells of the cat retina. *Vis. Neurosci.* **6**, 159–74 (1991).
28. Lloyd, A. C. The Regulation of Cell Size. *Cell* **154**, 1194–1205 (2013).
29. Kwon, C. H. *et al.* Pten regulates neuronal arborization and social interaction in mice. *Neuron* **50**, 377–388 (2006).
30. Roy, D. & Tedeschi, A. The Role of Lipids, Lipid Metabolism and Ectopic Lipid Accumulation in Axon Growth, Regeneration and Repair after CNS Injury and Disease. *Cells* **10**, 1078 (2021).
31. Pfenninger, K. H. Plasma membrane expansion: A neuron’s Herculean task. *Nat. Rev. Neurosci.* **10**, 251–261 (2009).
32. Bodakuntla, S., Jijumon, A. S., Villablanca, C., Gonzalez-Billault, C. & Janke, C. Microtubule-Associated Proteins: Structuring the Cytoskeleton. *Trends Cell Biol.* **29**, 804–819 (2019).
33. Janke, C. & Magiera, M. M. The tubulin code and its role in controlling microtubule properties and functions. *Nat. Rev. Mol. Cell Biol.* **21**, 307–326 (2020).
34. Scott, E. K. & Luo, L. How do dendrites take their shape? *Nat. Neurosci.* **4**, 359–365 (2001).
35. Lowery, L. A. & Van Vactor, D. The trip of the tip: understanding the growth cone machinery. *Nat. Rev. Mol. Cell Biol.* **10**, 332–343 (2009).
36. Tanaka, E., Ho, T. & Kirschner, M. W. The role of microtubule dynamics in growth cone motility and axonal growth. *J. Cell Biol.* **128**, 139–55 (1995).
37. Schaefer, A. W., Kabir, N. & Forscher, P. Filopodia and actin arcs guide the assembly and transport of two populations of microtubules with unique dynamic parameters in neuronal growth cones. *J. Cell Biol.* **158**, 139–52 (2002).
38. Mitchison, T. & Kirschner, M. Cytoskeletal dynamics and nerve growth. *Neuron* **1**, 761–72 (1988).
39. Santos, T. E. *et al.* Axon Growth of CNS Neurons in Three Dimensions Is Amoeboid and Independent of Adhesions. *Cell Rep.* **32**, (2020).
40. Leonetti, M. *Branching in Nature*. *Branching in Nature* (Springer Berlin Heidelberg, 2001). doi:10.1007/978-3-662-06162-6.

41. Kalil, K. & Dent, E. W. Branch management: mechanisms of axon branching in the developing vertebrate CNS. *Nat. Rev. Neurosci.* **15**, 7–18 (2014).
42. Lewis, T. L., Courchet, J. & Polleux, F. Cellular and molecular mechanisms underlying axon formation, growth, and branching. *J. Cell Biol.* **202**, 837–848 (2013).
43. Guerrier, S. *et al.* The F-BAR Domain of srGAP2 Induces Membrane Protrusions Required for Neuronal Migration and Morphogenesis. *Cell* **138**, 990–1004 (2009).
44. Cooper, J. A. Mechanisms of cell migration in the nervous system. *J. Cell Biol.* **202**, 725–734 (2013).
45. López-Bendito, G. & Molnár, Z. Thalamocortical development: how are we going to get there? *Nat. Rev. Neurosci.* **4**, 276–289 (2003).
46. Stanfield, B. B., O’Leary, D. D. M. & Fricks, C. Selective collateral elimination in early postnatal development restricts cortical distribution of rat pyramidal tract neurones. *Nature* **298**, 371–373 (1982).
47. McLaughlin, T. & O’Leary, D. D. M. Molecular gradients and development of retinotopic maps. *Annu. Rev. Neurosci.* **28**, 327–55 (2005).
48. Spillane, M., Ketschek, A., Merianda, T. T., Twiss, J. L. & Gallo, G. Mitochondria Coordinate Sites of Axon Branching through Localized Intra-axonal Protein Synthesis. *Cell Rep.* **5**, 1564–1575 (2013).
49. Courchet, J. *et al.* Terminal Axon Branching Is Regulated by the LKB1-NUAK1 Kinase Pathway via Presynaptic Mitochondrial Capture. *Cell* **153**, 1510–1525 (2013).
50. Moradi, M. *et al.* Differential roles of α -, β -, and γ -actin in axon growth and collateral branch formation in motoneurons. *J. Cell Biol.* **216**, 793–814 (2017).
51. Cui-Wang, T. *et al.* Local zones of endoplasmic reticulum complexity confine cargo in neuronal dendrites. *Cell* **148**, 309–321 (2012).
52. Winkle, C. C. *et al.* A novel netrin-1-sensitive mechanism promotes local SNARE-mediated exocytosis during axon branching. *J. Cell Biol.* **205**, 217–232 (2014).
53. Plooster, M. *et al.* TRIM9-dependent ubiquitination of DCC constrains kinase signaling, exocytosis, and axon branching. *Mol. Biol. Cell* **28**, 2374–2385 (2017).
54. Shimojo, M. *et al.* SNAREs Controlling Vesicular Release of BDNF and Development of Callosal Axons. *Cell Rep.* **11**, 1054–1066 (2015).
55. Schmidt, H. *et al.* The receptor guanylyl cyclase Npr2 is essential for sensory axon bifurcation within the spinal cord. *J. Cell Biol.* **179**, 331–40 (2007).
56. Ma, L. & Tessier-Lavigne, M. Dual branch-promoting and branch-repelling actions of Slit/Robo signaling on peripheral and central branches of developing sensory axons. *J. Neurosci.* **27**, 6843–51 (2007).
57. Armijo-Weingart, L. & Gallo, G. It takes a village to raise a branch: Cellular mechanisms of the initiation of axon collateral branches. *Mol. Cell. Neurosci.* **84**, 36–47 (2016).
58. Gibson, D. A. & Ma, L. Developmental regulation of axon branching in the vertebrate nervous system. *Development* **138**, 183–195 (2011).
59. Ketschek, A. & Gallo, G. Nerve growth factor induces axonal filopodia through localized microdomains of phosphoinositide 3-kinase activity that drive the formation of cytoskeletal precursors to filopodia. *J. Neurosci.* **30**, 12185–12197 (2010).

60. Spillane, M. *et al.* Nerve Growth Factor-Induced Formation of Axonal Filopodia and Collateral Branches Involves the Intra-Axonal Synthesis of Regulators of the Actin-Nucleating Arp2/3 Complex. *J. Neurosci.* **32**, 17671–17689 (2012).
61. Leondaritis, G. & Eickholt, B. J. Short Lives with Long-Lasting Effects: Filopodia Protrusions in Neuronal Branching Morphogenesis. *PLoS Biol.* **13**, e1002241 (2015).
62. Flynn, K. C., Pak, C. W., Shaw, A. E., Bradke, F. & Bamberg, J. R. Growth cone-like waves transport actin and promote axonogenesis and neurite branching. *Dev. Neurobiol.* **69**, 761–779 (2009).
63. Withers, G. S. & Wallace, C. S. Transient lamellipodia predict sites of dendritic branch formation in hippocampal neurons. *Cell Tissue Res.* (2020) doi:10.1007/s00441-020-03194-w.
64. Yu, W. *et al.* The Microtubule-severing Proteins Spastin and Katanin Participate Differently in the Formation of Axonal Branches. *Mol. Biol. Cell* **19**, 1485–1498 (2008).
65. Basnet, N. *et al.* Direct induction of microtubule branching by microtubule nucleation factor SSNA1. *Nat. Cell Biol.* **20**, 1172–1180 (2018).
66. Dent, E. W. & Kalil, K. Axon branching requires interactions between dynamic microtubules and actin filaments. *J. Neurosci.* **21**, 9757–69 (2001).
67. Ketschek, A. *et al.* Drebrin coordinates the actin and microtubule cytoskeleton during the initiation of axon collateral branches. *Dev. Neurobiol.* 1092–1110 (2016) doi:10.1002/dneu.22377.
68. Peris, L. *et al.* A key function for microtubule-associated-protein 6 in activity-dependent stabilisation of actin filaments in dendritic spines. *Nat. Commun.* **9**, (2018).
69. Gallo, G. & Letourneau, P. C. Different Contributions of Microtubule Dynamics and Transport to the Growth of Axons and Collateral Sprouts. *J. Neurosci.* **19**, 3860–3873 (1999).
70. Tymanskyj, S. R., Yang, B., Fahnkar, A., Lepore, A. C. & Ma, L. MAP7 regulates axon collateral branch development in dorsal root ganglion neurons. *J. Neurosci.* **37**, 1648–1661 (2017).
71. Tymanskyj, S. R. & Ma, L. MAP7 Prevents Axonal Branch Retraction by Creating a Stable Microtubule Boundary to Rescue Polymerization. *J. Neurosci.* **39**, 7118–7131 (2019).
72. Hu, J. *et al.* Septin-driven coordination of actin and microtubule remodeling regulates the collateral branching of axons. *Curr. Biol.* **22**, 1109–1115 (2012).
73. Willige, D. *et al.* Cytolinker Gas2L1 regulates axon morphology through microtubule-modulated actin stabilization. *EMBO Rep.* **20**, 1–20 (2019).
74. Agi, E., Kulkarni, A. & Hiesinger, P. R. Neuronal strategies for meeting the right partner during brain wiring. *Curr. Opin. Neurobiol.* **63**, 1–8 (2020).
75. Grueber, W. B. & Sagasti, A. Self-avoidance and Tiling: Mechanisms of Dendrite and Axon Spacing. *Cold Spring Harb. Perspect. Biol.* **2**, a001750–a001750 (2010).
76. Riccomagno, M. M. & Kolodkin, A. L. Sculpting Neural Circuits by Axon and Dendrite Pruning. *Annu. Rev. Cell Dev. Biol.* **31**, 779–805 (2015).
77. Southwell, D. G. *et al.* Intrinsically determined cell death of developing cortical interneurons. *Nature* **491**, 109–113 (2012).
78. Braitenberg, V. & Schüz, A. *Cortex: Statistics and Geometry of Neuronal Connectivity*. *Cortex: Statistics and Geometry of Neuronal Connectivity* (Springer Berlin Heidelberg, 1998).

79. Dumitriu, D., Cossart, R., Huang, J. & Yuste, R. Correlation between axonal morphologies and synaptic input kinetics of interneurons from mouse visual cortex. *Cereb. Cortex* **17**, 81–91 (2007).
80. Winnubst, J. *et al.* Reconstruction of 1,000 Projection Neurons Reveals New Cell Types and Organization of Long-Range Connectivity in the Mouse Brain. *Cell* **179**, 268–281.e13 (2019).
81. Baas, P. W., Deitch, J. S., Black, M. M. & Banker, G. A. Polarity orientation of microtubules in hippocampal neurons: uniformity in the axon and nonuniformity in the dendrite. *Proc. Natl. Acad. Sci. U. S. A.* **85**, 8335–9 (1988).
82. Kollins, K. M., Bell, R. L., Butts, M. & Withers, G. S. Dendrites differ from axons in patterns of microtubule stability and polymerization during development. *Neural Dev.* **4**, 26 (2009).
83. Burute, M. & Kapitein, L. C. Cellular Logistics: Unraveling the Interplay Between Microtubule Organization and Intracellular Transport. *Annu. Rev. Cell Dev. Biol.* **35**, 29–54 (2019).
84. Farías, G. G. *et al.* Feedback-Driven Mechanisms between Microtubules and the Endoplasmic Reticulum Instruct Neuronal Polarity. *Neuron* **102**, 184–201.e8 (2019).
85. Albus, C. A., Rishal, I. & Fainzilber, M. Cell length sensing for neuronal growth control. *Trends Cell Biol.* **23**, 305–310 (2013).
86. Morris, R. L. & Hollenbeck, P. J. The regulation of bidirectional mitochondrial transport is coordinated with axonal outgrowth. *J. Cell Sci.* **104**, 917–927 (1993).
87. Hornberg, H. & Holt, C. RNA-binding proteins and translational regulation in axons and growth cones. *Front. Neurosci.* **7**, 81 (2013).
88. Vance, J. E., Campenot, R. B. & Vance, D. E. The synthesis and transport of lipids for axonal growth and nerve regeneration. *Biochim. Biophys. Acta - Mol. Cell Biol. Lipids* **1486**, 84–96 (2000).
89. Lee, Y. *et al.* Oligodendroglia metabolically support axons and contribute to neurodegeneration. *Nature* **487**, 443–448 (2012).
90. Mingorance-Le Meur, A. & O'Connor, T. P. Neurite consolidation is an active process requiring constant repression of protrusive activity. *EMBO J.* **28**, 248–260 (2009).
91. Sun, Y. C. *et al.* Integrating barcoded neuroanatomy with spatial transcriptional profiling enables identification of gene correlates of projections. *Nat. Neurosci.* **24**, 873–885 (2021).
92. Buzsáki, G. & Mizuseki, K. The log-dynamic brain: how skewed distributions affect network operations. *Nat. Rev. Neurosci.* **15**, 264–278 (2014).
93. Betzel, R. F. & Bassett, D. S. Specificity and robustness of long-distance connections in weighted, interareal connectomes. *Proc. Natl. Acad. Sci.* **115**, E4880 LP-E4889 (2018).
94. Polleux, F., Ince-Dunn, G. & Ghosh, A. Transcriptional regulation of vertebrate axon guidance and synapse formation. *Nat. Rev. Neurosci.* **8**, 331–340 (2007).
95. Parrish, J. Z., Kim, M. D., Jan, L. Y. & Jan, Y. N. Genome-wide analyses identify transcription factors required for proper morphogenesis of *Drosophila* sensory neuron dendrites. *Genes Dev.* **20**, 820–835 (2006).
96. Yao, Z. *et al.* A taxonomy of transcriptomic cell types across the isocortex and hippocampal formation. *Cell* **184**, 3222–3241.e26 (2021).
97. Leterrier, C. The Axon Initial Segment: An Updated Viewpoint. *J. Neurosci.* **38**, 2135–2145 (2018).

98. Holland, S. M. & Thomas, G. M. Roles of palmitoylation in axon growth, degeneration and regeneration. *J. Neurosci. Res.* **95**, 1528–1539 (2017).
99. Tortosa, E. *et al.* Dynamic Palmitoylation Targets MAP6 to the Axon to Promote Microtubule Stabilization during Neuronal Polarization. *Neuron* **94**, 809-825.e7 (2017).
100. Tedeschi, A. *et al.* ADF/Cofilin-Mediated Actin Turnover Promotes Axon Regeneration in the Adult CNS. *Neuron* **103**, 1073-1085.e6 (2019).
101. Hall, A. & Lalli, G. Rho and Ras GTPases in axon growth, guidance, and branching. *Cold Spring Harb. Perspect. Biol.* **2**, 1–18 (2010).
102. Stankiewicz, T. R. & Linseman, D. A. Rho family GTPases: Key players in neuronal development, neuronal survival, and neurodegeneration. *Front. Cell. Neurosci.* **8**, 1–14 (2014).
103. Dong, X., Shen, K. & Bülow, H. E. Intrinsic and Extrinsic Mechanisms of Dendritic Morphogenesis. *Annu. Rev. Physiol.* **77**, 271–300 (2015).
104. O’Donnell, M., Chance, R. K. & Bashaw, G. J. Axon growth and guidance: Receptor regulation and signal transduction. *Annu. Rev. Neurosci.* **32**, 383–412 (2009).
105. Fincher, J., Whiteneck, C. & Birgbauer, E. G-Protein-Coupled Receptor Cell Signaling Pathways Mediating Embryonic Chick Retinal Growth Cone Collapse Induced by Lysophosphatidic Acid and Sphingosine-1-Phosphate. *Dev. Neurosci.* **36**, 443–453 (2014).
106. Leyva-Díaz, E. *et al.* FLRT3 Is a Robo1-Interacting Protein that Determines Netrin-1 Attraction in Developing Axons. *Curr. Biol.* **24**, 494–508 (2014).
107. Poulain, F. E. & Yost, H. J. Heparan sulfate proteoglycans: a sugar code for vertebrate development? *Development* **142**, 3456–3467 (2015).
108. Santiago-Medina, M., Gregus, K. A., Nichol, R. H., O’Toole, S. M. & Gomez, T. M. Regulation of ECM degradation and axon guidance by growth cone invadosomes. *Development* (2015) doi:10.1242/dev.108266.
109. Gomez, T. M. & Zheng, J. Q. The molecular basis for calcium-dependent axon pathfinding. *Nat. Rev. Neurosci.* **7**, 115–125 (2006).
110. Spillane, M. & Gallo, G. Involvement of Rho-family GTPases in axon branching. *Small GTPases* **5**, e27974 (2014).
111. Goldberg, J. L. *et al.* Retinal Ganglion Cells Do Not Extend Axons by Default. *Neuron* **33**, 689–702 (2002).
112. Ohnami, S. *et al.* Role of RhoA in Activity-Dependent Cortical Axon Branching. *J. Neurosci.* **28**, 9117–9121 (2008).
113. Hutchins, B. I. & Kalil, K. Differential Outgrowth of Axons and their Branches Is Regulated by Localized Calcium Transients. *J. Neurosci.* **28**, 143–153 (2008).
114. Ruthazer, E. S., Li, J. & Cline, H. Stabilization of Axon Branch Dynamics by Synaptic Maturation. *J. Neurosci.* **26**, 3594–3603 (2006).
115. Uesaka, N., Hayano, Y., Yamada, A. & Yamamoto, N. Interplay between Laminar Specificity and Activity-Dependent Mechanisms of Thalamocortical Axon Branching. *J. Neurosci.* **27**, 5215 LP – 5223 (2007).
116. Cline, H. & Haas, K. The regulation of dendritic arbor development and plasticity by glutamatergic synaptic input: a review of the synaptotrophic hypothesis. *J. Physiol.* **586**, 1509–1517 (2008).

117. Ledda, F. & Paratcha, G. Mechanisms regulating dendritic arbor patterning. *Cell. Mol. Life Sci.* **74**, 4511–4537 (2017).
118. Almén, M. S., Nordström, K. J. V, Fredriksson, R. & Schiöth, H. B. Mapping the human membrane proteome: a majority of the human membrane proteins can be classified according to function and evolutionary origin. *BMC Biol.* **7**, 50 (2009).
119. Seiradake, E., Jones, E. Y. & Klein, R. *Structural Perspectives on Axon Guidance. Annual Review of Cell and Developmental Biology* vol. 32 (2016).
120. Boyer, N. P. & Gupton, S. L. Revisiting netrin-1: One who guides (Axons). *Front. Cell. Neurosci.* **12**, 1–18 (2018).
121. Vanhaesebroeck, B., Stephens, L. & Hawkins, P. PI3K signalling: the path to discovery and understanding. *Nat. Rev. Mol. Cell Biol.* **13**, 195–203 (2012).
122. Lee, Y. R., Chen, M. & Pandolfi, P. P. The functions and regulation of the PTEN tumour suppressor: new modes and prospects. *Nat. Rev. Mol. Cell Biol.* **19**, 1–16 (2018).
123. Rademacher, S. & Eickholt, B. J. PTEN in autism and neurodevelopmental disorders. *Cold Spring Harb. Perspect. Med.* **9**, 1–18 (2019).
124. Martin-Belmonte, F. *et al.* PTEN-mediated apical segregation of phosphoinositides controls epithelial morphogenesis through Cdc42. *Cell* **128**, 383–397 (2007).
125. Haugh, J. M., Codazzi, F., Teruel, M. & Meyer, T. Spatial sensing in fibroblasts mediated by 3' phosphoinositides. *J. Cell Biol.* **151**, 1269–1279 (2000).
126. Iijima, M., Huang, Y. E. & Devreotes, P. Temporal and spatial regulation of chemotaxis. *Dev. Cell* **3**, 469–478 (2002).
127. Kakumoto, T. & Nakata, T. Optogenetic Control of PIP3: PIP3 Is Sufficient to Induce the Actin-Based Active Part of Growth Cones and Is Regulated via Endocytosis. *PLoS One* **8**, 1–17 (2013).
128. Kath, C. *et al.* PTEN suppresses axon outgrowth by downregulating the level of deetyrosinated microtubules. *PLoS One* **13**, 1–18 (2018).
129. Akiyama, H. & Kamiguchi, H. Phosphatidylinositol 3-Kinase Facilitates Microtubule-dependent Membrane Transport for Neuronal Growth Cone Guidance. *J. Biol. Chem.* **285**, 41740–41748 (2010).
130. Amiri, A. *et al.* Pten Deletion in Adult Hippocampal Neural Stem/Progenitor Cells Causes Cellular Abnormalities and Alters Neurogenesis. *J. Neurosci.* **32**, 5880–5890 (2012).
131. Wong, F. K. *et al.* Pyramidal cell regulation of interneuron survival sculpts cortical networks. *Nature* **557**, 668–673 (2018).
132. Chadborn, N. H. *et al.* PTEN couples Sema3A signalling to growth cone collapse. *J. Cell Sci.* **119**, 951–7 (2006).
133. Christie, K. J., Webber, C. A., Martinez, J. A., Singh, B. & Zochodne, D. W. PTEN Inhibition to Facilitate Intrinsic Regenerative Outgrowth of Adult Peripheral Axons. *J. Neurosci.* **30**, 9306–9315 (2010).
134. Drinjakovic, J. *et al.* E3 Ligase Nedd4 Promotes Axon Branching by Downregulating PTEN. *Neuron* **65**, 341–357 (2010).
135. Zhang, Y. *et al.* The MicroRNA-17-92 Cluster Enhances Axonal Outgrowth in Embryonic Cortical Neurons. *J. Neurosci.* **33**, 6885–6894 (2013).

136. Gallo, G. *Mechanisms Underlying the Initiation and Dynamics of Neuronal Filopodia. From Neurite Formation to Synaptogenesis. International Review of Cell and Molecular Biology* vol. 301 (Elsevier, 2013).
137. Horiguchi, K., Hanada, T., Fukui, Y. & Chishti, A. H. Transport of PIP3 by GAKIN, a kinesin-3 family protein, regulates neuronal cell polarity. *J. Cell Biol.* **174**, 425–436 (2006).
138. Kreis, P., Leondaritis, G., Lieberam, I. & Eickholt, B. J. Subcellular targeting and dynamic regulation of PTEN: implications for neuronal cells and neurological disorders. *Front. Mol. Neurosci.* **7**, 23 (2014).
139. Menager, C., Arimura, N., Fukata, Y. & Kaibuchi, K. PIP3 is involved in neuronal polarization and axon formation. *J Neurochem* **89**, 109–118 (2004).
140. Shi, S. H., Jan, L. Y. & Jan, Y. N. Hippocampal neuronal polarity specified by spatially localized mPar3/mPar6 and PI 3-kinase activity. *Cell* vol. 112 63–75 (2003).
141. Kuiper, J. W. P., Sun, C., Magalhães, M. A. O. & Glogauer, M. Rac regulates PtdInsP3 signaling and the chemotactic compass through a redox-mediated feedback loop. *Blood* **118**, 6164–6171 (2011).
142. Schink, K. O., Tan, K.-W. & Stenmark, H. Phosphoinositides in Control of Membrane Dynamics. *Annu. Rev. Cell Dev. Biol.* **32**, 143–171 (2016).
143. Balla, T., Wymann, M. & York, J. D. *Phosphoinositides II: The Diverse Biological Functions.* vol. 59 (Springer Netherlands, 2012).
144. Falkenburger, B. H., Jensen, J. B., Dickson, E. J., Suh, B.-C. & Hille, B. Phosphoinositides: lipid regulators of membrane proteins. *J. Physiol.* **588**, 3179–3185 (2010).
145. Zhang, H. *et al.* PIP2 Activates KCNQ Channels, and Its Hydrolysis Underlies Receptor-Mediated Inhibition of M Currents. *Neuron* **37**, 963–975 (2003).
146. Suh, B.-C. & Hille, B. PIP2 Is a Necessary Cofactor for Ion Channel Function: How and Why? *Annu. Rev. Biophys.* **37**, 175–195 (2008).
147. Logothetis, D. E., Jin, T., Lupyán, D. & Rosenhouse-Dantsker, A. Phosphoinositide-mediated gating of inwardly rectifying K⁺ channels. *Pflügers Arch. - Eur. J. Physiol.* **455**, 83–95 (2007).
148. Rohacs, T. Phosphoinositide regulation of non-canonical transient receptor potential channels. *Cell Calcium* **45**, 554–565 (2009).
149. McLaughlin, S., Wang, J., Gambhir, A. & Murray, D. PIP2 and proteins: interactions, organization, and information flow. *Annu. Rev. Biophys. Biomol. Struct.* **31**, 151–75 (2002).
150. McLaughlin, S. & Murray, D. Plasma membrane phosphoinositide organization by protein electrostatics. *Nature* **438**, 605–611 (2005).
151. Yung, Y. C., Stoddard, N. C., Mirendil, H. & Chun, J. Lysophosphatidic Acid Signaling in the Nervous System. *Neuron* **85**, 669–682 (2015).
152. Bräuer, A. U. *et al.* A new phospholipid phosphatase, PRG-1, is involved in axon growth and regenerative sprouting. *Nat. Neurosci.* **6**, 572–578 (2003).
153. McDermott, M. I., Sigal, Y. J., Sciorra, V. a & Morris, A. J. Is PRG-1 a new lipid phosphatase? *Nat. Neurosci.* **7**, 789; author reply 789-90 (2004).
154. Bräuer, A. U. *et al.* Reply to ‘Is PRG-1 a new lipid phosphatase?’ *Nat. Neurosci.* **7**, 789–790 (2004).

155. Sigal, Y. J., Quintero, O. a, Cheney, R. E. & Morris, A. J. Cdc42 and ARP2/3-independent regulation of filopodia by an integral membrane lipid-phosphatase-related protein. *J. Cell Sci.* **120**, 340–52 (2007).
156. Wu, C. *et al.* BioGPS: an extensible and customizable portal for querying and organizing gene annotation resources. *Genome Biol* vol. 10 R130 (2009).
157. Hruz, T. *et al.* Genevestigator V3: A Reference Expression Database for the Meta-Analysis of Transcriptomes. *Adv. Bioinformatics* **2008**, 1–5 (2008).
158. Zhang, Y. *et al.* An RNA-sequencing transcriptome and splicing database of glia, neurons, and vascular cells of the cerebral cortex. *J. Neurosci.* **34**, 11929–11947 (2014).
159. Gaaya, A. *et al.* Plasticity-related gene-1 inhibits lysophosphatidic acid-induced vascular smooth muscle cell migration and proliferation and prevents neointima formation. *Am J Physiol Cell Physiol* **303**, C1104-14 (2012).
160. Trimbuch, T. *et al.* Synaptic PRG-1 modulates excitatory transmission via lipid phosphate-mediated signaling. *Cell* **138**, 1222–1235 (2009).
161. Vogt, J. *et al.* Molecular cause and functional impact of altered synaptic lipid signaling due to a prg-1 gene SNP. *EMBO Mol Med* **8**, 25–38 (2015).
162. Geist, B., Vorwerk, B., Coiro, P., Ninnemann, O. & Nitsch, R. PRG-1 transcriptional regulation independent from Nex1/Math2-mediated activation. *Cell Mol Life Sci* **69**, 651–661 (2012).
163. Velmans, T. *et al.* Plasticity-related gene 3 promotes neurite shaft protrusion. *BMC Neurosci.* **14**, 36 (2013).
164. Brauer, A. U. *et al.* A new phospholipid phosphatase, PRG-1, is involved in axon growth and regenerative sprouting. *Nat Neurosci* **6**, 572–578 (2003).
165. Coiro, P., Stoenica, L., Strauss, U. & Brauer, A. U. Plasticity-related gene 5 promotes spine formation in murine hippocampal neurons. *J Biol Chem* **289**, 24956–24970 (2014).
166. Broggin, T. *et al.* Plasticity Related Gene 3 (PRG3) overcomes myelin-associated growth inhibition and promotes functional recovery after spinal cord injury. *Aging (Albany. NY)*. **8**, 1–25 (2016).
167. Cheng, J. *et al.* Precise Somatotopic Thalamocortical Axon Guidance Depends on LPA-Mediated PRG-2/Radixin Signaling. *Neuron* **92**, 126–142 (2016).
168. van Coevorden-Hameete, M. H. *et al.* Plasticity-related gene 5: A novel surface autoantigen in paraneoplastic cerebellar degeneration. *Neurol. Neuroimmunol. Neuroinflammation* **2**, e156–e156 (2015).
169. Fink, K. L., López-Giráldez, F., Kim, I.-J., Strittmatter, S. M. & Cafferty, W. B. J. Identification of Intrinsic Axon Growth Modulators for Intact CNS Neurons after Injury. *Cell Rep.* **18**, 2687–2701 (2017).
170. Peeva, G. P. *et al.* Improved outcome of facial nerve repair in rats is associated with enhanced regenerative response of motoneurons and augmented neocortical plasticity. *Eur. J. Neurosci.* **24**, 2152–2162 (2006).
171. Ni, H., Jiang, Y. wu, Tao, L. yang, Jin, M. fang & Wu, X. ru. ZnT-1, ZnT-3, CaMK II, PRG-1 expressions in hippocampus following neonatal seizure-induced cognitive deficit in rats. *Toxicol. Lett.* **184**, 145–150 (2009).

172. Ni, H., Feng, X., Xiao, Z. J., Tao, L. Y. & Jin, M. F. Dynamic pattern of gene expression of ZnT-4, caspase-3, LC3, and PRG-3 in rat cerebral cortex following flurothyl-induced recurrent neonatal seizures. *Biol. Trace Elem. Res.* **143**, 1607–1615 (2011).
173. Savaskan, N. E., Bräuer, A. U. & Nitsch, R. Molecular cloning and expression regulation of PRG-3, a new member of the plasticity-related gene family. *Eur. J. Neurosci.* **19**, 212–220 (2004).
174. Sun, Y. *et al.* Effects of Melatonin on Neurobehavior and Cognition in a Cerebral Palsy Model of *plppr5*^{-/-} Mice. *Front. Endocrinol. (Lausanne)*. **12**, 1–15 (2021).
175. Bao, Y. *et al.* Transcriptome profiling revealed multiple genes and ECM-receptor interaction pathways that may be associated with breast cancer. *Cell. Mol. Biol. Lett.* **24**, 38 (2019).
176. Aaberg-Jessen, C. *et al.* Co-expression of TIMP-1 and its cell surface binding partner CD63 in glioblastomas. *BMC Cancer* **18**, 270 (2018).
177. Fan, Z. *et al.* PRG3 induces Ras-dependent oncogenic cooperation in gliomas. *Oncotarget* **7**, 26692–708 (2016).
178. Boonsongserm, P. *et al.* Tumor-induced DNA methylation in the white blood cells of patients with colorectal cancer. *Oncol. Lett.* **18**, 3039–3048 (2019).
179. Li, Y. *et al.* Exome analysis reveals differentially mutated gene signatures of stage, grade and subtype in breast cancers. *PLoS One* **10**, e0119383–e0119383 (2015).
180. Sagiv, E. *et al.* Targeting CD24 for Treatment of Colorectal and Pancreatic Cancer by Monoclonal Antibodies or Small Interfering RNA. *Cancer Res.* **68**, 2803–2812 (2008).
181. Talukder, A. K., Agarwal, M., Buetow, K. H. & Denèfle, P. P. Tracking Cancer Genetic Evolution using OncoTrack. *Sci. Rep.* **6**, 29647 (2016).
182. Orentas, R. J. *et al.* Identification of cell surface proteins as potential immunotherapy targets in 12 pediatric cancers. *Front. Oncol.* **2**, 194 (2012).
183. Zang, D. *et al.* LPPR4 promotes peritoneal metastasis via Sp1/integrin α /FAK signaling in gastric cancer. *Am J Cancer Res* **10**, 1026–1044 (2020).
184. Unichenko, P. *et al.* Plasticity-Related Gene 1 Affects Mouse Barrel Cortex Function via Strengthening of Glutamatergic Thalamocortical Transmission. *Cereb. Cortex* **26**, 3260–72 (2016).
185. Brogгинi, T., Nitsch, R. & Savaskan, N. E. Plasticity-related Gene 5 (PRG5) Induces Filopodia and Neurite Growth and Impedes Lysophosphatidic Acid- and Nogo-A-mediated Axonal Retraction. *Mol. Biol. Cell* **21**, 521–537 (2010).
186. Yu, P. *et al.* Cooperative interactions of LPPR family members in membrane localization and alteration of cellular morphology. *J Cell Sci* **128**, 3210–3222 (2015).
187. Liu, X. *et al.* PRG-1 Regulates Synaptic Plasticity via Intracellular PP2A/ β 1-Integrin Signaling. *Dev. Cell* 1–16 (2016) doi:10.1016/j.devcel.2016.06.019.
188. Kimmelman, J., Mogil, J. S. & Dirnagl, U. Distinguishing between Exploratory and Confirmatory Preclinical Research Will Improve Translation. *PLoS Biol.* **12**, 12–15 (2014).
189. Wang, X., He, Y., Zhang, Q., Ren, X. & Zhang, Z. Direct Comparative Analyses of 10X Genomics Chromium and Smart-seq2. *Genomics. Proteomics Bioinformatics* (2021) doi:https://doi.org/10.1016/j.gpb.2020.02.005.
190. Yao, Z. *et al.* A taxonomy of transcriptomic cell types across the isocortex and hippocampal formation. *bioRxiv* (2020) doi:10.1101/2020.03.30.015214.

191. Dudok, B. *et al.* Alternating sources of perisomatic inhibition during behavior. *Neuron* **109**, 997-1012.e9 (2021).
192. Samata, B. *et al.* L1CAM Is a Marker for Enriching Corticospinal Motor Neurons in the Developing Brain . *Frontiers in Cellular Neuroscience* vol. 14 31 (2020).
193. Cheng, J. *et al.* Precise Somatotopic Thalamocortical Axon Guidance Depends on LPA-Mediated PRG-2 / Radixin Signaling. 1–17 (2016).
194. Caputi, A., Melzer, S., Michael, M. & Monyer, H. The long and short of GABAergic neurons. *Curr. Opin. Neurobiol.* **23**, 179–186 (2013).
195. Leranth, C., Carpi, D., Buzsaki, G. & Kiss, J. The entorhino-septo-supramammillary nucleus connection in the rat: morphological basis of a feedback mechanism regulating hippocampal theta rhythm. *Neuroscience* **88**, 701–718 (1999).
196. Unal, G. *et al.* Spatio-temporal specialization of GABAergic septo-hippocampal neurons for rhythmic network activity. *Brain Struct. Funct.* **223**, 2409–2432 (2018).
197. Brosig, A. *et al.* The Axonal Membrane Protein PRG2 Inhibits PTEN and Directs Growth to Branches. *Cell Rep.* **29**, 2028-2040.e8 (2019).
198. Heintzmann, R. & Huser, T. Super-Resolution Structured Illumination Microscopy. *Chem. Rev.* **117**, 13890–13908 (2017).
199. Demmerle, J. *et al.* Strategic and practical guidelines for successful structured illumination microscopy. *Nat. Protoc.* **12**, 988–1010 (2017).
200. Fan, J., Huang, X., Li, L., Tan, S. & Chen, L. A protocol for structured illumination microscopy with minimal reconstruction artifacts. *Biophys. Reports* **5**, 80–90 (2019).
201. Wen, G. *et al.* High-fidelity structured illumination microscopy by point-spread-function engineering. *Light Sci. Appl.* **10**, (2021).
202. Madeira, F. *et al.* The EMBL-EBI search and sequence analysis tools APIs in 2019. *Nucleic Acids Res.* **47**, W636–W641 (2019).
203. Katoh, K. & Standley, D. M. MAFFT multiple sequence alignment software version 7: Improvements in performance and usability. *Mol. Biol. Evol.* **30**, 772–780 (2013).
204. Tokumitsu, H. *et al.* Identification and characterization of PRG-1 as a neuronal calmodulin-binding protein. *Biochem J* **431**, 81–91 (2010).
205. Jiang, W. & Hunter, T. Analysis of cell-cycle profiles in transfected cells using a membrane-targeted GFP. *Biotechniques* **24**, 349–50, 352, 354 (1998).
206. Brosig, A. Analysis of a PTEN-associated protein scaffold containing the transmembrane protein PRG2. (Freie Universität Berlin, 2018).
207. Xu, C. & Ng, D. T. W. Glycosylation-directed quality control of protein folding. *Nat. Rev. Mol. Cell Biol.* **16**, 742–752 (2015).
208. Barilà, D. *et al.* The Dri 42 gene, whose expression is up-regulated during epithelial differentiation, encodes a novel endoplasmic reticulum resident transmembrane protein. *J. Biol. Chem.* **271**, 29928–29936 (1996).
209. Zhang, Q. X., Pilquil, C. S., Dewald, J., Berthiaume, L. G. & Brindley, D. N. Identification of structurally important domains of lipid phosphate phosphatase-1: Implications for its sites of action. *Biochem. J.* **345**, 181–184 (2000).

210. Rocks, O. *et al.* An acylation cycle regulates localization and activity of palmitoylated ras isoforms. *Science (80-.)*. **307**, 1746–1752 (2005).
211. Rocks, O. *et al.* The palmitoylation machinery is a spatially organizing system for peripheral membrane proteins. *Cell* **141**, 458–471 (2010).
212. Charollais, J. & Van Der Goot, F. G. Palmitoylation of membrane proteins. *Mol. Membr. Biol.* **26**, 55–66 (2009).
213. Ren, J. *et al.* CSS-Palm 2.0: An updated software for palmitoylation sites prediction. *Protein Eng. Des. Sel.* **21**, 639–644 (2008).
214. Michelsen, K., Yuan, H. & Schwappach, B. Hide and run. *EMBO Rep.* **6**, 717–722 (2005).
215. Scott, D. B., Blanpied, T. A. & Ehlers, M. D. Coordinated PKA and PKC phosphorylation suppresses RXR-mediated ER retention and regulates the surface delivery of NMDA receptors. *Neuropharmacology* **45**, 755–767 (2003).
216. Parmar, H. B., Barry, C. & Duncan, R. Polybasic trafficking signal mediates golgi export, ER retention or ER export and retrieval based on membrane-proximity. *PLoS One* **9**, 1–10 (2014).
217. Shiwarski, D. J., Crilly, S. E., Dates, A. & Puthenveedu, M. A. Dual RXR motifs regulate nerve growth factor-mediated intracellular retention of the delta opioid receptor. *Mol. Biol. Cell* **30**, 680–690 (2019).
218. Agbaegbu Iwaka, C., Hussein, R. K., Yu, P., Katagiri, Y. & Geller, H. M. The lipid phosphatase-like protein PLPPR1 associates with RhoGDI1 to modulate RhoA activation in response to axon growth inhibitory molecules. *J. Neurochem.* **157**, 494–507 (2021).
219. Petzold, S. *et al.* NT-3 protein levels are enhanced in the hippocampus of PRG1-deficient mice but remain unchanged in PRG1/LPA2 double mutants. *Neurosci Lett* **612**, 145–148 (2016).
220. Fan, J., Jiang, D., Zhao, Y., Liu, J. & Zhang, X. C. Crystal structure of lipid phosphatase Escherichia coli phosphatidylglycerophosphate phosphatase B. *Proc. Natl. Acad. Sci. U. S. A.* **111**, 7636–7640 (2014).
221. Tong, S. *et al.* Structural Insight into Substrate Selection and Catalysis of Lipid Phosphate Phosphatase PgpB in the Cell Membrane. *J. Biol. Chem.* **291**, 18342–18352 (2016).
222. Garneau, J. E. *et al.* The CRISPR/Cas bacterial immune system cleaves bacteriophage and plasmid DNA. *Nature* **468**, 67–71 (2010).
223. Horvath, P. & Barrangou, R. CRISPR/Cas, the immune system of bacteria and archaea. *Science (80-.)*. **327**, 167–170 (2010).
224. Singh, P., Schimenti, J. C. & Bolcun-Filas, E. A Mouse Geneticist’s Practical Guide to CRISPR Applications. *Genetics* **199**, 1–15 (2014).
225. Harms, D. W. *et al.* Mouse Genome Editing Using the CRISPR/Cas System. *Curr Protoc Hum Genet* **83**, 15 7 1-15 7 27 (2014).
226. Lein, E. S. *et al.* Genome-wide atlas of gene expression in the adult mouse brain. *Nature* **445**, 168–176 (2007).
227. Miller, J. A. *et al.* Transcriptional landscape of the prenatal human brain. *Nature* **508**, 199–206 (2014).
228. Sauer, B. & Henderson, N. Site-specific DNA recombination in mammalian cells by the Cre recombinase of bacteriophage P1. *Proc. Natl. Acad. Sci. U. S. A.* **85**, 5166–5170 (1988).

229. Fuchs, J. In vitro and in vivo analyses of Plasticity-Related Gene 2 function in neuronal development. (Charité Universitätsmedizin Berlin, 2015).
230. Chen, F. *et al.* High-frequency genome editing using ssDNA oligonucleotides with zinc-finger nucleases. *Nat. Methods* **8**, 753–755 (2011).
231. Yang, H. *et al.* One-step generation of mice carrying reporter and conditional alleles by CRISPR/cas-mediated genome engineering. *Cell* **154**, 1370–1379 (2013).
232. Schaefer, K. A. *et al.* Unexpected mutations after CRISPR–Cas9 editing in vivo. *Nat. Methods* **14**, 547–548 (2017).
233. Kim, S., Kim, D., Cho, S. W., Kim, J. & Kim, J. S. Highly efficient RNA-guided genome editing in human cells via delivery of purified Cas9 ribonucleoproteins. *Genome Res.* **24**, 1012–1019 (2014).
234. <http://www.sanger.ac.uk/htgt/wge/>; Hodgkins, A. *et al.* WGE: a CRISPR database for genome engineering. *Bioinformatics* (2015) doi:10.1093/bioinformatics/btv308.
235. Cong, L. *et al.* Multiplex genome engineering using CRISPR/Cas systems. *Science (80-.)*. **339**, 819–823 (2013).
236. Chaudhari, H. G. *et al.* Evaluation of Homology-Independent CRISPR-Cas9 Off-Target Assessment Methods. *Cris. J.* **3**, 440–453 (2020).
237. Banan, M. Recent advances in CRISPR/Cas9-mediated knock-ins in mammalian cells. *J. Biotechnol.* **308**, 1–9 (2020).
238. Yao, X. *et al.* Tild-CRISPR Allows for Efficient and Precise Gene Knockin in Mouse and Human Cells. *Dev. Cell* **45**, 526-536.e5 (2018).
239. Miura, H., Gurumurthy, C. B., Sato, T., Sato, M. & Ohtsuka, M. CRISPR/Cas9-based generation of knockdown mice by intronic insertion of artificial microRNA using longer single-stranded DNA. *Sci. Rep.* **5**, 12799 (2015).
240. Quadros, R. M. *et al.* Easi-CRISPR: A robust method for one-step generation of mice carrying conditional and insertion alleles using long ssDNA donors and CRISPR ribonucleoproteins. *Genome Biol.* **18**, 1–15 (2017).
241. Edgar, D., Timpl, R. & Thoenen, H. The heparin-binding domain of laminin is responsible for its effects on neurite outgrowth and neuronal survival. *EMBO J.* **3**, 1463–1468 (1984).
242. Lein, P. J., Banker, G. A. & Higgins, D. Laminin selectively enhances axonal growth and accelerates the development of polarity by hippocampal neurons in culture. *Dev. Brain Res.* **69**, 191–197 (1992).
243. Hashimoto, T. *et al.* Plasticity-related gene 1 is important for survival of neurons derived from rat neural stem cells. *J Neurosci Res* **91**, 1402–1407 (2013).
244. van Diepen, M. T. *et al.* MyosinV controls PTEN function and neuronal cell size. *Nat. Cell Biol.* **11**, 1191–6 (2009).
245. Nieuwenhuis, B. *et al.* PI3-kinase delta enhances axonal PIP3 to support axon regeneration in the adult CNS. *EMBO Mol. Med.* 1–24 (2020) doi:10.15252/emmm.201911674.
246. Shi, Y. *et al.* PTEN is a protein tyrosine phosphatase for IRS1. *Nat. Struct. Mol. Biol.* **21**, 522–527 (2014).
247. Fuchs, J., Eickholt, B. J. & Leondaritis, G. Harnessing PTEN’s Growth Potential in Neuronal Development and Disease. *Neurosci. Insights* **15**, 263310552095905 (2020).

248. Sohal, V. S. & Rubenstein, J. L. R. Excitation-inhibition balance as a framework for investigating mechanisms in neuropsychiatric disorders. *Mol. Psychiatry* **24**, 1248–1257 (2019).
249. Petersen, C. C. H. The Functional Organization of the Barrel Cortex. *Neuron* **56**, 339–355 (2007).
250. Garion, L. *et al.* Texture coarseness responsive neurons and their mapping in layer 2–3 of the rat barrel cortex in vivo. *Elife* **3**, (2014).
251. Witte, H., Neukirchen, D. & Bradke, F. Microtubule stabilization specifies initial neuronal polarization. *J. Cell Biol.* **180**, 619–632 (2008).
252. Inami, Y., Omura, M., Kubota, K. & Konishi, Y. Inhibition of glycogen synthase kinase-3 reduces extension of the axonal leading process by destabilizing microtubules in cerebellar granule neurons. *Brain Res.* **1690**, 51–60 (2018).
253. Srivatsa, S., Parthasarathy, S., Molnár, Z. & Tarabykin, V. Sip1 downstream effector ninein controls neocortical axonal growth, ipsilateral branching, and microtubule growth and stability. *Neuron* **85**, 998–1012 (2015).
254. Gallo, G. The cytoskeletal and signaling mechanisms of axon collateral branching. *Dev. Neurobiol.* **71**, 201–220 (2011).
255. Klein, J. P. & Moeschberger, M. L. *Survival Analysis*. (Springer New York, 2003). doi:10.1007/b97377.
256. Therneau, T. M. & Grambsch, P. M. *Modeling Survival Data: Extending the Cox Model*. (Springer New York, 2000). doi:10.1007/978-1-4757-3294-8.
257. Portera-Cailliau, C., Weimer, R. M., De Paola, V., Caroni, P. & Svoboda, K. Diverse modes of axon elaboration in the developing neocortex. *PLoS Biol.* **3**, (2005).
258. Greenacre, M. & Primicerio, R. *Multivariate Analysis of Ecological Data*. (2013).
259. James, F. C. & McCulloch, C. E. Multivariate analysis in ecology and systematics: Panacea or Pandora's box? *Annu. Rev. Ecol. Syst.* **21**, 129–166 (1990).
260. Greenland, S., Pearl, J. & Robins, J. J. M. Causal Diagrams for Epidemiologic Research. *Epidemiology* **10**, 37–48 (1999).
261. Hernán, M. & Robins, J. *Causal Inference: What If*. (Boca Raton: Chapman & Hall/CRC, 2020).
262. Pearl, J. Causal diagrams for empirical research. *Biometrika* **82**, 669–688 (1995).
263. Suttorp, M. M., Siegerink, B., Jager, K. J., Zoccali, C. & Dekker, F. W. Graphical presentation of confounding in directed acyclic graphs. *Nephrol. Dial. Transplant.* **30**, 1418–1423 (2015).
264. Rohrer, J. M. Thinking Clearly About Correlations and Causation: Graphical Causal Models for Observational Data. *Adv. Methods Pract. Psychol. Sci.* **1**, 27–42 (2018).
265. Pearl, J., Glymour, M. & Jewell, N. P. *Causal Inference in Statistics: A Primer*. (John Wiley & Sons, Inc., 2016).
266. Peters, J., Mooij, J. M., Janzing, D. & Schölkopf, B. Causal discovery with continuous additive noise models. *J. Mach. Learn. Res.* **15**, 2009–2053 (2014).
267. Winans, A. M., Collins, S. R. & Meyer, T. Waves of actin and microtubule polymerization drive microtubule-based transport and neurite growth before single axon formation. *Elife* **5**, 1–22 (2016).
268. Cojoc, D. *et al.* Properties of the Force Exerted by Filopodia and Lamellipodia and the Involvement of Cytoskeletal Components. *PLoS One* **2**, e1072 (2007).

269. Janson, M. E., de Dood, M. E. & Dogterom, M. Dynamic instability of microtubules is regulated by force. *J. Cell Biol.* **161**, 1029–1034 (2003).
270. Dogterom, M. & Koenderink, G. H. Actin-microtubule crosstalk in cell biology. *Nat. Rev. Mol. Cell Biol.* **20**, 38–54 (2019).
271. Conde, C. & Cáceres, A. Microtubule assembly, organization and dynamics in axons and dendrites. *Nat. Rev. Neurosci.* **10**, 319–332 (2009).
272. Su, Y. S. *et al.* Protein 600 is a microtubule/endoplasmic reticulum-associated protein in CNS neurons. *J. Neurosci.* **28**, 3604–3614 (2008).
273. Seno, T. *et al.* Kinesin-1 sorting in axons controls the differential retraction of arbor terminals. *J. Cell Sci.* **129**, 3499–3510 (2016).
274. Fu, X. *et al.* Doublecortin (Dcx) Family Proteins Regulate Filamentous Actin Structure in Developing Neurons. *J. Neurosci.* **33**, 709–721 (2013).
275. Winans, A. M., Collins, S. R. & Meyer, T. Waves of actin and microtubule polymerization drive microtubule-based transport and neurite growth before single axon formation. *Elife* **5**, 1–22 (2016).
276. Kesarwani, S. *et al.* Genetically encoded live-cell sensor for tyrosinated microtubules. *J. Cell Biol.* **219**, (2020).
277. Knafo, S. & Esteban, J. A. PTEN: Local and Global Modulation of Neuronal Function in Health and Disease. *Trends Neurosci.* **40**, 83–91 (2017).
278. Zhang, J., Yang, D., Huang, H., Sun, Y. & Hu, Y. Coordination of Necessary and Permissive Signals by PTEN Inhibition for CNS Axon Regeneration. *Front. Neurosci.* **12**, 558 (2018).
279. Zhang, J. *et al.* SHIP2 controls PtdIns(3,4,5)P3 levels and PKB activity in response to oxidative stress. *Cell. Signal.* **19**, 2194–2200 (2007).
280. Blero, D. *et al.* Phosphatidylinositol 3,4,5-trisphosphate modulation in SHIP2-deficient mouse embryonic fibroblasts. *FEBS J.* **272**, 2512–2522 (2005).
281. Irino, Y., Tokuda, E., Hasegawa, J., Itoh, T. & Takenawa, T. Quantification and visualization of phosphoinositides by quantum dot-labeled specific binding-domain probes. *J. Lipid Res.* **53**, 810–819 (2012).
282. Malek, M. *et al.* PTEN Regulates PI(3,4)P₂ Signaling Downstream of Class I PI3K. *Mol. Cell* 566–580 (2017) doi:10.1016/j.molcel.2017.09.024.
283. Pacheco, J. *et al.* A high-avidity biosensor reveals plasma membrane PI(3,4)P₂ is predominantly a class I PI3K signaling product. *J. Cell Biol.* **218**, jcb.201809026 (2018).
284. Ebner, M., Lučić, I., Leonard, T. A. & Yudushkin, I. PI(3,4,5)P₃ Engagement Restricts Akt Activity to Cellular Membranes. *Mol. Cell* **65**, 416–431.e6 (2017).
285. Liu, S.-L. *et al.* Quantitative Lipid Imaging Reveals a New Signaling Function of Phosphatidylinositol-3,4-Bisphosphate: Isoform- and Site-Specific Activation of Akt. *Mol. Cell* 1–13 (2018) doi:10.1016/j.molcel.2018.07.035.
286. Zhang, S.-X., Duan, L.-H., He, S.-J., Zhuang, G.-F. & Yu, X. Phosphatidylinositol 3,4-bisphosphate regulates neurite initiation and dendrite morphogenesis via actin aggregation. *Cell Res.* **27**, 253–273 (2017).
287. Sharma, V. P. *et al.* Tks5 and SHIP2 Regulate Invadopodium Maturation, but Not Initiation, in Breast Carcinoma Cells. *Curr. Biol.* **23**, 2079–2089 (2013).

288. Krause, M. *et al.* Lamellipodin, an Ena/VASP Ligand, Is Implicated in the Regulation of Lamellipodial Dynamics. *Dev. Cell* **7**, 571–583 (2004).
289. Höglinger, D., Nadler, A. & Schultz, C. Caged lipids as tools for investigating cellular signaling. *Biochim. Biophys. Acta - Mol. Cell Biol. Lipids* **1841**, 1085–1096 (2014).
290. Delos Santos, R. C., Garay, C. & Antonescu, C. N. Charming neighborhoods on the cell surface: Plasma membrane microdomains regulate receptor tyrosine kinase signaling. *Cell. Signal.* **27**, 1963–1976 (2015).
291. Sezgin, E., Levental, I., Mayor, S. & Eggeling, C. The mystery of membrane organization: Composition, regulation and roles of lipid rafts. *Nat. Rev. Mol. Cell Biol.* **18**, 361–374 (2017).
292. Hyman, A. A., Weber, C. A. & Jülicher, F. Liquid-Liquid Phase Separation in Biology. *Annu. Rev. Cell Dev. Biol.* **30**, 39–58 (2014).
293. Levental, I., Levental, K. R. & Heberle, F. A. Lipid Rafts: Controversies Resolved, Mysteries Remain. *Trends Cell Biol.* 1–13 (2020) doi:10.1016/j.tcb.2020.01.009.
294. Stone, M. B., Shelby, S. A., Nñez, M. F., Wisser, K. & Veatch, S. L. Protein sorting by lipid phase-like domains supports emergent signaling function in b lymphocyte plasma membranes. *Elife* **6**, 1–33 (2017).
295. Wang, J. & Richards, D. a. Segregation of PIP2 and PIP3 into distinct nanoscale regions within the plasma membrane. *Biol. Open* **1**, 857–62 (2012).
296. Tong, J. *et al.* Role of GAP-43 in sequestering phosphatidylinositol 4,5-bisphosphate to Raft bilayers. *Biophys. J.* **94**, 125–133 (2008).
297. Chichili, G. R. & Rodgers, W. Cytoskeleton-membrane interactions in membrane raft structure. *Cell. Mol. Life Sci.* **66**, 2319–2328 (2009).
298. Cizmecioglu, O., Ni, J., Xie, S., Zhao, J. J. & Roberts, T. M. Rac1-mediated membrane raft localization of PI3K/p110 β is required for its activation by GPCRs or PTEN loss. *Elife* **5**, 1–21 (2016).
299. Gao, X. *et al.* PI3K/Akt signaling requires spatial compartmentalization in plasma membrane microdomains. *Proc. Natl. Acad. Sci.* **108**, 14509–14514 (2011).
300. Igarashi, M., Honda, A., Kawasaki, A. & Nozumi, M. Neuronal Signaling Involved in Neuronal Polarization and Growth: Lipid Rafts and Phosphorylation. *Front. Mol. Neurosci.* **13**, 1–11 (2020).
301. Hernaiz-Llorens, M., Martínez-Mármol, R., Roselló-Busquets, C. & Soriano, E. One raft to guide them all, and in axon regeneration inhibit them. *Int. J. Mol. Sci.* **22**, (2021).
302. Sciorra, V. A. & Morris, A. J. Sequential Actions of Phospholipase D and Phosphatidic Acid Phosphohydrolase 2b Generate Diglyceride in Mammalian Cells. *Mol. Biol. Cell* **10**, 3863–3876 (1999).
303. Kai, M. *et al.* Lipid phosphate phosphatases 1 and 3 are localized in distinct lipid rafts. *J. Biochem.* **140**, 677–686 (2006).
304. Kusumi, A., Suzuki, K. G. N., Kasai, R. S., Ritchie, K. & Fujiwara, T. K. Hierarchical mesoscale domain organization of the plasma membrane. *Trends Biochem. Sci.* **36**, 604–615 (2011).
305. Lillemeier, B. F., Pfeiffer, J. R., Surviladze, Z., Wilson, B. S. & Davis, M. M. Plasma membrane-associated proteins are clustered into islands attached to the cytoskeleton. *Proc. Natl. Acad. Sci.* **103**, 18992–18997 (2006).

306. Fritzsche, M. *et al.* Self-organizing actin patterns shape membrane architecture but not cell mechanics. *Nat. Commun.* **8**, 14347 (2017).
307. Feng, S. *et al.* A rapidly reversible chemical dimerizer system to study lipid signaling in living cells. *Angew. Chemie - Int. Ed.* **53**, 6720–6723 (2014).
308. Tilve, S. *et al.* Phospholipid phosphatase related 1 (PLPPR1) increases cell adhesion through modulation of Rac1 activity. *Experimental Cell Research* vol. 1 (Elsevier Inc., 2020).
309. Fusco, L. *et al.* Computer vision profiling of neurite outgrowth dynamics reveals spatiotemporal modularity of Rho GTPase signaling. *J. Cell Biol.* **212**, 91–111 (2016).
310. Yanagisawa, M., Nakamura, K. & Taga, T. Roles of lipid rafts in integrin-dependent adhesion and gp130 signalling pathway in mouse embryonic neural precursor cells. *Genes to Cells* **9**, 801–809 (2004).
311. Yaguchi, H. *et al.* TRIM67 protein negatively regulates Ras activity through degradation of 80K-H and induces neuritogenesis. *J. Biol. Chem.* **287**, 12050–12059 (2012).
312. Menon, S. *et al.* The TRIM9/TRIM67 neuronal interactome reveals novel activators of morphogenesis. 1–34 (2020) doi:10.1101/2020.10.02.323980.
313. Menon, S. *et al.* The E3 Ubiquitin Ligase TRIM9 Is a Filopodia Off Switch Required for Netrin-Dependent Axon Guidance. *Dev. Cell* **35**, 698–712 (2015).
314. Winkle, C. C. *et al.* Trim9 Deletion Alters the Morphogenesis of Developing and Adult-Born Hippocampal Neurons and Impairs Spatial Learning and Memory. *J. Neurosci.* **36**, 4940–4958 (2016).
315. Boyer, N. P., McCormick, L. E., Menon, S., Urbina, F. L. & Gupton, S. L. A pair of E3 ubiquitin ligases compete to regulate filopodial dynamics and axon guidance. *J. Cell Biol.* **219**, (2020).
316. Fowler, P. C., Garcia-Pardo, M. E., Simpson, J. C. & O'Sullivan, N. C. Neurodegeneration: The Central Role for ER Contacts in Neuronal Function and Axonopathy, Lessons From Hereditary Spastic Paraplegias and Related Diseases. *Front. Neurosci.* **13**, 1–20 (2019).
317. McMahon, H. T. & Gallop, J. L. Membrane curvature and mechanisms of dynamic cell membrane remodelling. *Nature* **438**, 590–596 (2005).
318. Busch, D. J. *et al.* Intrinsically disordered proteins drive membrane curvature. *Nat Commun* **6**, 7875 (2015).
319. Zhao, H., Pykäläinen, A. & Lappalainen, P. I-BAR domain proteins: Linking actin and plasma membrane dynamics. *Curr. Opin. Cell Biol.* **23**, 14–21 (2011).
320. Yang, C., Hoelzle, M., Disanza, A., Scita, G. & Svitkina, T. Coordination of Membrane and Actin Cytoskeleton Dynamics during Filopodia Protrusion. *PLoS One* **4**, e5678 (2009).
321. Disanza, A. *et al.* CDC42 switches IRSp53 from inhibition of actin growth to elongation by clustering of VASP. *EMBO J.* **32**, 2735–2750 (2013).
322. Khuong, T. M. *et al.* Synaptic PI(3,4,5)P3 is required for Syntaxin1A clustering and neurotransmitter release. *Neuron* **77**, 1097–1108 (2013).
323. Khelashvili, G., Galli, A. & Weinstein, H. Phosphatidylinositol 4,5-bisphosphate (PIP2) lipids regulate the phosphorylation of syntaxin N-terminus by modulating both its position and local structure. *Biochemistry* **51**, 7685–7698 (2012).
324. Buckley, P. T., Khaladkar, M., Kim, J. & Eberwine, J. Cytoplasmic intron retention, function, splicing, and the sentinel RNA hypothesis. *Wiley Interdiscip. Rev. RNA* **5**, 223–230 (2014).

325. Glanzer, J. *et al.* RNA splicing capability of live neuronal dendrites. *Proc. Natl. Acad. Sci. U. S. A.* **102**, 16859 LP – 16864 (2005).
326. Song, A. H. *et al.* A Selective Filter for Cytoplasmic Transport at the Axon Initial Segment. *Cell* **136**, 1148–1160 (2009).
327. Klymchenko, A. S. & Kreder, R. Fluorescent probes for lipid rafts: From model membranes to living cells. *Chem. Biol.* **21**, 97–113 (2014).
328. Danylchuk, D. I., Jouard, P.-H. & Klymchenko, A. S. Targeted Solvatochromic Fluorescent Probes for Imaging Lipid Order in Organelles under Oxidative and Mechanical Stress. *J. Am. Chem. Soc.* **143**, 912–924 (2021).
329. Lorent, J. H. *et al.* Structural determinants and functional consequences of protein affinity for membrane rafts. *Nat. Commun.* **8**, 1219 (2017).
330. Diaz-Rohrer, B. B., Levental, K. R., Simons, K. & Levental, I. Membrane raft association is a determinant of plasma membrane localization. *Proc. Natl. Acad. Sci.* **111**, 8500 LP – 8505 (2014).
331. Furne, C. *et al.* The dependence receptor DCC requires lipid raft localization for cell death signaling. *Proc. Natl. Acad. Sci. U. S. A.* **103**, 4128 LP – 4133 (2006).
332. Lorent, J. H. *et al.* Structural determinants and functional consequences of protein affinity for membrane rafts. *Nat. Commun.* **8**, 1–9 (2017).
333. Liu, Y. *et al.* Sexually dimorphic BDNF signaling directs sensory innervation of the mammary gland. *Science* **338**, 1357–1360 (2012).
334. Pollitt, S. L., Myers, K. R., Yoo, J. & Zheng, J. Q. LIM and SH3 protein 1 localizes to the leading edge of protruding lamellipodia and regulates axon development. *Mol. Biol. Cell* **31**, 2718–2732 (2020).
335. Meyer, M. P. & Smith, S. J. Evidence from *In Vivo* Imaging That Synaptogenesis Guides the Growth and Branching of Axonal Arbors by Two Distinct Mechanisms. *J. Neurosci.* **26**, 3604 LP – 3614 (2006).
336. Krause, M. & Gautreau, A. Steering cell migration: Lamellipodium dynamics and the regulation of directional persistence. *Nat. Rev. Mol. Cell Biol.* **15**, 577–590 (2014).
337. Valiente, M. & Marín, O. Neuronal migration mechanisms in development and disease. *Curr. Opin. Neurobiol.* **20**, 68–78 (2010).
338. Heiman, M. G. & Shaham, S. Twigs into branches: how a filopodium becomes a dendrite. *Curr. Opin. Neurobiol.* **20**, 86–91 (2010).
339. Korobova, F. & Svitkina, T. Molecular Architecture of Synaptic Actin Cytoskeleton in Hippocampal Neurons Reveals a Mechanism of Dendritic Spine Morphogenesis. *Mol. Biol. Cell* **21**, 165–176 (2010).
340. Gascon, E. *et al.* GABA regulates dendritic growth by stabilizing lamellipodia in newly generated interneurons of the olfactory bulb. *J. Neurosci.* **26**, 12956–12966 (2006).
341. Hannezo, E. *et al.* A Unifying Theory of Branching Morphogenesis. *Cell* **171**, 242–255.e27 (2017).
342. Snider, J., Pillai, A. & Stevens, C. F. A Universal Property of Axonal and Dendritic Arbors. *Neuron* **66**, 45–56 (2010).
343. Palavalli, A., Tizón-Escamilla, N., Rupprecht, J.-F. & Lecuit, T. Deterministic and Stochastic Rules of Branching Govern Dendrite Morphogenesis of Sensory Neurons. *Curr. Biol.* 1–14 (2020) doi:10.1016/j.cub.2020.10.054.

344. Castro, A. F. *et al.* Achieving functional neuronal dendrite structure through sequential stochastic growth and retraction. *Elife* **9**, 1–38 (2020).
345. Idevall-Hagren, O. & De Camilli, P. Detection and manipulation of phosphoinositides. *Biochim. Biophys. Acta - Mol. Cell Biol. Lipids* **1851**, 736–745 (2015).
346. Mücksch, F. *et al.* Quantification of phosphoinositides reveals strong enrichment of PIP2 in HIV-1 compared to producer cell membranes. *Sci. Rep.* **9**, 17661 (2019).
347. Yip, S.-C. *et al.* Quantification of PtdIns(3,4,5)P(3) dynamics in EGF-stimulated carcinoma cells: a comparison of PH-domain-mediated methods with immunological methods. *Biochem. J.* **411**, 441–8 (2008).
348. Ueda, Y. & Hayashi, Y. PIP3 Regulates Spinule Formation in Dendritic Spines during Structural Long-Term Potentiation. *J. Neurosci.* **33**, 11040–11047 (2013).
349. Hammond, G. R. V, Schiavo, G. & Irvine, R. F. Immunocytochemical techniques reveal multiple, distinct cellular pools of PtdIns4P and PtdIns(4,5)P(2). *Biochem. J.* **422**, 23–35 (2009).
350. Sampathkumar, C. *et al.* Loss of MeCP2 disrupts cell autonomous and autocrine BDNF signaling in mouse glutamatergic neurons. *Elife* **5**, e19374 (2016).
351. Aktar, S. *et al.* A New Electron Microscopic Method to Observe the Distribution of Phosphatidylinositol 3,4-bisphosphate. *Acta Histochem. Cytochem.* **50**, 141–147 (2017).
352. Götz, R. *et al.* Nanoscale imaging of bacterial infections by sphingolipid expansion microscopy. *Nat. Commun.* **11**, 6173 (2020).
353. Ferreira, T. *et al.* tferr/Scripts: BAR 1.5.1. *Zenodo* doi:10.5281/ZENODO.495245.
354. Meijering, E. *et al.* Design and validation of a tool for neurite tracing and analysis in fluorescence microscopy images. *Cytometry* **58A**, 167–176 (2004).
355. Frangi, A. F., Niessen, W. J., Vincken, K. L. & Viergever, M. A. Multiscale vessel enhancement filtering BT - Medical Image Computing and Computer-Assisted Intervention — MICCAI'98. in (eds. Wells, W. M., Colchester, A. & Delp, S.) 130–137 (Springer Berlin Heidelberg, 1998).
356. Soille, P. *Morphological Image Analysis*. (Springer Berlin Heidelberg, 2004). doi:10.1007/978-3-662-05088-0.
357. Schmitz, S. K. *et al.* Automated analysis of neuronal morphology, synapse number and synaptic recruitment. *J. Neurosci. Methods* **195**, 185–193 (2011).
358. Trotman, L. C. *et al.* Pten Dose Dictates Cancer Progression in the Prostate. *PLoS Biol.* **1**, e59 (2003).
359. Schindelin, J. *et al.* Fiji: an open-source platform for biological-image analysis. *Nat. Methods* **9**, 676–682 (2012).
360. R Core Team. R: A language and environment for statistical computing. *R Foundation for Statistical Computing, Vienna, Austria* <http://www.r-project.org/index.html> (2020).
361. Mashiko, D. *et al.* Generation of mutant mice by pronuclear injection of circular plasmid expressing Cas9 and single guided RNA. *Sci Rep* **3**, 3355 (2013).
362. Truett, G. E. *et al.* Preparation of PCR-quality mouse genomic dna with hot sodium hydroxide and tris (HotSHOT). *Biotechniques* **29**, 52–54 (2000).
363. Wickham, H. *et al.* Welcome to the Tidyverse. *J. Open Source Softw.* **4**, 1686 (2019).

PUBLICATIONS RELATED TO THIS THESIS

Brosig A*, **Fuchs J***, Ipek F, Kroon C, Schrötter S, Vadhvani M, Polyzou A, Ledderose J, van Diepen M, Holzhütter HG, Trimbuch T, Gimber N, Schmoranzler J, Lieberam I, Rosenmund C, Spahn C, Scheerer P, Szczepek M, Leondaritis G, Eickholt BJ.

(2019). The Axonal Membrane Protein PRG2 Inhibits PTEN and Directs Growth to Branches. *Cell Reports* 29:2028-2040.e8. doi:10.1016/j.celrep.2019.10.039

* contributed equally

Nieuwenhuis B, Barber AC, Evans RS, Pearson CS, **Fuchs J**, MacQueen AR, Erp S, Haenzi B, Hulshof LA, Osborne A, Conceicao R, Khatib TZ, Deshpande SS, Cave J, Ffrench-Constant C, Smith PD, Okkenhaug K, Eickholt BJ, Martin KR, Fawcett JW, Eva R.

(2020). PI3-kinase delta enhances axonal PIP3 to support axon regeneration in the adult CNS. *EMBO Mol Med* 1–24. doi:10.15252/emmm.201911674

Fuchs J, Eickholt BJ, Leondaritis G.

(2020). Harnessing PTEN's Growth Potential in Neuronal Development and Disease. *Neurosci Insights* 15:263310552095905. doi:10.1177/2633105520959056

Fuchs J & Eickholt BJ.

(2021) Precursor types predict the stability of neuronal branches. *BioRxiv* doi: 10.1101/2021.04.23.441127, currently under revision

Zehtabian A, **Fuchs J**, Eickholt BJ, Ewers, H.

(2021, in preparation).

STATEMENT OF AUTHORSHIP

I hereby declare that I wrote my thesis “Studies on the function of PRG2/PLPPR3 in neuron morphogenesis” independently and with no other sources than quoted. All presented original data were generated by me unless stated otherwise (in case of collaborations or data generated under my supervision I clearly labelled the individual contributions).

Berlin,

Joachim Fuchs

ACKNOWLEDGEMENTS

This work would not have been possible without the constant support from several people. First and foremost, I want to thank Britta Eickholt for providing the opportunity for this project, and Helge Ewers for acting as my second reviewer.

I am very grateful to you, Britta, for the unquestioned security you provided regarding resources and contract, but especially also morally! You managed to create an amazing workspace environment where I could both learn from others and develop my own ideas without having to worry about contracts or conflicts. I furthermore want to thank you for initiating so many fruitful collaborations, for introducing me to the exciting world of scientific conferences, for helping me develop didactic skills by teaching medical students, and for giving me the chance to develop and share my passion for scientific practice. Last but not least, I really enjoyed our conversations about culture, politics, and practice of science. I learned a lot!

I also want to thank all present and past members of the lab for the amazing time we had both working, planking, thinking, or drinking (coffee...). Special thanks go to the PRG2-crew – Annika Brosig, George Leondaritis, Cristina Kroon, Shannon Bareesel and Fatih Ipek – and Mayur Vadhvani, Willem Bintig, Till Mack, and Juliane Schiweck for all the stimulating discussions about methods and models. Many thanks also go to Alexandra Polyzou, Vanessa Schulmann, Lars Landgraf, Nils Wachsmann, and Leandre Ravatt for bearing with me as their supervisor, for their great interest and their practical help with my ideas – and for asking so many challenging questions.

Furthermore, I want to thank our technicians Kerstin Schlawe, Kristin Lehmann and Beate Diemer as well as Katrin Büttner for the great help in the lab, be it preparing neuronal cultures or cell lines, or helping with another one of my cloning projects. Many thanks also go to Thorsten Trimbuch, Katja Pötschke and Bettina Brokowski from the Viral Core Facility of Charité for teaching me how to clone and for never getting tired answering all my questions. I am also very grateful to both the AMBIO and Leica Microscopy facilities of the Charité (especially Niclas Gimber, Jan Schmoranzer and Jörg Rösner), and Kai Murk and Amin Zehtabian for introducing me to the wonderful methodology of microscopy and image analysis.

I furthermore want to thank Julia Ledderose, Fatih Ipek, and Sebastian Rademacher for their contributions to the PLPPR3-project and my main collaborators for the CRISPR-project (Christian Rosenmund, Thorsten Trimbuch, Geert Michel, Adrian Landsberger, Charlotte Schick & Tilman Breiderhoff), for the PI3K-axon-regeneration project (Richard Eva, Bart Nieuwenhuis & James Fawcett), and for the automated-neuron-analysis (Helge Ewers & Amin Zehtabian).

Finally, I want to thank Britta, Cristina, Shannon, Juliane and Ecem for proofreading at various stages of this thesis and my friends, family and loved ones for their support!